

2014

# Dynamic electrical transport in carbon nanotubes and nanodiamond films



George Chimowa

*A thesis submitted to the Faculty of Science, University of the  
Witwatersrand, Johannesburg, in fulfilment of the requirements for  
the degree of Doctor of Philosophy.*

Supervisor


Prof Somnath Bhattacharyya

# Declaration

---

I declare that this thesis is my own, unaided work. It is being submitted for the Degree of Doctor of Philosophy in the University of the Witwatersrand, Johannesburg. It has not been submitted before for any degree or examination in any other University.

The work of other researchers is greatly acknowledged when used as references.

A handwritten signature in black ink, consisting of a large, circular, scribbled initial followed by a long, horizontal, wavy line that ends in a small loop.

---

Candidate Signature

15<sup>th</sup>

Day of

September

20 14

...Thesis for a Doctor of Philosophy Degree.

# Abstract

---

A comprehensive experimental study on alternating current (AC) electrical transport in the three forms of carbon nanotubes (CNTs) and nanodiamond films is presented. It is termed dynamic electrical transport to differentiate it from direct current measurements, which may be referred as static transport. The results and analysis are based on the scattering parameter measurements of a few horizontally aligned single, double, multi-walled carbon nanotubes and nanodiamond films. Which were measured in the frequency range 10 MHz to 65 GHz, at room and cryogenic temperatures using a vector network analyser.

The work is motivated by the fact that AC transport in 1D systems has not been fully studied and is not well understood. From direct current measurements, it is known that one dimensional (1D) electrical transport is very different from its two or three dimensional counterpart. This is because adding an electron to a 1D system tends to affect the whole system in ways which to date cannot be fully explained theoretically. CNTs present an ideal platform to study the AC or dynamic transport behaviour of 1D systems because of the high mobility and electrical conductivity at nano-scale. Therefore from the AC complex impedance and conductance, this work demonstrates quantum effects of collectively excited strongly interacting electrons (Luttinger Liquid), which had been predicted theoretically but not observed experimentally using this technique. Ballistic transport at room temperature is also demonstrated by setting the stimulus frequency higher than the scattering rate in the CNTs. A crossover from capacitive to inductive behaviour in the imaginary component of impedance has been shown by improving the CNT-electrode coupling. Furthermore the effect of metal contacts on microwave/ radio frequency transmission is also demonstrated. The results are consolidated by RF simulations, as strong conclusions are drawn.

Studies on the dynamic transport in nanodiamond films revealed a crossover from the insulating to semi-metallic regime by nitrogen incorporation. The crossover is explained by considering the changes of the grain boundary morphology. This work shows that AC transport in polycrystalline nanodiamond films is similar to DC transport.

---

---

**Dedication**

*To*

*my*

*boys*

*(Nathaniel & Ian)*

*"You can do much in anything if you put your heart and mind to it"*

# Acknowledgements

---

I know no words enough to express my sincere gratitude to all those who made this work possible. Firstly I would to thank my Supervisor, Prof Somnath Bhattacharyya for introducing me to nanoscience, providing an interesting research project and excellent facilities in his laboratory. I also want to thank the DST - NRF Centre of Excellence in Strong Materials for funding. I am thankful to Dr Z. Chiguvare and Dr D. Churochkin who helped with instrumentation and theoretical understanding of the subject, in the early days of my postgraduate work.

I am also thankful, to Prof J. Carter, Prof D. Joubert, Prof J.P. Rodrigues, Prof E.S. Haddad, Prof A. Every and Dr R. Erasmus in the school of Physics as well as the rest of the staff members. I also would like to take this opportunity to thank our collaborators namely Prof N.J. Coville – Wits School of Chemistry, Prof E. Flahaut – Toulouse, France, Prof M. Sendova – Florida, USA and Dr G. Bepete – Wits School of Chemistry.

I would like to pass my gratitude to members of the mechanical workshop who helped with their expertise during the modification and servicing of some equipment. These members include Mr C. Sandrock, Mr J. Augustine, Mr V. Govinder and Mr L. Mafemba. I also like to thank my colleagues in the Nano-scale Transport Physics Laboratory for moral support and any other discussions formal or informal. These include, Mr T. Aslan, Miss S. Ncube, Mr C. Coleman, Mr R. McIntosh, and Miss K. Sanders.

Adding to this long list, I would like to thank my friends Mr J. Kuria, who helped with some discussions during Matlab programming, and Mr K. Jakata who helped in proof reading of this thesis. I am also thankful to the following companies, DETEK for waveguide fabrication, GGB Industries, Vacutec, Concillium and ALS for technical support.

Finally I will end by passing my heart felt gratitude to my family for their support during the whole postgraduate program. It was not easy but your support alleviated the stress, above all many thanks to my maker who works in me both to will and to do.

# Table of Contents

Chapter 1 - Introduction .....	14
1.0: General Overview .....	14
1.1: Why Carbon? and Why Nano?.....	15
1.2: Objectives .....	17
1.3: Technical challenges .....	18
1.4: Thesis Outline .....	18
Chapter 2 - Literature review.....	20
2.1: General on-wafer probing .....	20
2.2: Evolution of microwave on-wafer waveguides .....	21
2.3: General scattering parameter measurements .....	24
2.4: Calibration.....	28
2.5: De-embedding techniques.....	29
2.6: General overview of dynamic electrical transport .....	31
2.6.1: Drude – Kubo- Landau to NEGF Formalisms.....	31
2.6.2: Luttinger liquid theory .....	34
2.3: Diffusive to ballistic transport.....	35
2.6.4: The transmission line approach.....	36
2.6.5: Kinetic Inductance .....	37
2.6.6: Quantum capacitance.....	38
2.7: Carbon nanotubes as HF devices.....	39
2.7.1: Electronic Properties of CNTs .....	41
2.8: Nano-diamond for HF devices .....	44
Chapter 3 – Experimental Techniques.....	47
3.1: Synthesis and Characterisation of Carbon Nanotubes .....	47
3.1.1: Single Walled Carbon nanotubes (SWNTs).....	47
3.1.2: Double Walled Carbon nanotubes (DWNTs) .....	48
3.1.3: Multi-walled Carbon nanotubes (MWNTs).....	49
3.2: Alignment of CNTs using dielectrophoresis.....	49
3.3: Calibration of the vector network analyser.....	51
3.3.1: SOLT calibration technique.....	52
3.3.2: The VNA twelve error model .....	57

3.3.3: The Open – Short De-embedding technique .....	59
3.4: Device fabrication .....	61
3.4.1: Electron beam (e-beam) lithography.....	63
3.4.2: High frequency Device SEM micrographs.....	64
3.4.3: Synthesis of nanodiamond films by hot filament CVD .....	69
3.5: Chapter Summary .....	73
Chapter 4 – Dynamic Transport in CNTs.....	74
4.0: Accuracy test measurements .....	74
4.1: RF transmission in SWNTs .....	77
4.1.1: Oscillatory Impedance in SWNT devices.....	83
4.1.2: Diffusive to Ballistic Transport in SWNTs.....	89
4.1.3: DC Measurements in SWNTs .....	91
4.1.4: RF transmission in SWNTs at cryogenic temperatures.....	94
4.1.5: RF Equivalent Circuit.....	98
4.2: RF transmission in double walled CNTs (DWNTs).....	103
4.3: RF transmission in multi-walled CNTs (MWNTs) .....	114
4.3.1: Effect of metal contacts .....	118
4.4: Chapter Summary .....	128
Chapter 5 – Dynamic Transport in Nano-diamond films .....	129
5.0: Introduction .....	129
5.1: DC Transport in nitrogen incorporated nano-diamond films - Review .....	130
5.2: AC Transport in nitrogen incorporated nano-diamond films .....	137
5.3: Chapter Summary .....	150
Chapter 6 – Conclusions .....	151
6.1: Future recommendations .....	154
Appendix.....	162
A1: Matlab code used for De-embedding waveguide parasitic .....	162
A2: Matlab code used for Simulating S-parameters .....	164
Selected Publications.....	165

# List of Figures

---

Figure 2.1: Schematic diagram of test fixture RF measurement [20].....	20
Figure 2.2: Schematic diagram of a strip line microwave – waveguide. G points to the ground plates. .....	22
Figure 2.3: Schematic diagram of a micro-strip waveguide. ....	22
Figure 2.4 : (a) Schematic illustration of CPW waveguide made of a bilayer of gold (brown layer) and titanium (grey layer). (b) Cross-sectional view of Electric and magnetic field distribution on the same CPW [23]......	23
Figure 2.5: Schematic illustration of the S- parameters for a two port measurement system. ....	25
Figure 2.6: Schematic diagram of a Smith chart. ....	27
Figure 2.7: Block diagram illustrating the total Hamiltonian for a two terminal device. ....	33
Figure 2.8: An Illustration of transition from diffusive to ballistic conduction (a) when the separation between contacts ( $W$ ) is greater than the mean free path ( $l$ ), the conduction is diffusive, (b) if ( $W$ ) and ( $l$ ) are comparable the conduction is quasi ballistic and (c) if ( $W$ ) is less than ( $l$ ), the conduction is ballistic [43]. ....	36
Figure 2.9: Schematic equivalent circuit for a classical transmission line.....	37
Figure 2.10: The cut-off frequency versus gate length for some common FET transistors in comparison to CNT FETs [65]......	40
Figure 2.11: Schematic representation of the different CNT forms. Adapted from Ref [66]. ....	41
Figure 2.12: (a) Schematic illustration of the band structure of carbon nanotubes in general. Adapted from Ref [67]. (b) An illustration of the band structure of a metallic and semiconducting carbon nanotube. ....	42
Figure 2.13: Schematic illustration of the different chiralities of CNTs. Adapted from Ref [69]......	43
Figure 2.14: Schematic illustration of the tetrahedral structure of (a) diamond, (b) Silicon and (c) Gallium arsenide [72]......	44
Figure 2.15: Output power and operating frequency currently required for specific devices in systems along with the semiconductor materials [74]. ....	45
Figure 3.1: (a) Raman Spectra of SWNTs taken at 514.5 nm optical laser excitation. The inset highlights the radial breathing mode. (b) TEM micrograph of the SWNT ropes. The two figures were adapted from reference [78]......	48
Figure 3.2: (a) Cross-sectional, (b) Translational, TEM micrographs of DWNTs. Images adapted from references [80] and [81] respectively. ....	48



Figure 3.3: TEM micrographs of MWNT samples showing that the average external diameter is about 70 nm [82].	49
Figure 3.4: Schematic diagram illustrating the setup for dielectrophoresis. A pipette is used to drop a small amount of the CNTs in solution.	50
Figure 3.5: Photograph of the S-parameter measurement set-up. It shows the VNA and semiconductor analyser that were used for HF and DC transport measurements respectively.	51
Figure 3.6: (a) Illustrating the various calibration standards as they appear on the substrate cal kit. (b) Probe placements on the cal-bars.	52
Figure 3.7: PNA E8361C displayed window for setting the stimulus properties, i.e. power, frequency range and IF bandwidth.	53
Figure 3.8: Front panel buttons of the Agilent E8361C PNA.	54
Figure 3.9: Shows the displayed window after pressing the Cal button.	54
Figure 3.10: Shows the displayed window after pressing Start Cal icon.	55
Figure 3.11: Shows the displayed window after pressing NEXT.	55
Figure 3.12: Shows the displayed window after selecting the Cal kit.	56
Figure 3.13: A typical window that shows an ideal good calibration.	57
Figure 3.14: Signal flow diagram of the forward two-port error terms. Adapted from Ref [84].	58
Figure 3.15: Illustration of the dummy structures and test structure device to be used for de – embedding.	59
Figure 3.16: Schematic illustration of the equivalent circuit models for the dummies used for de-embedding [85].	60
Figure 3.17: JEOL7001F SEM used for in-suit device fabrication making use of the e-beam writer, Gas injection system (GIS) and nano-manipulaotors.	61
Figure 3.18: SEM micrograph illustrating the process of pulling out CNTs from carbonaceous material.	62
Figure 3.19: SEM micrograph showing placing of a CNT on the SiO <sub>2</sub> substrate.	62
Figure 3.20: Schematic illustration of (a) E-beam writing- GIS system and (b) high frequency measurement set-up.	64
Figure 3.21: SEM micrograph of device MW 10 which was used for the systematic error routine tests. It shows an approximately 90 nm MWNT with platinum contacts.	64
Figure 3.22: SEM micrograph before and after making contacts on device CPt 1, which was used to investigate the effect of metal contacts.	65
Figure 3.23: SEM micrograph before and after making contacts on device CPt 3, which was used to investigate the effect of metal contacts.	65
Figure 3.24: SEM micrograph before and after making contacts on device CW 2, which was used to investigate the effect of metal contacts.	66

Figure 3.25: SEM micrograph device DW 1, showing two of the eleven individual DWNTs aligned.	66
Figure 3.26: SEM micrograph DW 1, shows five of the eleven DWNTs aligned. ....	67
Figure 3.27: SEM micrograph device DW 2, showing one of the four DWNTs aligned. ....	67
Figure 3.28: Shows the SEM micrograph of Device SW2, which had six SWNT bundles aligned across the CPW. The image shows two parallel SWNTs. The other cannot be seen because of the scale. ....	68
Figure 3.29: SEM micrograph of device SW7, which had two SWNT bundles. The other bundle cannot be seen because of the scale. ....	68
Figure 3.30: Photograph of the modified substrate back heater pointed by the arrow of the HFCVD chamber. ....	70
Figure 3.31: SEM micrograph of single ~ 1 micron (Diam 5A- 20%N <sub>2</sub> ) ND cluster. The small arrows point to the metal contacts. ....	70
Figure 3.32: SEM micrograph of multiple ND clusters (a) Diam 2 with 0% nitrogen and (b) Diam 3 with 5% nitrogen. The arrows point to the metal contacts. ....	71
Figure 3.33: SEM micrograph of multiple ND clusters Diam 5B with 20% nitrogen. The arrows point to the metal contacts. ....	72
Figure 3.34: SEM micrograph of multiple ND clusters Diam 14 with 25% nitrogen. The arrows point to the metal contacts. ....	72
Figure 4.1: S-parameter data for a MWNT sample 9 measured at different times. MW 9 B was measured 30 minutes after MW 9 A. It clearly shows that there is insignificant instrument drift with time as the data sets overlap strongly. ....	75
Figure 4.2: Shows the test done to check the effect of solvent on the S-parameter measurement. The Open data is for an open dummy waveguide with the solvent dichlorobenzene dispersed on the one micron gap. The Control is for the same dummy without the solvent. ....	76
Figure 4.3: Shows the test to check measurement reproducibility, MWNT samples 9 and 10 were measured repeatedly every time lifting up the probes. The graph shows very good reproducibility. ....	77
Figure 4.4: Schematic illustration of a CNT transmission line. The diagram is courtesy of Ref [15]. ....	78
Figure 4.5: Predicted dynamic impedance for Ohmic contacts, for two different values with two different LL parameter (g) values, Adapted from reference [15]. ....	79
Figure 4.6: Transmission coefficient (S <sub>21</sub> ) in dB for samples SW2 with 6 CNT bundles and SW7 with 2 CNT bundles. The open and short data is for the short and open dummy waveguides used to extract the waveguide parasitics. ....	81
Figure 4.7: (a) Low frequency region for the same samples SW2 and SW7 shown in Fig. 4.6, while (b) shows the high frequency region. ....	82
Figure 4.8: Real impedance of SW2 and SW7, showing oscillatory behaviour that is exponentially damped with increase in frequency. ....	84

Figure 4.9: *Real impedance of sample SW7 (black dots), fitted with Burke’s model (Red line). The graph clearly shows that the model and experimental data have almost the same period. ....* 85

Figure 4.10: *Imaginary impedance for samples SW2, SW7 and Open dummy, showing a transition from capacitive to inductive behaviour. ....* 86

Figure 4.11: *The real and imaginary impedance of sample SW7, showing a crossover of the two at around 10.3 GHz. ....* 89

Figure 4.12: *Differential conductance versus bias potential for sample SW2 at room temperature. .* 92

Figure 4.13: *Transmission coefficient of sample SW2 (with 6 CNT bundles) in the low temperature range of 80 K – 140 K. ....* 94

Figure 4.14: (a): *Transmission coefficient for sample SW2 measured in the temperature range 80 K to 140 K, show small increases in power transmission with temperature in the low frequency regime. (b) Is the same data but showing the high frequency region end. ....* 95

Figure 4.15: *Real impedance of sample SW2 at 80 K and 120 K, and shows low amplitude oscillations compared to room temperature oscillations. ....* 96

Figure 4.16: *Imaginary impedance of sample SW7 at 80 K and 120 K showing predominantly positive impedance. The transition from negative to positive occurs at much lower frequency close to 100 MHz. ....* 97

Figure 4.17: *A device equivalent circuit used to simulate the experimental S-parameters for all the devices. The circuit components  $R_1, R_2, R_3$  and  $C_1$  are the same of both input contact and the output contact.  $R_4, L_1$  and  $C_2$  are for the aligned CNTs. ....* 98

Figure 4.18: (a) *Transmission coefficient ( $S_{12}$ ) for sample SW2 fitted with the simulated data from the equivalent circuit for room temperature measurements. (b) Is the fitted data for 80 K measurements for the same sample. ....* 99

Figure 4.19: *Low temperature two terminal I-V measurements for sample SW2. ....* 101

Figure 4.20: *The main figure shows that the differential conductance for SW7 at different low temperatures collapsing to a single gradient at high bias voltages. The inset shows the power law dependence of the current at 29.5 K for SW2. ....* 102

Figure 4.21: *Transmission coefficient for samples DW 1 & 2 at room and 77K temperatures. ....* 104

Figure 4.22: *Real Impedance of DW1 at three different temperatures, it shows a reduction in impedance with temperature. ....* 105

Figure 4.23: *Imaginary impedance for DW1 at different temperatures showing a capacitive to inductive transition with temperature decrease. ....* 106

Figure 4.24: *Complex impedance of DW1, measured at 4 K. It shows a transition from diffusive to ballistic transport at about 1.5 GHz. ....* 107

Figure 4.25: *Complex impedance of DW1, measured at 77 K. It shows a crossover from diffusive to ballistic transport at around 9 GHz. ....* 108

Figure 4.26: Complex impedance of DW1, measured at room temperature. It does not show any crossover to ballistic transport as was observed from other devices. ....	109
Figure 4.27: The transmission coefficient $S_{12}$ at 293 K for sample DW1, fitted with simulation model so as to determine the circuit parameters. ....	110
Figure 4.28: The transmission coefficient $S_{12}$ at 77 K for sample DW1, fitted with simulation model so as to determine the circuit parameters. ....	111
Figure 4.29: I-V measurements for sample DW 1 and DW 11(inset) fitted with the Landauer – Büttiker equation to determine the CNT – electrode coupling strength. ....	112
Figure 4.30: Transmission coefficient of MWNTs devices MW10 and 11 with different diameters. There is no significant difference between the samples. ....	114
Figure 4.31: Magnitude of $S_{12}$ (dB), of MWNT device in comparison with the SWNT device. The inset shows the high frequency part of the data. ....	115
Figure 4.32: Real impedance of MWNT tubes, showing impedance oscillations that are exponentially damped as the frequency increases. ....	116
Figure 4.33: Complex impedance of MWNT sample MW 10, showing smooth oscillations and a crossover from diffusive to ballistic transport. ....	117
Figure 4.35: Magnitude of $S_{21}$ for platinum (Pt) and tungsten (W) samples measured before (bfc) and after (afc) the contacts were fabricated. The Short and Open data is for the Short waveguide and a blank waveguide respectively. ....	121
Figure 4.36: The phase of $S_{12}$ for MWNTs measured before (bfc) and after (afc) platinum or tungsten contacts were fabricated. ....	122
Figure 4.37: Imaginary impedance of different platinum and tungsten contacted MWNTs before (bfc) and after (afc) the contacts fabrication. ....	123
Figure 4.38: Imaginary impedance of different platinum and tungsten contacted MWNTs before (bfc) and after (afc) the contacts fabrication. ....	124
Figure 4.39: Schematic diagram illustrating the CNT-Electrode configuration and the effects of the contacts to current and voltage. ....	125
Figure 4.41: Fractional power loss relative to that of the Open waveguide for Platinum contacted sample. ....	127
Figure 5.1: DC conductance vs temperature graph showing an increase in conductance with nitrogen incorporation. The red dotted lines are WL fits. [121]. ....	130
Figure 5.2: Illustration of the effect of disorder on the conduction mechanism in nitrogen incorporated nano-diamond films. ....	131
Figure 5.3: Full width at half maxima of the Raman G-peak vs nitrogen level as well as the film DC conductivity. ....	132

Figure 5.4: Schematic illustration of a super-lattice like structure that could exist in the GB of nano-diamond films. [128].	133
Figure 5.5: Width of the Raman TRP- peak vs nitrogen level as well as the film conductivity.	135
Figure 5.6: Schematic band diagram illustrating our suggested band structure of the grain boundary in nano-diamond films [118].	136
Figure 5.7: Transmission coefficient ( $S_{12}$ ) for different nitrogen incorporated nano-diamond samples with different morphologies shown in figures 3.32 to 3.34.	137
Figure 5.8: Transmission coefficient for the “undoped” and “doped” multiple cluster samples. The short and open data is used to de-embed waveguide parasitic effects.	139
Figure 5.9: Raman spectroscopy of “doped” and “undoped” nano-diamond samples. The insets are the optical images from which the spectra were obtained.	140
Figure 5.10: Raman spectrum for the 25% nitrogen sample fitted with five Gaussian peaks to determine the FWHM of the ND characteristic peaks.	141
Figure 5.11: Resistive component of the AC impedance for Diam 3 (5%), Diam 5B (20%) and Diam 14 (25%) samples.	143
Figure 5.12: Reactive component of the AC impedance for Diam 3 (5%), Diam 5B (20%) and Diam 14 (25%) samples.	144
Figure 5.13: The real admittance of a “5% doped” sample Diam 3 fitted with the localization theory for AC conductivity.	145
Figure 5.14: The real admittance of a “20% doped” sample Diam 5B fitted with the localization theory for AC conductivity.	146
Figure 5.15: The real conductance of a “25% doped” sample Diam 14 fitted with the localization theory for AC conductivity.	147
Figure 5.16: Nyquist plots for the 5%, 20% and 25% doped samples showing a semi-circular shape for the 5% sample. The blue dotted lines are to guide the eyes.	148

# List of Publications

---

1. **George Chimowa, Emmanuel Flahaut and Somnath Bhattacharyya** – *Temperature dependent diffusive to ballistic transition in double walled carbon nanotubes in the high frequency regime* – Applied Physics Letters **105**, 173511 (2014).
2. **George Chimowa and Somnath Bhattacharyya** – *The effect of metal-contacts on carbon nanotubes for high frequency interconnects and devices* – AIP Advances **4**, 087136 (2014).
3. **Siphephile Ncube, George Chimowa, Z. Chiguvare and Somnath Bhattacharyya** – *Realizing One dimensional quantum and high frequency transport features in aligned single-walled carbon nanotubes* – Journal of Applied Physics **116**, 024306 (2014).
4. **George Chimowa, Dmitry Churochkin and Somnath Bhattacharyya** – *Conductivity crossover in nano-crystalline diamond films: Realization of a disordered super-lattice structure* – Euro- Physics Letters **99**, 27004 (2012).
5. **George Chimowa, Ella C. Liganiso, Dmitry Churochkin, Neil J. Coville, and Somnath Bhattacharyya** – *Origin of conductive crossover in entangled multi-walled carbon nanotubes filled by Iron* – Physical Review B **84**, 205429 (2011).
6. **George Chimowa, Mariana Sendova, Emmanuel Flahaut, Dmitry Churochkin and Somnath Bhattacharyya** – *Tuning the electrical transport properties of double walled carbon nanotubes by semiconductor and semi-metal filling* – Journal of Applied Physics **110** , 123708 (2011).
7. **Ella C. Liganiso, George Chimowa, Paul J. Franklyn, Somnath Bhattacharyya, and Neil J. Coville,**– *The effect of tube filling on the electronic properties Fe filled carbon nanotubes*– Materials Chemistry and Physics **132**, 300 (2012).
8. **George Chimowa, Rudolph M. Erasmus and Somnath Bhattacharyya** – *High frequency electrical transport in nitrogen incorporated nano-crystalline diamond films in the GHz regime* – **Accepted**, in Euro- Physics Letters (2015).

# Chapter 1 - Introduction

## 1.0: General Overview

The introduction of solid state electronics propelled by semiconductor materials such as silicon, germanium and gallium arsenide, has in no uncertain terms, technologically revolutionized our society. Beginning the list, from agricultural technology, broadcasting, commerce, education, medicine and all the way to zoology, electronics has had a huge positive impact. The electronic advances were preceded by some ground breaking fundamental science. Some of these were not readily accepted by the scientific community and some required a radical paradigm shift in the way we look at matter and the associated physics.

With the advancement of this technological dispensation, miniaturisation of electronic devices has been one of the key drivers of the progress. There has been mass production of devices with millions of components integrated on a square inch semiconductor chip. These new devices have low energy consumption and nano-second switching speeds. It is becoming evident, however, that the miniaturisation of these traditional semiconductors cannot continue below 20 nm without adverse consequences [1]. Yet there is a growing need for even faster speeds and lower energy consumption devices. To give an example Intel Corporation has abandoned silicon oxide as gate insulators of less than 10 nm because of leakage problems [2]. This is just one of the many problems that come with the scaling down to nano-scale of the common semiconductors. It therefore highlights the need for alternative materials if the scaling down of materials is to be continued to the edge of nano-scale.

Therefore, as the curtain is being brought down on silicon, carbon based (carbon nanotubes, graphene and nanodiamond films) materials are entering the scene and there are indications that they might out shine the traditional semiconductors [3] [4]. However before that happens, carbon materials and in particular nanodiamond, have another added advantage in that there can be synthesized on silicon or its oxide and hence offer the opportunity to marry the two technologies i.e. silicon and diamond (carbon).

Having said this, it is not surprising that the authors joined an already loaded wagon of researchers working on trying to understand some fundamental physics governing electrical transport in carbon based nano materials. This work focuses primarily on alternating current (AC), transport in carbon nanotubes and nanodiamond films.

Electrical transport (flow of charge carriers) is generally a dynamic process in the sense that the charge carriers are constantly being taken in and out of equilibrium due to many physical perturbations. In this work however, the response of charge carriers to high frequency AC signals is referred as dynamic transport, differentiating it from direct current (DC) response which may be considered as static. The two terms (AC transport or dynamic transport) will therefore be used interchangeably in this thesis.

## **1.1: Why Carbon? and Why Nano?**

Some of the best inventions of this generation, especially in medicine, owe their success from copying Mother Nature. Nature has ways of renewing and purifying itself, though slow but it has sustained the life of our planet for over 13 billion years. If we are therefore to succeed in our ambitions for “green technology”, i.e. technology that is environmentally friendly, there is need among other things for materials that are bio-degradable after disposal, consume less energy and are compatible with the human body for medicinal purposes. It is not a secret that the traditional semiconductor technology has had its issues with the disposal of e.g. cathode ray tubes, florescent tubes, and the billions of active components from electronic gadgets disposed daily, just to name but a few.

Nature has dictated that all life is hinged on carbon, and this carbon has the potential to arrange itself in so many forms giving many materials with very unique properties from the slippery and soft graphite to the hardest diamond. It is therefore not an over ambitious idea to think that carbon has the potential to make one of the best unconventional narrow gap semiconductor materials.

In fact since the discovery of nano-scale rolled up few layers of graphene (a layer of graphite) now known as single and multi-walled carbon nanotubes (CNTs) by Iijima in 1991 [5], research has shown that it is possible to make transistors using carbon which are the backbone of the electronics. A single walled CNT can be semiconducting or metallic



depending on the longitudinal roll up (known as chirality) of the graphene. This property makes it possible to make single molecular devices that are strong and flexible, and thus can be incorporated into bio-degradable plastic electronic devices that are lighter in mass.

Diamond, which is another form of carbon, has been synthesized in the laboratory since 1954 [6]. It is also known to be semiconducting if doped with boron producing films that are superconducting depending on the doping level [7]. Synthetic diamond can be produced as nano-scale grains ranging from less than 10 nm called ultra-nano-crystalline diamond (UNCD) to about 100 nm known simply as nano-crystalline diamond (NCD). The intrinsic properties of these nano-scale grains are found to be comparable with that of bulk diamond. More information on these properties and how they relate to the transport properties is discussed in later chapters. A lot of research work has shown that this material in the nano-scale can be used for drug delivery in human bodies because it is bio-compatible [8].

This research work focused on studying carbon based materials because they can be scaled down to nano-meter sizes and whilst being able to function as semiconductors with high mobility, and reliability. The technological implication of the scaling down is obvious in that it means more components can be integrated into chips that are even smaller and will use less energy. Furthermore, the high mobility in both CNTs and diamond grains make them promising candidates for fast switching devices capable of operating in the terahertz (THz) regime.

Therefore just as Sir N.F. Mott said in one of his famous talks defending a theory on electrical transport in non-crystalline materials, “.....*So in amorphous theory, as in theology, one must declare one’s faith and I will begin by saying that I believe this theorem to be true, and that one can get nowhere in understating the experiments without it.....*” [9]. In the same vein, we in the Nano-Scale Transport Physics Laboratory (NSTPL) at Wits believe (have faith) that carbon shall one day be the material of choice for the electronics industry in the not so distant future.

## 1.2: Objectives

As alluded earlier the overall objective of this work is to understand dynamic electrical transport in carbon nanotubes and nanodiamond films. This work comes at a time when a lot of research efforts has been focused on the DC transport of carbon based nano materials [10] [11] [12]. These research efforts have revealed that CNTs can exhibit ballistic (unscattered) transport, show quantised conductance at room temperature and Coulomb blockade at low temperatures [13] [14]. Theory and some DC experiments have also shown that tunnelling into a 1D system of interacting electrons is very different from tunnelling into a 2D or 3D system. All these are significant findings regarding electrical transport in CNTs. While so much is known about DC transport, it is not the same with AC transport. However, full commercial use of these materials in future electronics will still require understanding of AC transport as well. So far there have been theoretical predications on how AC transport will behave in strongly interacting electrons in a clean 1D system sometimes known as Luttinger liquid which has not been proven experimentally [15]. It appears AC transport offers additional information to electrical transport in general but unfortunately not much work has been done.

To date a number of questions are still being asked about quantum transport, such as is AC transport fundamentally different from DC transport? What is the AC conductance of a CNT? Is it also quantised? It is against this background that we endeavoured to try and get more insight about this transport phenomenon.

On the diamond side, boron doping is known to produce p-type semiconductors and the conduction mechanism is well established [16] [17]. However n-type conductivity in diamond is still not understood. Nitrogen produces a very deep donor level in diamond grains. It is now established that nitrogen incorporation in nano-diamond films produces n-type films but the exact conduction mechanism is still unclear [18]. This is another reason why this work probed these films with high frequency AC signals in an effort to get better clarity about the mechanism.

### **1.3: Technical challenges**

One of the reasons AC transport has not been investigated as much as DC transport is the complexity of the measurement techniques. In principle high frequency measurements are scattering parameter measurements and they rely on the reflection and transmission capabilities of the material under investigation. Therefore unlike DC transport, dynamic transport will require very good waveguides in which the high frequency signal can be propagated. One of the challenges is to obtain good impedance matching between the devices under test (DUT) and the waveguide. Most CNT materials are highly resistive with resistance in the  $k\Omega$  and yet the input impedance of the instrument and waveguide is usually  $50 \Omega$ .

The impedance mis-match results in very weak transmission signals and a lot of noise. It is therefore important that efforts must be made to reduce load mis-match. In cases when it cannot be avoided measurements must be repeated many times to draw any meaningful conclusions.

Another challenge is the effect of contacts and how to quantify it. The reduced dimensions of materials to nano-scale imply that the aspect of surface effects and contacts become significant making it difficult to differentiate these effects from those of DUT. High levels of accuracy are therefore a prerequisite in the dynamic transport measurements.

### **1.4: Thesis Outline**

This thesis is organised into six chapters that can be read independently, although some little background knowledge on electrical transport is assumed. The first chapter is this introductory short one. Chapter two covers some important background theory on the technique and evolution of on-wafer probing and electrical transport in general. This chapter highlights the Drude, AC model, non-equilibrium Green's formula and the transmission line approach to the Luttinger Liquid model.

Chapter three describes the technical details of how to do scattering parameter measurements using a vector network analyser, how to calibrate the instrument, how to remove parasitic effects due to the substrates as well as details of the device fabrication. It

also covers some details on the microscopy work showing some of the devices that were made and studied.

Chapter four covers all the results relating to dynamic transport in the three forms of CNTs. Single walled CNTs are discussed first and the novel results obtained are explained in relation to some theoretical predictions. The chapter also covers the results unique to double walled CNTs. The analysis of these CNTs was also aided by some computational simulations which are also covered in this segment. It then ends with a discussion on the results on multi-walled CNTs and the effect of metal contacts which was found to be universal in all CNTs.

Chapter five is dedicated to the results on the dynamic transport in nitrogen incorporated nano-diamond films. This chapter briefly reviews the DC transport findings and then using some results obtained from Raman spectroscopy makes an effort to correlate film micro-structure with the electrical transport.

Chapter Six gives the overall conclusions from the entire work. It also includes some of the published papers. An appendix has been added that gives some of the basic computer codes that were used for simulations and calculations.

# Chapter 2 - Literature review

## The art of High frequency on-wafer probing

### 2.1: General on-wafer probing

Early radio frequency characterisation of materials used fixture measurements which involve connecting large coaxial input cables of a vector network analyser (VNA) to a device as shown in Figure 2.1 below. This technique however cannot be used on planar PCB substrate because fixture de-embedding is very difficult when the DUT is very small, such as is found in nano-materials which are the subject of this thesis. Most commercial network analysers to-date use coaxial cables and hence there is a need for a new technique to handle on-wafer devices as miniaturisation moves into the nano-scale regime.

On-wafer probing was adopted in 1983 as a technique that ensures good radio frequency (RF) transition from VNA coaxial cables to substrate devices [19]. Following these inventions, a number of waveguides came into use, such as micro-strip, strip line and coplanar waveguides just to name a few. The technique uses probe tips that are usually made of tungsten which is gold plated to reduce skin effect losses. A nickel under plating is also used to prolong the life of the probe by keeping the gold from rubbing off [20].

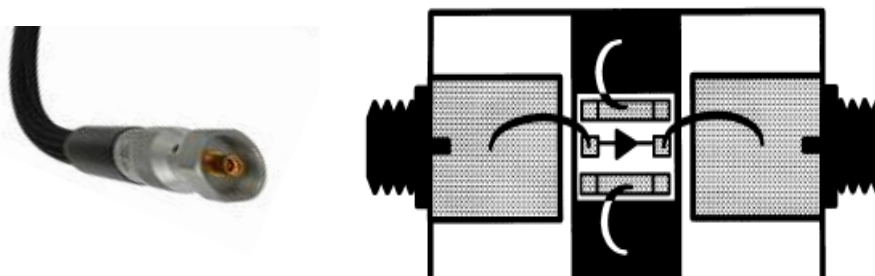


**Figure 2.1:** Schematic diagram of test fixture RF measurement [20].

In all high frequency measurements (particularly on-wafer probing) it is important to ensure good RF transition which can be achieved by ensuring [20]:

- (1) Smooth impedance ( $Z$ ) transformation from one characteristic  $Z_0$  to another.
- (2) Transformation of electromagnetic (EM) field pattern from one mode to another.

In many cases impedance matching is relatively easier to achieve (with the exception of nano-materials) and the only challenge will be the EM field pattern which can be achieved by a good choice of the best waveguide. Coplanar waveguides shown in Figure 2.4 (a) have since become a popular option for launching high frequency (HF) signals onto and off a wafer because they offer excellent transition of the RF signal from one transmission medium to another and hence proper use will give a high degree of accuracy compared to test fixturing. The section below gives a brief outline of the different on-wafer waveguides with their merits and demerits.

## **2.2: Evolution of microwave on-wafer waveguides**

Science and technology has constantly been adapting to new challenges of device miniaturisation, in radio frequency systems this has brought about an evolution of microwave waveguides. From the old (with limited bandwidth of rectangular solid waveguides) to the current popular, wide bandwidth coplanar wave guides. The transition from one waveguide to another was nevertheless not sequential in time but the improvements were a build- up process from one waveguide to another.

### **(a) Strip line waveguide**

This was probably the first step towards on-wafer high frequency measurements. It was born from the rectangular waveguide in which the two side walls were removed and the signal terminal flattened unlike the cylindrical wire found in coaxial cables [21]. A schematic diagram of the waveguide is shown in Figure 2.2. The advantages of this type of waveguide are that the two side-walls provide natural shielding from incoming spurious signals and it is also non-dispersive. The biggest set-back however, is that it is difficult to fabricate onto small devices and even more challenging for nano-materials. In addition, grounding of the top and bottom requires great care otherwise they would introduce parasitic capacitance if they are at different potentials [20].

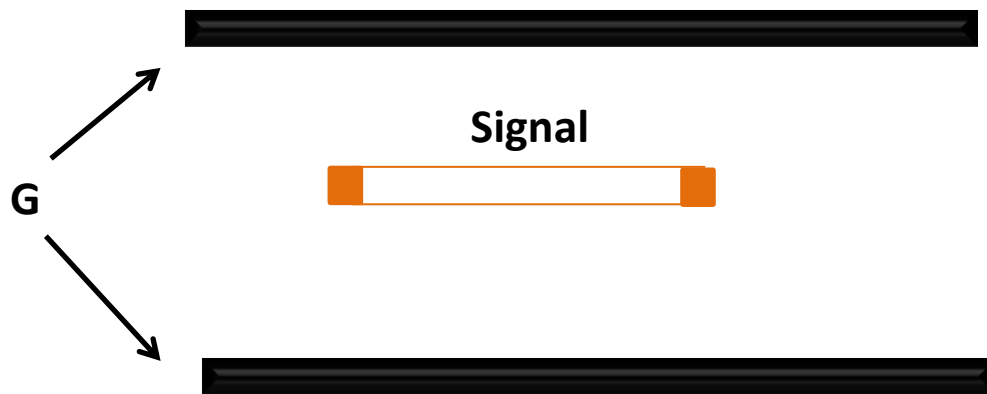


**Figure 2.2:** Schematic diagram of a strip line microwave – waveguide. G points to the ground plates.

The finite conductivity of its conductors is the main source of attenuation and the characteristic impedance depends strongly on the dielectric constant and cross-sectional geometry of the strip centre-conductor and ground planes labelled as G in the diagram.

**(b) Micro-strip waveguide**

Further modification of the strip-line removed the top sidewall, leaving only the strip at the bottom to make the micro-strip waveguide. This waveguide (shown in Figure 2.3, below) is still being used because it has an exposed signal layer making component assembly easy. It is however dispersive by nature, because the phase velocity of EM waves is different in the air above the signal conductor than through the dielectric of the material [22]. Another disadvantage of this waveguide is that the backside ground prevents the signal line from coupling to the wafer surface, shielding the signal tip from the wafer.

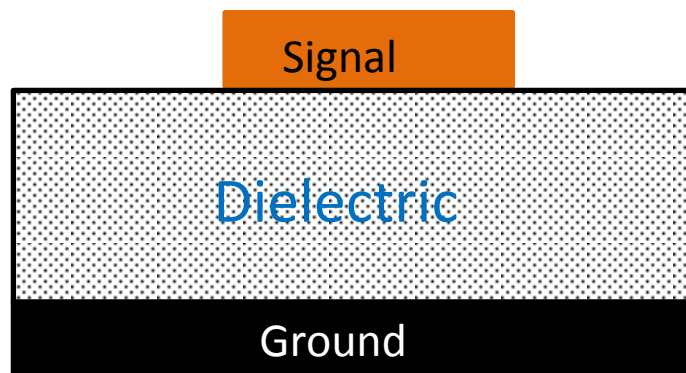


**Figure 2.3:** Schematic diagram of a micro-strip waveguide.

### (c) Coplanar waveguide (CPW)

This is by far the most common on-wafer waveguide and was used for the work discussed in this thesis. It is usually made of a bi-layer of titanium and gold as shown in the figure below (Figure 2.4). The impedance is determined by the width of the signal probe, as well as the gap spacing between the ground and signal terminals [23]. Its popularity has been primarily due to the fact that it is easy to use and calibrate. Attenuation of the signal is mainly due to skin loss and radiation. Mechanical tapering of the CPW assists in smooth transition of the EM fields from coaxial to CPW.

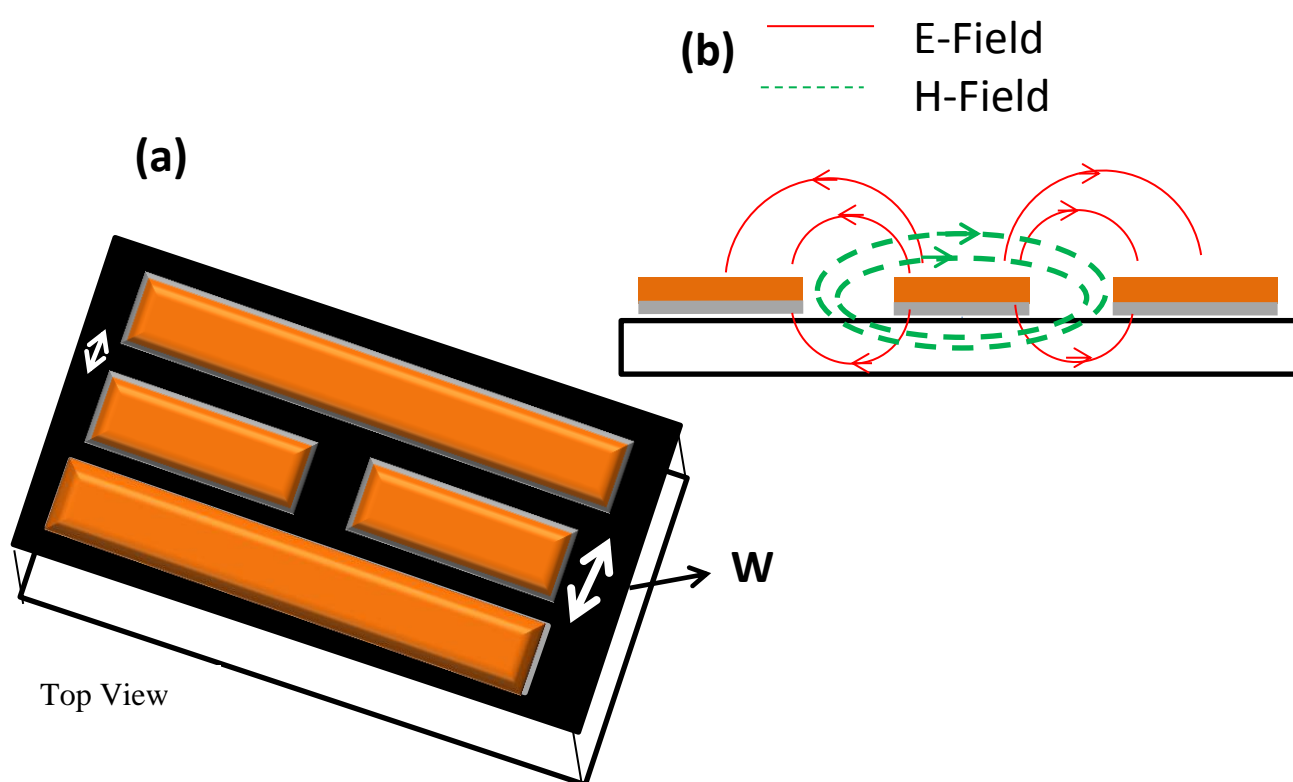


**Figure 2.4 :** (a) Schematic illustration of CPW waveguide made of a bilayer of gold (brown layer) and titanium (grey layer). (b) Cross-sectional view of electric and magnetic field distribution on the same CPW [23].

They are two common configurations of CPW i.e. ground-signal-ground (G-S-G), Figure 2.4(a) and the simple ground-signal (G-S), not shown. The G-S-G configuration has the advantage of lower ground inductance compared to its counterpart. It further controls the fields around the signal probe as shown in the schematic diagram (Fig. 2.4(b)). This balance



reduces measurement error especially when probing unbalanced load. Unlike the microstrip, the tight coupling at the G-S-G interface of CPW makes it to have less dispersion, since more of the E-field occurs in air to reduce the effective inhomogeneity of wave travel through different media [24]. Furthermore G-S-G configuration is very good in minimizing the excitation of an undesirable mode of propagation where all top side conductors form a micro strip with the bottom of the wafer [25]. This helps in modelling of results in which single mode propagations are often assumed.

G-S-G however suffers crosstalk at high frequencies which nevertheless can be eliminated by calibration if the secondary modes, radiation or extra parasitic are constant for any or all devices. Hence a clean, well designed probing system with good quality transmission-line interconnects will minimize these errors. With all these positives, it is not surprising why the G-S-G CPW was our waveguide of choice.

### **2.3: General scattering parameter measurements**

The dynamic transport properties of CNTs and nano-diamond films were probed by measuring their scattering parameters commonly known simply as S-parameters. It is therefore essential that we briefly give an overview picture of these S-parameters. They are voltage wave ratios of the transmitted or reflected wave with respect to the incident voltage wave or energy; see schematic illustration in Figure 2.5. Since S-parameters are signal flow and transmission line based, with only one mode of propagation at the device terminals being assumed it is important that multiple mode propagation is minimized to ensure a high degree of accuracy. This requirement, emphasizing the importance of good calibration and waveguide design [25].

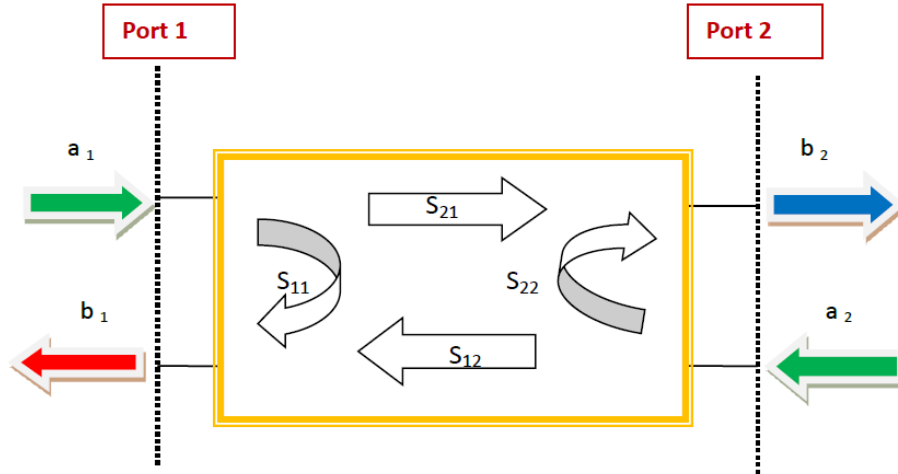


**Figure 2.5:** Schematic illustration of the  $S$ -parameters for a two port measurement system.

In Figure 2.5, the parameters  $a_1$ ,  $a_2$ ,  $b_1$  and  $b_2$  are normalized complex wave voltages. They are defined in terms of the terminal voltage ( $V_i$ ) and current ( $I_i$ ) and an arbitrary reference impedance ( $Z_i$ ) [26].

$$a_1 = \frac{V_i + Z_i I_i}{\sqrt{|\operatorname{Re}(Z)|}} \quad b_1 = \frac{V_i - Z_i^* I_i}{\sqrt{|\operatorname{Re}(Z)|}} \quad (2.1)$$

The asterisk represents the complex conjugate and  $|\operatorname{Re}(Z)|$  represents the modulus of the real part of impedance. In most measurements  $Z_i$  will be the characteristic impedance of the network  $Z_0$  of which for well-designed waveguides with matching loads it can be set at 50  $\Omega$ . The linear equations describing the two port network will then be:

$$\begin{aligned} b_1 &= S_{11} a_1 + S_{12} a_2 , \\ b_2 &= S_{21} a_1 + S_{22} a_2 . \end{aligned} \quad (2.2)$$

In the above two equations the  $S$ -parameters are then define as shown below with each output port terminated by a matched load [27].

$$S_{11} = \frac{b_1}{a_1} \quad \frac{\text{reflected}}{\text{incident from port 1}} ,$$

$$S_{12} = \frac{b_2}{a_1} \frac{\textit{transmitted}}{\textit{incident from port 1}},$$

$$S_{21} = \frac{b_1}{a_2} \frac{\textit{transmitted}}{\textit{incident from port 2}},$$

$$S_{22} = \frac{b_2}{a_2} \frac{\textit{reflected}}{\textit{incident from port 2}}.$$

In symmetric devices  $S_{11}$  will be equal to  $S_{22}$ , and  $S_{12}$  has the same value as  $S_{21}$ . It can be shown mathematically that the reflection coefficients  $S_{11}$  and  $S_{22}$  are related to the system impedance by:

$$S_{11} = \frac{Z_i - Z_o}{Z_i + Z_o} \tag{2.3}$$

This forms the basis for the Smith chart (a graphical mapping of microwave (MW) and RF data discussed in the next section).

S-parameters are commonly chosen for MW and RF measurements because they are easier to measure and work with at high frequencies than any other parameters. They do not necessarily require the circuit to be short circuited or open-circuited which is difficult to do in the RF range due to lead inductance and capacitance respectively [28]. In short, it can be said that they are analytically convenient and provide more insight about the network in question.

A vector network analyser is the workhorse for S-parameter measurement. Recent technological improvements and increased functionality of these instruments made manufacturers to give them a more descriptive name - precision network analysers (PNA). They measure vector wave ratios and so they are stimulus-response measurement systems. In other words, they determine the properties of devices rather than the properties of signals, as is done by oscilloscopes and spectrum analysers [29].

## The Smith chart

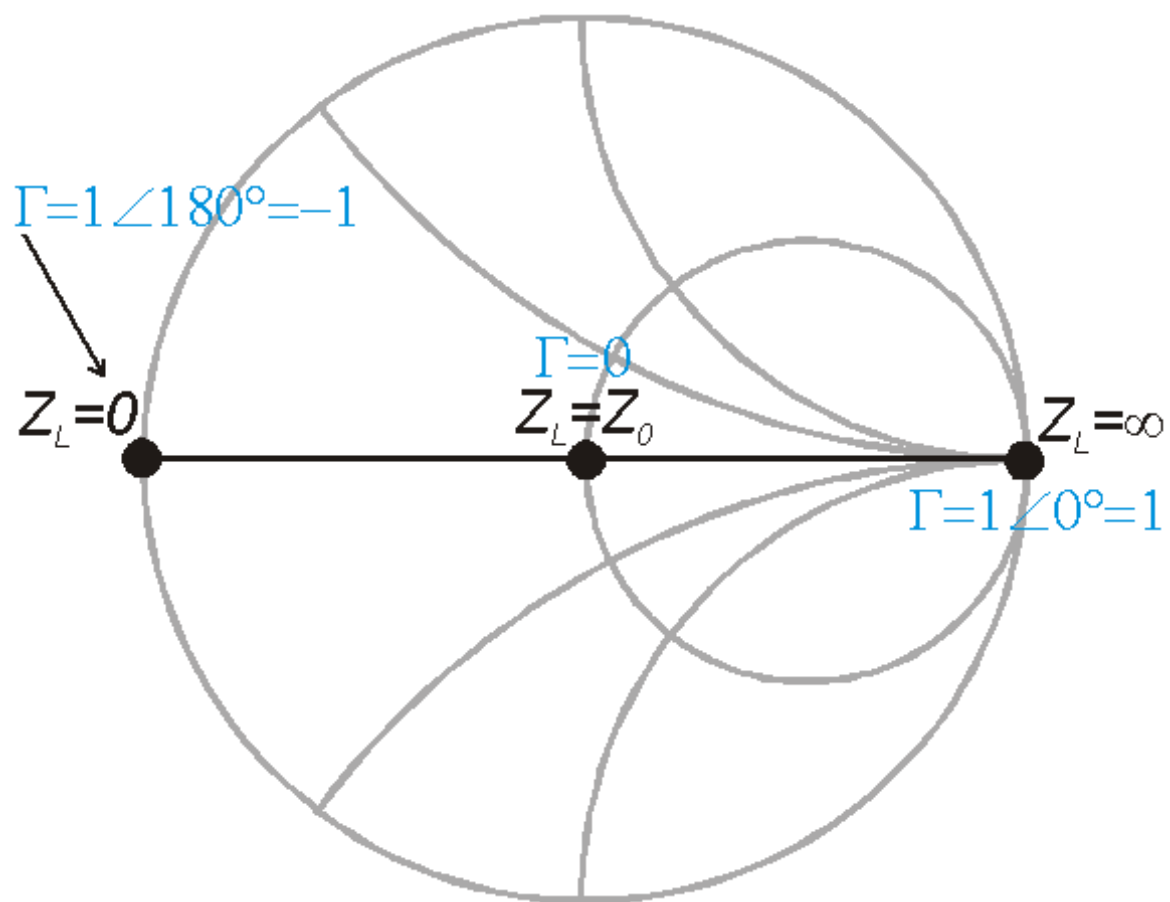


**Figure 2.6:** Schematic diagram of a Smith chart.

The Smith chart shown in Figure 2.6 is an ingenious invention by P. Smith of Bell laboratories in the 1930s for solving, calculating and displaying microwave data [30]. In principle it's a graphical mapping between two planes, the normalized impedance ( $Z$ ) and reflection coefficient ( $\Gamma$ ) plane. The circles represent constant resistance while the arcs are a representation of constant reactance. Above the horizontal line of the chart represents inductive reactance while the lower part is for capacitive reactance. At the extreme left point on the constant resistance circle is the short circuit point, while the extreme right is for an open circuit. The easiness of getting valuable information from a Smith chart during measurement makes it an ideal display format in most VNAs. For example, parasitic resonances are readily observed as circular loops with diameter which is indicative of the Q factor of resonance [31].

## 2.4: Calibration

The primary task with network measurement is to first define the “Reference plane” i.e. a boundary where measurement system ends and the device under test (DUT) begins. Normally, for on-wafer probing, it is set at the probe tips by calibration.

Calibration is the process of measuring devices with or partly known characteristics called cal-standards and using these to establish the measurement reference. It also corrects for imperfections of the system such as non-ideal nature of cables, probes and internal characteristics of the VNA itself namely directivity of couplers and crosstalk. The absolute accuracy of a calibrated VNA is determined by the technique and completeness of the error model used as well as accuracy of the calibration (cal-) standards [32].

Calibration standards are thin film resistors with known specific electrical behaviours that depend upon the probe pitch used. It is always desirable and recommended to have on-wafer standards fabricated on the same wafer as the DUT since the probe –to –standard transition can be designed to be very similar to the transition on the DUT. However, in cases where the transition to on-wafer is dramatically different from that of the cal-standard; the use of a set of dummy pads can be implemented to remove additional pad parasitics. This latter technique was used in this work. The parasitic values of pads and stubs depend heavily on the properties of the substrate (its permittivity and conductivity) as well as pad dimensions i.e. area [33]. In general if area increases, capacitance and conductance increases while inductance and resistance will decrease. In most cases capacitance is the dominant parasitic and therefore well-designed probes will result in low probe parasitic and hence wide-band measurements as well as a less rigorous calibration process.

There are two main forms of calibration techniques available:

- 1) Short-Open- Load- Thru (SOLT).
- 2) Thru- Reflect- Line (TRL).

The second technique comes in several forms such as the Line –Reflect –Line (LRL) and the Line-Reflect-Match (LRM). The choice for use will depend on the frequency range and required accuracy. We shall give a detailed account (which includes the error model) on the

SOLT and how it is done in the next chapter. Techniques that have not been mentioned in this report can be found in the following articles [34] [35] [36].

## 2.5: De-embedding techniques

De-embedding is a mathematical technique of removing probe pads and interconnects parasitic and thus shifting the reference from the probe tips to the DUT plane. Like calibration techniques, there are also two main approaches to parasitic de-embedding. For measurements done on wafers of the same dimensions and geometry as cal-standards, the VNA can be calibrated in such a manner that the de-embedding is done internally by the instrument. On the other hand if the cal-standards are different from waveguides used for device mounting then a set of dummy loads can be used.

### (a) De-embedding using the VNA

It is done by including the test fixture waveguide as part of the VNA calibration error coefficients. The process begins by defining a model that describes the DUT before the mathematics can be used to remove fixture characteristics. A typical model defines the whole network as a cascaded network of two test ports (input and output) and the DUT.



The corresponding transfer matrix for this cascaded network will be [37]:

$$T_m = [T_{IN}][T_{DUT}][T_{OP}], \quad (2.4)$$

where  $T_m$  is the measured parameter and  $T_{IN}$ ,  $T_{OP}$  and  $T_{DUT}$  are the parameters for the input fixture, output fixture and the DUT respectively. Using mathematical laws of matrices i.e. multiplying the cascaded network with inverse matrices of the two test fixtures we then obtain  $[T_{DUT}]$  which can be converted to S-parameters. The simplest model for a test fixture can be a lossless transmission line (TL) with known length; such models can be done using computer simulation software. In using the TL, the task is to shift the measurement plane to

the DUT plane by rotating the phase angle of the measured S- parameters. If the phase angles at the input and output are  $\theta_{in}$  and  $\theta_{op}$ , then the S-parameter model for the input and output will be [38]:

$$S_{IN} = \begin{bmatrix} 0 & e^{-j\theta_{in}} \\ e^{-j\theta_{in}} & 0 \end{bmatrix} \quad S_{OP} = \begin{bmatrix} 0 & e^{-j\theta_{op}} \\ e^{-j\theta_{op}} & 0 \end{bmatrix} \quad (2.5)$$

The phase angle is a function of the length of the fixture multiplied by the phase constant of the TL, while the phase constant is defined as the ratio of phase velocity and frequency in radians.

Once the simulator calculates all the S-parameters for the circuit, the data can be fed into the VNA and real time de-embedded data for the DUT can thus be obtained. An improved model will include the insertion losses of the fixture and the actual characteristic impedance of the test fixture. Further improvements can be made by a more complex but accurate model which incorporates EM simulator to include dispersion, radiation and coupling of parts [39].

### **(b) De-embedding using Dummy loads**

This was the technique utilised for this work because the cal-standards are different from the waveguides used. As a rule of thumb the more dummy structures used for de-embedding the better the measurement accuracy. In principle, an open dummy can be used to study the effects of leakage through the substrate, while a short dummy can be used to study interconnects losses. When the input impedance of DUT is large (e.g. CNTs) the probe pads become significant sources of noise. In general if DUT gets smaller, then the pad noise increases. Pad coupling to the substrate reduces DUT's gain, increases its noise figure and degrades its port-to-port isolation. The solution therefore is to: (1), design low noise pad e.g. G-S-G with oxide layer and (2), de embedding of probe pads. Further details on this de-embedding technique are given in the methodology chapter.

When the S-parameters of the DUT have been accurately determined they can then be converted to impedance or admittance data using standard equations given in reference [40]. Once this has been accomplished the analysis of the data begins by making reference to known electronic transport models. It is therefore fit that we give a brief overview of quantum dynamic (AC) electronic transport in nano-materials.

## 2.6: General overview of dynamic electrical transport

This chapter lays a foundation that will help with the understanding of dynamic transport in nano-materials which shall be discussed extensively in chapters 4 and 5.

The discussion begins by a brief overview of some of the well-established DC transport models and theories that have been successful in the past decades. This is because AC transport inherits most of its arguments from DC transport and this is why we still have some unanswered questions in physics such as, is AC transport fundamentally different from DC transport in nano-materials? What is AC impedance of a 1D wire? Is it quantised as DC conductance at small scales? [41]. The dc circuit model however breaks down at high frequency because when the wavelength is reduced to approximate circuit dimensions, lumped elements are replaced by distributed elements. It is well known that AC conductivity measurements provide more information such as electrochemical capacitance, non-equilibrium charge distribution and dynamic coupling of a device which will not be observed with DC measurements [42]. This is because increased quantum scattering leads to an enhancement in the conductance fluctuations under DC or low-frequency, which are instead washed out at high frequencies.

### 2.6.1: Drude – Kubo- Landau to NEGF Formalisms

Nano-scale science has been rapidly changing the way we think about electronic transport. It has in fact further expanded the breadth and depth of the subject. As a starting point we note that electron conduction is strongly dependent on the availability of states around the Fermi-level, which can be filled or empty [43]. This is particularly true at low temperatures and hence doing low temperature transport experiments can be seen as analogous to optical experiments using monochromatic light, i.e. it simplifies the analysis. The first known AC conductivity relation is the Drude model [44].

$$\sigma(\omega) = \frac{ne^2\tau}{m(1+\omega^2\tau^2)} - i\frac{ne^2\omega\tau^2}{m(1+\omega^2\tau^2)}, \quad (2.6)$$

Where  $m$  = effective mass,  $n$  = carrier number density,  $\tau$  = relaxation time (collision time),  $\omega$  = frequency, and  $e$  = electron charge.



The imaginary part is the kinetic inductance equal to  $\omega L_k$  where  $\omega$  is the frequency in radians. Kinetic inductance arises due to the fact that in high mobility materials the effective mass of electrons results in some initial acceleration to the effect of the bias potential. The above equation (2.6) shows that kinetic inductance becomes observable in high frequency and high mobility materials when the term  $\omega^2 \tau^2$  becomes negligible. The Drude model also shows that the real physical origin of resistance is momentum change due to collisions.

This model (Drude) was further improved by using the Kubo formalism which expresses the linear response of the current due to a time dependent perturbation [45]. A time dependent perturbation will drive the system in and out of equilibrium depending on its form. To incorporate disorder perturbations, the Kubo formula was extended to the Kubo-Greenwood formula [46].

Another transport model that has been successful has been the Boltzmann approach. While its derivation is rather complex it relates the statistical behaviour of charge carriers (treated as a gas) to the potential gradient. The Kubo and Boltzmann models are mainly based on inelastic collisions and hence they have strong energy dependence. In the coherent regime where elastic scattering dominate such as is found in nano-scale systems and at low temperatures, electron transmission dominates and therefore the Landauer approach is more appropriate, which can be expressed as shown below [2] [43].

$$I(V) = \frac{2e}{h} \int_{-\infty}^{+\infty} \frac{\Gamma^2}{(E - \Delta E)^2 + \Gamma^2} \left[ f_L \left( E - E_F - \frac{eV}{2} \right) - f_R \left( E - E_F + \frac{eV}{2} \right) \right] dE, \quad (2.7)$$

where  $\Gamma$  is the CNT-electrode coupling strength (a measure of the transparency of the contact to charge flow),  $\Delta E$  is the energy difference between the Fermi levels of the CNT and electrode.  $f_{L,R}$  are the Fermi-Dirac functions for the left and right terminals for a two probe set-up, which can be expressed as shown in equation 2.8 [43].

$$f_{L/R}(E) = \frac{1}{1 + \exp\left[\frac{E - E_f}{k_B T}\right]} \quad (2.8)$$

This Landauer formula goes beyond the Kubo approach in allowing bias voltage outside the linear response regime. This formalism was used to fit some of the  $I$ - $V$  data and gave very good insight into the high frequency transport given in chapter 4.

Since the Landauer approach does not incorporate inelastic scattering, a more generalized approach was introduced, which is the non-equilibrium Greens function (NEGF) theory,

which has today become a popular approach for high frequency AC transport. The NEGF permits full treatment of interactions and inelastic scattering. In the non-interacting limit the total Hamiltonian for a two terminal set up is given by equation 2.9 [47];

$$H_{tot} = H_L + [ V_L + H_C + V_R ] + H_R, \quad (2.9)$$

where  $V_L$  and  $V_R$  are coupling matrix elements and  $H_L$  and  $H_R$  are the Hamiltonians for the semi-infinite left and right ideal leads or terminals.

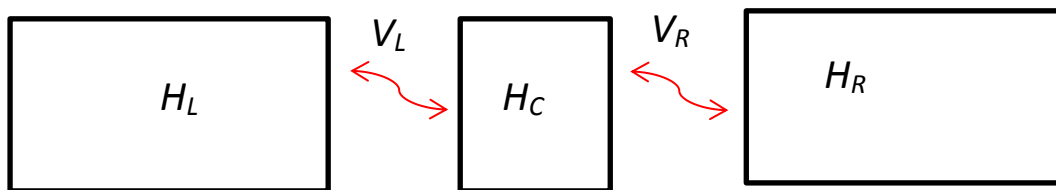


**Figure 2.7:** Block diagram illustrating the total Hamiltonian for a two terminal device.

This approach treats the three pieces described by the Hamiltonians separately unlike the other previous approaches. It is perhaps appropriate to point out that some previous theoretical work using NEGF, predicted a decrease in the real part of the conductance and an increase of the imaginary part at low frequencies below 0.5 eV, which is consistent with the Drude theory [48]. Using the same approach it has been shown that AC response shows chirality dependence in the presence of contact resistance in single walled carbon nanotubes. The imaginary part of AC conductance provides information about the phase shift between current and voltage.

## 2.6.2: Luttinger liquid theory

When the dimensions of materials are reduced from 3D to 1D, and the size approaches the de Broglie wavelength, strong correlations of fermions become increasingly important. In one dimension strongly correlated fermions are characterised by bosonic (quasi-particles that can carry the same quantum number) excitations of collective charge and spin fluctuations moving with different velocities and this state has been termed as Luttinger liquid (LL) [49]. The inhomogeneous electron interactions in 1D vary with the velocity and charge of the charge-wave excitations, which may be regarded as charge-wave reflection resulting in charge-spin separation. The charge and spin separation has become the hallmark signature of the LL. It is pointed out here, that spin-charge separation only occurs in systems with dynamical correlations [50], which can be achieved by the use of time-dependant signals. Unlike the Fermi liquid, which treats fermions as non-interacting, the LL theory incorporates these strong correlations. The boson variable describes collective excitations in the electron gas called 1D plasmons. These variables are responsible for the mass-less current flow. Since the correlations between the excitations are anomalous, they show up as interaction-dependent non-universal power laws in many physical quantities [51]. This differentiates them from ordinary metals that are characterised by universal interaction independent powers. It enables experimentalists to infer the LL behaviour from both AC and DC measurements, as was done in this work. The correlation parameter  $g$  commonly known as the Luttinger liquid parameter was determined, which is basically a ratio of single-electron charging energy to the single particle energy spacing [52].

Currently, most experimental measurements probe correlations on energy scales small compared to the Fermi energy  $E_F$  so that only the low energy sector of a given model is important [53]. In addition to that, its only in low energy that we can excite few degrees of freedom, from which we can make comparisons with theoretical models. This fact was a key component to this experimental work and it is believed it enabled the observation of some elusive quantum transport features reported in chapter 4.

Previous DC measurements have shown indirect LL through tunnelling experiments but there is still some ambiguity in these interpretations. Direct observations of the electronic states in nano-materials are therefore needed to resolve these uncertainties [53].

Luttinger liquid behaviour is known to be observable in very few systems, namely 1D electron-phonon, metals with impurities and edge states in the quantum Hall effect. This is why an investigation of this phenomenon in CNTs which are one dimensional, was done. In such 1D systems the scattering rate is proportional to the density of states so the mean free path along the channel and can be written as shown in equation 2.10 [54]:

$$l_x = l_0 \left( \frac{V_x}{V_0} \right)^2, \quad (2.10)$$

where  $V_x$  and  $V_0$  are the Fermi velocity of the material along the channel and at high energies respectively. The above expression indicates the importance of managing scattering effects in CNTs as it determines the mean free path.

In metallic systems with impurities, LL behaviour might be difficult to achieve because fermion interactions are very strong but the correlations are much weaker than what would constitute a LL system [55]. Some recent work suggests that certain impurity models do produce marginal Fermi-liquid behaviour, which is an intermediate state between Fermi and Luttinger liquid [56]. This is however, beyond the scope of this work.

### **2.3: Diffusive to ballistic transport**

As highlighted in the discussion above LL response is easily observable if the scattering mechanisms are minimised. This implies a transition from a diffusive transport mechanism to ballistic transport in which scattering is significantly less. In DC transport this can be achieved by reducing the dimensions of the conduction channel so that it is comparable to the mean free path as illustrated by the schematic diagram below [43].

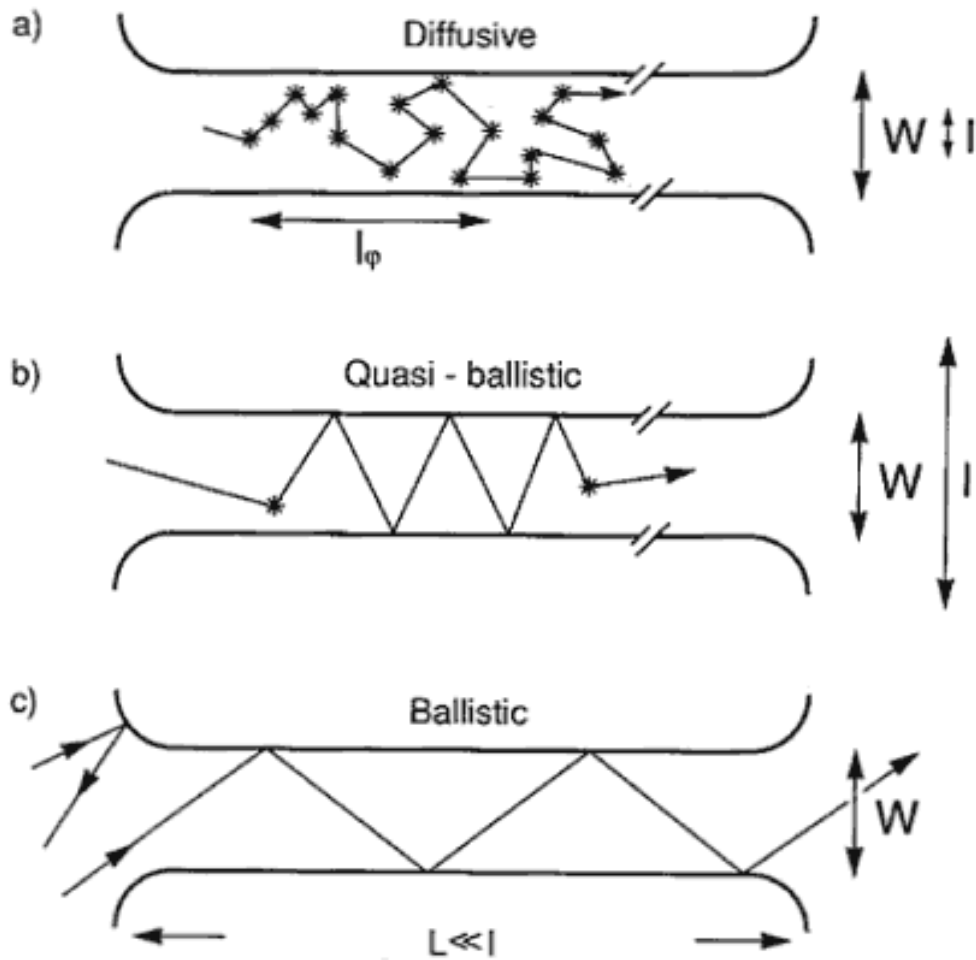


**Figure 2.8:** An Illustration of transition from diffusive to ballistic conduction (a) when the separation between contacts ( $W$ ) is greater than the mean free path ( $l$ ), the conduction is diffusive, (b) if ( $W$ ) and ( $l$ ) are comparable the conduction is quasi ballistic and (c) if ( $W$ ) is less than ( $l$ ), the conduction is ballistic [43].

In the case of AC transport, the scattering length is not the main factor but the scattering rate. This means ballistic transport can be achieved even if the mean free path is less than the conduction channel as shall be explained later.

#### 2.6.4: The transmission line approach

Having established that LL behaviour is observable in 1D systems, with a high degree of dynamical correlations of plasmons, the next major question is how then does one experimentally excite the plasmons into the LL state? The answer to this very important question was provided by a hand full of researchers [53] [57] but made famous by Peter J.

Burke of the University of California, Irvine [15], using a semi-classical transmission line approach.

In the model, Burke, suggests that, the creation of an electron is equivalent to exciting an infinite number of 1D plasmons. Therefore setting up standing wave resonances in a CNT which is incorporated in a transmission line of finite length enables one to measure the plasmon velocity and hence determine the correlation parameter for the 1D plasmon which invariably is the Luttinger liquid parameter.

An ordinary classical transmission line at low frequencies can be modelled by a telegrapher's equivalent circuit shown in Figure 2.9. In which the parameters resistance ( $R$ ), inductance ( $L$ ), capacitance ( $C$ ) and conductance ( $G$ ) are lumped components.

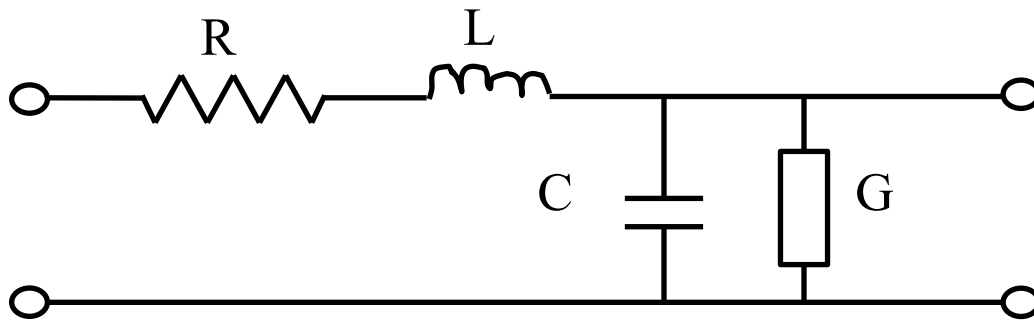


**Figure 2.9:** Schematic equivalent circuit for a classical transmission line.

At high frequency the lumped circuit model cannot accurately model the real complex impedance of the transmission line. The circuit components are instead replaced by distributed components over the whole network. If the transmission line is a nano-material with high carrier mobility two additional circuit components, the kinetic inductance and quantum capacitance are introduced to account for the quantum effects.

### 2.6.5: Kinetic Inductance

Scattering and the large number of carriers limits the drift velocity of the carriers in macro-systems. This results in the potential energy stored in the inertia of the electrons being negligible. The magnetic field created by the current dominates the inductances. In 1D systems such as CNTs however, the carrier density is low and as a result the scattering can

be low, the kinetic energy of the electrons becomes significant. The Fermi-level in metallic CNTs, intersects two bands of the 1D conduction band structure which corresponds to two modes of conduction. This two mode conduction contributes to kinetic inductance which is an important factor in high frequency applications [58].

The distributed kinetic inductance ( $L_k$ ) is calculated from the kinetic energy per unit length equated to the energy of the kinetic inductance. In physical terms  $L_k$  relates to the dwell time an electron is within the conduction channel. Kinetic energy is the sum of the left and right movers in 1D and therefore the kinetic inductance per unit length is given as in equation 2.11 [15]:

$$L_K = \frac{h}{2e^2v_F}, \quad (2.11)$$

where the symbols have their usual meanings.

When the kinetic inductance is compared to the magnetic inductance it is observed that the latter is by far too small such that it can be neglected.

### 2.6.6: Quantum capacitance

The other additional component to the transmission line is the quantum capacitance defined as in equation 2.12 [15]:

$$C_q = \frac{2e^2}{hv_F}, \quad (2.12)$$

This capacitance arises from the fact that it costs energy to add an electron to the quantum electron gas, according to Pauli's exclusion principle. It is described by the density of states at the Fermi level. This capacitance is found to be comparable to the electrostatic one and as such in quantum systems both capacitances need to be incorporated in the equivalent circuit. In nano-materials quantized energy levels result in quantized capacitance as the charge carriers in the system are noticeably discrete [59].

Having defined the additional circuit components, the wave velocity of the plasmons can be calculated using a simple equation (2.13) that has been used in RF engineering for a long time [15].

$$V_{wave} = \sqrt{\frac{1}{LC}}, \quad (2.13)$$

In 1D system the plasmon velocity for spinless non-interacting system will be:

$$V_{spinless} = \sqrt{\frac{1}{L_K C_q}}, \quad (2.14)$$

The above simple equation will enable the determination of a very important Luttinger liquid parameter after measuring the resonance frequency for the standing waves from equation 2.15 below [15].

$$f_{resonance} = \frac{V_{plasmon}}{4L} \frac{1}{g}, \quad (2.15)$$

where  $L$  is the length of the transmission line and  $g$  is the Luttinger liquid parameter.

The incorporation of kinetic inductance and quantum capacitance into the ordinary transmission line provides a window into the world of quantum effects using a semi-classical approach. Measuring the quantum capacitance, which is depended on the density of states, provides a way to experimental estimate the density of states at any desired temperature.

## 2.7: Carbon nanotubes as HF devices

After a lengthy discussion on the measurement techniques and the general electrical transport mechanisms. The attention is now directed briefly, to the properties of the material under investigation and highlights mainly those properties that pertain to electrical transport. Structurally, carbon nanotubes are a cylindrical 1D form of graphene (one layer of graphite) that can have single or multiple concentric layers. They have promising exceptional electronic and mechanical properties and this makes them ideal for high frequency devices and RF nano-electromechanical (NEMS) systems [60] [61] [62]. Their chemical inertness makes them structurally stable during fabrication processes with organic solvents that are used daily in the microelectronics industry.



Their nano-scale size and large aspect ratio means they are a bridge between the macro and the nano-world. This unveils the hidden quantized energy levels available to electron states normally blurred out in larger systems [63]. CNTs also offer greater flexibility when compared to silicon because they come in different varieties and the low dimensionality promises to be ideal in applications where power-saving, radiation hardness and heat dissipation are major concerns.

A current major limitation to their application is that the measured performance is far below the predicated intrinsic capabilities e.g. the highest measured cut-off frequency is about 40 to 100 GHz compared to the predicated 1 THz theoretically value [64] [65]. The figure below (Fig.2.10) shows the cut-off frequency versus gate length for some CNT field effect transistors (FET) compared to other standard semiconductor devices [65]. It is such challenges that are a motivation to the research community in this field.

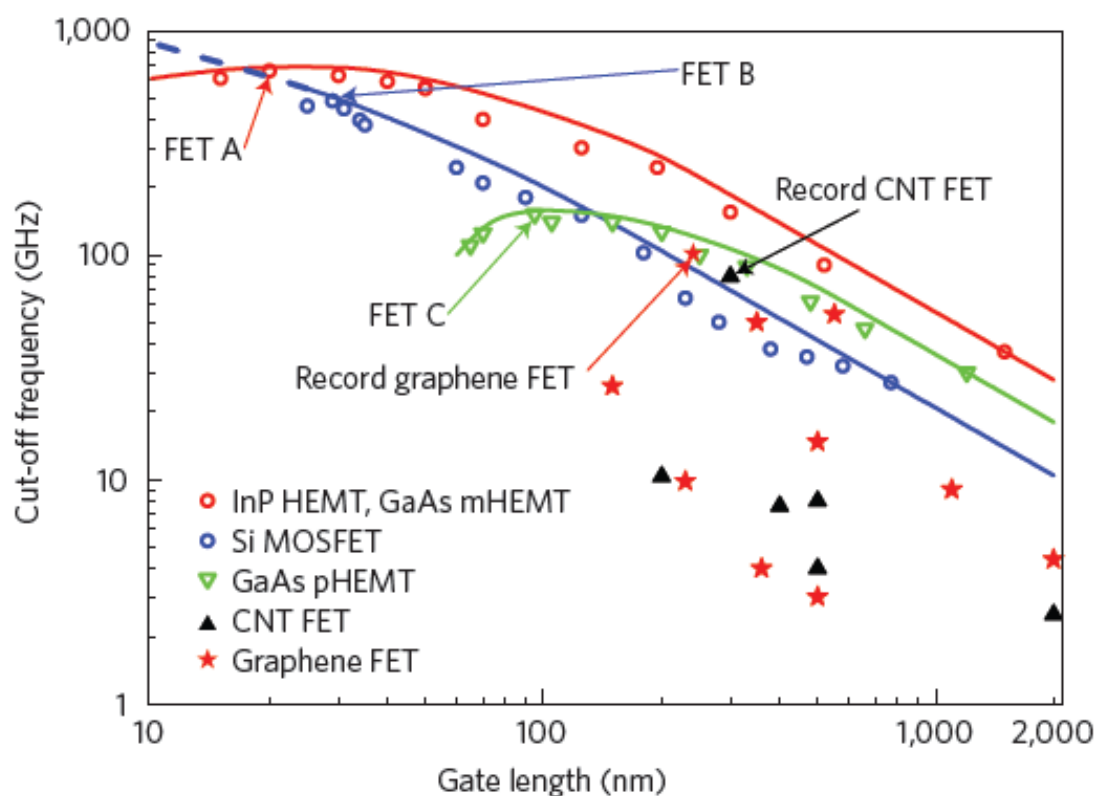


**Figure 2.10:** The cut-off frequency versus gate length for some common FET transistors in comparison to CNT FETs [65].

The variety of CNTs is in two forms, namely chiral and structural differences. The chiral differences will be discussed in the next section on the electronic properties. The number of concentric layers is what determines the different structural forms. Single walled CNTs (SWNTs), as the name implies are made from one rolled graphene layer. Double walled (DWNTs), have only two layers and are not so common because they are not easy to synthesize. Multiple walled CNTs, have many graphene layers and can be as large as 100 nm in diameter. The different forms are depicted in the schematic diagram in Figure 2.11.

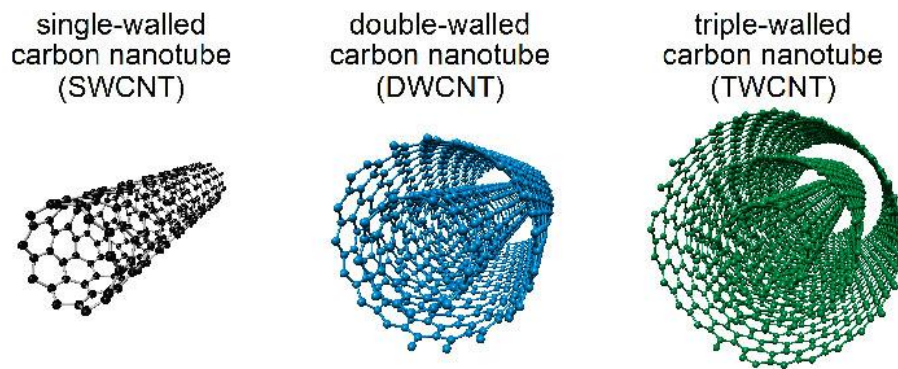


**Figure 2.11:** Schematic representation of the different structural forms of CNTs. Adapted from Ref [66].

### 2.7.1: Electronic Properties of CNTs

The chemical bonding which is primarily carbon in the  $sp^2$  hybridized form allows the coupling of the unbonded p-orbital electron with other corresponding electrons to form overlapping  $\pi$ -orbitals that are responsible for the high electrical conductivity of CNTs just like in other graphitic carbon. The electronic band structure of CNTs is therefore a modification of the band structure of graphene. The schematic diagrams in Figure 2.12 illustrate the band structure of CNTs [67].

The modification depends on how the 2D material has been rolled up [68]. The variation of the orientation of the nanotube axis with respect to the lattice vectors of the graphene wall, allows a pair of indexes  $n_1$  and  $n_2$  to be used to identify the type of nanotube. The translational vector which connects two crystallographically equivalent sites is defined as in equation 2.16 [68]:

$$C_h = n_1 a_1 + n_2 a_2, \quad (2.16)$$

where  $a_1$  and  $a_2$  are lattice vectors and  $n_1$  and  $n_2$  are the coefficients or “roll-up” vectors.

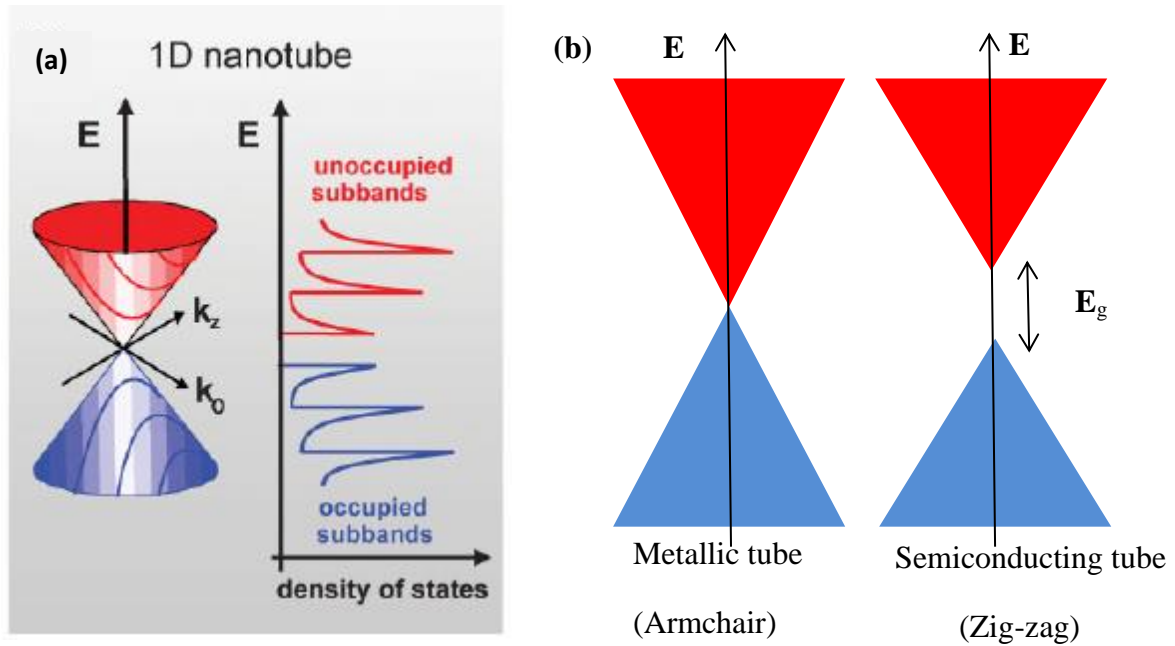


**Figure 2.12:** (a) Schematic illustration of the band structure and density of states for carbon nanotubes in general. Adapted from Ref [67]. (b) An illustration of the band structure of a metallic and semiconducting carbon nanotube.

The “roll-up” vector  $(n_1, n_2)$  represents the circumference of the nanotube relative to that lattice, such that the nanotube axis is perpendicular to it. The schematic diagram, Figure 2.13, shows the three basic possible roll-up forms of CNTs. The values of the coefficients determine the roll-up (Chirality) for example if  $n_1 = n_2$ , corresponds to armchair CNTs and are always metallic. When  $n_2 = 0$ , corresponds to zig-zag CNTs that can either be metallic or semiconducting. Any other possible values of the coefficients result in chiral CNTs.

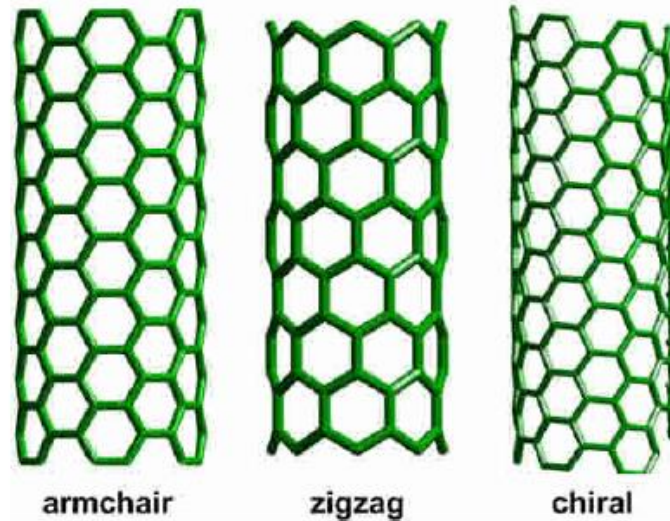


**Figure 2.13:** Schematic illustration of the different chiralities of CNTs. Adapted from Ref [69].

The length and roll-up vector are so important that they are the only two parameters that are needed to specify both the physical and fundamental electronic properties of CNTs. Preserving the periodicity around the circumference of the CNTs during the roll-up process causes quantization of the transverse wave-vector, which dictates the allowed  $K$  spacing of the sub-bands [68]. The consequence of this is on the number of sub-bands that depended on the diameter of the tube. Generally large diameter tubes will have more-sub-bands compared to smaller tubes.

Another important parameter in electron transport is the mean free path in the CNTs. At room temperature, it is known to be unusually large in comparison to what it is in other metallic materials. This is because of weak electron-phonon scattering. Electron-phonon scattering involves small energies and momentum transfers occurs very frequently at macro-scales resulting in small mean free paths even in good conductors such as copper and gold [43] [70]. The available electron states in CNTs are limited and this makes the momentum difference between the forward and backward moving states huge and therefore the majority of room temperature phonons lack the momentum to scatter such charge carriers. This results in the large mean free path in CNTs of the order of  $1\mu\text{m}$ . It is also this limited number of momentum states in CNTs that result in poor coupling with substrate phonons [70].

Another factor that makes 1D transport in CNTs unique is the nature of electron screening. In 3D systems, the interface between two 3D materials is a 2D surface and the result is a 2D dipole that forms across this interface and shields both sides of the junction. However the interface between 1D materials, is zero-dimensional and thus incapable of effectively shielding the 1D channel from the dipole field at the interface [71]. Therefore electronic effects of the junction have a huge effect on the transport in the channel for a much longer distance. This emphasise the importance of good contacts which is discussed in chapter 4.

## 2.8: Nano-diamond for HF devices

The application of diamond in active electronics has been a promising idea which propelled significant research in the field in the early 80s. The idea was born out of the knowledge that a diamond crystal is the model phase for all semiconductor materials i.e. tetrahedral bonded atomic structure see Figure 2.14.

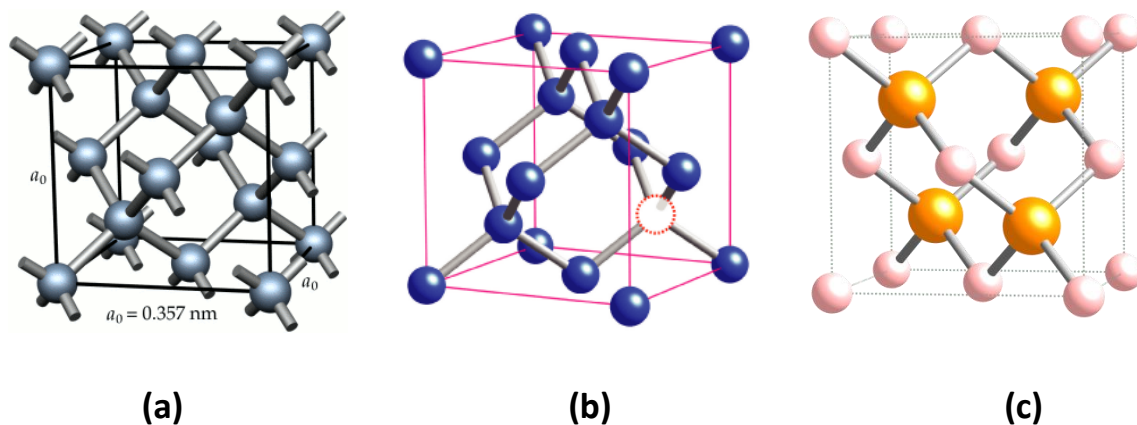


**Figure 2.14:** Schematic illustration of the tetrahedral structure of (a) diamond, (b) Silicon and (c) Gallium arsenide [72].

There was therefore much expectation that diamond would then make a good semiconductor by virtue of its structure. The expectation was further raised by the diamond's high figure of

merits used in the semiconductor industry such as the Johnson figure of merit (JFM) and the Keyels figure of merit (KFM) when compared to other semiconductor materials [73]. The JFM and KFM figures indicate diamond's potential for power microwave applications and that it is ideal for high temperature, high frequency and high power device applications. The graph in Figure 2.15 shows the potential high frequency applications of diamond compared to other semiconductor materials [74].

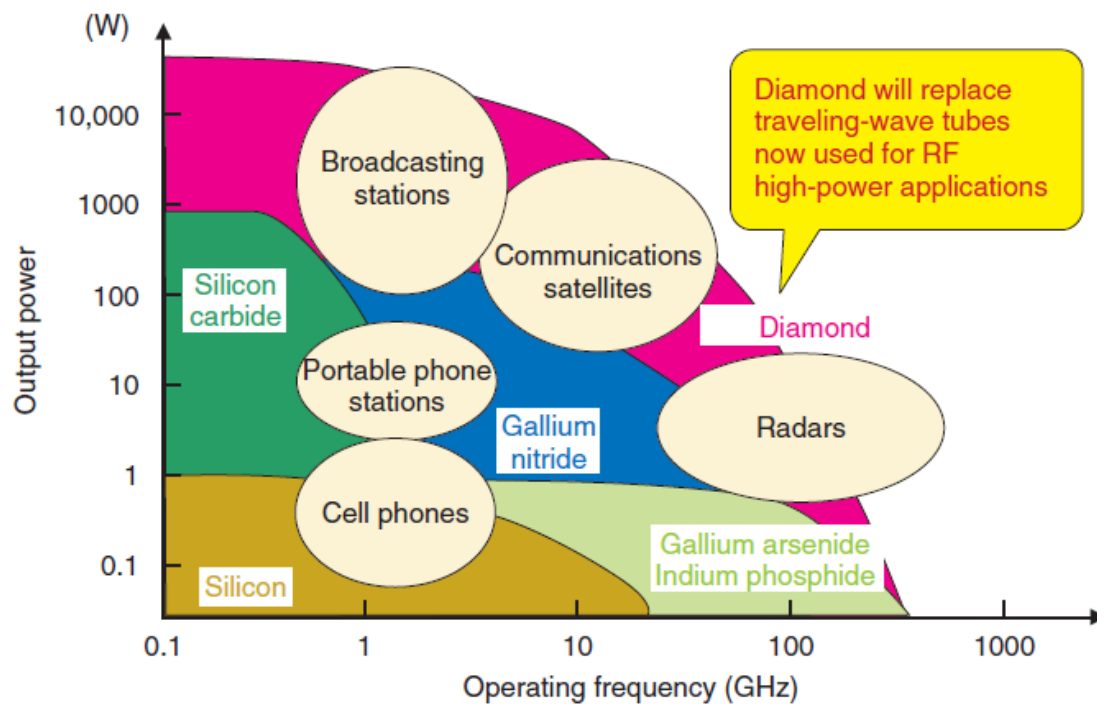


**Figure 2.15:** Output power and operating frequency currently required for specific devices in systems along with the semiconductor materials [74].

The promise however has remained, far from being realized primarily because of the failure to achieve shallow donors in diamond. Shallow donors enable conductivity to be achieved at room temperature activation i.e. 0.025 eV. Boron doping, which produces a p-type semiconductor, is 0.36 eV below the conduction band and as a result only 0.2% holes are activated at room temperature [75]. Increasing the temperature improves the conductivity but unfortunately lowers the mobility and this limits its high frequency performance.

The research community has thus shifted its attention to the passive electronic application of this material. One promising field is in RF micro-electro-mechanical (MEMs) switches with high bandwidth, high isolation and high linearity. Diamond has negligible RF losses up to

about 65 GHz [76], and the low conductivity that can be achieved allows the material to provide a conductive path for potential trapped charges when used as a leaky dielectric material. Dielectric charging (i.e. charge injected into and retained by the dielectric material) is a major problem in MEMs and the use of weakly conducting diamond films has been suggested as a possible solution [77]. An investigation on this aspect was therefore done using nano-diamond films doped with nitrogen. The use of nanodiamond is motivated by the fact that the roughness of nanodiamond films can be manipulated by varying the grain size, which is an important factor in RF MEMs. The primary focus will therefore be on the RF loss and non-zero conductivity as the frequency is increased to 50 GHz.

# Chapter 3 – Experimental Techniques

In this chapter an outline of the standard as well as the newly developed experimental techniques that were utilised to achieve the project objectives is presented.

## **3.1: Synthesis and Characterisation of Carbon Nanotubes**

The dynamic electrical transport properties of the three main forms of carbon nanotubes (namely MWNT, DWNT and SWNTs) were studied. Some of the CNTs were synthesized by colleagues in the research group (NSTPL) and some by international collaborators. A brief description of the synthesis methods is given below.

### **3.1.1: Single Walled Carbon nanotubes (SWNTs)**

Single walled carbon nanotubes were synthesized by laser ablation of a compressed graphite target composed of 1% Nickel, 1% Cobalt and 98% graphite using Spectra Pro 270 Nd:YAG laser. Argon flow rate of 200 sccm (standard cubic centimetres per minute) was used as the carrier gas to transport the SWNTs from the hot region (~ 1373 K) of the CVD chamber to the cooler ends where they were collected. The synthesised SWNTs were purified by a combination of concentrated nitric acid (2M) and refluxing for 30 hours to remove carbonaceous material. For more details on the synthesis and purification process see Ref [78].

The figures (Fig.3.1) next page shows the TEM micrograph and Raman spectra of the end product. The radial breathing mode (RBM) confirms the presence of single walled CNTs although the TEM shows external diameters of approximately 20 nm, indicating that these are not individual tubes but bundles. Previous high frequency studies of individual SWNTs have shown that the signal to noise to ratio is weak making it difficult to easily de-embed [79]. And for this reason the use of bundles was the better option in this research work with an objective to improve the signal to noise ratio.



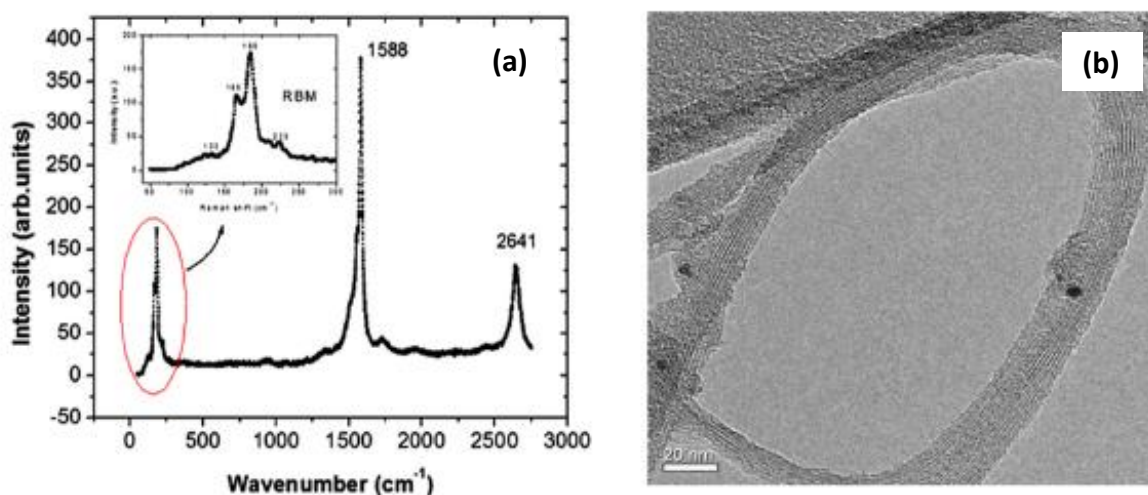


**Figure 3.1:** (a) Raman Spectra of SWNTs taken at 514.5 nm optical laser excitation. The inset highlights the radial breathing mode. (b) TEM micrograph of the SWNT ropes. The two figures were adapted from reference [78].

### 3.1.2: Double Walled Carbon nanotubes (DWNTs)

These were prepared by one of our international collaborators by catalytic vapour deposition through decomposition of a  $H_2 - CH_4$  mixture over an MgO based catalyst. Further details on the synthesis and purification of these tubes are given in Ref [80]. However two TEM micrographs are shown that illustrate the cross-sectional and translational view of the DWNTs mat.

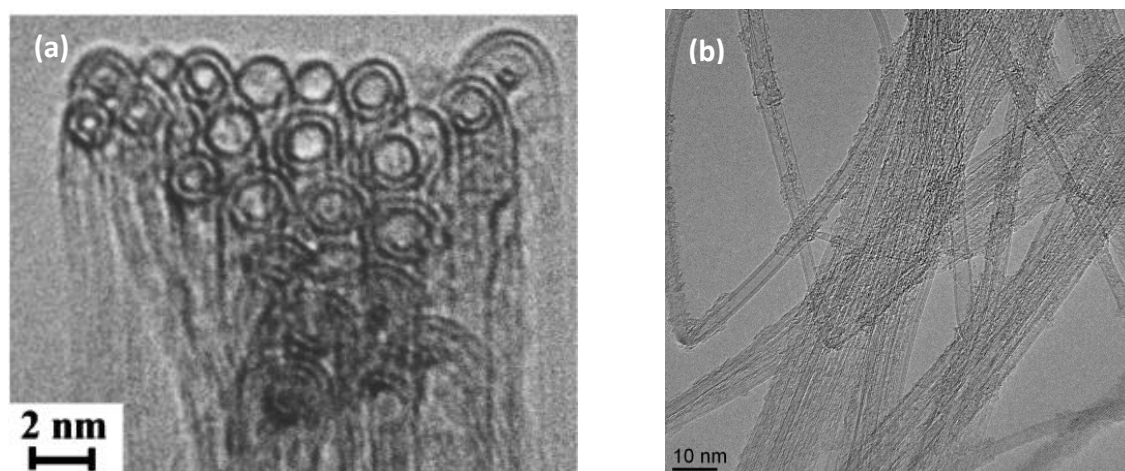


**Figure 3.2:** (a) Cross-sectional, (b) Translational, TEM micrographs of DWNTs. Images adapted from references [80] and [81], respectively.

### 3.1.3: Multi-walled Carbon nanotubes (MWNTs)

Multi-walled carbon nanotubes were synthesised in the Chemistry department at the University of the Witwatersrand using the chemical vapour deposition process. The CVD conditions were as follows: Substrate temperature of  $\sim 1200$  K, gas flow rate 600 sccm. For more details see reference [82]. The TEM micrographs below were obtained from the samples. The TEM image shows that the average external diameter is about 70 nm.

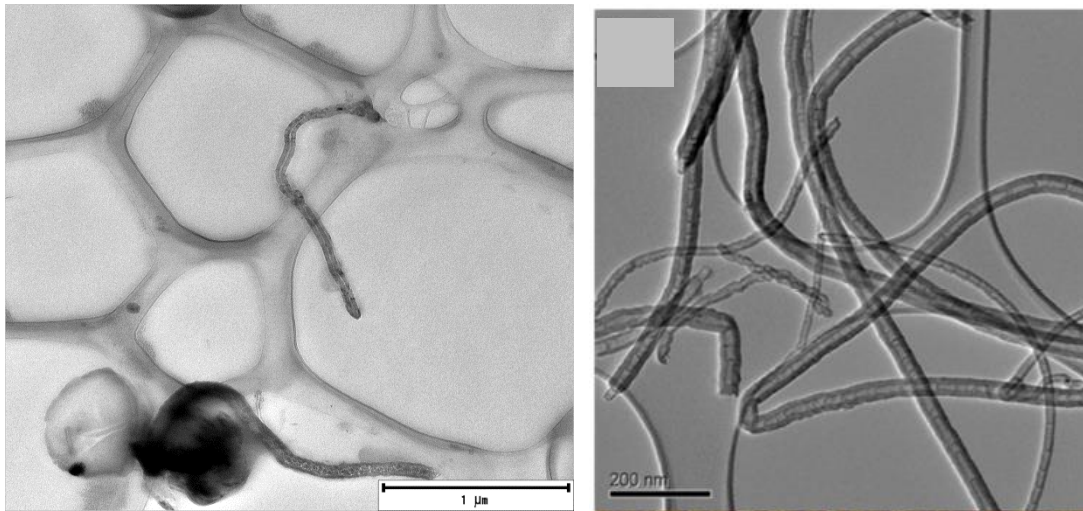


**Figure 3.3:** TEM micrographs of MWNT samples showing that the average external diameter is about 70 nm [82].

### 3.2: Alignment of CNTs using dielectrophoresis

Dielectrophoresis (DEP) was used to align CNTs that were dispersed in dichlorobenzene onto the coplanar waveguides and this technique is known to favour the alignment of predominately metallic tubes. It (DEP) is in principle the motion of uncharged particles in a non-uniform field that can be polarizable [83]. The alignment is necessitated by the interaction of the electric field with the dipole induced in the particles. Alternating current is known to be better than its direct current counterpart in two ways. Firstly, it suppresses electrophoresis (due to surface charges that occur in suspensions) and secondly using two-layer capacitive actuation of the electrodes prevents burning of the CNTs after they have bridged the signal gap of the waveguide [83].

In electrostatics, nanotubes can be approximated to prolate ellipsoid and hence the electric field ( $E$ ) making angle theta ( $\theta$ ) is given by equation 3.1 [38]:

$$\mathbf{E} = E(\sin \theta \mathbf{e}_y + \cos \theta \mathbf{e}_z) \quad (3.1)$$

In this same vein the torque on the nanotubes is given by:

$$N = \frac{v}{2} [\varepsilon_p - \varepsilon_m] \left[ \frac{1}{1 + L_y (\varepsilon_p - \varepsilon_m) / \varepsilon_m} - \frac{1}{1 + L_z (\varepsilon_p - \varepsilon_m) / \varepsilon_m} \right] E^2 \sin 2\theta \mathbf{e}_x \quad (3.2)$$

Where  $\varepsilon_p$  and  $\varepsilon_m$  are the effective permittivity of the nano-particle and medium respectively, and  $v$  is the potential across the tube and  $L$  is the length [38]. These two equations show that the nanotubes will rapidly align with the electric field.

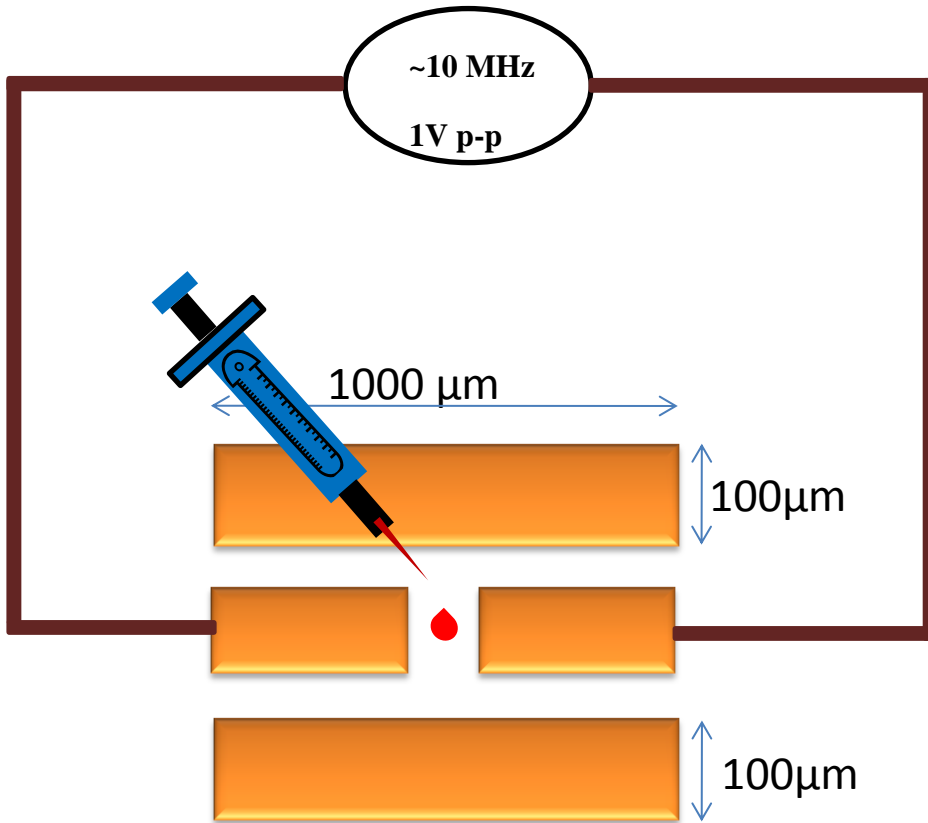


**Figure 3.4:** Schematic diagram illustrating the setup for dielectrophoresis. A pipette is used to drop a small amount of the CNTs in solution.

The schematic diagram Figure 3.4 shows the experimental setup for dielectrophoresis. A pipette was used to drop CNTs in solution and an alternating signal of 10 MHz and 1 Volt peak to peak was used to align CNTs across the signal terminal of the waveguide.

### 3.3: Calibration of the vector network analyser

High frequency measurements begin by calibration of the vector network analyser (VNA) which is the workhorse of S-parameter measurement. Proper calibration of the instrument is one of the important keys to ensure accurate measurements. An Agilent E8361C shown in the figure below (Fig.3.5) equipped with GGB microwave on-wafer probes mounted onto a Janis micro-manipulated cryogenic probe station was used. The instrument has measurement capability from 10 MHz to 65 GHz at both room and low temperatures. It is also equipped with a 3 T superconducting magnet which allows the measurement of devices in high magnetic fields and low temperatures down to 4 K. The coaxial cables of the VNA are connected to a specialized set of 70 cm MW probes with G-S-G probe tips which enables on-wafer measurements to be done. These long probe extensions require good calibration that incorporates port extension subtraction, which is a new added functionality in modern VNAs.

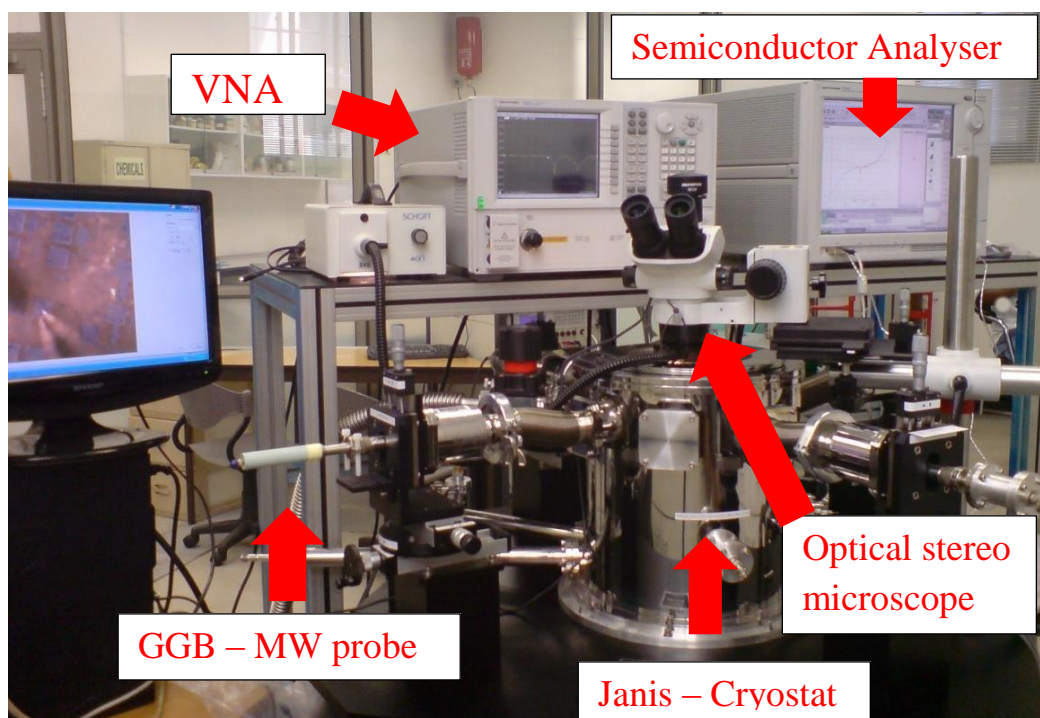


**Figure 3.5:** Photograph of the S-parameter measurement set-up. It shows the VNA and semiconductor analyser that were used for HF and DC transport measurements respectively.

All S-parameter measurements were done in a dark cryostat under vacuum of  $10^{-5}$  mbar to try and eliminate photon assisted tunnelling which complicates the analysis. The stimulus

power was set at -17 dBm for both probes which is equivalent to 31.6 mV so that the AC current is below saturation and ensure we promote low energy excitations. The measurements were done from 0.01 to 50 / 65 GHz and the Intermediate Frequency (IF) bandwidth was reduced to 500 Hz to improve the accuracy by reducing random noise from the VNA. A standard Short-Open-Load-Thru (SOLT) calibration technique was implemented for all measurements.

### 3.3.1: SOLT calibration technique

As highlighted in chapter 2, the purpose of calibrating the instrument is to set the reference point of the signal at the probe tips. It is achieved by measuring standard known calibration substrates from which 12 error parameters are obtained and used to correct for signal and phase delay due to the coaxial and probe extensions. In this work the SOLT was used for calibration using the GGB Industries Ltd's CS – 15 cal kit.

The cal-standards are implemented by contacting one of the corresponding bars see schematic diagram below (Fig. 3.6).

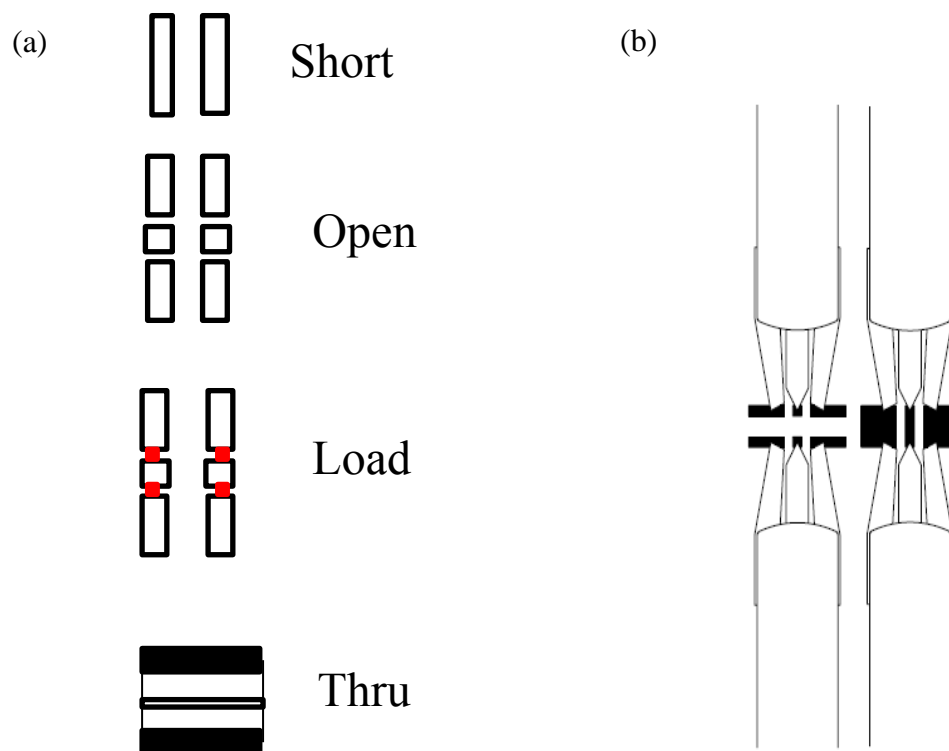


**Figure 3.6:** (a) *Illustrating the various calibration standards as they appear on the substrate cal kit.* (b) *Probe placements on the cal-bars.*

The matched load consists of a pair of precision 100  $\Omega$  thin film (in red in Figure 3.6) to provide 50  $\Omega$  termination, accurate to 0.25% at low frequencies. The capacitance of the open, the inductance of the short and the inductance or capacitances of the loads are entered into the instrument for automatic de-embedding of these parasitic effects.

In this next section, a step-by-step calibration process is described. After switching ON the instrument, the stimulus properties are set, by clicking the stimulus icon shown below. These include the power and the frequency range as well as the IF bandwidth as indicated on the window (Figure 3.7) shown below.

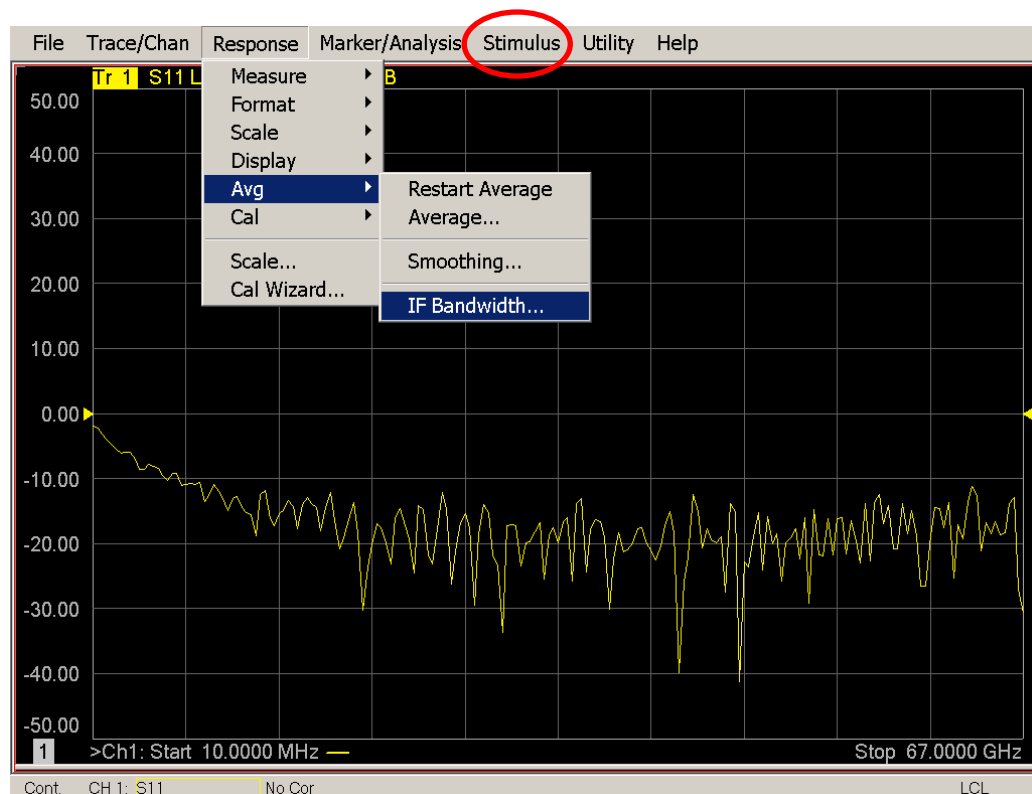


**Figure 3.7:** PNA E8361C displayed window for setting the stimulus properties, i.e. power, frequency range and IF bandwidth.

The intermediate frequency (IF) bandwidth is reduced to about 500 Hz for a frequency range of 10 MHz to 50 GHz. This improves the accuracy by reducing random noise as the instrument sweeps slowly through the chosen frequency band. After setting the stimulus properties, the calibration process was then started by pressing the Cal button on the left hand side of the VNA front panel see Figure 3.8, next page.



**Figure 3.8:** Front panel buttons of the Agilent E8361C PNA.

After pressing the Cal button, the instrument will display the window below:

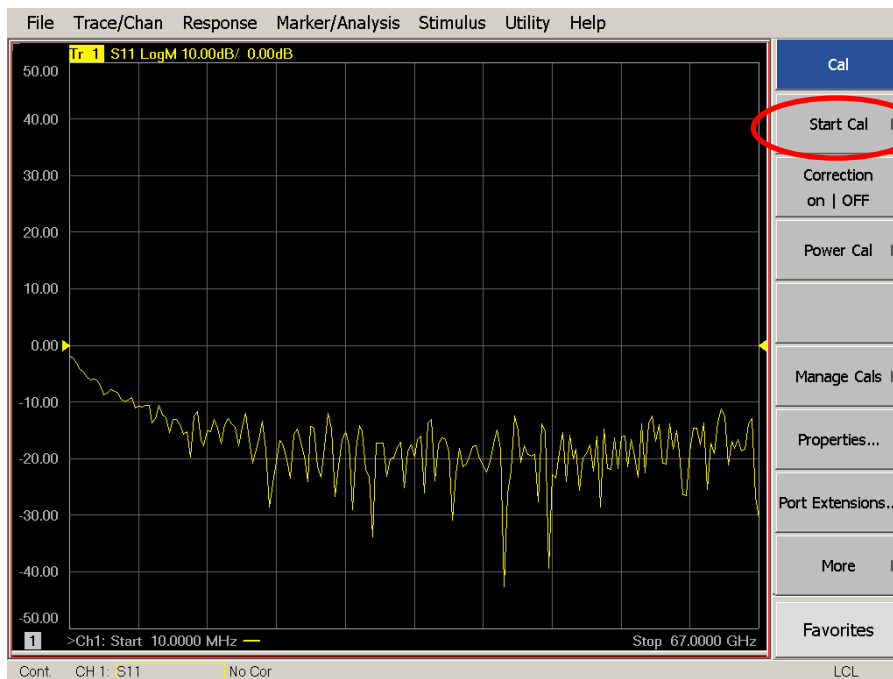


**Figure 3.9:** Shows the displayed window after pressing the Cal button.

On this window (Figure. 3.9), the Start Cal icon was clicked and the Instrument displayed a new window shown in Fig. 3.10.

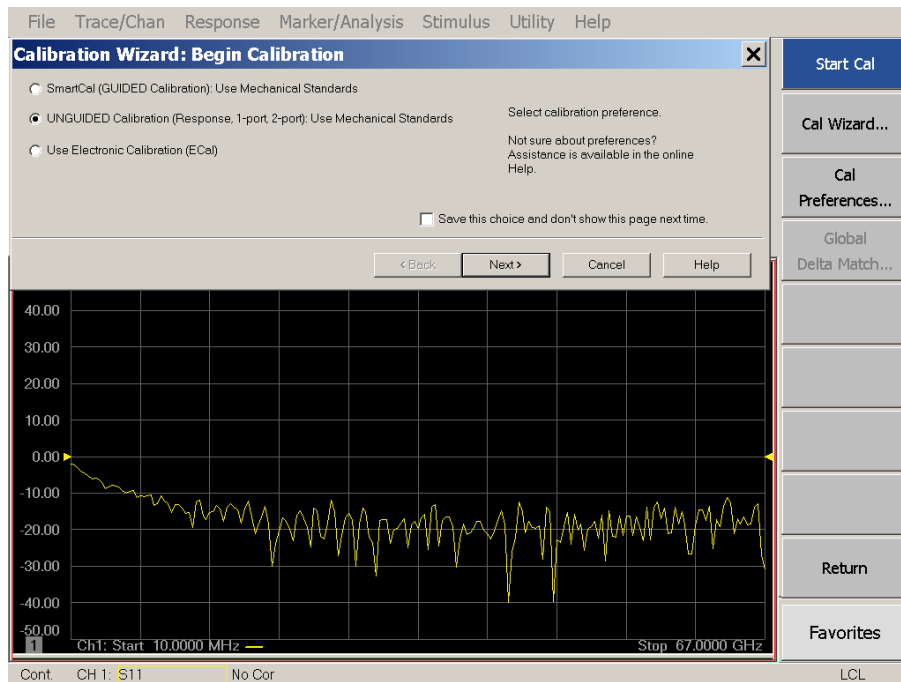


**Figure 3.10:** Shows the displayed window after pressing Start Cal icon.

The unguided calibration was selected followed by clicking next icon and the instrument displayed the window below.

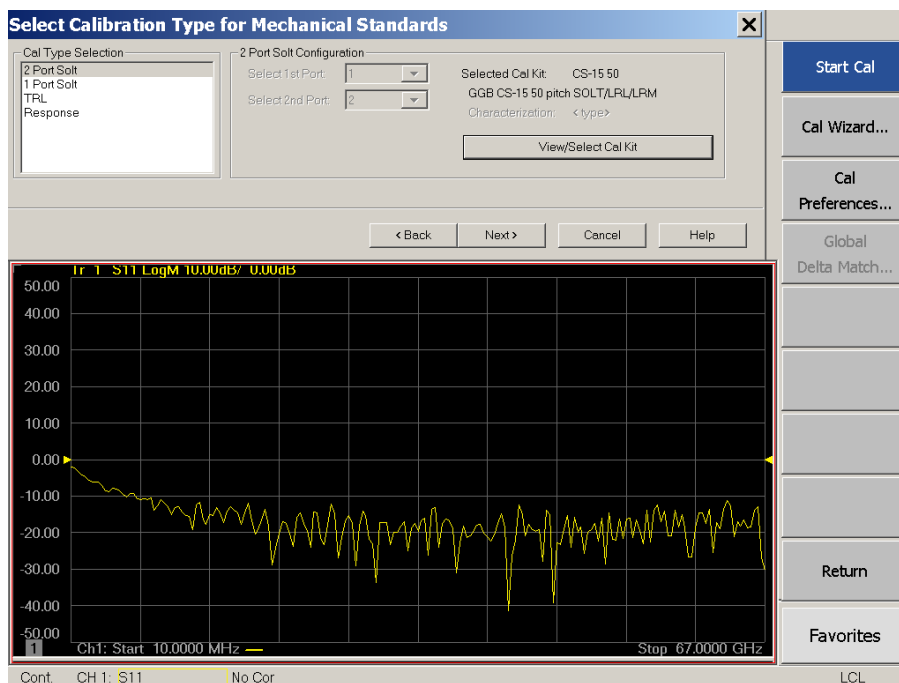


**Figure 3.11:** Shows the displayed window after pressing NEXT.

For two probe calibration the 2 Port Slot was selected, followed by the calibration standard chosen by clicking the view/select cal kit icon and then next.



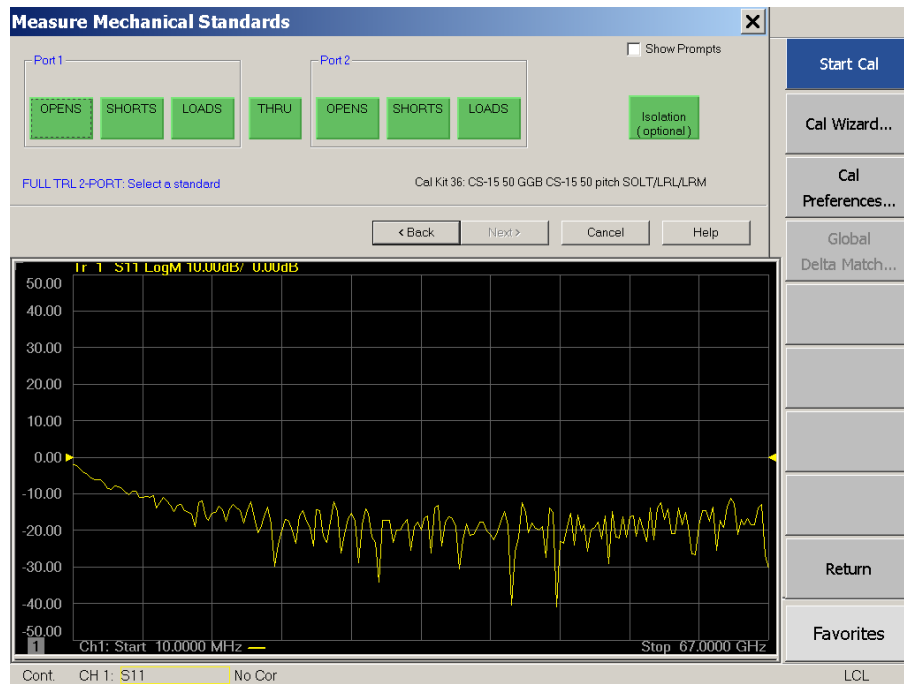


**Figure 3.12:** Shows the displayed window after selecting the Cal kit.

The calibration was then done by first landing the probes on the appropriate calibration standard and then clicking the corresponding software icon. At every stage the changes on the spectra were noted. Caution was exercised to avoid excess pressure on landing the probe as this could damage both the probe and the calibration substrate. A useful technique was to land the probe about 10 microns before the Cal standard and then allow the probe to slide forward as the pressure was applied gently. During two probe calibrations the distance between the probes was always kept constant so as to ensure the crosstalk error signal remains constant for improved accuracy during de-embedding. The thru Cal standard was the last standard measured. In the event that a certain Cal standard had to be repeated it was done at any time and the previous Cal would be overwritten. When all the standards were measured, the calibration was saved and used only at later stage if the stimulus parameters were still the same and the atmospheric conditions had not changed as well. The picture next page shows a typical window in the Smith chart format after an ideal calibration when all the probes are lifted. The transmission parameters  $S_{12}$  and  $S_{21}$  are small dots at the  $50 \Omega$  point of the Smith chart and the reflection parameters are on the extreme right as very small dots indicating open probes.

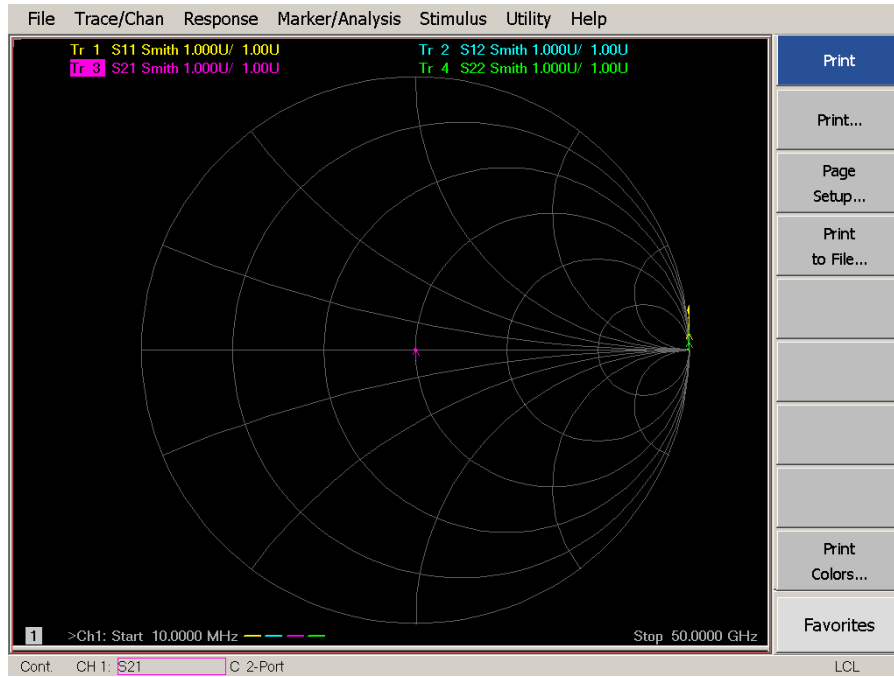


**Figure 3.13:** A typical window that shows an ideal good calibration.

After obtaining such a typical calibration setting, the calibration was confirmed by measuring known standards with known parameters, using one of the standards that were not used for calibration.

### 3.3.2: The VNA twelve error model

Measurement errors are unavoidable in any network analysis, but proper calibration and de-embedding can significantly reduce these errors. Systematic errors, which are normal due to non-ideal measurement system, can easily be removed as they are repeatable. The directivity of VNA couplers, cable losses and load mismatches are some of the common systematic errors encountered in microwave measurements. A two port measurement system can be modelled with twelve errors that are characterised during system calibration and removed mathematically [84]. Six of the errors are associated with the forward transmission signal and the other six deals with the reverse signal. The diagram Figure 3.14 is a schematic illustration of forward signal two port error model, curtsey of reference [84].



The error terms (last page) can be modified if fixture or probe pads are added to the system, between the VNA and the DUT.

### 3.3.3: The Open – Short De-embedding technique

This is one of the common techniques that have been used to remove RF parasitic effects by electronic Industrial companies for simple coplanar waveguide structures. In the case of gated or multiple port devices, many dummy calibration devices will be required. The simplicity of our devices enabled us to use the Open – Short technique because the approximation used are sufficient to describe accurately our devices.

The technique involves measuring three structures the Open dummy, Short dummy and the thru which is in this case the structure with the device under test (DUT). The diagram (Figure 3.15) below illustrates the structures including the actual device to be measured (DUT).

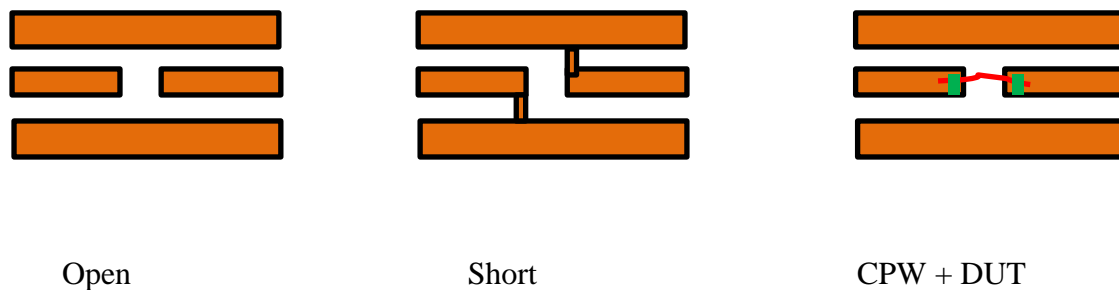


**Figure 3.15:** *Illustration of the dummy structures and test structure device to be used for de-embedding.*

The dummies in Figure 3.15 can accurately be modelled by the equivalent circuits shown in the next page.

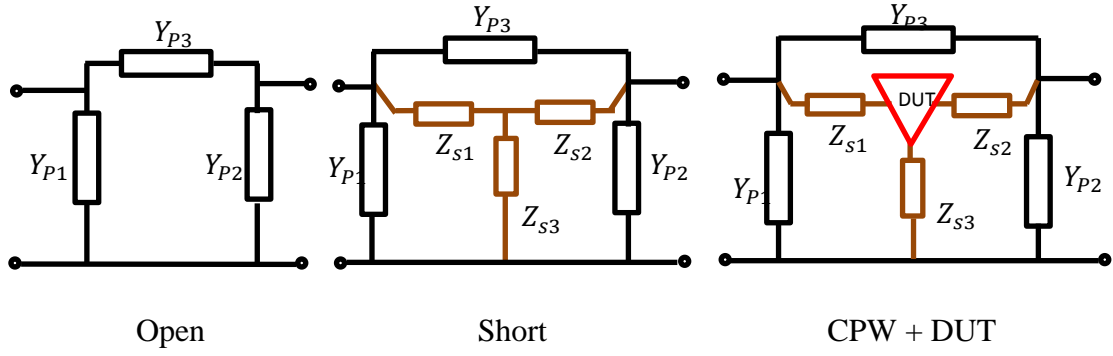


**Figure 3.16:** Schematic illustration of the equivalent circuit models for the dummies used for de-embedding [85].

By measuring the Open dummy, parasitic elements  $Y_{P1}$ ,  $Y_{P2}$  and  $Y_{P3}$  can be determined through making comparison with  $\pi$ -circuit parameters as shown in the matrix equation (3.4) below [85].

$$Y^{Open} = \begin{bmatrix} Y_{11} & Y_{12} \\ Y_{21} & Y_{22} \end{bmatrix} = \begin{bmatrix} Y_{P1} + Y_{P3} & -Y_{P3} \\ -Y_{P3} & Y_{P2} + Y_{P3} \end{bmatrix} \quad (3.4)$$

These parasitic elements can then be removed from the Y parameters of the short dummy i.e.  $Y^T = Y^{Short} - Y^{Open}$ . The short interconnects are then removed by comparing with a T- circuit after converting the  $Y^T$  to  $Z^T$  as shown by the matrix equation (3.5) below.

$$Z^T = \begin{bmatrix} Z_{11} & Z_{12} \\ Z_{21} & Z_{22} \end{bmatrix} = \begin{bmatrix} Z_{S1} + Z_{S3} & Z_{S3} \\ Z_{S3} & Z_{S2} + Z_{S3} \end{bmatrix} \quad (3.5)$$

The Y- parameters of the DUT can be obtained by subtracting  $Y^{Open}$  from  $Y^{DUT}$ . The whole process can be summarised by the equation (3.6) below.

$$Y_{DUT} = [(Y_{msd} - Y_{open})^{-1} - (Y_{short} - Y_{open})^{-1}]^{-1} \quad (3.6)$$

In equation 3.6, -1 implies the inverse of the matrix and  $Y_{msd}$  is the admittance of the measured device (DUT plus waveguide).

### 3.4: Device fabrication

A significant time on this project was spent fabricating devices, using both conventional and some newly developed technique. The rationale behind the new technique used particularly for nano-diamond (ND) high frequency devices was to avoid wet-processes that would alter the grain and cluster boundaries regions of the polycrystalline films. It is therefore appropriate to dedicate a small section of this thesis to outline these procedures and give a visual appreciation of some of the devices that were used for this work. Primarily the fabrication process was done using the JEOL 7001F SEM equipped with Kleindiek - nano-manipulators, Omni-probe - Gas injection system (GIS) and Raith - Elphy electron-beam writer software see Figure 3.17.

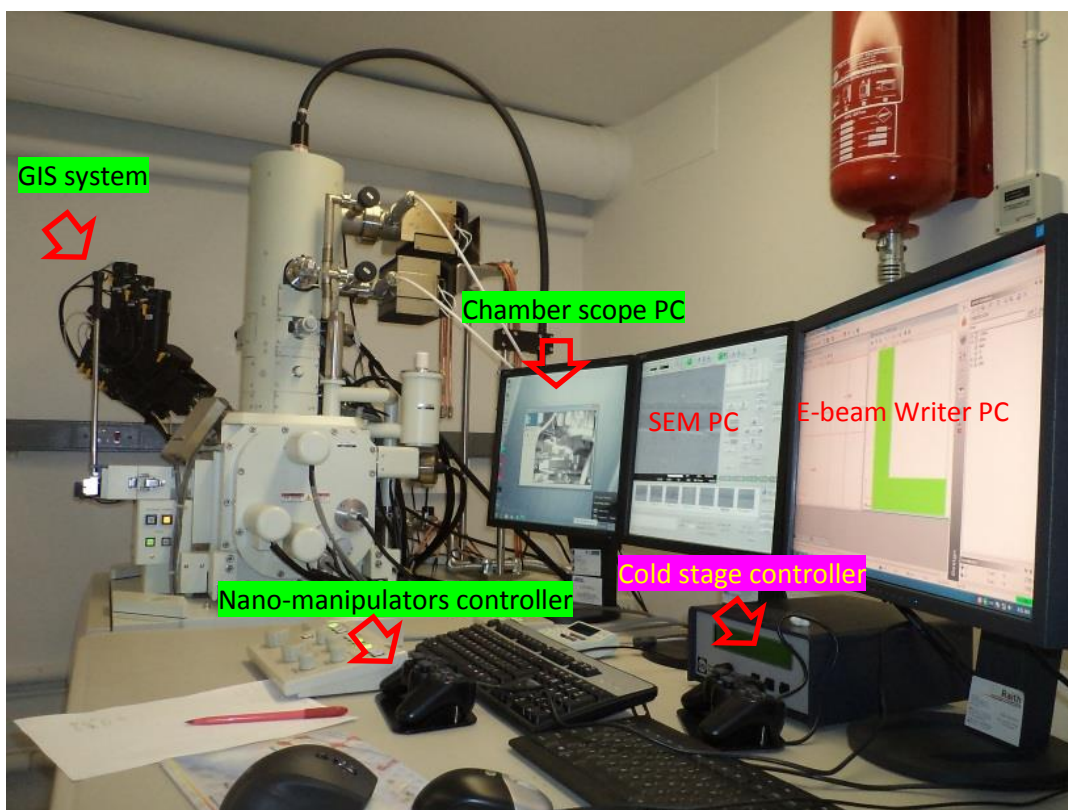


**Figure 3.17:** JEOL7001F SEM used for in-suit device fabrication making use of the e-beam writer, Gas injection system (GIS) and nano-manipulaotors.

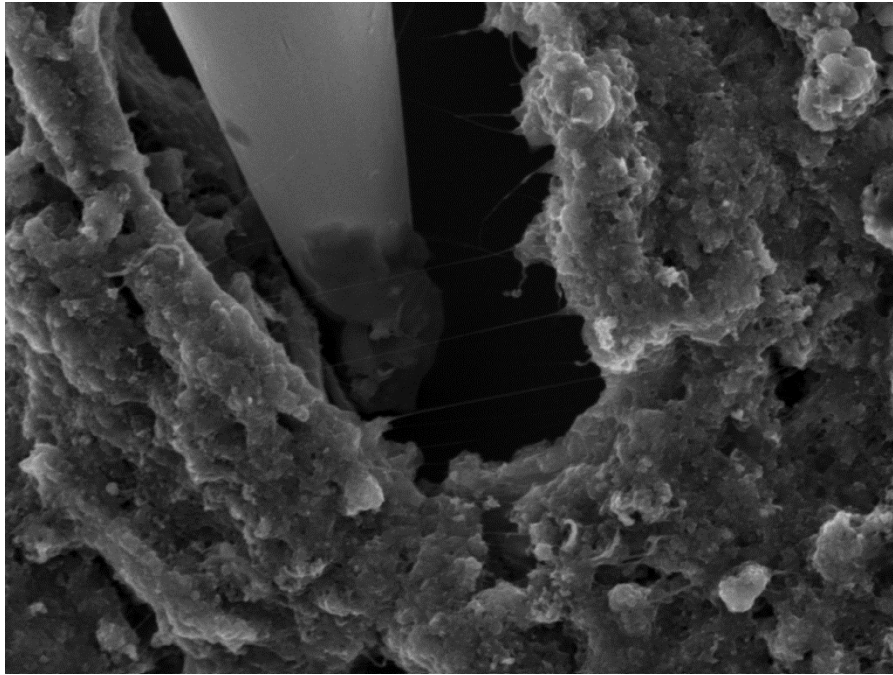


**Figure 3.18:** SEM micrograph illustrating the process of pulling out CNTs from carbonaceous material.

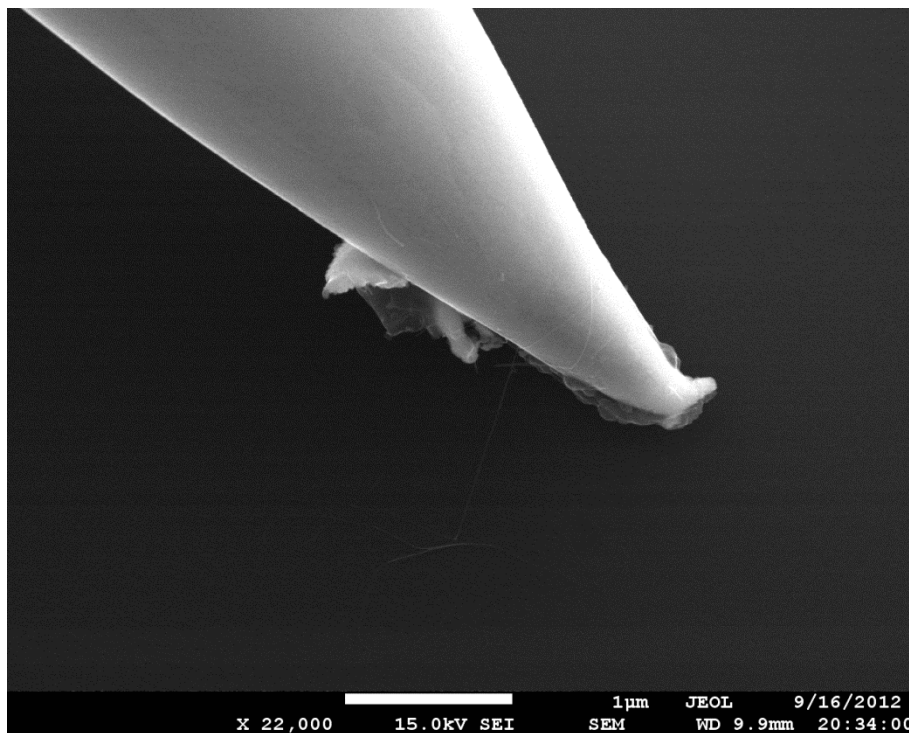


**Figure 3.19:** SEM micrograph showing placing of a CNT on the SiO<sub>2</sub> substrate.

Figures 3.18 and 3.19 illustrate the process of CNT manipulation using nano-manipulators which are mounted inside the SEM. In the case of CNTs that were aligned by dielectrophoresis, the nano-manipulators were used to select the number and quality of

CNTs to be kept on the waveguide or removed. This aspect offered control over the effective device impedance so that load mismatch between the VNA and the DUT can be reduced. While the above images may portray the process to be trivial, the actual fact is that it's a difficult and time consuming process. This highlights that the process in its current state cannot be used for commercial purposes and therefore work has to be done on how to make it useable for large – scale purposes. After placing the CNTs on the waveguide, the next task was to make metallic contacts so as to enhance the coupling between the electrode and the device (CNT or nanodiamond film). To achieve this, a combination of e-beam lithography and gas injection system was utilised.

### **3.4.1: Electron beam (e-beam) lithography**

The standard e-beam lithography technique involves using a high energy electron beam to define a pattern on a photo resist material such as PMMA used as a mask. Chemical solvents are then used to lift-off the resist that has been exposed to the electron beam leaving a pre-set defined pattern which can be metallized by sputtering processes. In our setup, however chemical wet processes were avoided but the e-beam was used, a form of direct lithography writing using the Gas Injection System from Omni-GIS.

The e-beam software is used to define the shape and size of the contacts and a metal – organic gas is carefully controlled into the SEM. Interaction of the e-beam with the gas results in deposition of the metal in solid form on the defined region. In this way, we were able to achieve what is now known as nano-welding, this is a new form of maskless lithography. It is at the moment an expensive process and perhaps not commercial viable. The schematic diagram below in Figure 3.20, illustrates the contacting process and HF measurement arrangement.

For these studies, two metals were used i.e. platinum and tungsten. And an investigation on how the two metals affect the high frequency response of our devices was carried out, a paper dedicated to this has since been published and the results from that work are given in the next chapter. The remainder of this chapter will now give the SEM micrographs of some of the devices that were used for these studies.



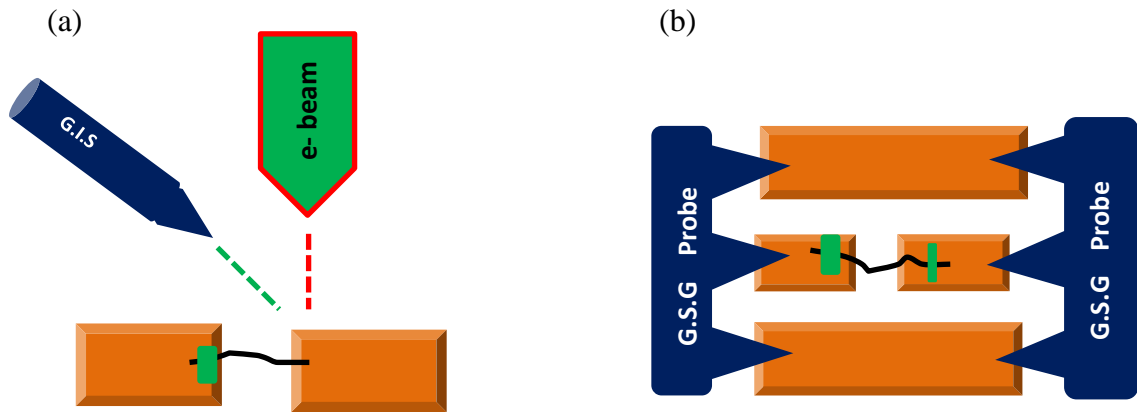


**Figure 3.20:** Schematic illustration of (a) e-beam writing and use of GIS system (b) high frequency measurement set-up.

### 3.4.2: High frequency Device SEM micrographs

The process of device fabrication began with multi-walled carbon nanotubes, the illustration below shows some of these devices.

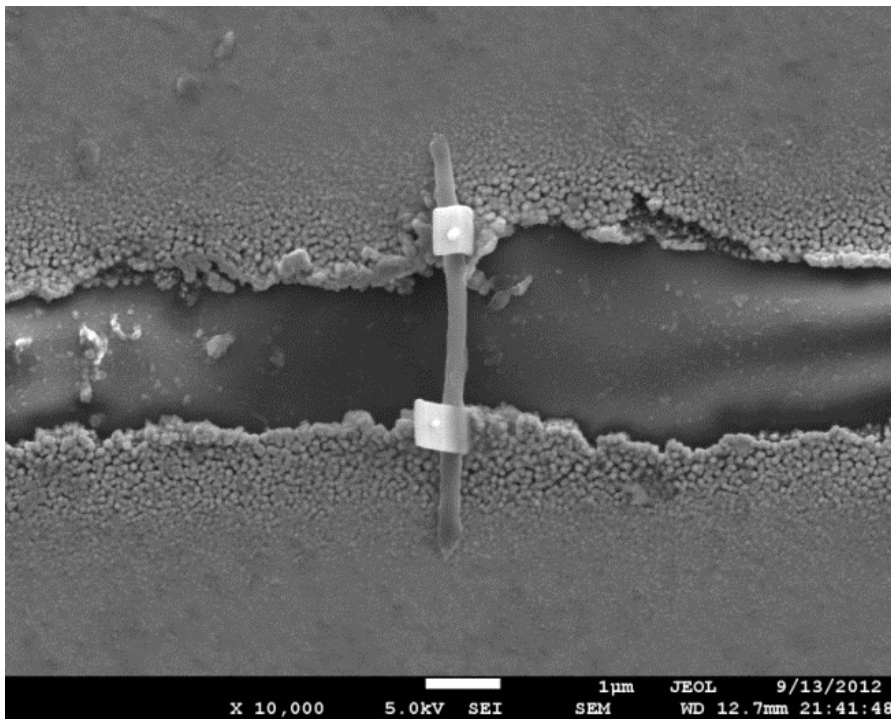


**Figure 3.21:** SEM micrograph of device MW 10 which was used for the systematic error routine tests. It shows an approximately 90 nm MWNT with platinum contacts.

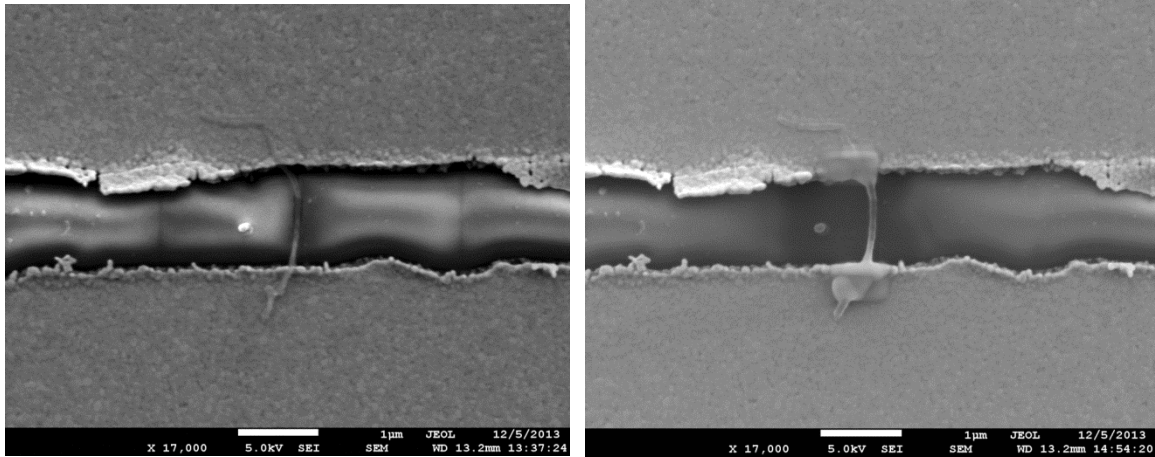


**Figure 3.22:** SEM micrograph before and after making platinum contacts on device CPt 1, which was used to investigate the effect of metal contacts.

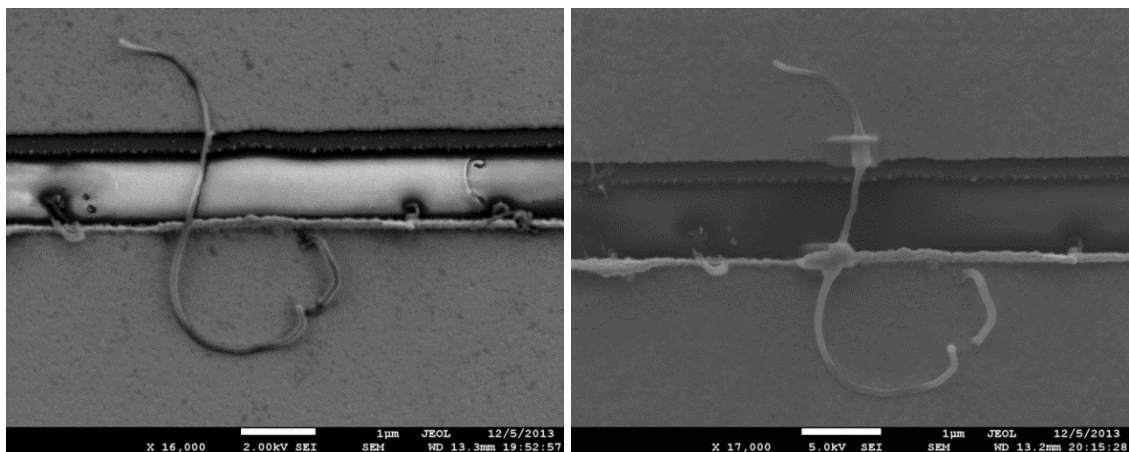


**Figure 3.23:** SEM micrograph before and after making platinum contacts on device CPt 3, which was used to investigate the effect of metal contacts.

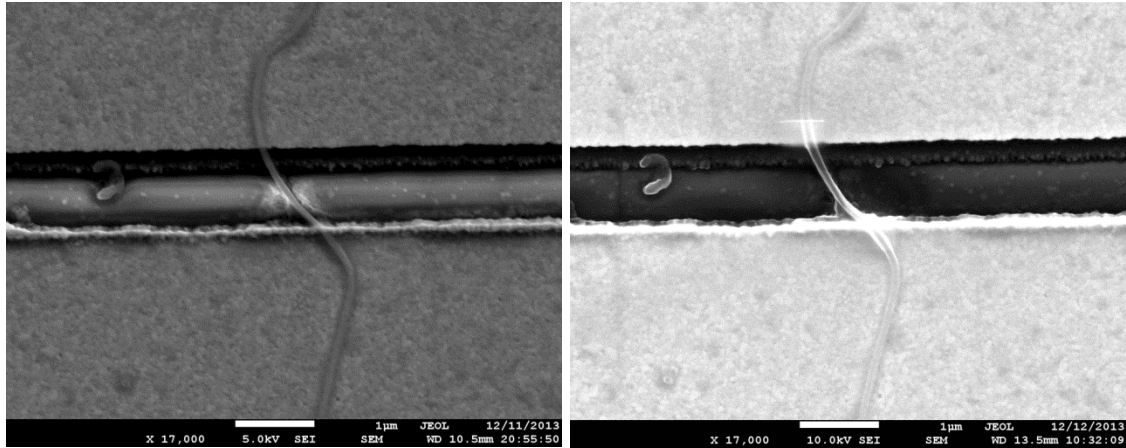


**Figure 3.24:** SEM micrograph before and after making tungsten contacts on device CW 2, which was used to investigate the effect of metal contacts.

Individual double walled carbon nanotubes were found to adhere very well onto the gold electrodes such that it was difficult to remove using nano-manipulators. As such no metal contacts were put on the DWNT devices. Figures 3.25 -27 give the SEM images of some of the devices.

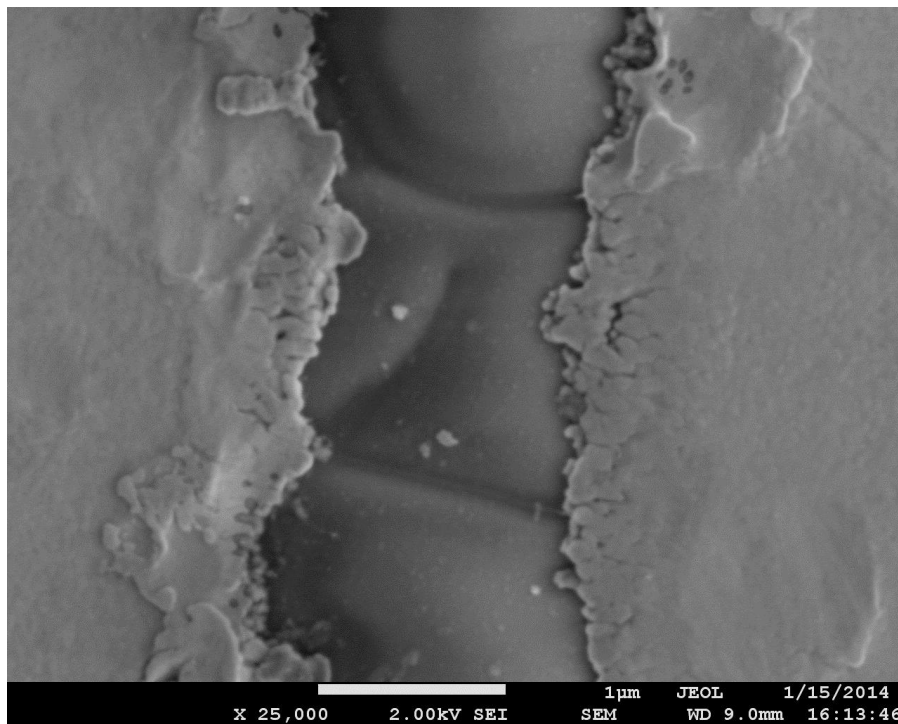


**Figure 3.25:** SEM micrograph device DW 1, showing two of the eleven individual DWNTs aligned.

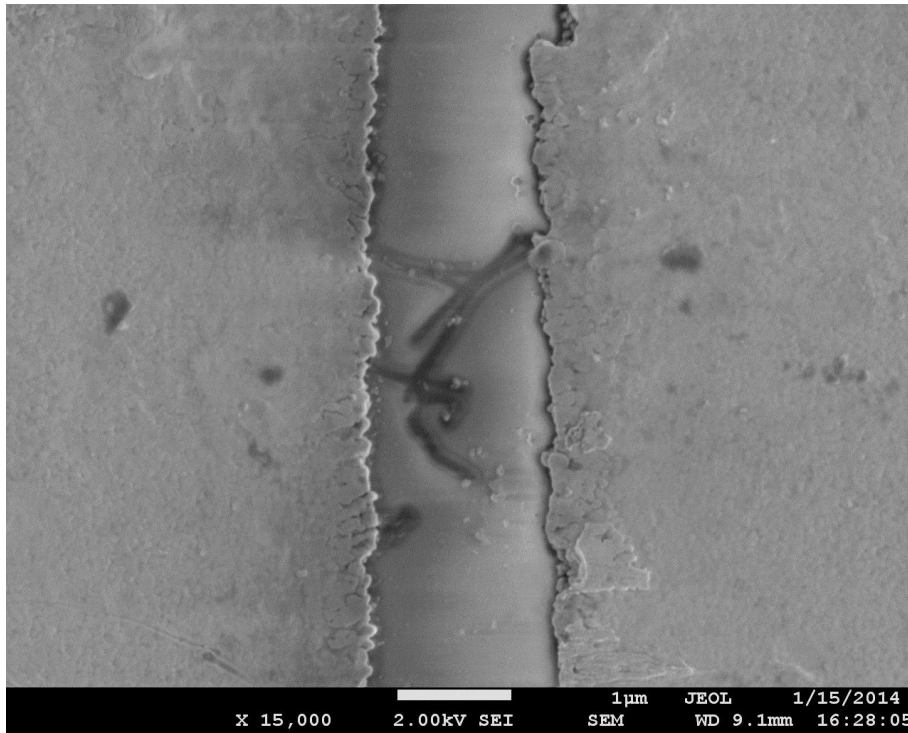


**Figure 3.26:** SEM micrograph DW 1 shows five of the eleven DWNTs aligned.

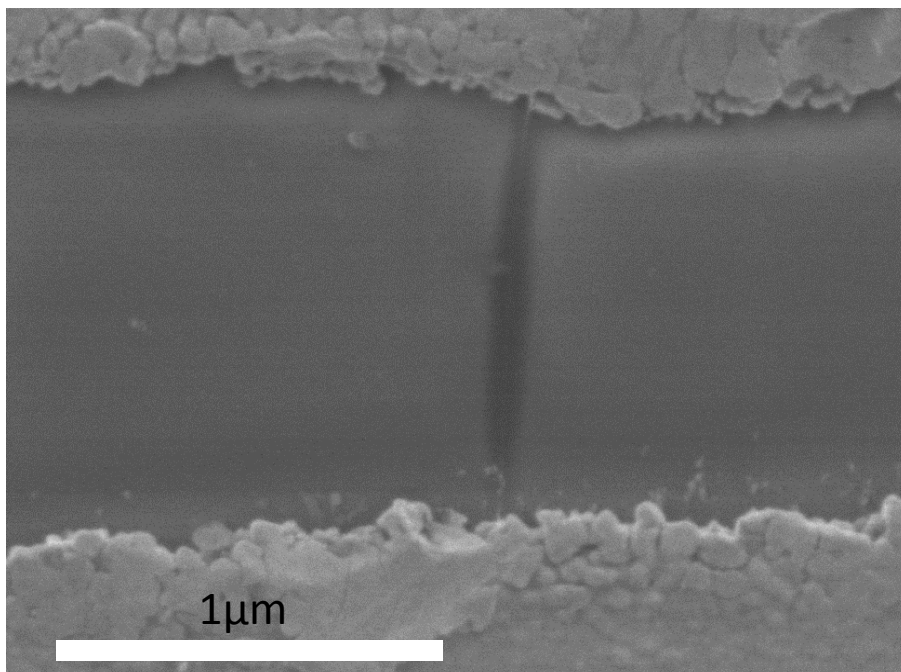


**Figure 3.27:** SEM micrograph device DW 2, showing one of the four DWNTs aligned.

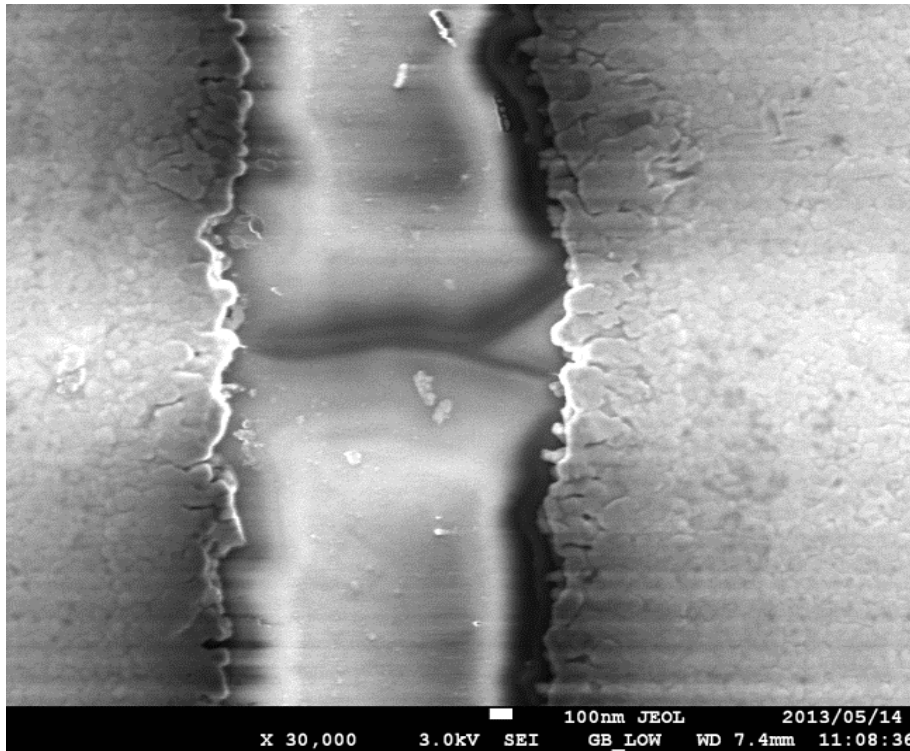


**Figure 3.28:** Shows the SEM micrograph of Device SW2, which had six SWNT bundles aligned across the CPW. The image shows two parallel swnts. The other cannot be seen because of the scale.

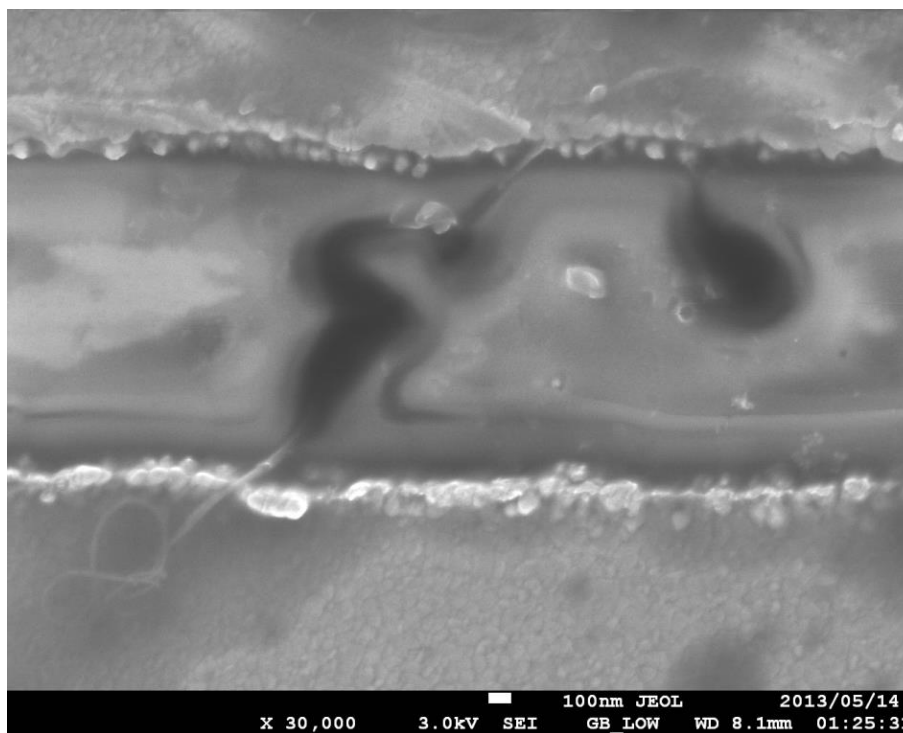


**Figure 3.29:** SEM micrograph of device SW7, which had two SWNT bundles. The other bundle cannot be seen because of the scale.

### **3.4.3: Synthesis of nanodiamond films by hot filament CVD**

Since the authors' MSc work, nitrogen incorporated nanodiamond films have been routinely deposited in the laboratory using hot filament chemical vapour deposition technique. The synthesis process was optimised during the MSc project but some modification on the CVD system was done during PhD work by introducing a homemade separate substrate back heater. This new addition was to improve the quality of the films as well as enhance film uniformity.

In a nutshell, the synthesis of nanodiamond is a two stage process, in which the substrate is first pre-treated by ultra-sound sonication in a diamond slurry after cleaning of the substrate. The second stage is the actual synthesis process in a commercial hot filament CVD chamber at a substrate temperature of approximately 800 °C and 2100 °C filament temperature [86]. Four reaction gases were used, which are methane, hydrogen, argon and nitrogen. The total flow rate was kept at 210 sccm, and the pressure was kept at 22 mbar on average. For more details on the synthesis and characterisation of the films see reference [86]. The photograph in the next page is the image of the modification of the CVD system which was done for this project.

After synthesis, the nanodiamond films were then scratched off the fused quartz substrate using a sharp needle onto the coplanar waveguide. The small film pieces were positioned at the centre of the signal terminals and bonded using tungsten metal. The bonding was done in a similar way to that of carbon nanotubes i.e. a combination of e-beam lithography and metal gas injection. The SEM images in the next pages show some of the devices that were used for high frequency measurement.

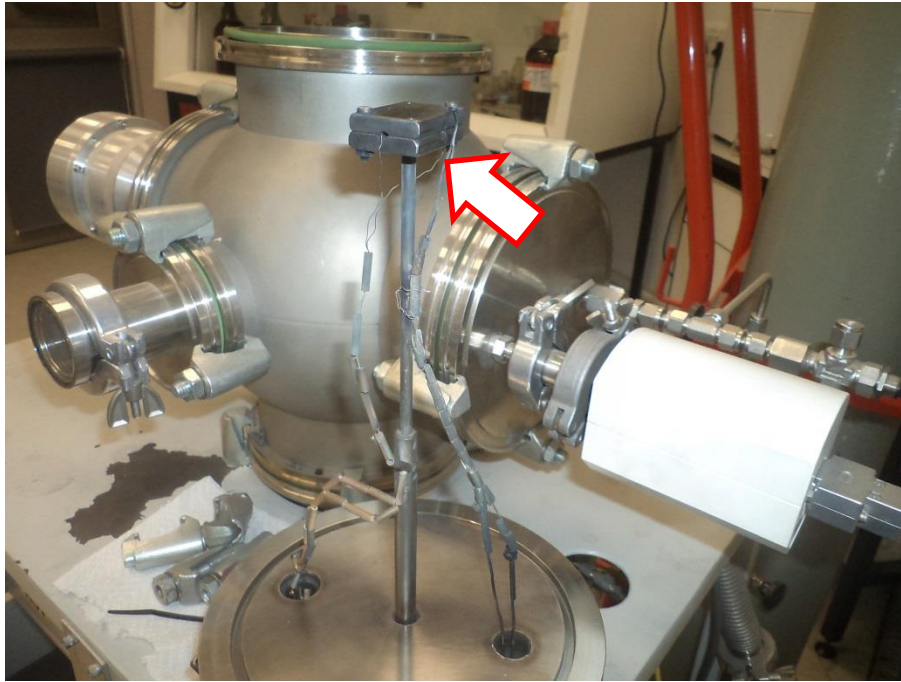


**Figure 3.30:** Photograph of the modified substrate back heater pointed by the arrow of the HFCVD chamber.

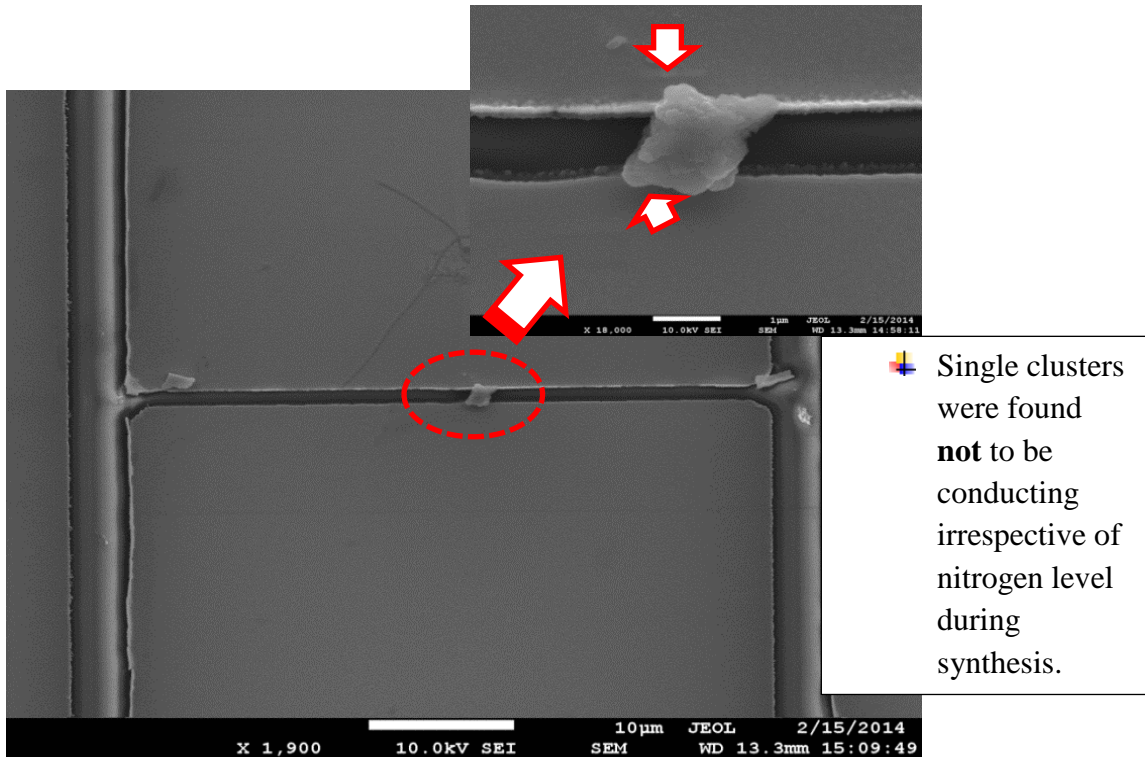


**Figure 3.31:** SEM micrograph of single ~ 1 micron (Diam 5A- 20% N<sub>2</sub>) ND cluster. The small arrows point to the metal contacts.

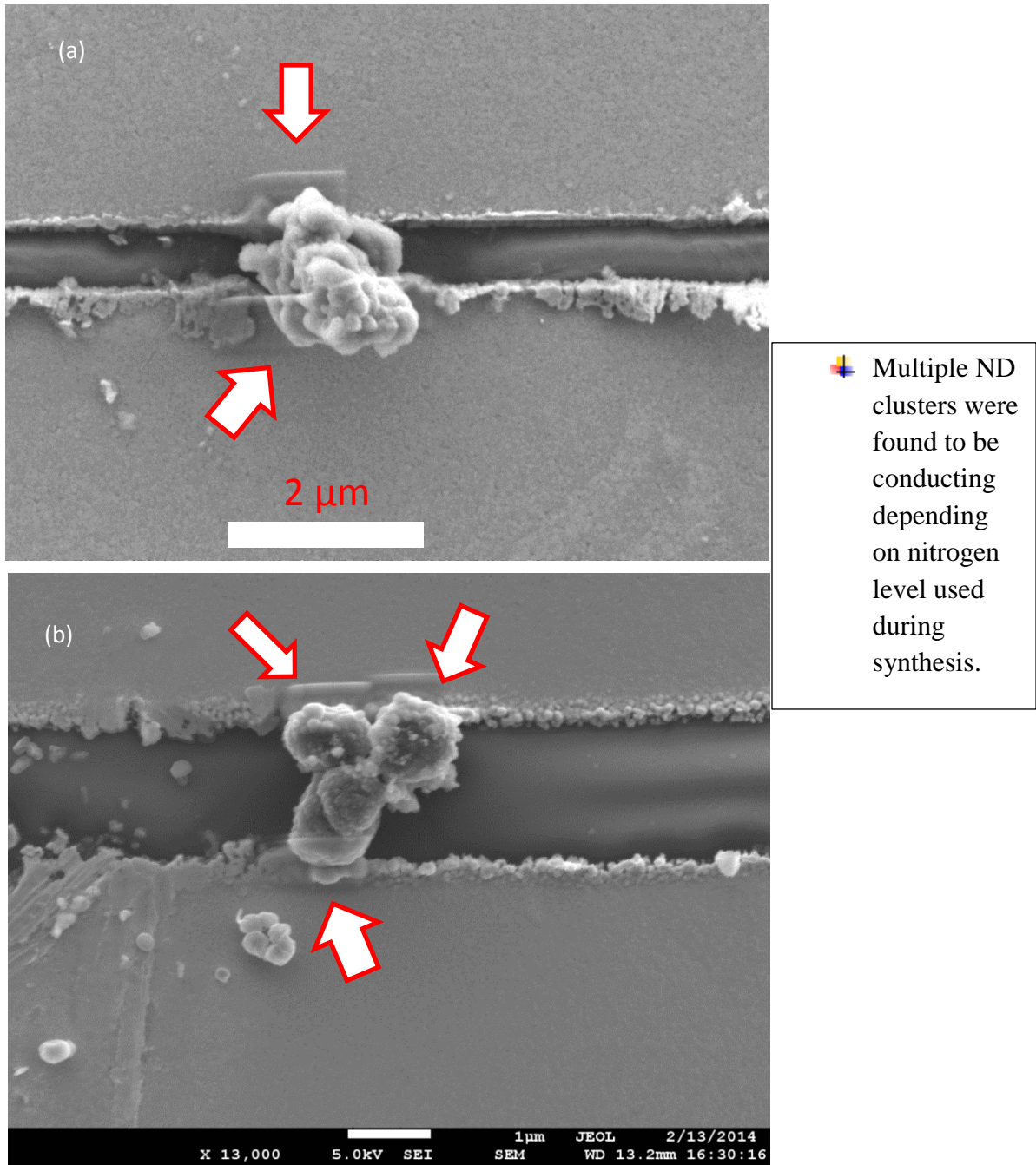


**Figure 3.32:** SEM micrograph of multiple ND clusters (a) Diam 2 with 0% nitrogen and (b) Diam 3 with 5% nitrogen. The arrows point to the metal contacts.



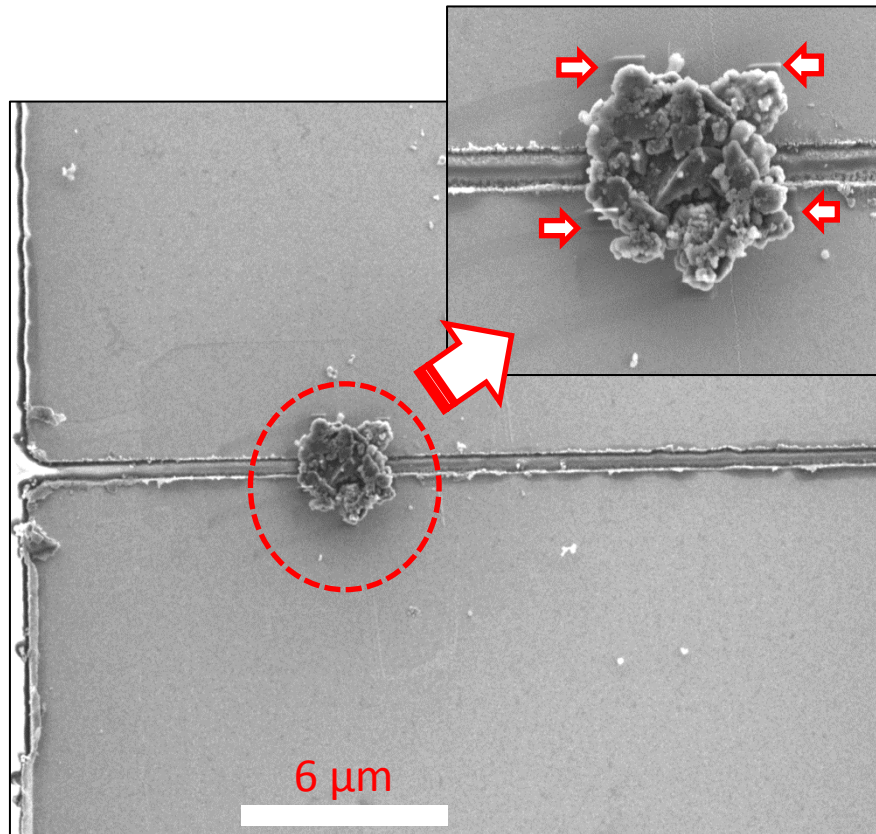


**Figure 3.33:** SEM micrograph of multiple ND clusters Diam 5B with 20% nitrogen. The arrows point to the metal contacts.

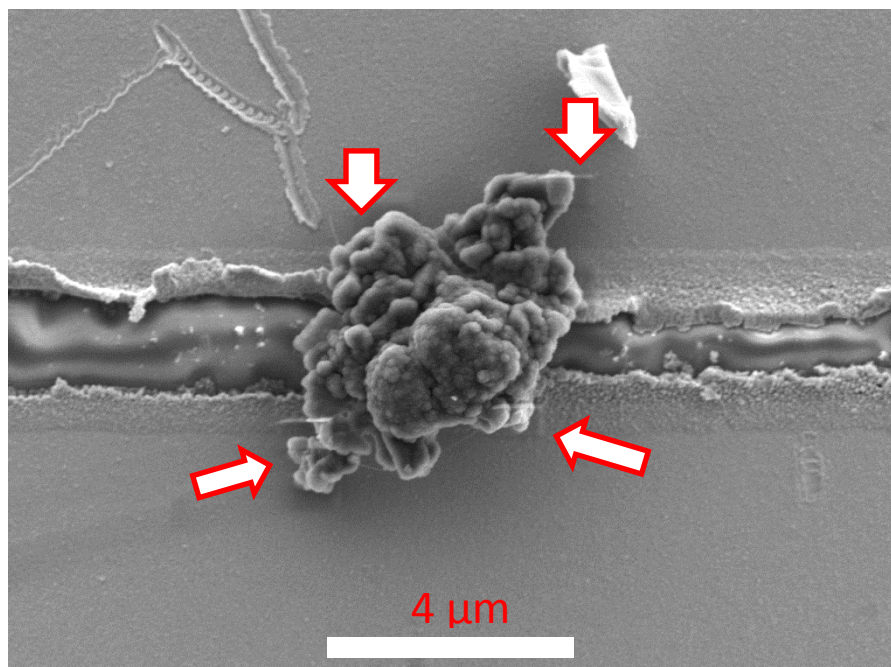


**Figure 3.34:** SEM micrograph of multiple ND clusters Diam 14 with 25% nitrogen. The arrows point to the metal contacts.

### 3.5: Chapter Summary

In brief, the three forms (MWNT, DWNT and SWNT) of carbon nanotubes were aligned on coplanar waveguides using dielectrophoresis and their scattering parameters measured using a vector network analyser at room and low temperatures. Individual multi-walled carbon nanotubes were used to investigate the effect of platinum and tungsten contacts. Bundles (between two to eight) of single walled were used to study the fundamental dynamic transport in carbon nanotubes. Individual double walled tubes (between four to twelve) were aligned in parallel and studied at both room and low temperatures to investigate the effect of temperature on the CNT-electrode coupling.

Nanodiamond films were synthesized by hot filament chemical vapour deposition on fused quartz substrate with different nitrogen levels from 5% to 25% of the total gas flow. Multiple cluster films were scratched from the substrate and positioned on the coplanar waveguide and the scattering parameters measured. The scattering parameters were measured after making of metal contacts using e-beam lithography and gas injection system.

Calibration of the vector network analyser was done using the SOLT technique to set the reference of the signal and the probe tips. While parasitic elements of the waveguide were extracted using the Open – short technique.

# Chapter 4 – Dynamic Transport in CNTs

This chapter presents a discussion on the results that were observed in the three forms of CNTs. It begins by looking at the routine tests that were done to ensure repeatable and accurate measurements. The chapter is sub-divided into three segments; a discussion on single walled CNTs, followed by double walled CNTs and then lastly multi-walled CNTs. In all cases the discussions begin with the raw scattering parameter data before eventually looking at the calculated impedance and/or simulated equivalent circuits. *I-V* DC measurements are also used to compliment the discussions wherever relevant.

## 4.0: Accuracy test measurements

On-wafer S-parameter measurements are sensitive and very much prone to random errors due to instrument drift, wrong calibration, and inconsistency in probe landing resulting in non-reproducible results. A lot of time was spent in the initial year of this project perfecting the skill and technique for these measurements. It is therefore important to begin the chapter with the results from the systematic error tests that were done.

### (a) Instrument Drift

The transmission coefficient component ( $S_{12}$  or  $S_{21}$ ) of the S-parameters is the main parameter from which most of the results and conclusions are drawn. This is because it is more reliable than the reflection coefficient ( $S_{11}$  or  $S_{22}$ ) that have significant error margin due to the inherent load mis-match between the device under test normally in the  $k\Omega$  range and the instrument set at  $50\ \Omega$ . The errors due to the load mis-match in  $S_{12}$  are easily reduced by the de-embedding technique due to the higher signal to noise ratio unlike in  $S_{11}$ . The transmission coefficient ( $S_{12}$ ) was thus used for most of the error tests and analysis.

Figure 4.1, shows the  $S_{12}$  measurements on one of the multi-walled CNT sample MW-9 at some time (marked A) and then thirty minutes later (marked B). It can be seen from the results that there is little or no significant instrument drift. Instrument drift is normally high if the atmospheric temperature is not stable, but since the instrument is in an air-conditioned facility and is still new, it probably explains why no problems were encountered in this regard.

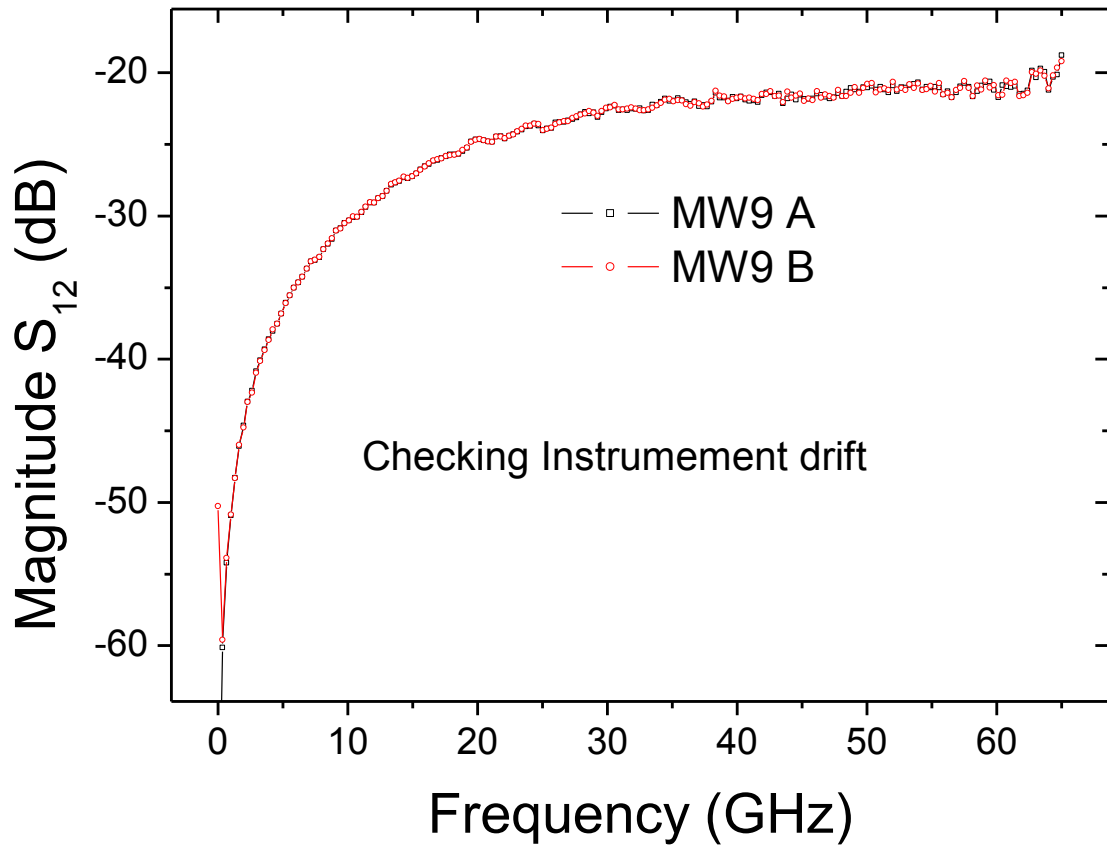


**Figure 4.1:** *S*-parameter data for a MWNT sample 9 measured at different times. MW 9 B was measured 30 minutes after MW 9 A. It clearly shows that there is insignificant instrument drift with time as the data sets overlap strongly.

Besides the aspect of instrument drift the above results also show the accuracy in precise placements of the probes on the same position, thirty minutes after the first measurement. The precision is aided by the micro-manipulated probes of the system.

#### **(b) Effect of Solvent**

As outlined in the methodology, chapter 3, dichlorobenzene was used to disperse the CNTs so that they can be aligned on the waveguides. This was therefore had to be checked, to see if it would affect the measurement. The Open data is for the dummy waveguide with no CNTs aligned but with dichlorobenzene dispersed, while the Control data is for the same dummy before the solvent was dispersed. Only the high frequency region is shown because in the lower end of the spectrum the results overlap strongly.

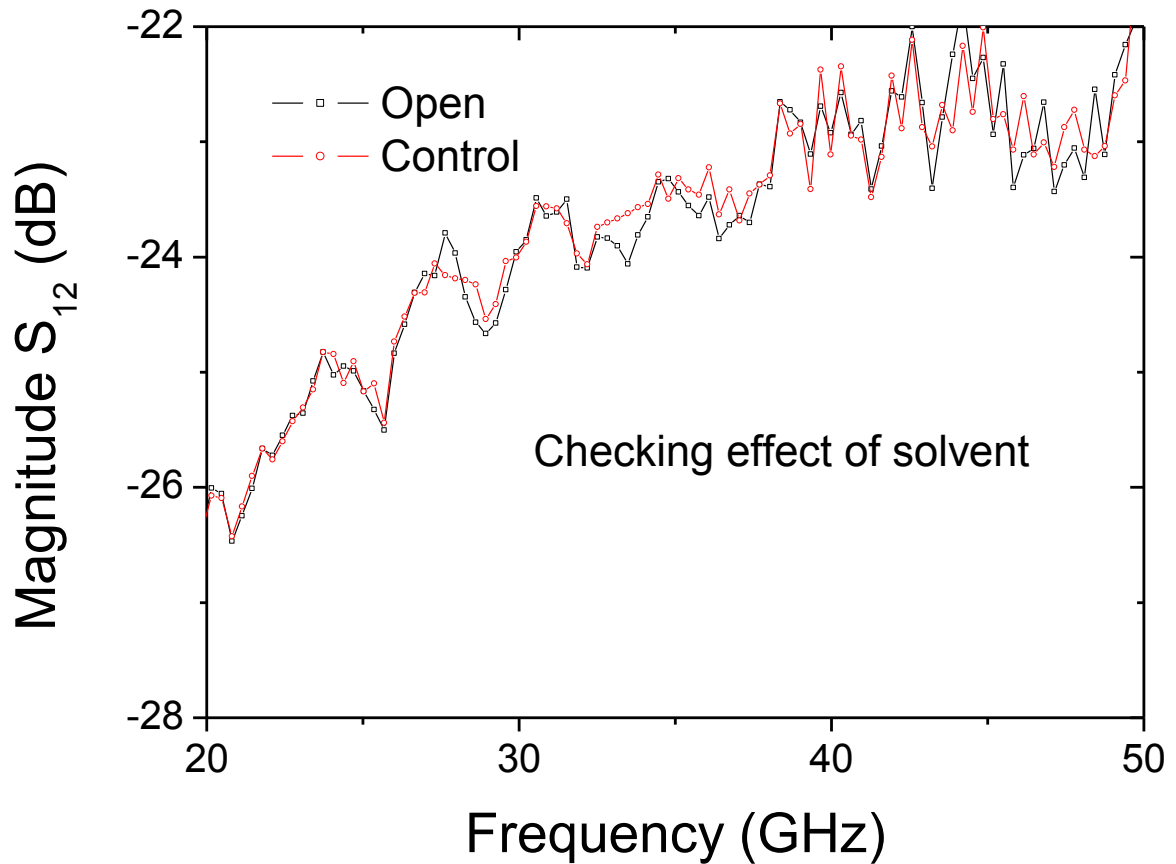


**Figure 4.2:** Shows the test done to check the effect of solvent on the  $S$ -parameter measurement. The Open data is for an open dummy waveguide with the solvent dichlorobenzene dispersed on the one micron gap. The Control is for the same dummy without the solvent.

### (c) Reproducibility Tests

A third and also very important systematic test was the test for reproducibility and two different multi-walled samples shown in Figure 4.3 were used. As in the previous data the focus on the high frequency region for the same reason as explained. The graph illustrates the reproducibility of the data and highlights the care practiced to ensure that the probe contact force is maintained constant. This was made easier by the probe's micro-meter graduated screw-gauges used to lower them down.

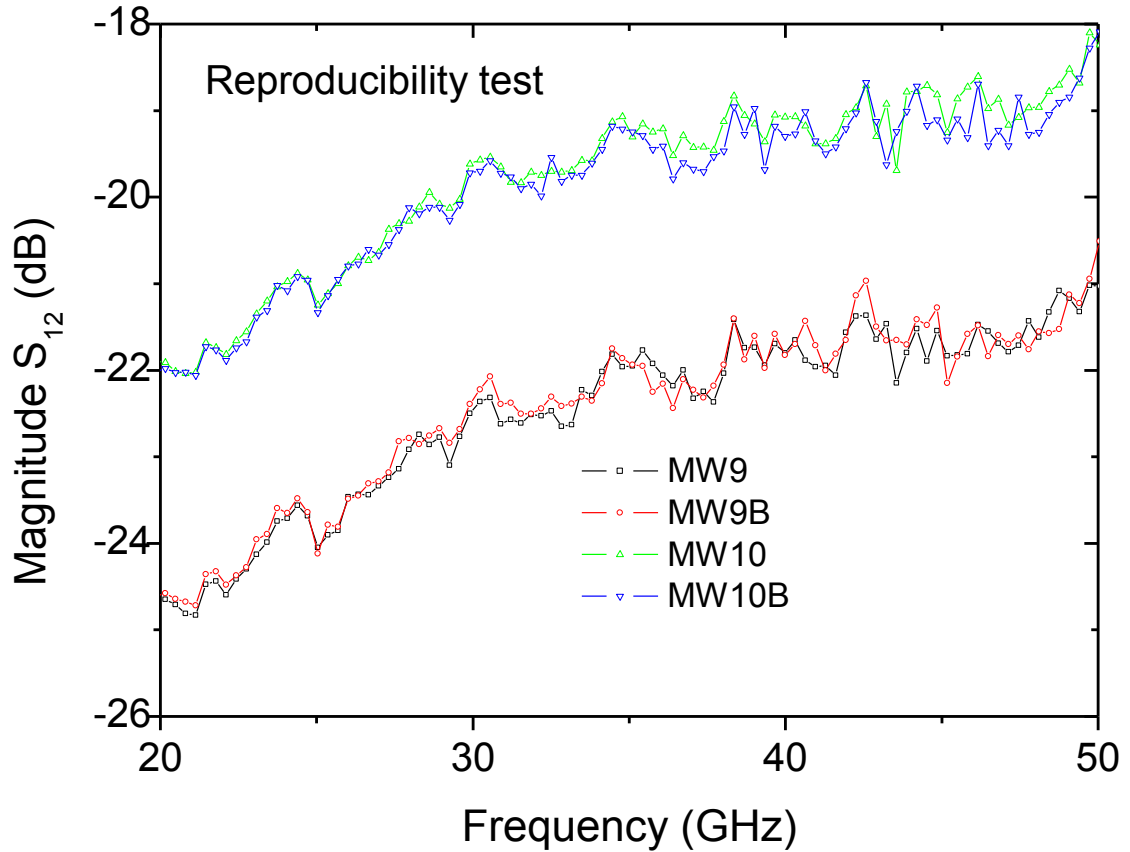


**Figure 4.3:** Shows the test to check measurement reproducibility, MWNT samples 9 and 10 were measured repeatedly every time lifting up the probes. The graph shows very good reproducibility.

Using the performed test, it was estimated that the highest possible random measurement uncertainty due to noise or other possible source of error at about 30 GHz will be about 0.02 dB on average. This was true for generally all the tests. This was calculated from  $\Delta S_{21} = S_{A21} - S_{B21}$ , where the A parameter is for the first measurement and parameter B is for the second repeated measurement.

#### 4.1: RF transmission in SWNTs

As outlined in chapter 3, the SWNTs used for this work were bundles of approximately 20 nm in diameter rather than single individual tubes see TEM micrograph Figure 3.1(b). The rationale behind the use of bundles was motivated by the fact that previous research efforts by other groups on individual tubes [79] encountered a very weak signal to noise ratio such

that it was difficult to effectively remove the noise. This led to the option of using bundles in the hope that it would improve the signal to noise ratio, which turned out to be the case. The concern however of this choice was that introduction of bundles would mean multi-channel conduction and the question then arose, on whether it will be still possible to observe quantum effects due to individual channels? Another question was how will the multi-channel interaction affect the system as a whole? From the author's earlier works on DC transport in multiwalled nanotubes it was shown that transport is dominated by single or few metallic tubes [87]. It was also further established that a weakly temperature dependent dephasing length in the metallic inner wall was possible suggesting applications for high frequency devices [87]. Using this background understanding the conclusion was that it should be possible to observe quantum effects even in bundles provided there is weak coupling of the multiple channels. The bundle nature however tend to result in significant defects and disorder which would definitely affect the electrical transport response.

To aid the understanding of the interpretation of the results outlined in this work, a brief look at some previous theoretical predictions on CNTs as high frequency devices is done. Using the transmission line approach previously highlighted in chapter 2, Peter Burke showed that metallic SWNTs can be modelled as a transmission line with kinetic inductance ( $L_k$ ) and quantum capacitance ( $C_Q$ ) incorporated as additional parameters to the already known magnetic inductance and electrostatic capacitance see Figure 4.4 [15].

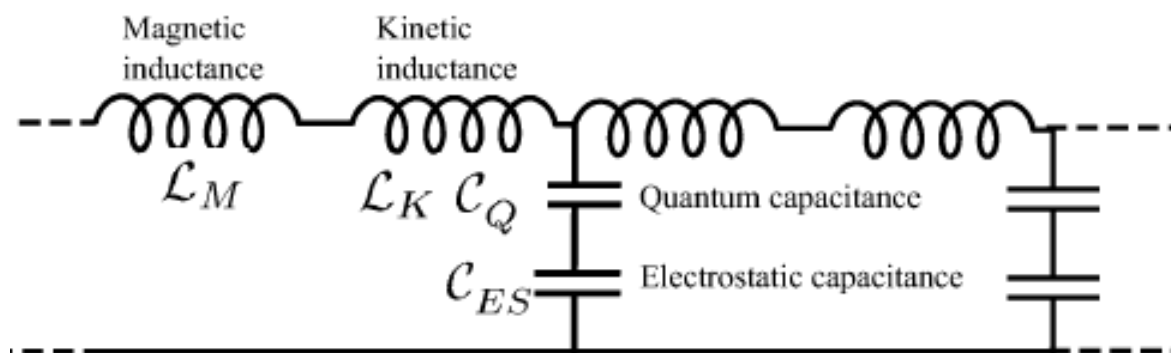


**Figure 4.4:** Schematic illustration of a CNT transmission line. The diagram is courtesy of Ref [15].

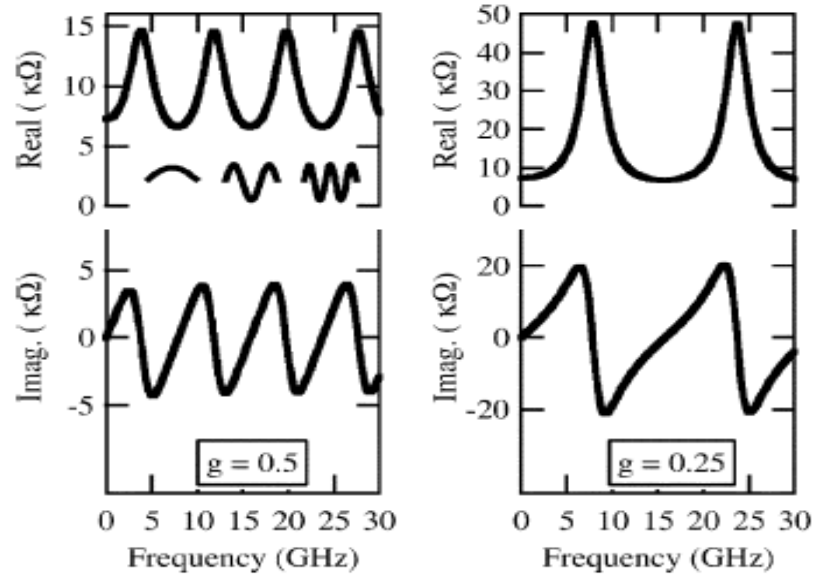


**Figure 4.5:** Predicted dynamic impedance for Ohmic contacts, for two different values with two different LL parameter ( $g$ ) values, Adapted from reference [15].

In such a transmission line the impedance was shown to resonate in the Giga-hertz range if the length is about hundred microns [15]. The graph Figure 4.5 is the expected results for different correlation parameters (Luttinger Liquid). The model and calculations were done using equation 4.1 and is based on the following assumptions:

- (a) The damping or scattering of 1D plasmons is comparable to the mean free path of electrons in CNTs at room temperature. This is because currently there is no numerical value for this, from either experiments or theoretical calculations [15]. The implication of this fact is that the 1D plasmon decay length can be greater than a transmission line in the micron range and hence the impedance can be resonant.
- (b) The effective length of the transmission line (CNT) is  $1000 \mu\text{m}$ . Current methods of CNT synthesis are capable of such lengths and therefore impedance resonance can occur in the GHz range.
- (c) The Fermi-velocity of electrons is about  $8 \times 10^5 \text{ m/s}$ . This implies that for a  $1 \mu\text{m}$  transmission line the impedance will resonant in the THz regime and hence the need for longer tubes to observe resonance in the GHz regime. [15].



$$Z_{CNT} = \frac{h}{8e^2} + Z_{c-eff} \frac{1 + \Gamma e^{-2Yl}}{1 - \Gamma e^{-2Yl}}, \quad (4.1)$$

In equation 4.1,  $Z_{c-eff}$  is the effective characteristic impedance,  $\Gamma$  is the transmission coefficient,  $Y$  is the propagation constant,  $l$  is the length of the transmission line and the other symbols have their usual meanings i.e. Planck's constant, electron charge etc.

Periodic oscillations in the impedance from the CNTs are shown from the theoretical calculations of reference [15]. There is also a phase change at resonance as the imaginary component changes sign at all resonant peaks. Increasing the correlation parameter (i.e. which means reducing the strength of correlations) results in a decrease of the period between consecutive resonant peaks. The model also produces resonant peaks of the same height implying that damping along the CNT due to the distributed resistance was neglected in the calculation. With this background insight the discussions now turns back to the results that were obtained in this work.

A number of devices were fabricated and tested, but nevertheless only two of the best samples (SW2, SW7) will be used, which differ in the number of bundles aligned across the signal terminal of the waveguide. SW2 had six bundles, while SW7 had two SWNT bundles.

Figure 4.6 shows that the transmission capabilities of CNTs, the data show no sign of saturation all the way up to 65 GHz indicating that the transmission capabilities are beyond this frequency. The maximum power transmission at high frequencies is approximately -15 dBm. It also appears that the power transmitted increases with frequency as shown by the difference between the  $S_{DUT}$  and  $S_{Open}$  which increase with frequency. A closer inspection of the data shown in Figure 4.7 (*a* and *b*) reveals much finer details.

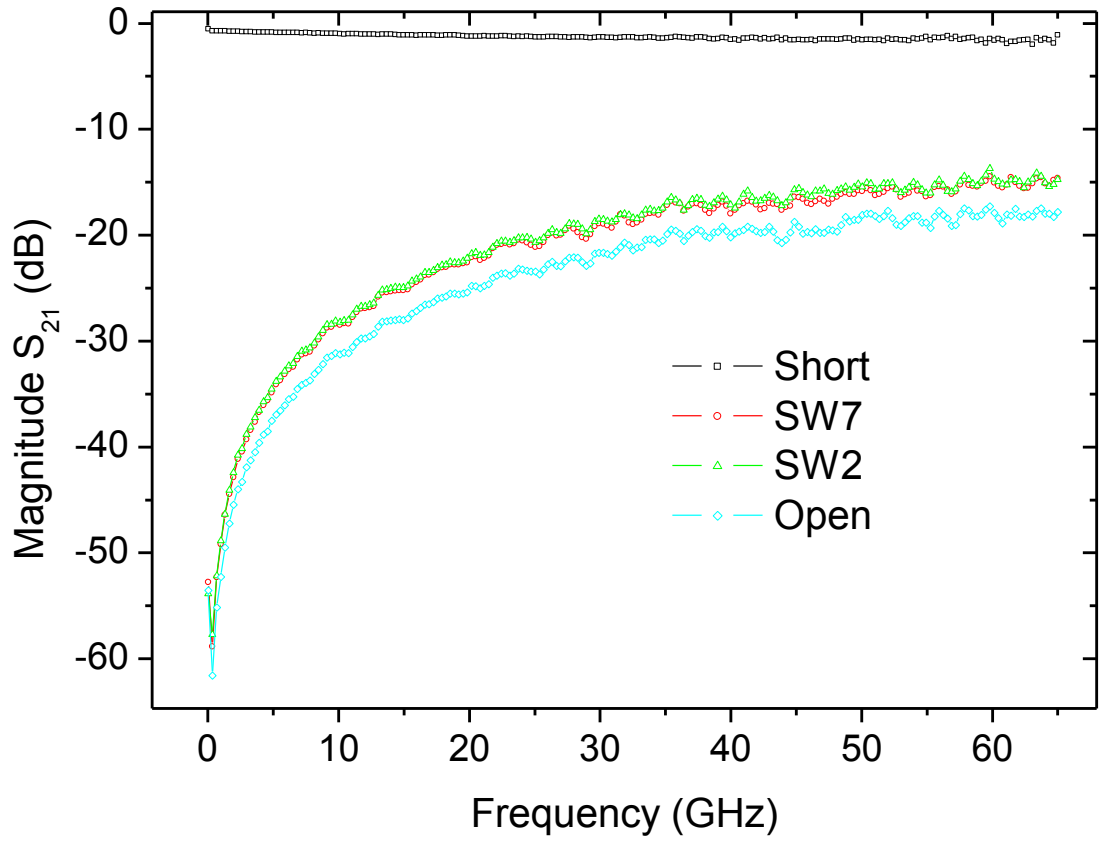


**Figure 4.6:** Transmission coefficient ( $S_{21}$ ) in dB for samples SW2 with 6 CNT bundles and SW7 with 2 CNT bundles. The open and short data is for the short and open dummy waveguides used to extract the waveguide parasitics.

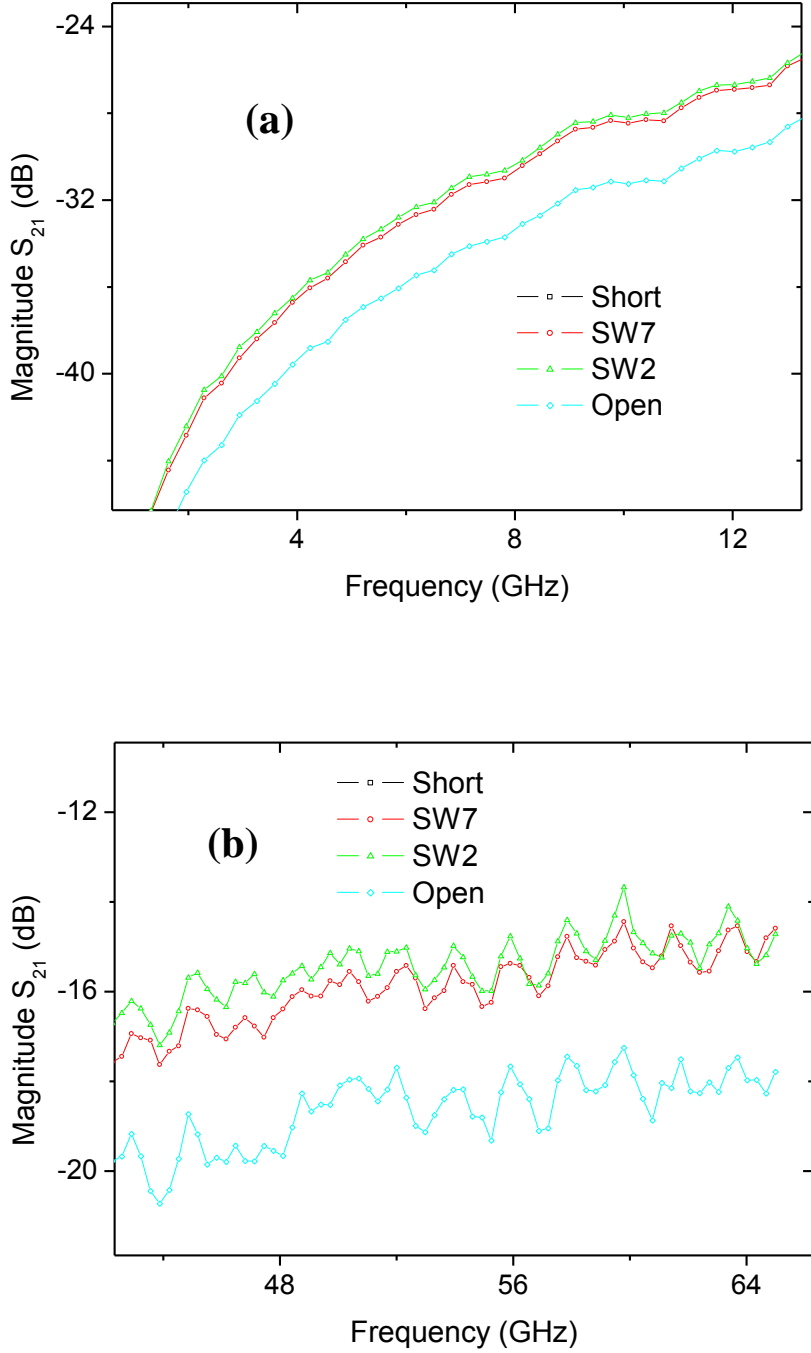


**Figure 4.7:** (a) Low frequency region for the same samples SW2 and SW7 shown in Fig. 4.6, while (b) shows the high frequency region.

After subtracting the  $|S_{21}|$  of the DUT from that of the Open dummy, it is apparent that the aligned SWNTs are responsible for the approximately  $3 \pm 0.1$  dB of power transmission in the high frequency region. SW2 which had six bundles aligned had slightly 1 dB higher power than the SW7 which had only two bundles. Taking into consideration the

measurement uncertainty of 0.1 dB, one should not read too much into the 1 dB difference and the number of bundles aligned. It is however safe to say that more CNTs aligned produces greater power transmitted because of the increased conduction channels or reduced reflection of the signal.

In Figure 4.7 (b) it was observed that the data for SW2 and SW7 begin to overlap, which is probably due to the parasitic effects becoming dominant at very high frequency mainly from the signal terminal capacitance due to the 1  $\mu\text{m}$  gap. For additional insight into the RF response SWNTs the complex impedance of the devices was extracted. This was done by first converting S-parameters into admittance ( $Y$ ) parameters before any mathematical calculations were done. Calculations using S-parameters are complex because they are normalized at 50  $\Omega$ . Using standard equations given in reference [40], and the open-short de-embedding technique, equation 3.6 (last chapter) the complex impedance of the devices was calculated.

#### 4.1.1: Oscillatory Impedance in SWNT devices

The real (resistive) component of the impedance (Figure 4.8) shows interesting results, the impedance is characterised by an oscillatory behaviour, suggesting standing wave resonances in the CNT devices. The standing waves created in CNTs can be envisioned as coming from the 1D plasmon waves of strongly correlated electrons as was explained earlier. The results of the open waveguide show no sign of the oscillations indicating that the presence of CNT on the transmission line is most likely to be the cause of the resonance.

Further similarities of this experimental data to the theoretical predications from reference [15] are also shown. Sample SW7, which had only two bundles of SWNTs show well defined impedance oscillations with a **constant** period of approximately 90 ps which is comparable to 63 ps from theory, for a single tube when the correlation parameter ( $g$ ) = 0.25. Sample SW2 which had six bundles does show these resonance peaks with smaller amplitude but almost equal period of approximately 110 ps. Such commensuration of figures is unlikely to be coincidental as it will be shown later with some additional calculations. Figure 4.9 shows the real impedance of SW7 plotted together with the theoretical one calculated using equation 4.1 from Burke's model. It is apparent that the model to some extent can describe our experimental data with the exception of the amplitude differences.

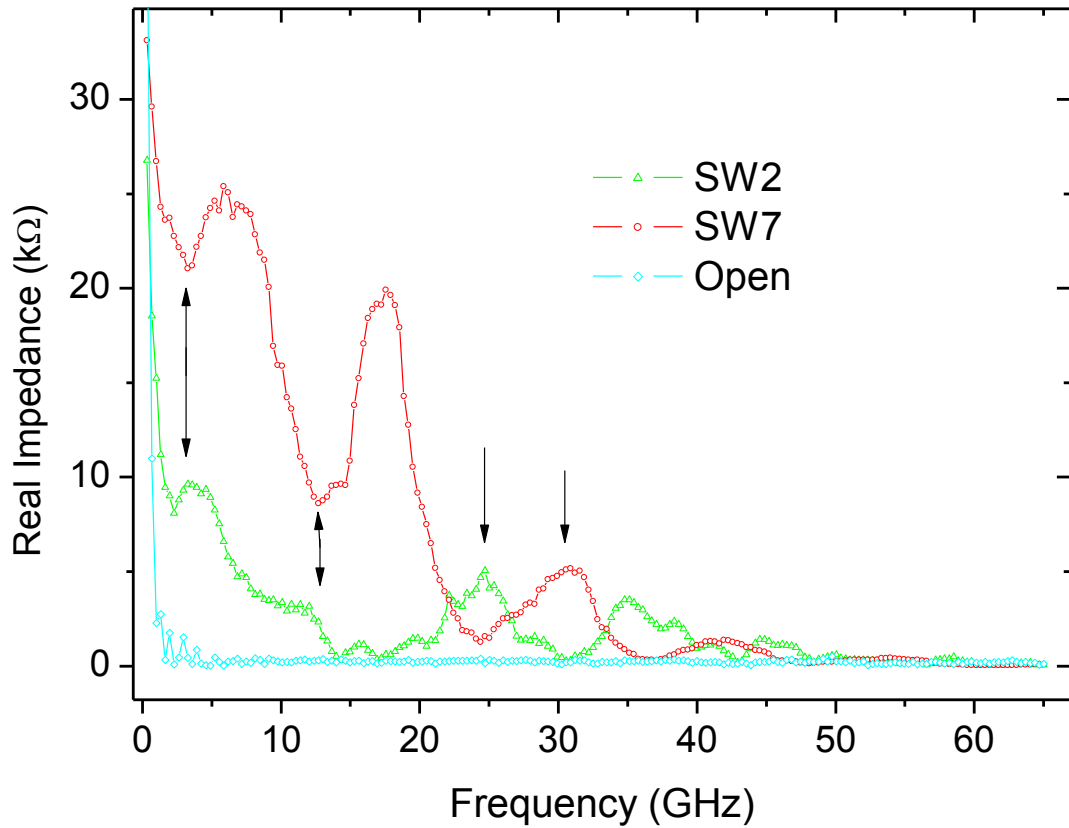


**Figure 4.8:** Real impedance of SW2 and SW7, showing oscillatory behaviour that is exponentially damped with increase in frequency.

One of the main differences between these results and the theoretical ones is in the amplitude of the oscillations. The experimental data given here shows significant damping of the amplitude with the frequency which is probably due to intrinsic CNT resistance or energy losses through the insulating substrate. This is not present in the theoretical data, indicating that this aspect was not incorporated in the theoretical model or that the assumptions made are too simplified to describe a practical problem.

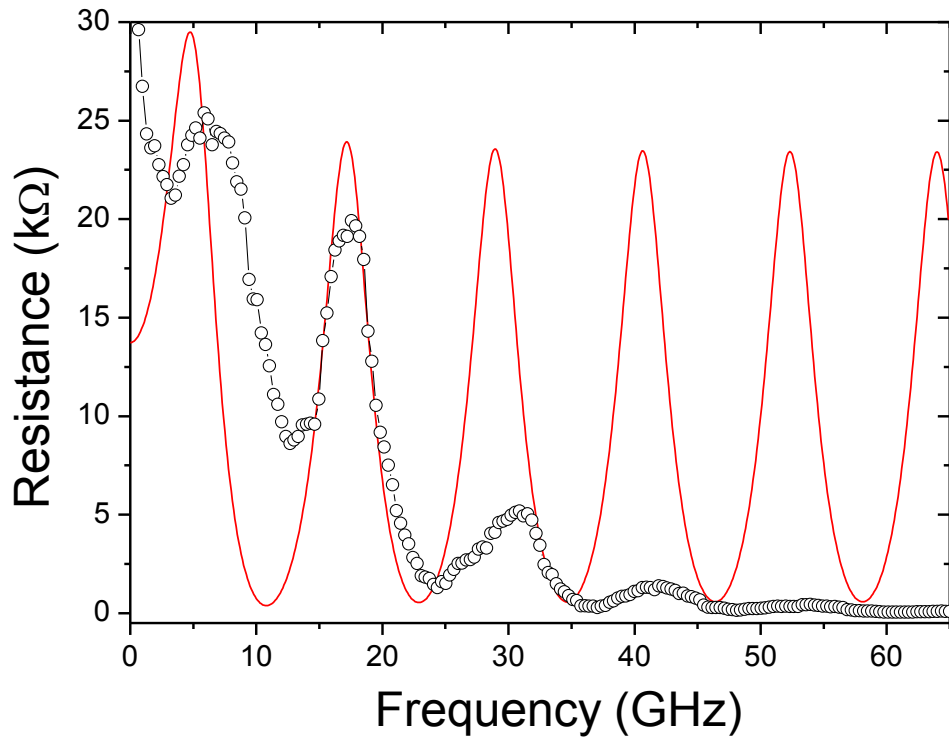


**Figure 4.9:** Real impedance of sample SW7 (black dots), fitted with Burke's model (Red line). The graph clearly shows that the model and experimental data have almost the same period.

Another unique feature about this experimental data is that the oscillations in the impedances of the samples are out of phase with each other, one is a maximum when the other is at a minimum as shown by the arrows in the figure (Fig.4.8). An explanation for the phase difference between samples is not yet clear but maybe linked to the number of conduction channels available resulting in different frequencies in the standing waves established.

The pronounced resonance peaks in SW7 with only two bundles compared to those of SW2 with six bundles, suggest that multi-conduction channels will tend to drown the 1D quantum effects. It was noted that theoretical work by Datta *et al.* showed that increased 1D conduction modes reduced the effect of  $C_Q$  and  $L_K$  [88]. This would explain why suppression in the resonance peaks was observed.

A glance at the imaginary component of the impedance in Figure 4.10 shows a transition from capacitive ( $\text{Im } Z = \text{negative}$ ) to inductive ( $\text{Im } Z = \text{positive}$ ) behaviour with no smooth oscillations but rather show sharp and irregular peaks.

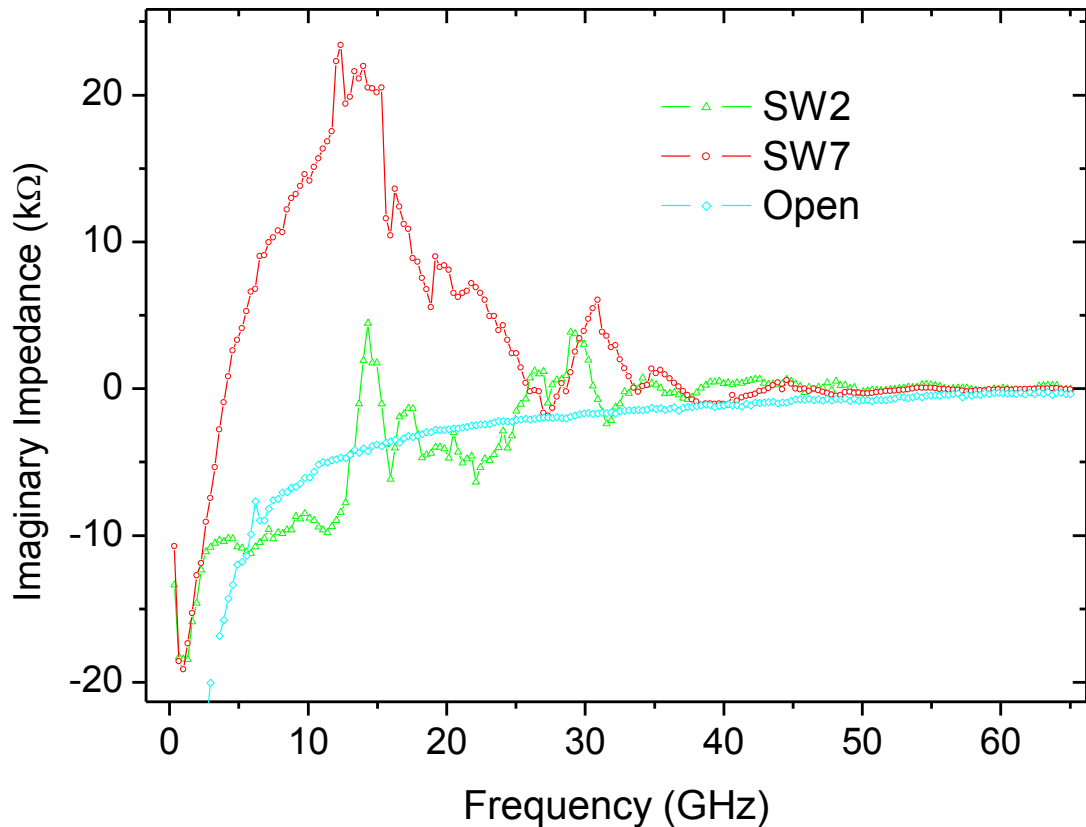


**Figure 4.10:** *Imaginary impedance for samples SW2, SW7 and Open dummy, showing a transition from capacitive to inductive behaviour.*

Similar to the real impedance, the imaginary impedance of the open dummy does not show the oscillations like those indicated by the CNT samples and it is purely capacitive throughout the frequency range measured. This is consistent with the experimental setup in which the signal just couples through the capacitance of the signal terminals and the substrate resistivity is so high that conductance through it is negligible.

Some theoretical work given in ref [89], has shown that LL behaviour is characterised by constant periodic oscillations differentiating them from other 1D system where long range electron-electron interaction and non-interacting electron systems are the dominate effects.

If these impedance oscillations are due LL behaviour, one immediate question that arises is how can there be impedance resonance in a 1  $\mu\text{m}$  transmission line in the gigahertz range. For such dimensions the resonance would be expected in the terahertz regime. The answer to this important question can be obtained from a simple wave propagation theory. If a wave propagates from one medium to another different medium, they will made wave velocity change. The stimulus signal from the VNA drives the chemical potential at the CNT electrodes. As the driven electrons/ charge carriers enter the CNT, they are slowed down due to both the structural defects and phonon scattering in the CNTs. Since the measurements were done at room temperature they would be significant scattering from both optical and acoustic phonons, furthermore the bundle nature of the samples would suggest many defects and as a result the Fermi velocity in such cases would be dramatically reduced. Some experimental work has estimated it to be in the range of  $10^4$  m/s [90] and not the commonly maximum achievable of  $8 * 10^5$  m/s at 0 K. The implication of this is that it translates to the wavelength being reduced from millimetre to the micrometer range making it comparable to the transmission line and hence resonance can be expected if the plasmon decay length is in the same range as the mean free path of electrons in CNTs. Latest experimental measurements have shown that the mean free path can be estimated to about 1.6  $\mu\text{m}$  at room temperature [91]. This estimated effective Fermi velocity was used to calculate the LL parameter of our devices.

The use of this estimated figure is justified by calculating the effective Fermi velocity in the samples using some theoretical prediction of the resonance frequency from Green's function calculations in the linear response regime. Under a time-dependent voltage, the charge waves appear in the 1D wire after being reflected from contacts and interfere therein. The resonant frequencies are given by [89]:

$$f_n = \frac{nV}{L} \sqrt{1 + \frac{ge^2}{\pi\epsilon V}} \lambda_{2n} , \quad (4.2)$$

where  $n$  is an integer,  $L$  is the length of the tube,  $g$  is the LL parameter,  $\epsilon$  is the dielectric constant ( $\sim -9$ ) for the CNTs and  $V$  is the wave velocity and  $\lambda_{2n} \approx \exp [2\pi^2(a/L)^2 n^2] \ddot{E}$ , where  $a$  is the diameter of the CNT,  $\ddot{E}$  is the exponential integral [89].

Therefore using equation 4.2,  $g$  obtained from the DC measurements and the first resonance frequency in the ballistic regime for SW7, the effective Fermi velocity was estimated to be  $7 * 10^4$  m/s. This value is one order of magnitude lower than the commonly cited value for  $V_F$



in CNTs and an order of magnitude higher than an experimentally estimated value in defective CNTs using a different technique [90].

Plotting the complex impedance (Real and Imaginary) on the same axis reveals another important dimension to the whole discussion which further supported our interpretation of the impedance oscillations. LL behaviour is expected in the ballistic regime and the results below show that this was achieved at room temperature.

Ballistic transport is regarded as the motion of charge carriers without any scattering and if contact resistance could be avoided, ballistic transport would mean extremely low resistance. It (ballistic transport) can be achieved in two ways, (1) reducing the sample dimensions to the range of the mean free path as was explained earlier or (2) using a time dependent signal whose frequency is greater than the scattering rate in the material. The Drude model for AC transport expresses the conductivity made of two parts e.g. real part and imaginary part see equation 4.3 below [92]:

$$\sigma(\omega) = \frac{ne^2\tau}{m^*} \frac{1}{1+i\omega\tau}, \quad (4.3)$$

where  $\tau$  is the momentum scattering time,  $m^*$  is the effective electron mass,  $e$  and  $n$  have been defined already. The imaginary part of the conductivity is given by  $i\omega\tau$  and it changes sign depending on whether it is capacitive or inductive. This aspect can therefore be used to determine experimentally whether the transport is the diffusive or ballistic regime if the real and imaginary impedance is known as shall be explained below. The achievement of ballistic transport at room temperature in a defective system can be realised when the stimulus frequency becomes higher than scattering rate as was explained earlier.

To understand the significance of plotting the real impedance with the imaginary impedance on the same axis it is noted that the impedance of a quasi 1D transmission line (TL) network can be expressed as [93]:

$$Z(\omega)^{-1} = \frac{i\omega C}{1+i\omega RC-\omega^2 LC} + \frac{1}{R_0+i\omega L_0}, \quad (4.4)$$

where  $R, C$ , and  $L$  are the resistance, capacitance and inductance of the TL respectively. When the impedance becomes inductive it means  $LC \gg RC$ , and equation 4.4 reduces to 4.5:

$$Z(\omega) = R_0 + i\omega L_0, \quad (4.5)$$

And  $R_0$  can be regarded as the intrinsic CNT resistance plus the contact resistance. Now using equations 4.3 and 4.5, when the real impedance is equal to the imaginary impedance this corresponds to the point when  $\omega\tau = 1$  if the contact resistance is neglected. This point will therefore signal the crossover point from diffusive where  $\omega\tau < 1$  to ballistic transport where  $\omega\tau > 1$ .

#### 4.1.2: Diffusive to Ballistic Transport in SWNTs

Figure 4.11, shows a crossover of the real and imaginary components of the impedance.

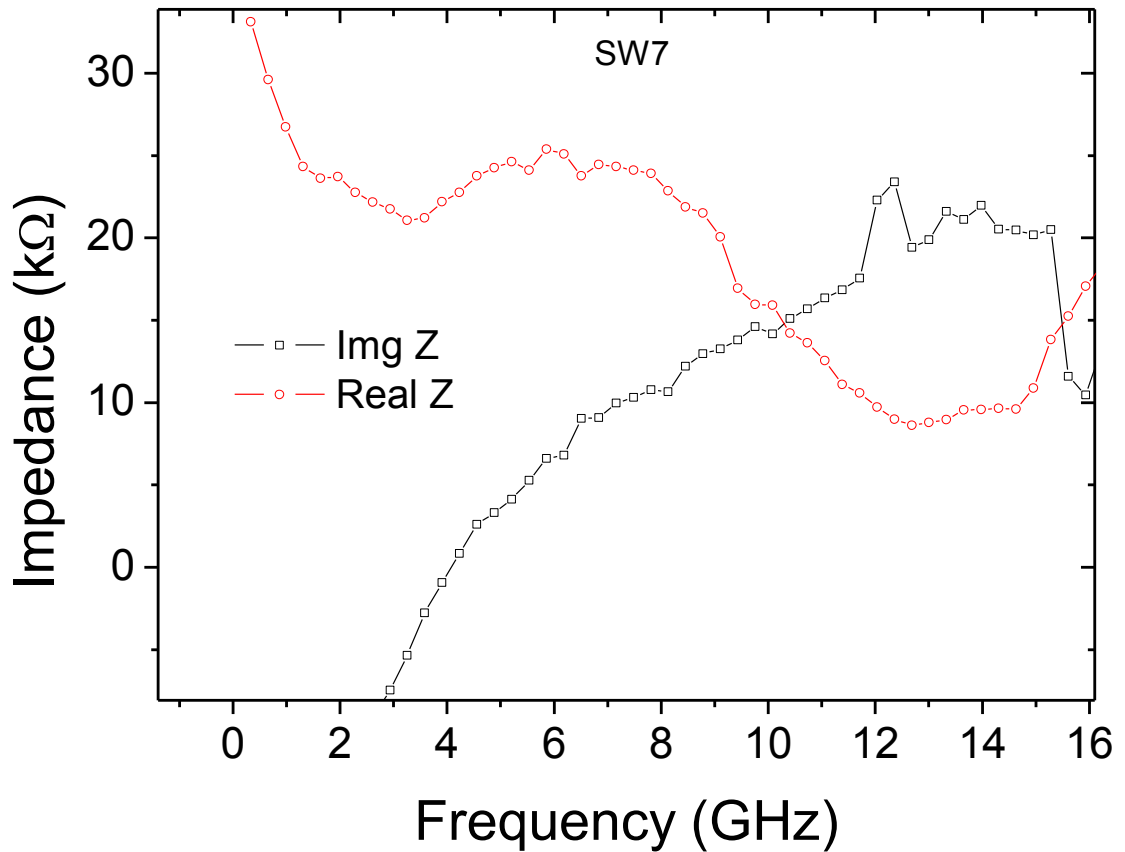


**Figure 4.11:** The real and imaginary impedance of sample SW7, showing a crossover of the two at around 10.3 GHz.

The impedance ( $Z_\omega$ ) of the system can be re-written as shown in equation 4.6.

$$Z_\omega = R_C + R_{CNT} + i\omega L, \quad (4.6)$$

where the first term is the contact resistance, the second is the real part of the CNT and the last term is the imaginary part. Therefore when the real part is equal to the imaginary part it corresponds to a case when  $\omega\tau = 1$ , where  $\tau$  is the momentum scattering time and  $\omega$  is the frequency.

$$Re(z) = Im(Z) \quad \longrightarrow \quad \omega\tau = 1$$

This is strictly true if the contact resistance is negligible as mentioned earlier, but it is known that this is a huge challenge in the present material.

The crossover point can be taken to mean a transition from a diffusive mechanism ( $\omega\tau < 1$ ) to ballistic transport when  $\omega\tau > 1$ . Figure 4.11, suggests that a transition from diffusive to ballistic transport is occurring at about 10.3 GHz for this sample (SW7). Incorporating the contact resistance would mean the transition should occur at much lower frequency than what the present results suggests. Sample SW2 showed a similar transition at 13.6 GHz, which is slightly higher than the other sample. The differences between the two samples under discussion here might be explained in terms of the differences in contact resistances as well as the number of conduction channels. The aspect of contacts shall be explored in the next section which details the investigation on CNT-electrode coupling. It will also later be shown that transition occurs at much lower frequencies in multi-walled CNTs with lower contact resistance.

At present the physics behind the transition from diffusive to ballistic transport in some kind of structurally imperfect CNTs is explained. As was already pointed out earlier, it is suspected that there is significant scattering in samples due to defects and phonon as they are bundles. The transition from diffusive to ballistic regime is realised when the frequency of the stimulus signal becomes greater than the scattering rate in the CNTs. For dynamic transport, scattering length is not so much an important parameter but the scattering rate instead [28]. In this regard ballistic transport was achieved in not so perfect devices by tuning the stimulus frequency. This factor was important in the ability to establish standing waves in the CNTs as the electrons are continuously reflected from the contact ends and hence plasmonic quantum features are realised, that are only achievable in the ballistic

regime. Such observations further emphasize the importance of AC transport over DC transport.

As was outlined in chapter 2, setting up standing voltage waves in a transmission line is equivalent to exciting 1D plasmon waves and measuring the plasmon velocity can be a measure of the Luttinger liquid parameter. Hence from the resonant impedance the resonance frequency can be used to calculate the LL parameter. Since the VNA stimulus was set at -17 dBm (equivalent to 31.6 mV), the excitations achieved here should be low lying energy excitations and thus should be able to give insight into the strength of interactions between the electrons which is measured by the correlation parameter  $g$  defined in terms of the resonance frequency shown in equation 4.7 [15].

$$g = \frac{v_F}{4LF_{res}}, \quad (4.7)$$

where the symbols have their usual meaning defined earlier and  $F_{res}$  is the frequency for the first resonant peak. Using  $v_F = 10^4$  m/s as the effective Fermi velocity (for reasons explained earlier) and the 13.6 GHz the first resonance frequency (in the ballistic regime) from this experimental data for SWNTs we obtain  $g$  to be  $\sim 0.18 \pm 0.02$ , similar to the TLL parameter obtained by Rauf *et al.* using a different technique [94]. This value is also not too far from the theoretically predicted value of 0.25 and lower than the one determined from  $I$ - $V$  measurements by 0.03 discussed in the next section. Since this value is calculated using resonance frequency which does not incorporate contact resistance it is therefore under estimates  $g$  and hence gives lower than the theoretical value.

### 4.1.3: DC Measurements in SWNTs

Previous current-voltage ( $I$ - $V$ ) DC measurements showed that tunnelling into a Luttinger liquid is very different from tunnelling into a Fermi liquid because the TLL is associated with the energy dependent tunnelling amplitude which is expected to vanish as a power law in the energy of the tunnelling electron [95]. This implies a power law dependence of the differential conductance at large bias voltage *i.e.*  $eV \gg k_B T$ ,  $dI/dV \propto V^\varphi$  [95]. The exponent of the voltage term depends on the number of 1D channels and on the geometry of the contacts, which determines whether the electron tunnels into the bulk or end of the TLL.

For our experimental set-up the electron tunnels into the end and hence,  $\varphi$  is given by equation 4.8 [96].

$$\varphi = \frac{(g^{-1}-1)}{4}, \quad (4.8)$$

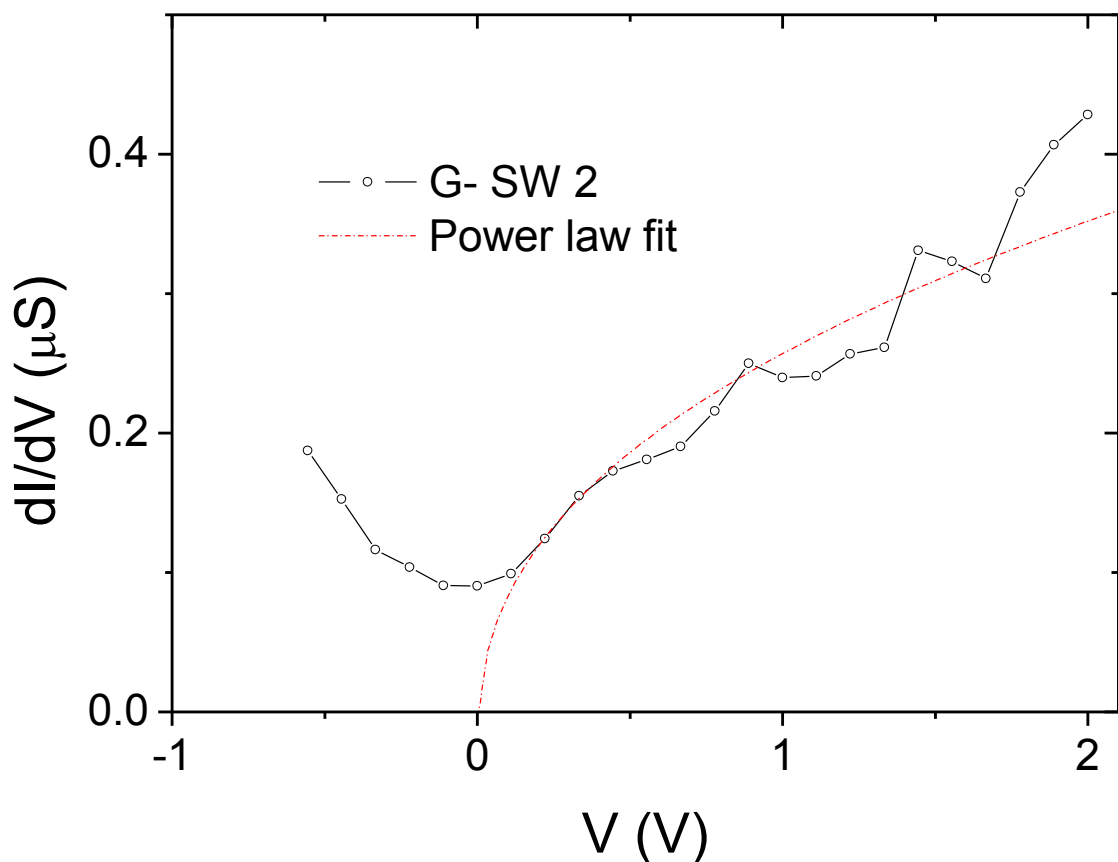


**Figure 4.12:** *Differential conductance versus bias potential for sample SW2 at room temperature.*

The differential conductance of the devices was found to obey power law dependence both at room temperature (Figure 4.12) and low temperature (discussed later) an aspect predicted by the Luttinger liquid theory. Observation of this power law dependence at room temperature suggests that this phenomenon is possible at these elevated temperatures as was also observed in other SWNT bundles by other researchers [97]. In the power law model, the

exponent ( $\varphi$ ) of  $V$  depends on the conduction channels as well as on how the electron tunnels into the Luttinger liquid, it therefore gives an indication of the Luttinger liquid parameter. The exponent ( $\varphi$ ) obtained from different samples ranged from 0.4 to 1.42.

Using the expression for  $\varphi$  given in equation 4.8 and the obtained numerical value from  $I$ - $V$  data of 1.42, for SW7 the Luttinger parameter ( $g$ ) was obtained to be  $0.21 \pm 0.01$ , which is 0.04 lower than the theoretically predicted [15]. The same parameter was obtained from high frequency measurements and thus this work shows measurement of this important parameter using two independent techniques.

#### 4.1.4: RF transmission in SWNTs at cryogenic temperatures

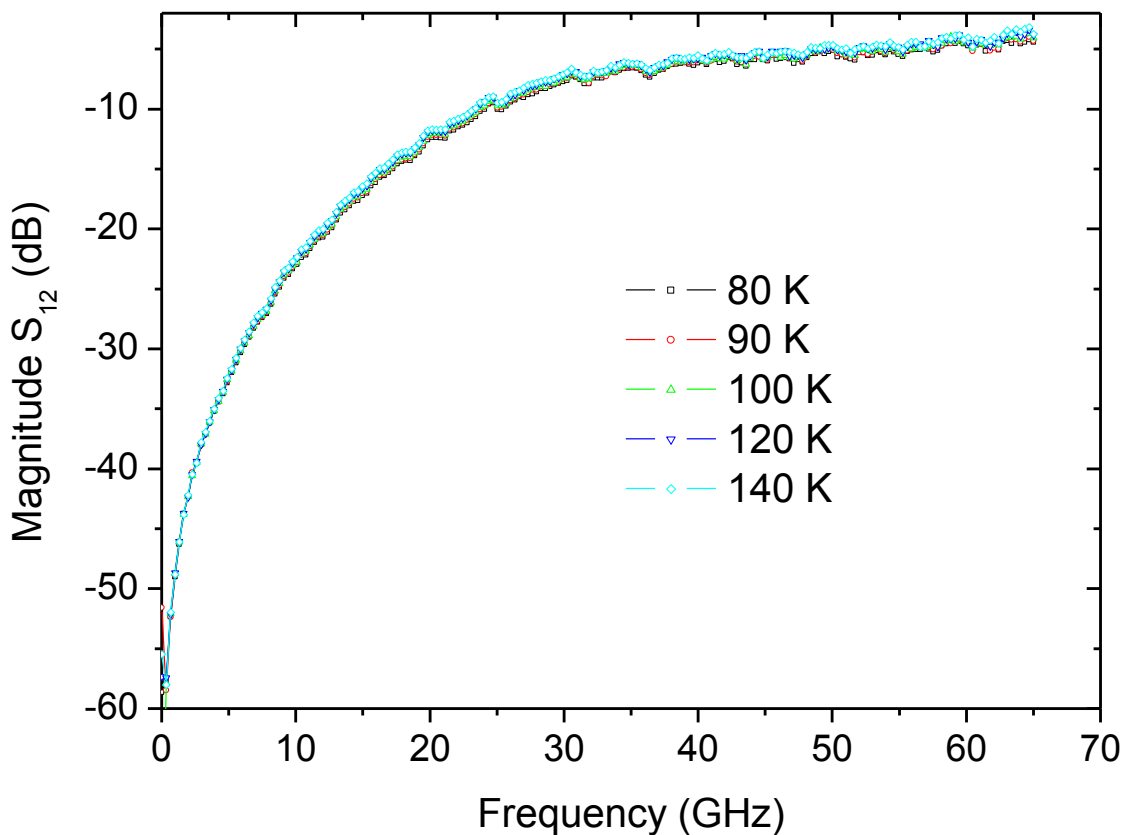


**Figure 4.13:** *Transmission coefficient of sample SW2 (with 6 CNT bundles) in the low temperature range of 80 K – 140 K.*

Reducing the temperature had an effect of increasing the maximum power transmitted by the CNT devices from -15 dB to -5 dB. This is in comparison with room temperature data (Figure 4.6) and low temperature results shown in Figure 4.13. Small incremental temperature steps from 80 K to 140 K, resulted in small increases in power of about 0.1 dB as shown in Figures 4.14 (a & b). Because the margin of measurement uncertainty is in the same range, not much conclusive discussion can be made from the measurements except that there is an increase in power transmission at low temperatures. The next question that can be asked is what is the source of this 10 dB increase in power transmission? This shall be addressed later.

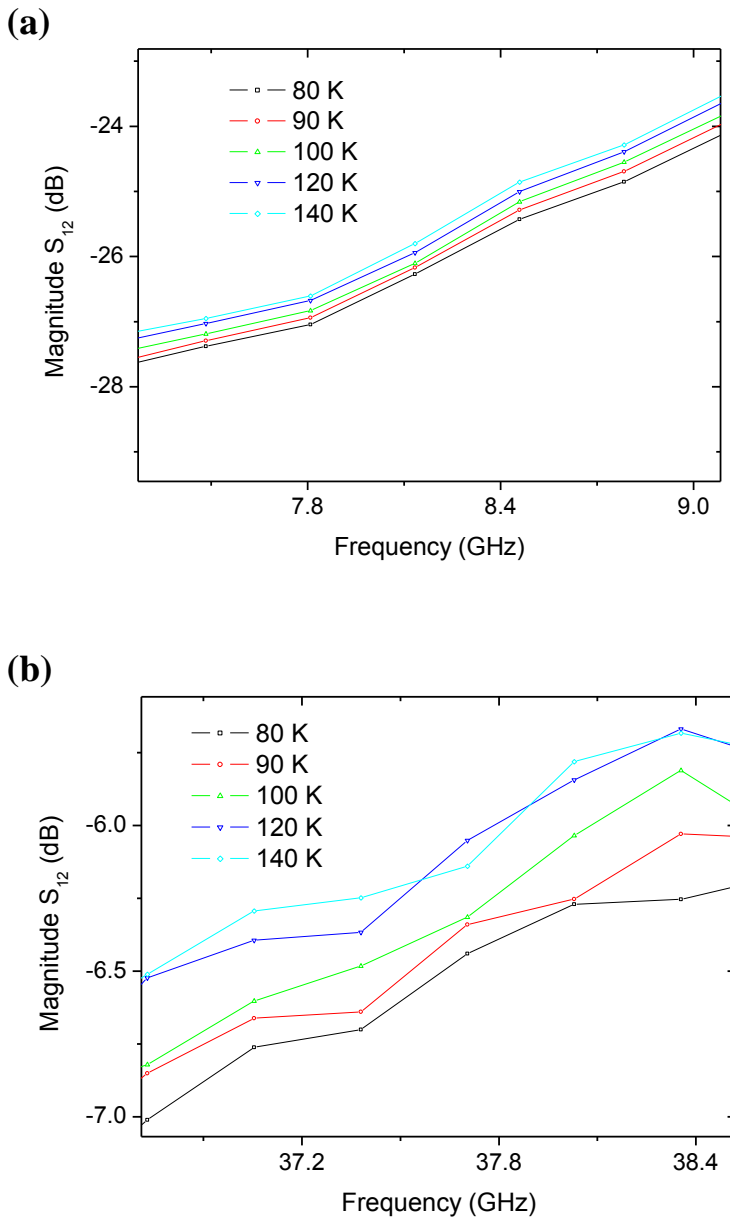


**Figure 4.14:** (a): Transmission coefficient for sample SW2 measured in the temperature range 80 K to 140 K, show small increases in power transmission with temperature in the low frequency regime. (b) The same data but showing the high frequency end of the spectrum.

Having established an increase in transmission by reducing the temperature, what then happens to the complex impedance of the CNTs at these temperatures? Does it also resonate as it was at room temperature? To answer this, the S-parameter data was converted to



impedance as was outlined earlier using standard equations, after de-embedding the parasitic effects.

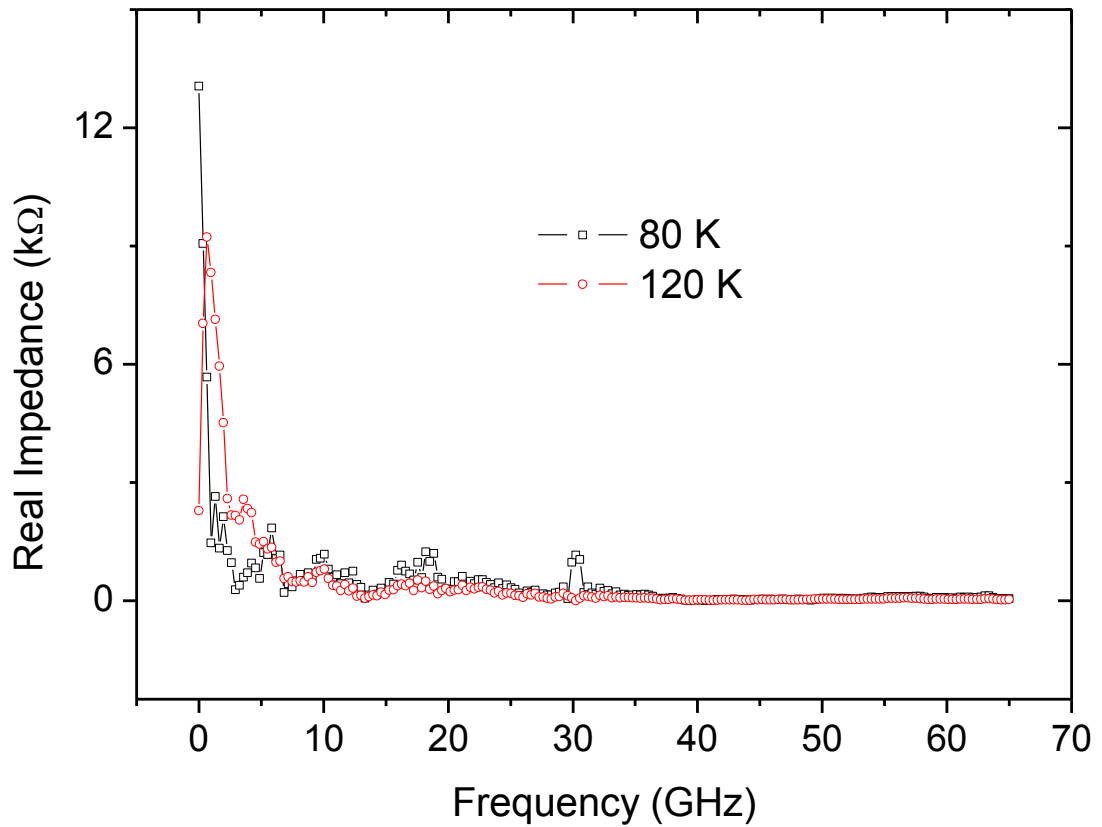


**Figure 4.15:** Real impedance of sample SW2 at 80 K and 120 K, and shows low amplitude oscillations compared to room temperature oscillations.

Since there was an observation of an increase in transmission by lowering the temperature, it was tempting to think that the resonance oscillations would increase in amplitude because damping of 1D plasmons would be suppressed at low temperatures. Unfortunately the results given here (Figure 4.15) suggest otherwise i.e. the amplitude of the oscillations is reduced. Before trying to find an answer to this unexpected result, a look at the imaginary component of the impedance Figure 4.16 is done.

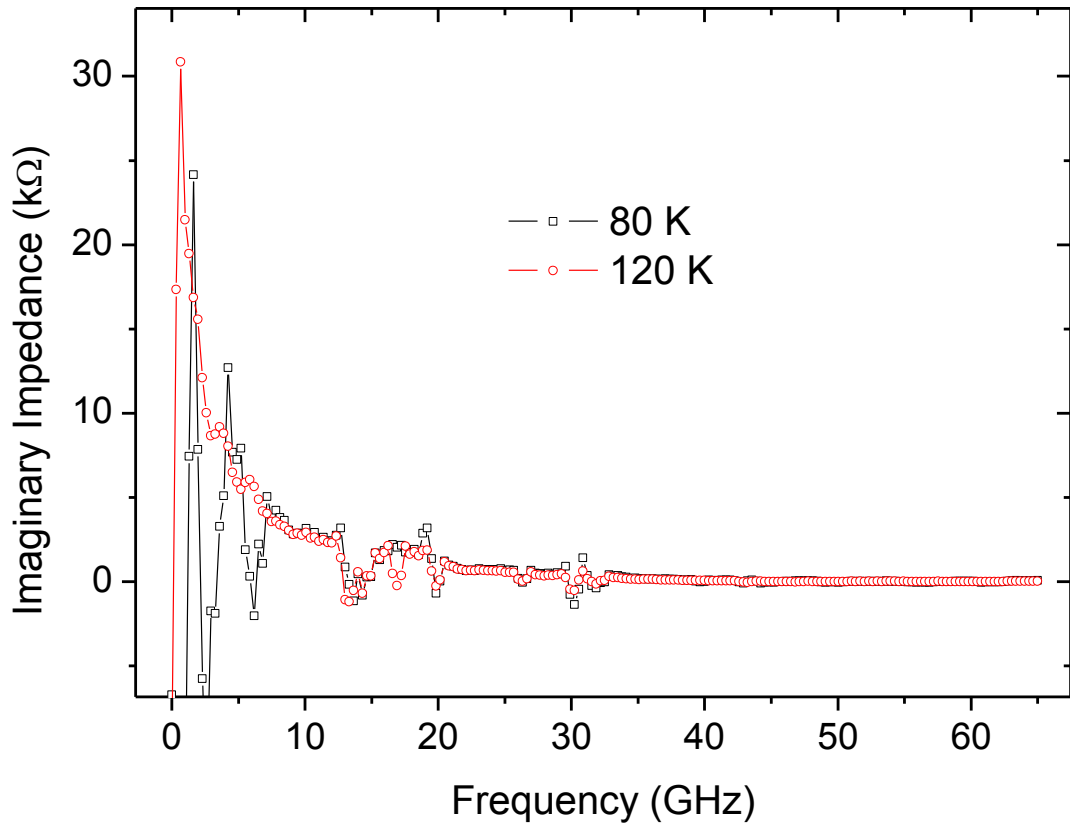


**Figure 4.16:** Imaginary impedance of sample SW7 at 80 K and 120 K showing predominantly positive impedance. The transition from negative to positive occurs at much lower frequency close to 100 MHz.

The imaginary component of the impedance (Figure 4.16) for the low temperature measurements reveals another interesting aspect to the high frequency transmission in CNTs at these temperatures. At room temperature it was observed that the imaginary impedance changed sign from negative (i.e. capacitive behaviour) to positive (Inductive behaviour) at around 10 GHz. The low temperature data shows a transition from capacitive to inductive behaviour at much lower frequency of approximately 100 MHz. It then appears that reducing the temperature is resulting in an increase in inductive response and a reduction in the capacitive behaviour. What is the source of this increased inductance? One possible reason could be that the contact resistance of the devices is reduced at low temperature allowing the inductance of the CNTs to dominate. To get clarification on these speculations,

the capacitance and inductance of the devices was calculated and a trend was observed as the temperature was lowered.

#### 4.1.5: RF Equivalent Circuit

The device parameters (capacitance and inductance) were obtained using Matlab RF Simulink software. An equivalent (RF circuit) component transmission line was modelled and used to fit the experimental data by simulating the S-parameters and by adjusting the values of the RF components for both the open and DUT devices to determine the approximate capacitance and inductance of both the contacts and CNTs. The circuit below (Figure 4.17) is the schematic diagram of the equivalent circuit.

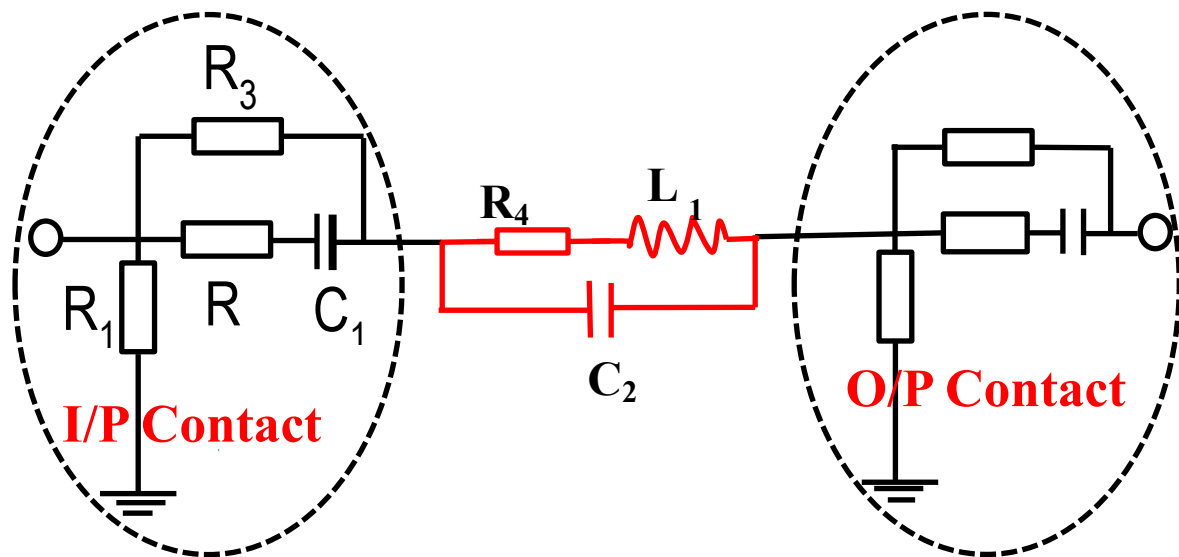


**Figure 4.17:** A device equivalent circuit used to simulate the experimental S-parameters for all the devices. The circuit components  $R_1, R_2, R_3$  and  $C_1$  are the same of both input contact and the output contact.  $R_4, L_1$  and  $C_2$  are for the aligned CNTs.

Using the equivalent circuit shown in Figure 4.17, the device parameters were obtained. The components  $R_4, L_1$  and  $C_2$  are the intrinsic resistance, inductance and capacitance respectively of the aligned CNTs. The other components  $R_1, R_2, R_3$  and  $C_1$  are for the

contacts assumed to be identical for both input and output terminals. The next two figures (Figures. 4.18 (a) and (b)) show the experimental data fitted with the simulation model.

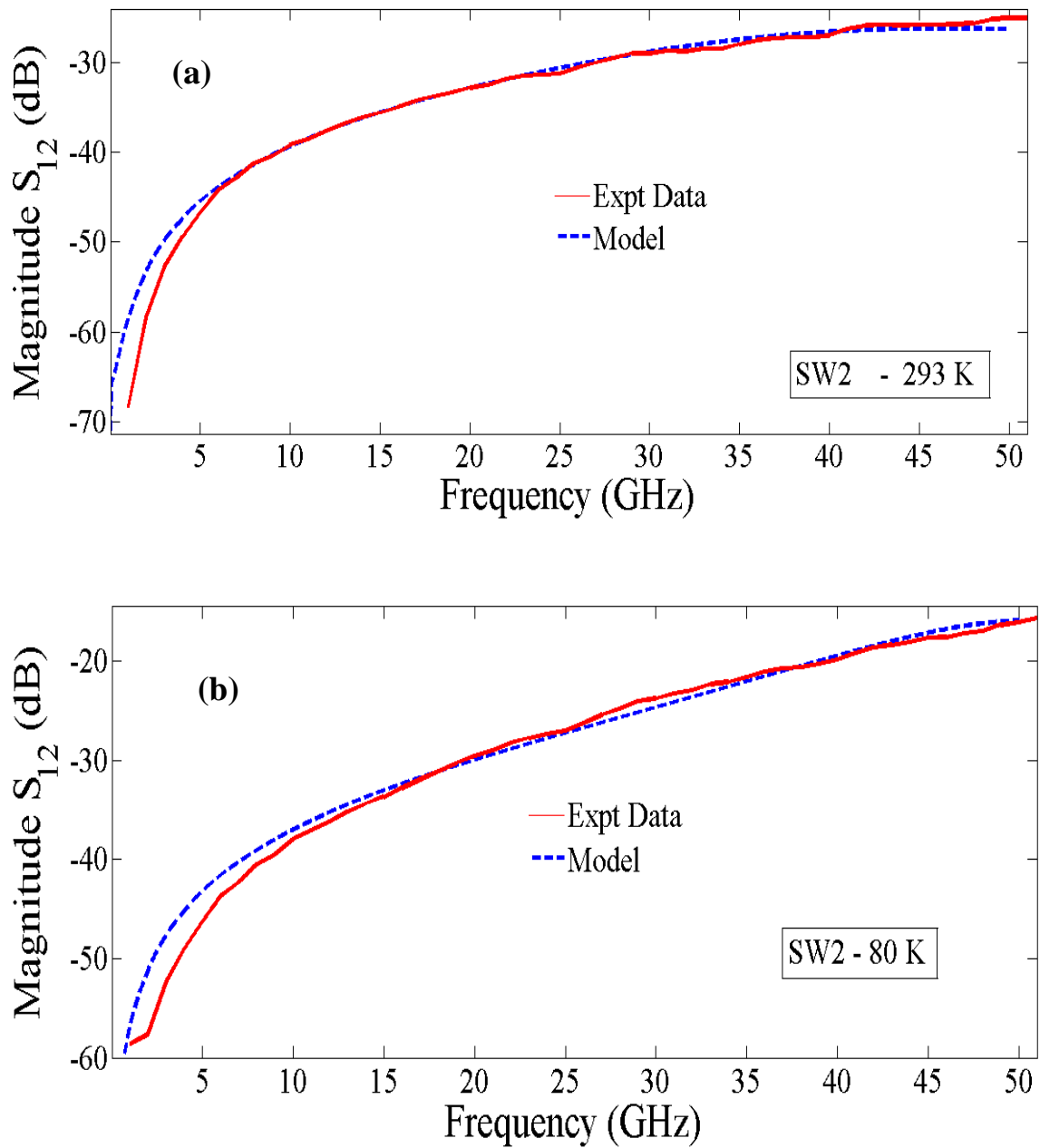


**Figure 4.18:** (a) Transmission coefficient ( $S_{12}$ ) for sample SW2 fitted with the simulated data from the equivalent circuit for room temperature measurements. (b) The fitted data for 80 K measurements for the same sample.

After fitting the experimental data with the model the device parameters were obtained which are tabulated in the table 4.1.

**Table 4.1:** Device parameters extracted from the simulation using the equivalent circuit for sample SW2.

Parameter	293 K	120 K	80 K
R <sub>1</sub>	1 MΩ	1 MΩ	1 MΩ
R <sub>2</sub>	110 Ω	10 Ω	10 Ω
R <sub>3</sub>	90 kΩ	45 kΩ	45 kΩ
R <sub>4</sub>	1.7 kΩ	0.5 kΩ	0.5 kΩ
C <sub>1</sub>	3.5 fF	9.9 fF	9.8 fF
C <sub>2</sub>	50 fF	39 fF	39 fF
L <sub>1</sub>	7.0 nH	5.5 nH	5.5 nH

The results in table 4.1, show that all the device parameters reduce as the temperature is lowered particularly the resistive components. This explains the increased transmission as the temperature is reduced. The contact parameters decrease significantly by a much larger margin than the intrinsic components. Due to measurement uncertainty at low temperatures and because of the complex instrument calibration, conclusive discussions cannot be drawn about the intrinsic parameters of the CNTs. It can however be confidently reported that the increase in transmission is due to the reduction in the contact resistance, which decrease by over 50 %.

The reduction in the contact resistance enables the inductive component of the device to be dominating as the temperature is lowered. The parameter C<sub>2</sub> is the total parallel equivalent of both the electrostatic and quantum capacitance, while the L<sub>1</sub> is the total equivalent of magnetic and kinetic inductance. As the frequency is increased the kinetic inductance dominates the magnetic inductance and theoretical calculations have shown that kinetic inductance is very significant in the terahertz regime [98]. To fully concretise on the above hypothesis, attention is drawn to the measured two terminal DC measurements at low temperatures.

As mentioned earlier current-voltage (*I-V*) DC measurements showed that tunnelling into a Luttinger liquid obeys a power law dependence of the differential conductance at large bias voltage *i.e.*  $eV \gg k_B T$ ,  $dI/dV \propto V^\varphi$  [95].

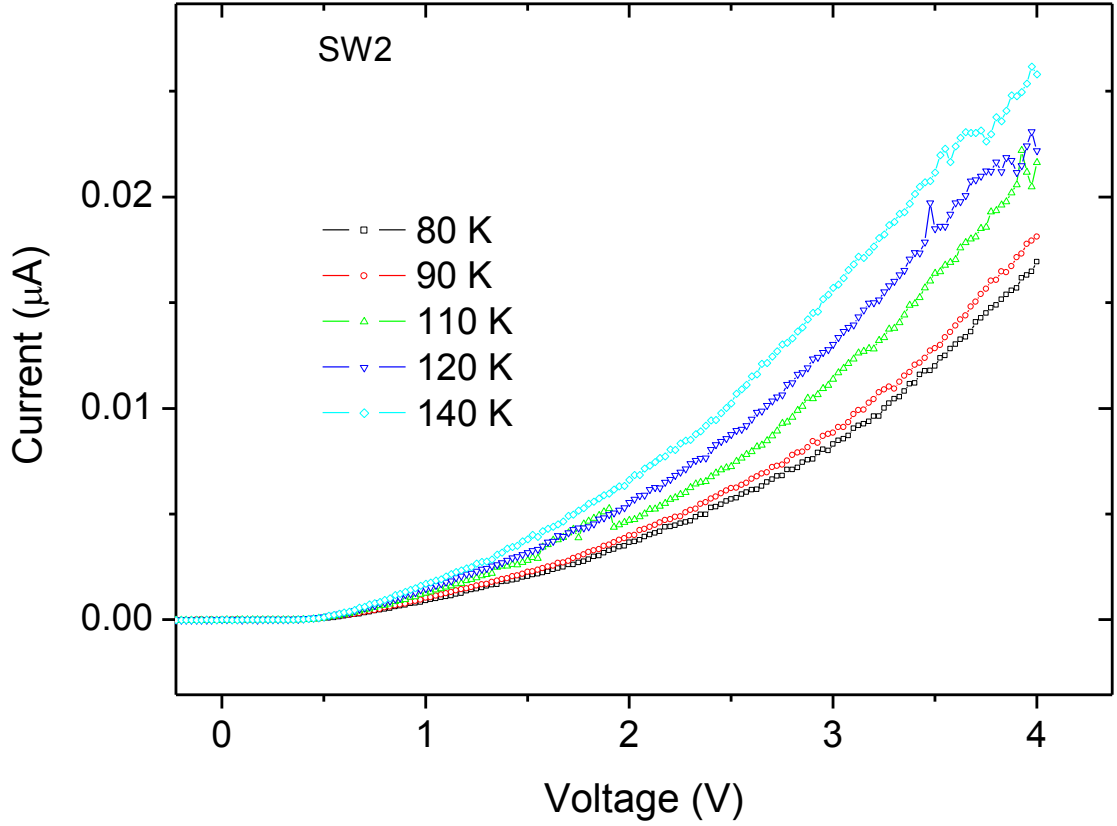


**Figure 4.19:** Low temperature two terminal  $I$ - $V$  measurements for sample SW2.

The two terminal  $I$ - $V$  measurements (Figure 4.19) show an increase in current with increase in temperature, which is an indication of increase in conductance of the device. The temperature was further reduced to below 50 K and another interesting aspect of the results was observed. Reducing the temperature of the devices to below 50 K further supported the Luttinger liquid tunnelling mechanism at low temperatures based on scaling law described by equation 4.10. In the LL model a universal expression for current, voltage and temperature dependence can be taken as in 4.10 [99]:

$$I = I_0 T^{\alpha+1} \sinh\left(\frac{eV}{2k_B T}\right) \times \left[ \Gamma\left(1 + \frac{\alpha}{2} + i \frac{eV}{2\pi k_B T}\right) \right]^2, \quad (4.10)$$

where  $\Gamma$  is the gamma function, and the other symbols have their usual meanings. This universal expression has two asymptotic behaviours in the low field and high field regime. For the  $I$ - $V$  data given here in the high field regime i.e.  $eV/k_B T > 1$ , then  $I \propto V^{\alpha+1}$ . And the

derivate  $dI/dV$  should obey a simple power law  $dI/dV \propto V^\alpha$ . The implication from this expression is that  $I$ - $V$  curves at different temperatures should collapse into a single curve as shown in Figure 4.20.

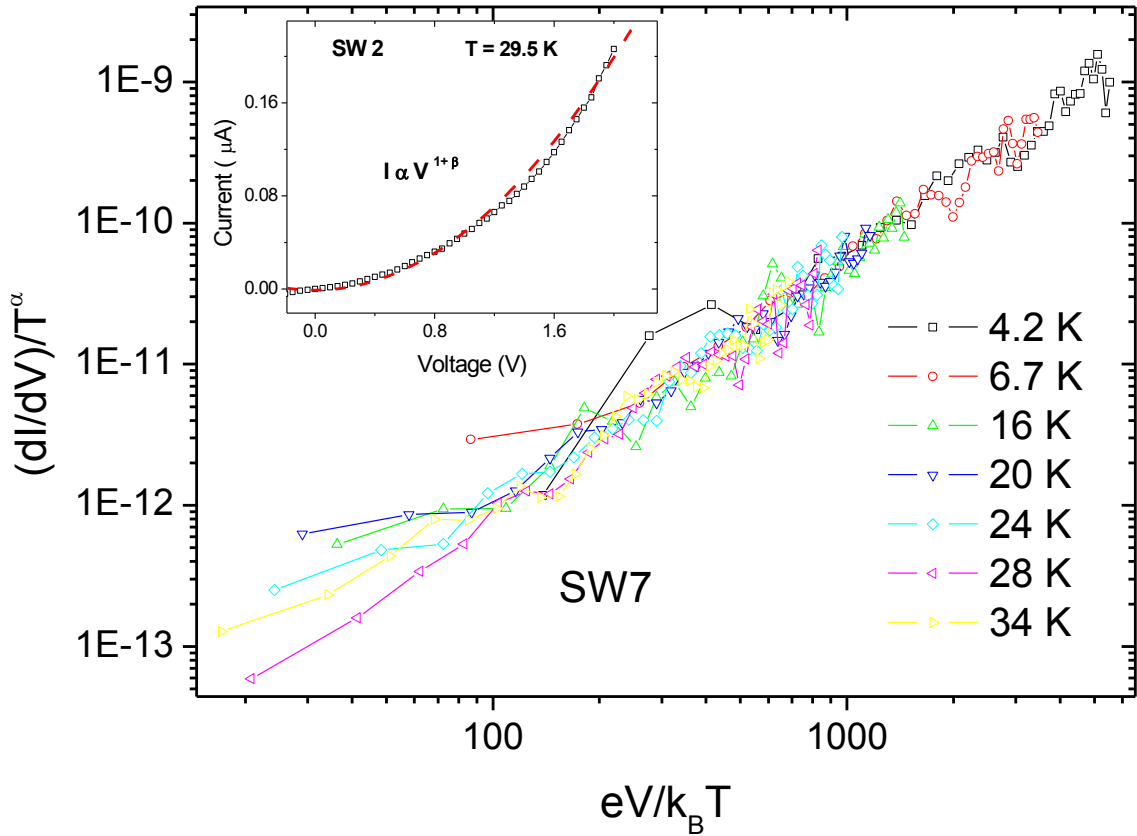


**Figure 4.20:** The main figure shows that the differential conductance for SW7 at different low temperatures collapsing to a single gradient at high bias voltages. The inset shows the power law dependence ( $I \propto V^{\alpha+1}$ ) of the current at 29.5 K for SW2.

The graph Fig 4.20, show a collapse of various temperature curves into one in accordance with LL theory [99]. The graphs shows that the condition is valid above 1 V satisfying the condition  $eV \gg k_B T$ . The inset is for sample SW2 showing  $I \propto V^{1+\phi}$ .

The author is cognisant of the fact that a power law dependence on its own is no proof of the Luttinger liquid state although many experimental work before have made that inference [100], [101]. It is known that dynamic Coulomb blockade can also result in power law dependence and can thus easily be mistaken to suggest an LL state. Another earlier

theoretical publication tried to find a distinction between the dynamic Coulomb blockade and the LL and came to a conclusion that in DC measurement there is no way of making the distinction but using AC measurements one can be able to differentiate the two [102]. In no uncertain terms the article [102] states that oscillations in the conductance or impedance can be used to differentiate the two effects. This work therefore has succeeded in this objective. And again this serves to show the advantage and significance of AC transport measurements over DC measurements as was earlier alluded to. Therefore in conclusion RF transport in SWNTs has shown us features associated with the Luttinger liquid excitations from both AC and DC measurements. The next question now is can this behaviour be observed in CNTs with many concentric walls, i.e. double walled and multi-walled. And the answers are in the next two sections that follow.

## **4.2: RF transmission in double walled CNTs (DWNTs)**

Double walled carbon nanotubes are some rare forms of nanotubes that have successfully been synthesized by a few groups in the science community. A brief outline on how the DWNTs discussed in this section were synthesized was provided in chapter 3. The significance of the unique structure of DWNTs with regards to electrical transport can be understood by looking at how electrical measurements have been done. We note that electrical transport properties of many carbon nanotubes (CNTs) are commonly measured after acid purification, surfactant stabilization and ultra-sonification dispersion prior to the deposition of electrodes [103]. These processes invariably cause significant damage and doping to the outer wall of the CNTs which will alter the transport mechanism. This is probably why most catalytically produced and lithographically contacted CNTs have been found to be diffusive at room temperature [103]. Coherent transport has only been observed in single walled (SWNT) and multi-walled nanotubes (MWNT) at cryogenic temperatures with the exception of pristine MWNTs measured by an in-situ microscopy technique [13].

In our previous DC measurement studies [104] of filled DWNTs, it was established that DWNTs have an advantage over single-walled CNTs because the inner wall is protected by the outer wall such that it will be free of defects and other effects due to interactions with the substrate. It was also shown that the filling material can alter significantly the transport



behaviour. The discussion presented here is for unfilled DWNTs that should have structurally perfect inner walls.

Previous non-equilibrium Green's function calculations have predicted AC response that is chirality dependent in SWNTs even in the presence of contact effects and a universal inductive to capacitive transition in the imaginary admittance with increase in contact resistance [105]. It was stated earlier that a semi-classical model based on a transmission line by Burke *et al.* has predicted possible Luttinger liquid excitations in metallic CNTs achievable in the gigahertz regime [15] by setting up standing voltage waves in the CNTs.

The current AC studies have shown greater sensitivity of the imaginary impedance to temperature changes. Unlike the single walled CNTs, the DWNT devices used in this work are not bundles but individual tubes between four and eleven aligned across the signal terminal of the waveguide. The figure (Fig.4.21) is the S-parameter data representative of the samples investigated.

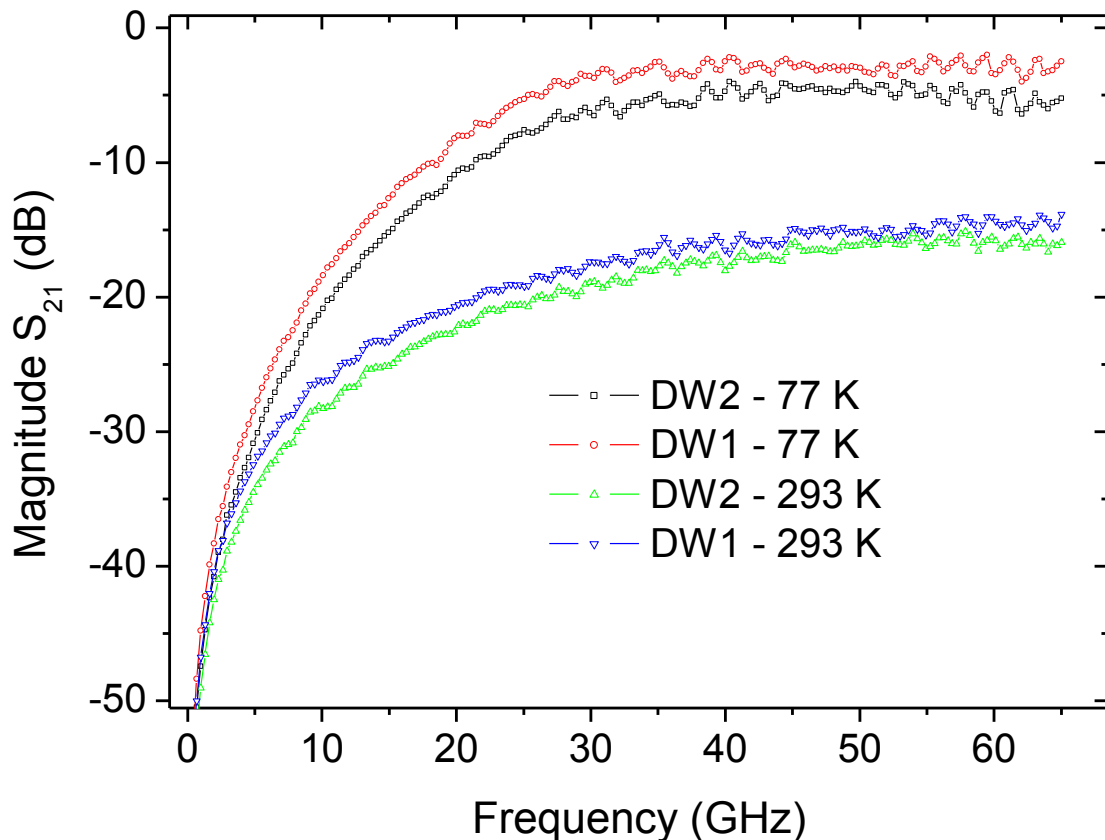


**Figure 4.21:** Transmission coefficient for samples DW 1 & 2 at room and 77K temperatures.

The sample DW1 had eleven individual DWNTs aligned across the wave guide gap, while sample DW2 had four DWNTs. The average outer diameter of each DWNT was about 2.5 nm see TEM images Figure 3.2. It is observed from Figure 4.21 that the eleven DWNTs of DW1 transmit on average about 2 dB more power than the four DWNTs of DW2 device at higher frequencies. A reduction in temperature is evidently accompanied by a 10 dB increase in transmission at 77 K measured at a frequency of around 24 GHz. Furthermore the low temperature data show transmission saturation at around 40 GHz which is not observed in the room temperature data. The reason for this saturation is not yet clear. However, to understand the significance of temperature on the transmission capabilities of the devices, the complex impedance was extracted using the technique already outlined.

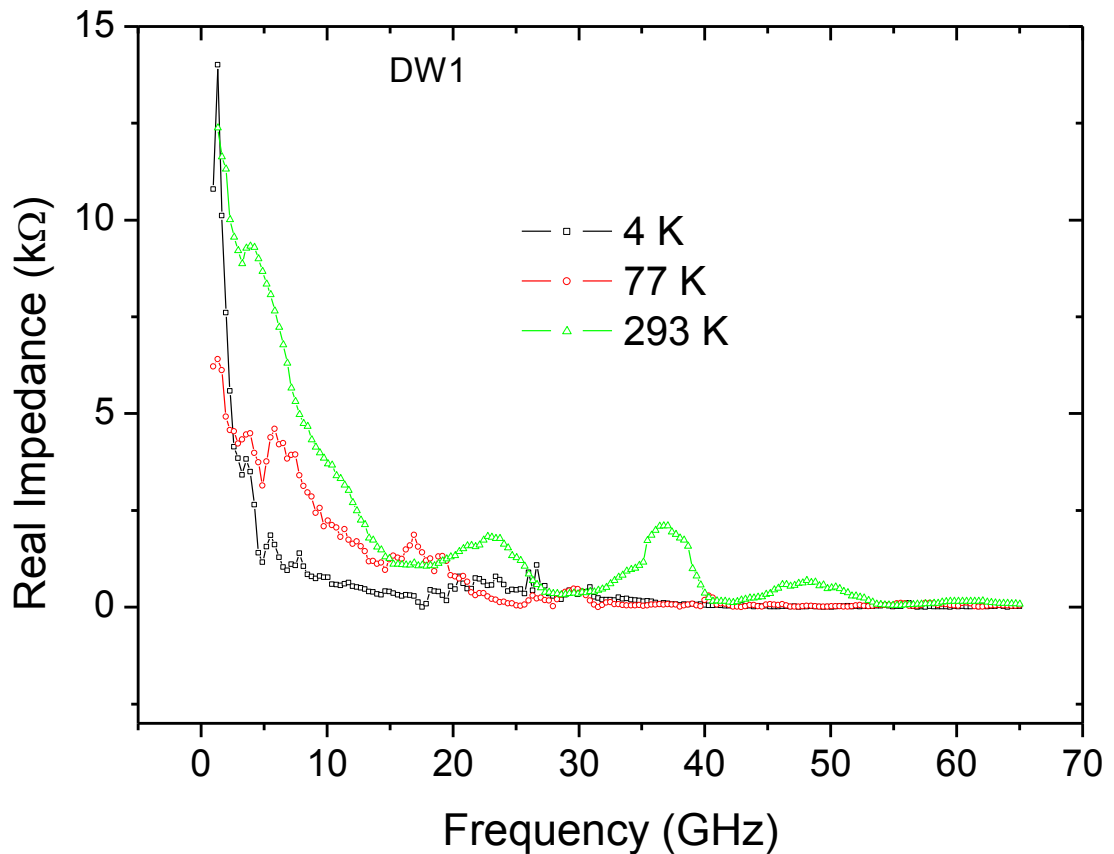


**Figure 4.22:** Real Impedance of DW1 at three different temperatures, it shows a reduction in impedance with temperature.

Figure 4.22, shows a general decrease of real impedance with temperature particularly in the frequency range between 1 GHz and 25 GHz. The reduction in the resistive component of the impedance probably explains the increase in power transmission observed in Figure 4.21. What is even more interesting however is the reactive component of the impedance, which shows a transition from capacitive to inductive behaviour with a decrease in temperature see Figure 4.23.

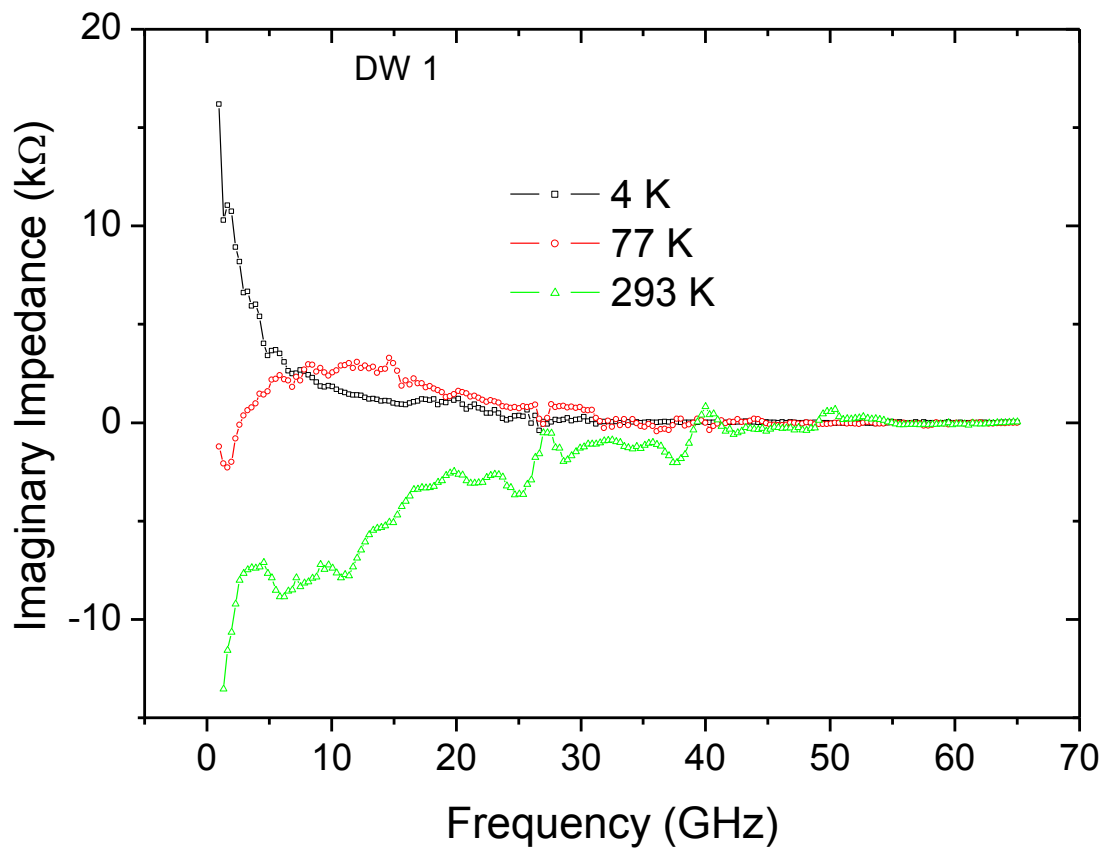


**Figure 4.23:** Imaginary impedance for DW1 at different temperatures showing a capacitive to inductive transition with temperature decrease.

The overall implication of the capacitive to inductive transition would be that the crossover from diffusive to ballistic transport occurs at much lower frequency at low temperatures than it would be at room temperature. The next three figures 4.24 to 4.26, illustrate this aspect. Similar results were also observed for other samples not shown here but in the article [81].

This perhaps is not surprising because at low temperatures phonon scattering is significantly suppressed and the transition to ballistic transport would occur at lower frequencies.

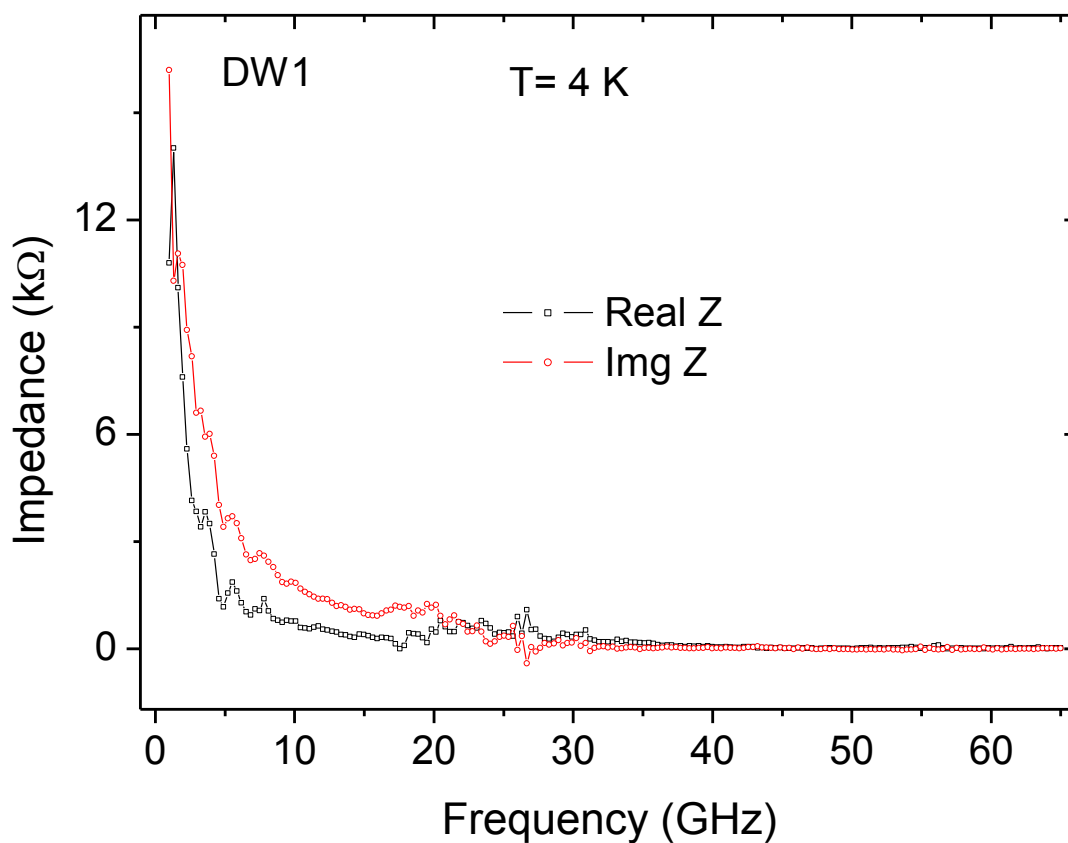


**Figure 4.24:** Complex impedance of DW1, measured at 4 K. It shows a transition from diffusive to ballistic transport at about 1.5 GHz.

It is believed that the crossover from diffusive to ballistic transport suggested by Figure 4.24 at about 1.5 GHz, could be shifted to much lower frequency because of the finite contact resistance as was mentioned in the last section on single walled CNTs.

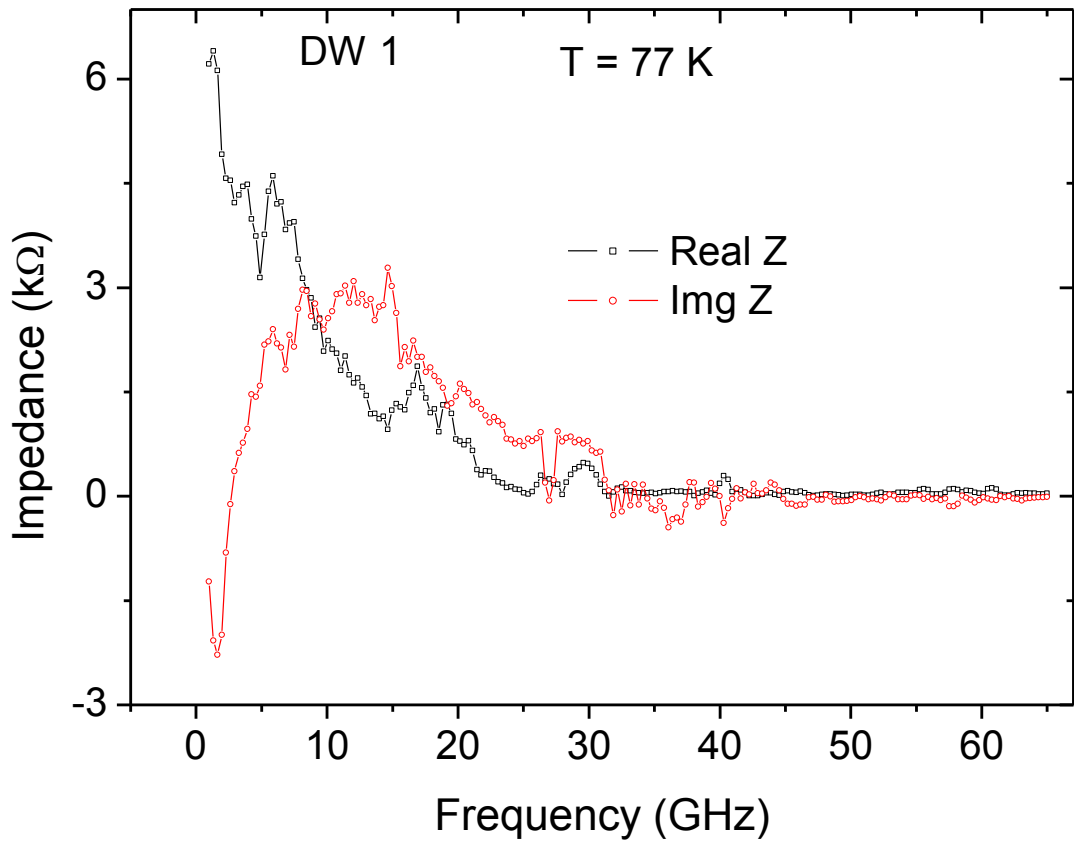


**Figure 4.25:** Complex impedance of DW1, measured at 77 K. It shows a crossover from diffusive to ballistic transport at around 9 GHz.

In addition to the transition from diffusive to ballistic transport seen in the figures above, low amplitude impedance oscillations at low temperatures (4 K and 77 K) are observed, when compared to the room temperature. The damping of the impedance oscillations at low temperature suggest that phonon scattering plays an important role to the observation of these oscillations. The author believes that the phonon scattering results in significant reduction of the effective Fermi velocity from  $10^5$  m/s to  $10^4$  m/s. This will result in impedance resonance occurring in the GHz frequency range for micron long transmission line as the case here. At low temperatures the oscillations are washed out as the effective velocity is increased and resonance moves to higher frequencies in the sub-THz range.

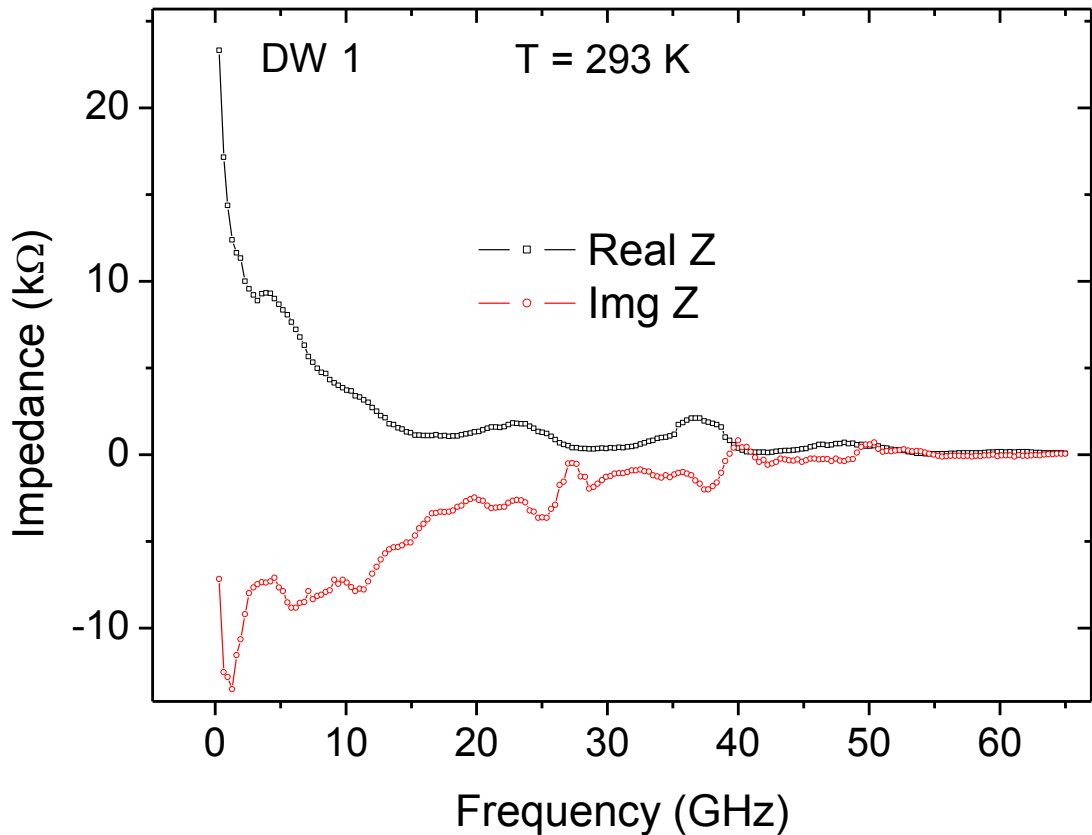


**Figure 4.26:** Complex impedance of DW1, measured at room temperature. It does not show any crossover to ballistic transport as was observed from other devices.

As highlighted earlier DWNTs have a more structurally perfect inner wall that is protected by the outer wall when compared to single walled CNTs. This will imply a higher effective Fermi velocity in the inner wall such that impedance resonance will not be observed in the GHz range but THz regime for a micron long device. This probably explains why the impedance oscillations are not as well defined in individual DWNTs as they were in bundles of SWNTs. While this maybe speculative, it was however the objective of this work to probe the origin of the capacitive to inductive transition as the temperature is reduced.

It is noted that previous, theoretical [105] and experimental [106] works had predicted and observed a similar capacitive to inductive transition which was explained in terms of the coupling strength between the electrodes and the CNT devices. This coupling effectively determines the contact resistance, which means when it is high, the resistance is low and hence the electrons encounter a smaller barrier to tunnel through. The current results and the

following section on multi-walled CNTs also agree with previous analysis. It is nevertheless shown that the coupling strength is dependent on the physical conditions as well as on the metal used for the contacts. The S-parameter data for the DWNTs was therefore fitted with model so as to estimate the contact resistance parameters.

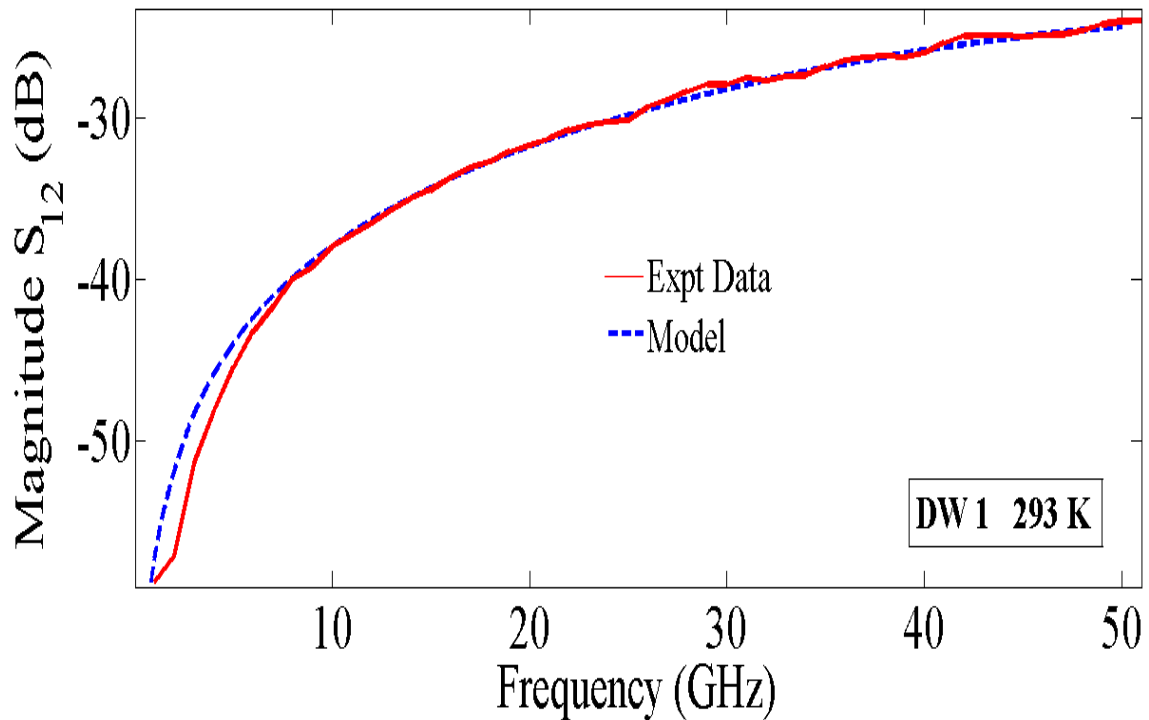


**Figure 4.27:** The transmission coefficient  $S_{12}$  at 293 K for sample DW1, fitted with simulation model so as to determine the circuit parameters.

A pronounced change in the contact resistance was observed from the fitting of both the room temperature (Fig.4.27) and low temperature (Fig.4.28) data by reducing the temperature. The results show a small change of the intrinsic properties of the CNT parameters with temperature. Table 4.2 in the next page shows the extracted circuit component parameters.

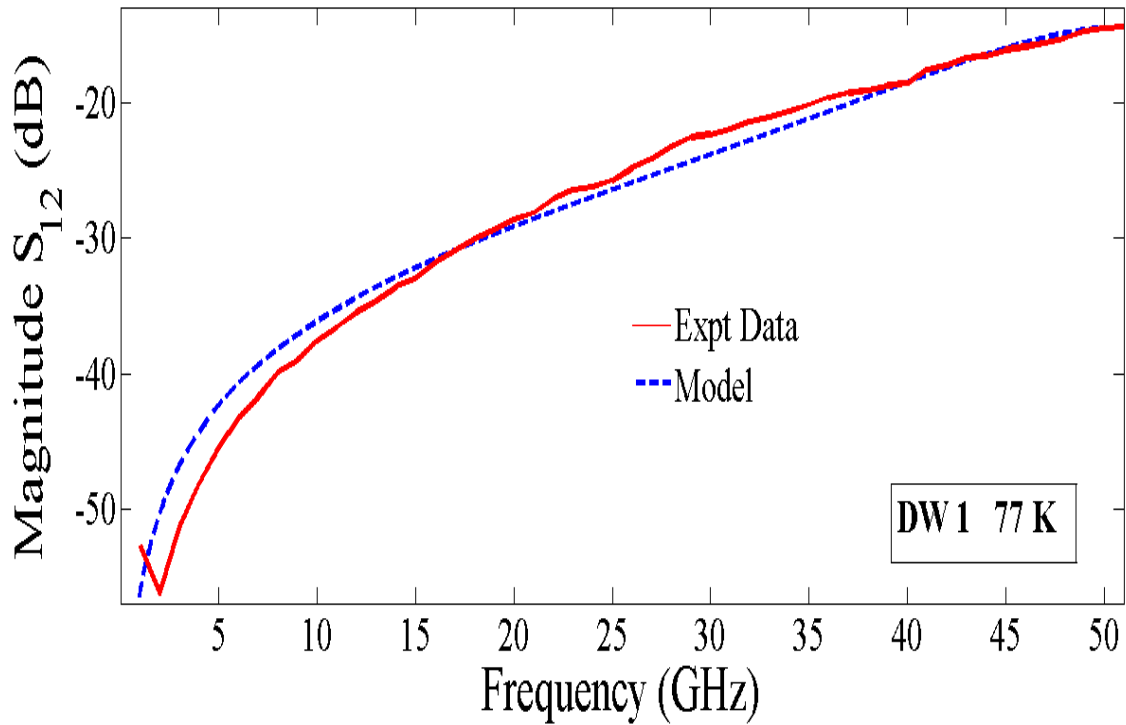


**Figure 4.28:** The transmission coefficient  $S_{12}$  at 77 K for sample DW1, fitted with simulation model so as to determine the circuit parameters.

Figure 4.28, show that the simulation model does not accurately describe the low frequency response particularly below 10 GHz of these devices. The exact reason for this is not yet clear but may be due to the complex low temperature calibration, more work is however required to clarify this.

**Table 4.2:** Showing the extracted circuit parameters from the fitting of DW1 S-parameters.

	293 K	77 K
$R_2$	110 $\Omega$	10 $\Omega$
$R_3$	90 k $\Omega$	90 k $\Omega$
$R_4$	1.2 k $\Omega$	0.4 k $\Omega$
$C_1$	4.2 fF	8 fF
$C_2$	50 fF	6 fF
$L_1$	3.0 nH	4.1 nH



It is however apparent that the CNT- electrode coupling seems to play a very important role on the high frequency response of these devices. Hence two terminal  $I$ - $V$  data (for DWNTs) was fitted with the Landauer – Büttiker equation (2.7) to obtain an idea on the CNT- electrode coupling see Figure 4.29.

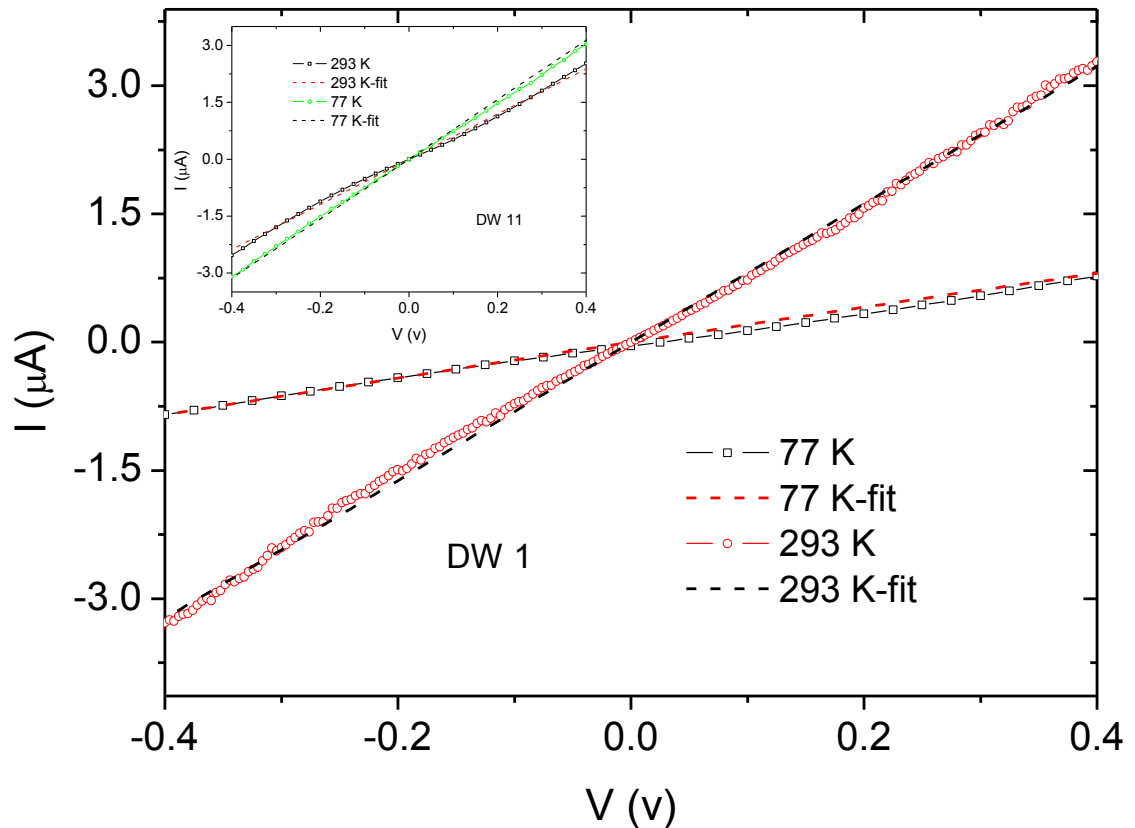


**Figure 4.29:**  $I$ - $V$  measurements for sample DW 1 and DW 11(inset) fitted with the Landauer – Büttiker equation to determine the CNT – electrode coupling strength.

The coupling strength of DW 1 increased by 1.9 meV, from 3.7 meV at room temperature to 5.6 meV at 77 K, similarly for DW11 (one of the eleventh device with five CNTs) it increased by 1.2 meV. This increase is associated with a decrease in the contact resistance and this supports simulation data and explains the increase in high frequency transmission observed earlier at low temperatures.

In conclusion the reactive impedance of DWNTs show higher sensitivity to temperature changes resulting in a transition from capacitive to inductive response as the temperature is lowered. This crossover is due to a significant reduction in the contact resistance and thus enhancing the electrode-DWNT coupling. The implication of this is that the contact barrier and capacitance is reduced resulting in the crossover to inductive response and more power transmission at low temperatures. As was alluded earlier a similar crossover was observed by other workers in the field although at much lower frequencies. This work is significant in the sense that it has established an impedance crossover at low temperatures due to contact effects and thus device engineering will need to incorporate this in their designs.

Impedance oscillations which may be associated with LL behaviour were also observed but the amplitude was significantly low compared to single walled CNTs. It is our belief that this could be due to the  $1\mu\text{m}$  dimension of the TL used. For such a TL in near perfect or defect free CNTs, oscillations should be expected in the THz regime and not GHz range as was the case in this work. Details of this work on doubled walled CNTs have recently been published in Applied Physics letters, see, Appendix for a selection of the published papers.

### 4.3: RF transmission in multi-walled CNTs (MWNTs)

Multi-walled nanotubes as the name implies are made of several concentric nanotubes with external diameters that can be as wide as 100 nm. They have since been known to be overall metallic although some inner walls might have different chiralities [107]. Because of their metallic nature they have been widely suggested for use as interconnects in RF and microwave devices [108]. They are relatively easy to manipulate when compared to SWNTs and DWNTs and for this reason it was easy to align single tubes on the waveguide and measure the scattering parameters. The nanotubes used for this work had an average external diameter of 80 nm.

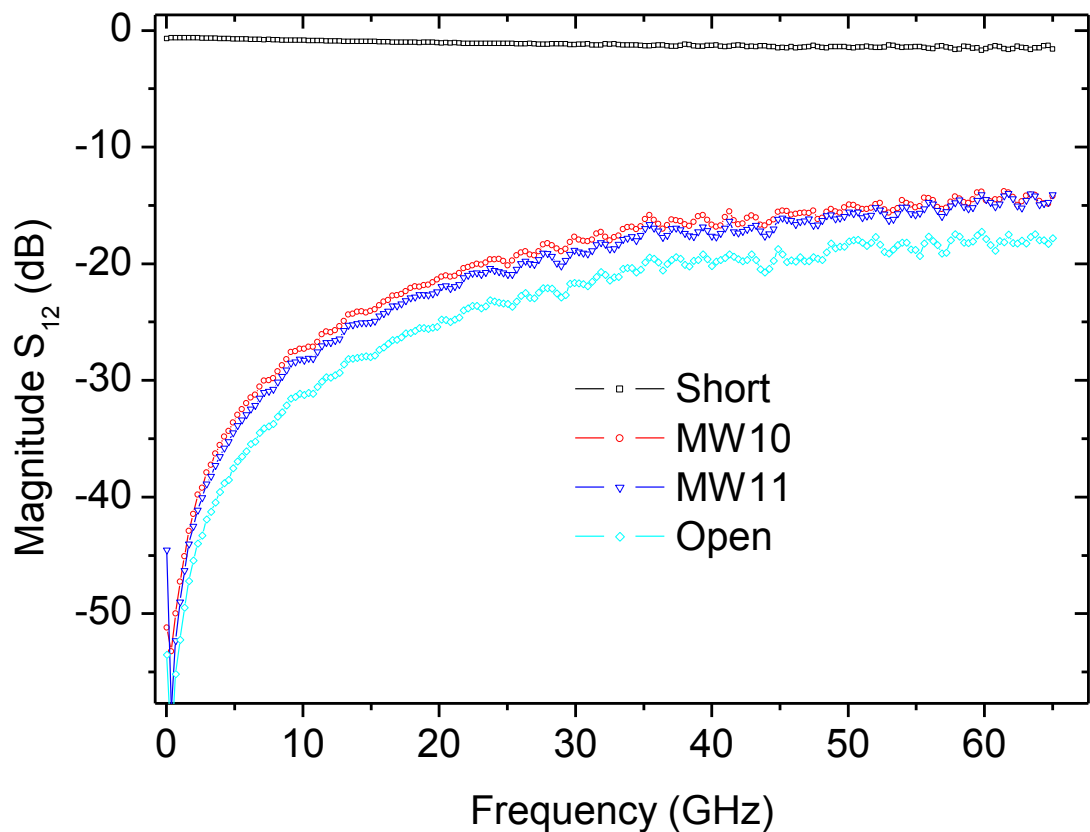


**Figure 4.30:** Transmission coefficient of MWNTs devices MW10 and 11 with different diameters. There is no significant difference between the samples.

One of the first attempts was to determine if there was a diameter dependence on the transmission capabilities of the tubes from the different MWNTs samples. A plot of the transmission coefficient of two MWNTs samples with a diameters 80 nm and 100 nm for MW 10 and MW 11 respectively do not reveal any significant diameter dependence in power transmission as shown in Figure 4.30. This is not to say, it is not there but we believe with current measurement accuracy it is not possible to resolve. An 80 nm (inner diameter) MWNT would theoretically be expected to have about 10 inner walls while a 100 nm tube should have approximately 12 inner walls [107]. With this small difference it is not easy to distinguish between the tubes using this level of accuracy and technique.

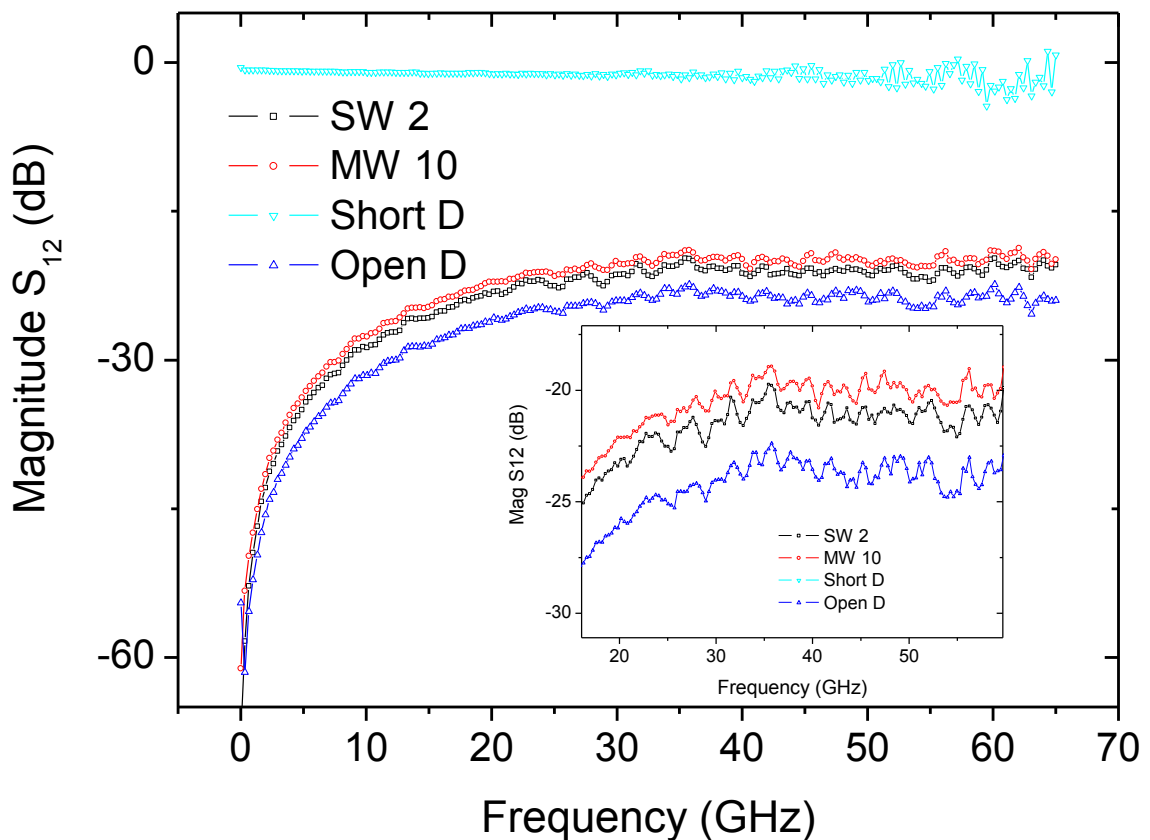


**Figure 4.31:** Magnitude of  $S_{12}$  (dB), of MWNT device in comparison with the SWNT device. The inset shows the high frequency part of the data.

Another attempt was to make comparison between MWNT devices and SWNT devices. The results show that an individual MWNT device could transmit about 1 dB more power than

six SWNT bundles as shown in the Figure 4.31. More studies will be required to draw sufficient conclusive results on the mentioned comparisons. This is based on the same argument about the measurement uncertainty being too high for such signal to noise ratio. However one question that is still relevant is; Are there still impedance oscillations observed in MWNTs as was with SWNTs? To answer this, the CNT impedance was extracted which gives more information than just the S-parameters.

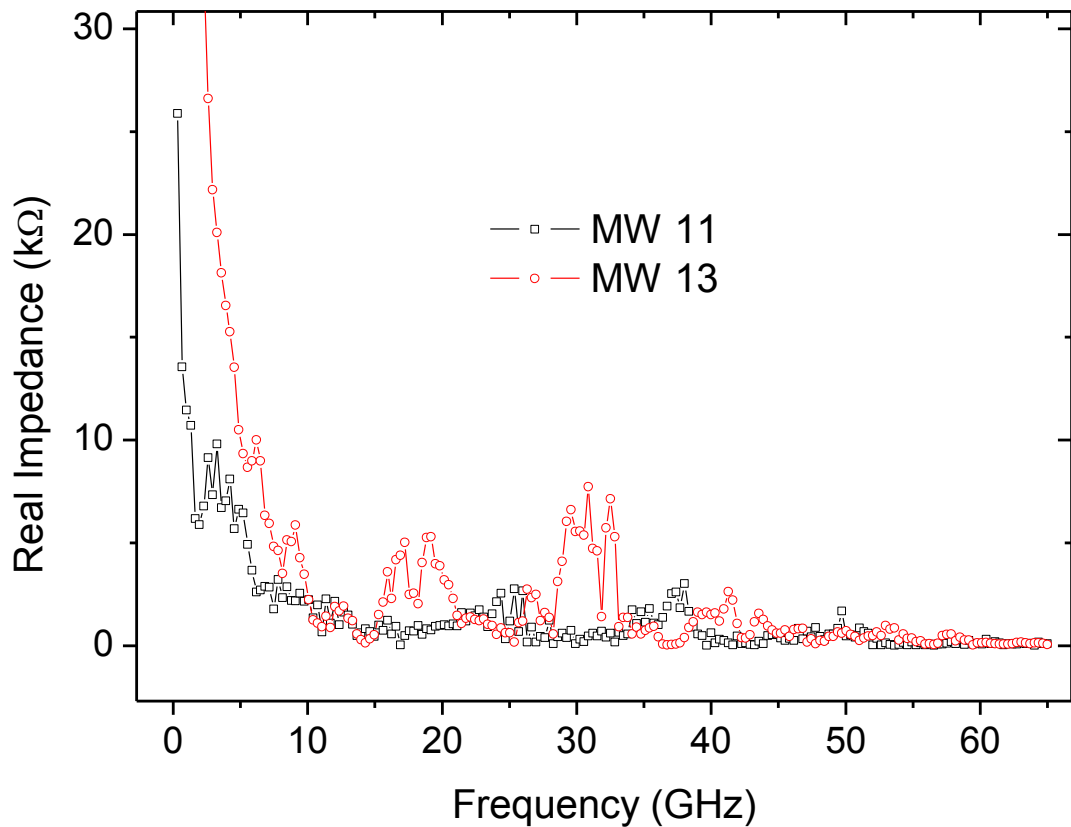


**Figure 4.32:** Real impedance of MWNT tubes, showing impedance oscillations that are exponentially damped as the frequency increases.

As was seen in SWNT bundles the real impedance of individual MWNT tubes show similar oscillations that are damped as the frequency increases see Figure 4.32. The oscillations are however of lower amplitude when compared to SWNTs as was the case with DWNTs. Two representatives' samples were picked from the many that were measured, MW 11 and MW 13. They show oscillations that appear to differ in phase as the frequency is increased. One

factor that is significant is the constant period of oscillations that is seen in the entire spectrum. As indicated earlier this constant period of about 81 ps, is comparable to the one obtained theoretically from the Burke model. This constant period has been indicated as a way to differentiate LL effects from other long range electron-electron effects [89]. If these oscillations are due to LL effects, it then supports the idea that in MWNTs, single or weakly coupled walls are responsible for the electrical transport as was observed in earlier DC transport measurements [87].

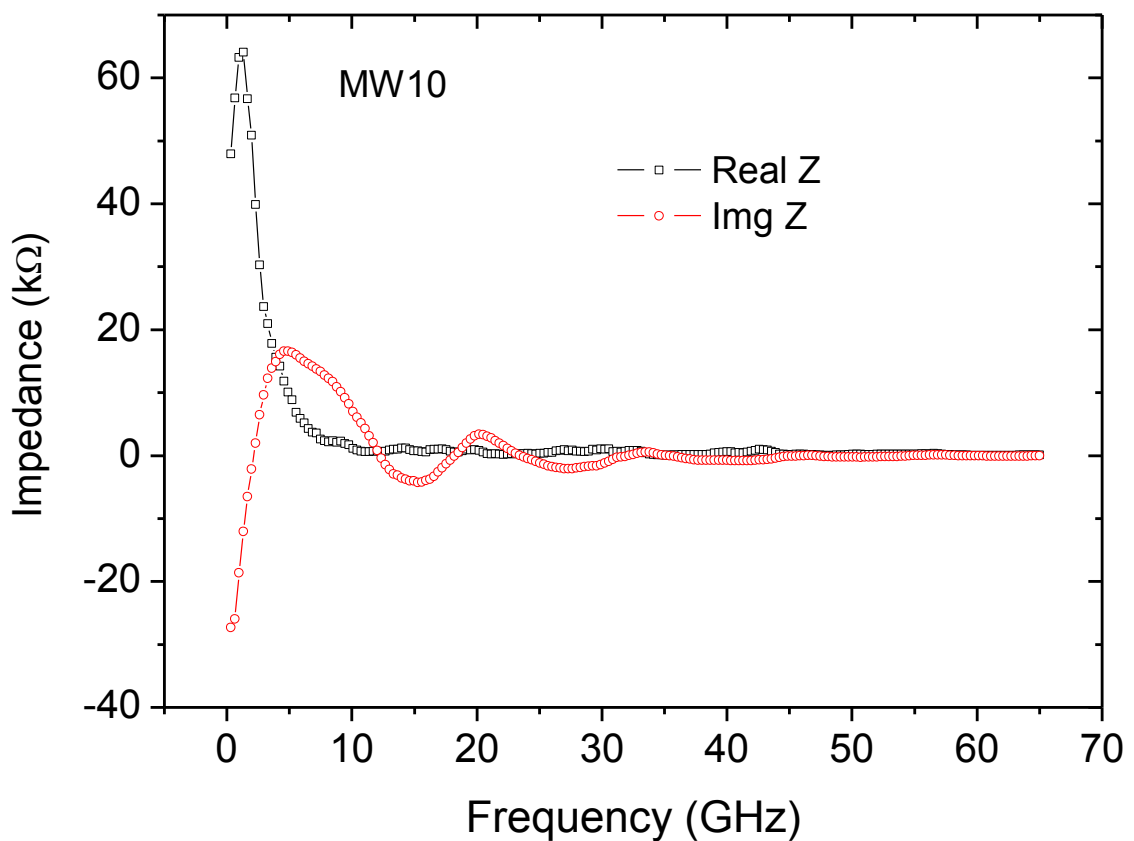


**Figure 4.33:** Complex impedance of MWNT sample MW 10, showing smooth oscillations and a crossover from diffusive to ballistic transport.

Plotting the two components of the complex impedance (the real and imaginary) on the same axis, shows a crossover from diffusive transport to ballistic transport as was observed in other CNTs samples discussed earlier. It was explained that this transition occurs at room temperature when the scattering rate in the CNTs is less than the stimulus frequency see

Figure 4.33. Interestingly the crossover appears to occur at about 5 GHz, a frequency much lower than what was observed in SWNTs bundles. This may suggest that the MWNTs may have lower contact resistance than SWNTs. As mentioned earlier because of finite contact resistance, the actual crossover from diffusive to ballistic occurs at much lower frequency than what the graph suggest. Having confirmed impedance oscillations in MWNT individual tubes which may be taken to indicate LL excitations at room temperature the next step was to investigate the effect of metal contacts on the RF transport in MWNTs.

### **4.3.1: Effect of metal contacts**

In order to realise commercial applications of carbon based nano-devices operating in the very high frequency (GHz to THz) range and elevated temperatures, understanding both the physics and technology of the electronic contacts has to be developed [109]. Nowadays electrical transport research is extensively being extended to fast switching devices that promise to out shine those of current technology and it is worth mentioning that full characterisation of the effect of nano-contacts must be accomplished.

The nature of contacts and chemical stability becomes crucial in the high frequency regime and at elevated temperatures. This perhaps, is not surprising because the type of contact determines the coupling between the one dimensional (1D) channel being measured and the electron reservoirs of the electrodes. Weak coupling will tend to promote tunnelling effects from the electrode to the 1D wire resulting in power law features of conductance with bias voltage [110]. In the high frequency regime the obvious consequences of weak coupling is an increase in load mismatch between the CNT device and waveguide/instrument normally set at  $50 \Omega$  and hence significant damping of 1D plasmon waves. It is thus the objective of this work to give an insight on the effect of various contacts, such as platinum and tungsten, which have not been explored much at high frequency. The choice of materials is guided by the fact that other noble metals such as gold and palladium have been routinely investigated [111] [112] and hence the objective here is to look for other options. The search is for metals that can be used for sensor devices that operate at elevated temperatures and because tungsten and platinum have very high melting points than many others they do not suffer much from electron migration [113]. Furthermore theoretical calculations have previously

suggested that the presence of  $d$ -states at the Fermi-level will improve electrode- CNT coupling [114], and hence the choice of tungsten.

To determine the coupling strength two terminal  $I$ - $V$  curves for the CNT devices was measured before and after metallisation with tungsten and platinum contacts. Using the Landauer - Buttiker equation 4.10, electron transmission through electrode - CNT junction can be characterised by two important parameters,  $\Delta E$  and  $\Gamma$ , the energy difference of the CNT from electrode Fermi level and the strength of CNT- electrode coupling respectively [43].

$$I(V) = \frac{2e}{h} \int_{-\infty}^{+\infty} \frac{\Gamma^2}{(E - \Delta E)^2 + \Gamma^2} \left[ f_F \left( E - E_F - \frac{eV}{2} \right) - f_F \left( E - E_F + \frac{eV}{2} \right) \right] dE, \quad (4.10)$$

In the above equation  $f_F$  and  $E_F$  are the Fermi distribution function and the Fermi energy, respectively. By fitting the Landauer - Buttiker equation to the experimental data the electrode - CNT coupling strength was determined. The fitting was mainly focused in the low bias regime in which the conductance is independent of the electric field and also so as to get a better understanding of how coupling affects AC transport that was done with a stimulus power that corresponds to 32 mV.



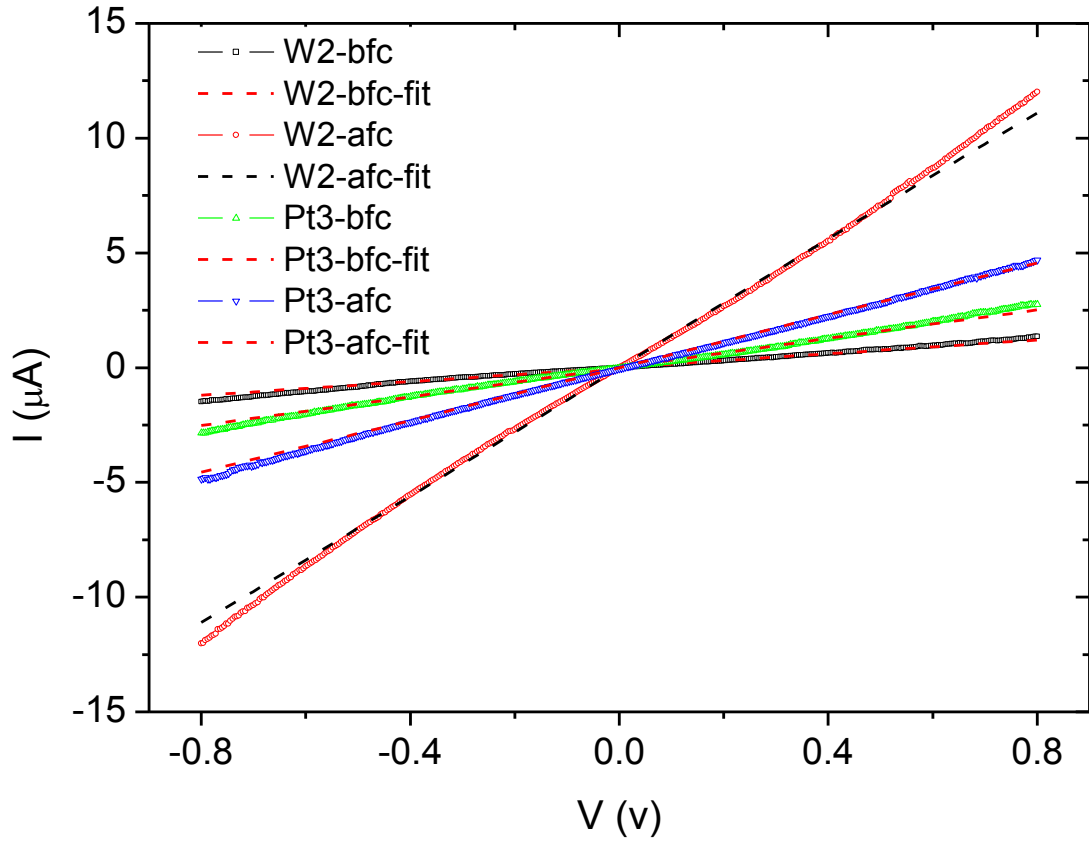


**Figure 4.34:** *I-V* data for a selected set of sample before (*bfc*) and after (*afc*) contact fabrication, the dotted lines are the respective fits.

The current-voltage (*I-V*) results, Figure 4.34, show that tungsten contacts significantly lowers the total resistance ( $R_T = 2R_c + R_{CNT}$ ) of the device when compared to platinum (as seen from the gradients of the curves), where  $R_c$  is the contact resistance and  $R_{CNT}$  is the DC resistance of the CNT.

The fitted data show that only one sample W2 –after contacts (*afc*) does not fit well above 0.6 V. This aspect is not a major concern for this analysis because the concern is with regard to the coupling in the very low bias region about 32 mV comparable to the AC stimulus power for the high frequency measurements. Tabulation of the fitting parameters in table 4.3 shows, that tungsten contacts increases the coupling strength between the electrodes and the CNT better than platinum. On average there is a 0.7 meV increase from tungsten compared to 0.2 meV from platinum contacts, this translates to lower contact resistance. A direct consequence of this is lower contact resistance is a significant change in the transport mechanism, for example, a reduction in tunnelling effects.

**Table 4.3:**  $\Gamma$  parameter obtained from the fitting of the I-V data before (bfc) and after (afc) metallisation together with total resistance ( $R_T$ ) obtained at 35 meV from the raw I-V data.

	$\Gamma$ (meV) bfc	$\Gamma$ (meV) afc	$R_T$ (k $\Omega$ )bfc	$R_T$ (k $\Omega$ )afc
Pt 2	0.92	1.13	80	20
Pt 3	0.78	1.05	404	242
W1	1.89	2.59	26	16
W2	0.65	1.65	707	78
W3	0.79	1.20	112	19

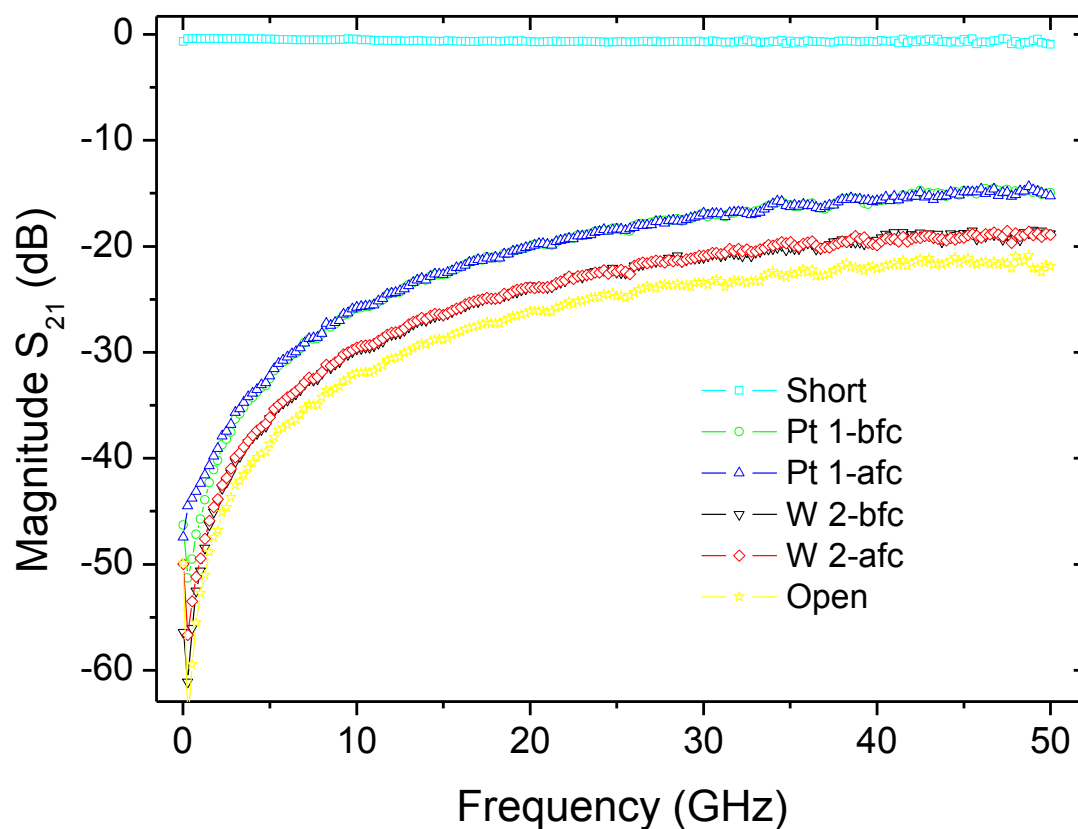


**Figure 4.35:** Magnitude of  $S_{21}$  for platinum (Pt) and tungsten (W) samples measured before (bfc) and after (afc) the contacts were fabricated. The Short and Open data is for the Short waveguide and a blank waveguide respectively.

Turning the attention back to the RF results, the magnitude of the transmission coefficient ( $S_{12}$ ) in Figure 4.35 does not show much difference in the measurement before or after metallisation except that individual CNTs are responsible for about  $3 \pm 0.2$  dB of power transmitted before contacts are made. This is significant power considering that the signal to noise ratio is about 15 dB. The results, (Figure 4.35) also show the reproducibility of the measurements and transmission capability beyond 50 GHz for all MWNT devices. The short and open data is for the waveguides as described in chapter 3. This data (open and short) is used to de-embed the parasitic effects of the waveguide as was mentioned earlier.

The phase of the transmission coefficient however, shows a maximum phase change of about  $20^\circ$  degree after metallisation below 10 GHz see Figure 4.36 giving a hint on the effect of the contacts.

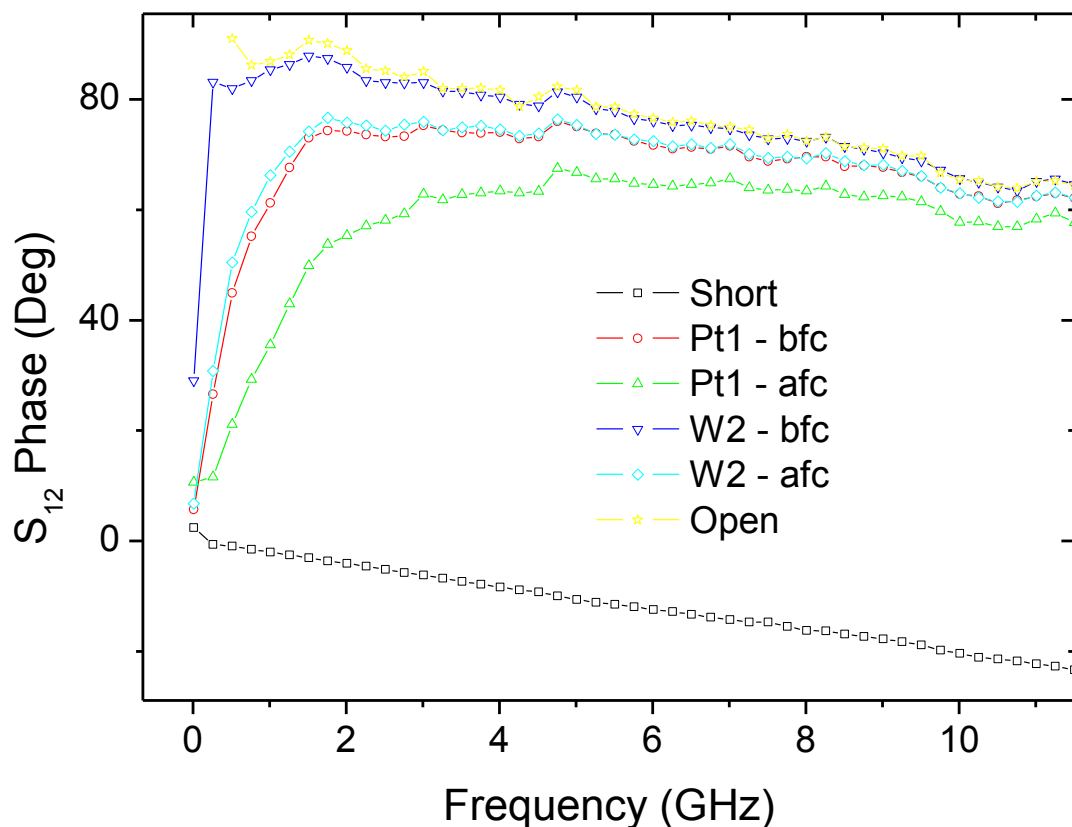


**Figure 4.36:** The phase of  $S_{12}$  for MWNTs measured before (bfc) and after (afc) platinum or tungsten contacts were fabricated.

The imaginary component of the impedance was then calculated after de-embedding waveguide parasitic which is shown in Figures 4.37 and 4.38 for different samples. They show that metal contacts induce a transition from capacitive to inductive nature, with tungsten having the largest effect. This result can be understood in terms of the additional states that the contacts provide (which we termed “contact states”) at the junction ends of the MWNTs that interact with the stimulus current resulting in the current lagging behind the voltage and hence the inductive behaviour.

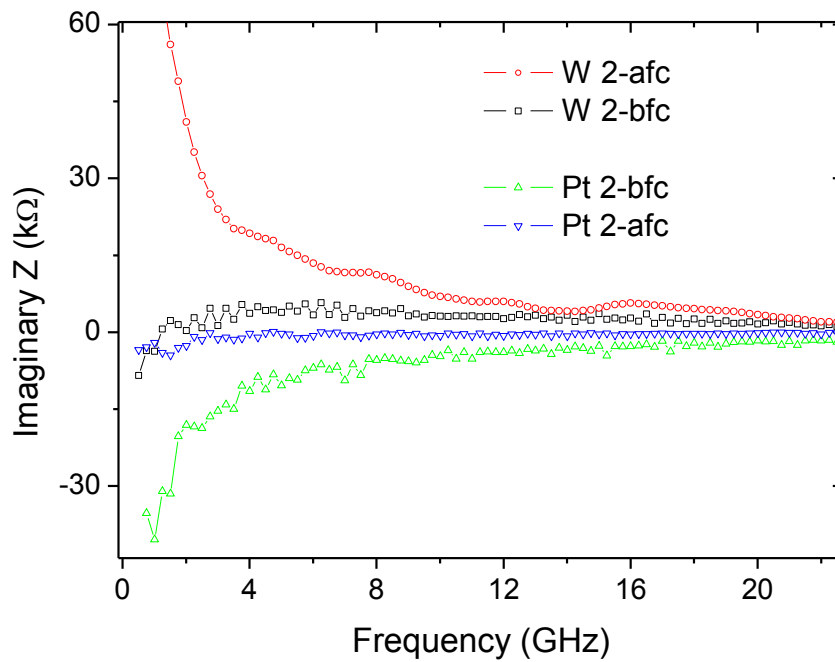


**Figure 4.37:** Imaginary impedance of different platinum and tungsten contacted MWNTs before (bfc) and after (afc) the contacts fabrication.

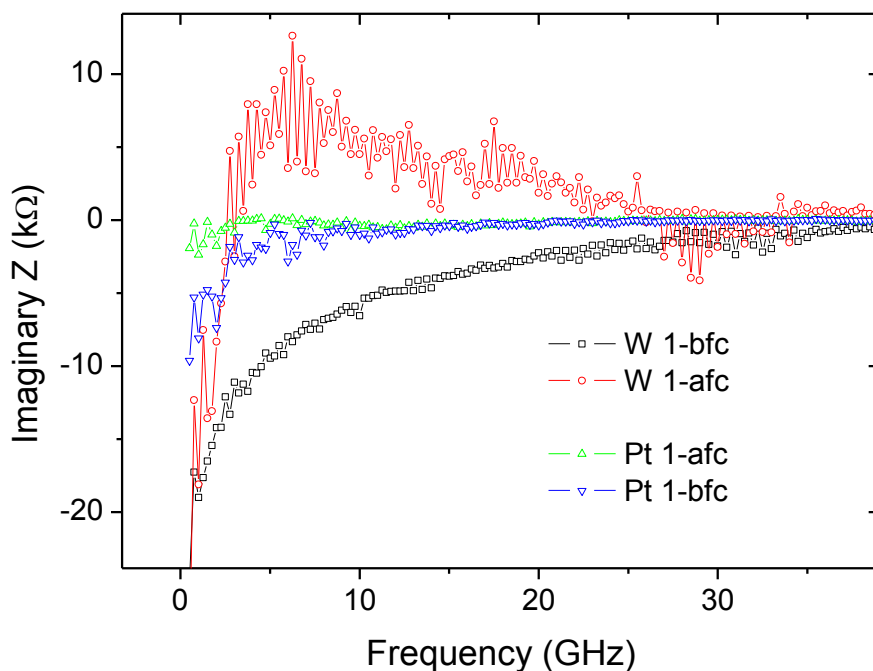


**Figure 4.38:** *Imaginary impedance of different platinum and tungsten contacted MWNTs before (bfc) and after (afc) the contacts fabrication.*

The whole process can be envisioned as defects caused by the e-beam used for bonding and contact metal, introducing multiple energy barriers of different widths and heights which result in the current lagging behind voltage as it rises and falls through the barriers as shown by the schematic diagram Figure 4.39. In this context it would imply that tungsten introduces more states by virtue of its electronic configuration (i.e. unoccupied *d*-states) and also from the defects it causes. As the frequency of the stimulus is increased localisation of these states begins to take effect and the inductive behaviour starts to diminish. What then dominate are the electron states or charge waves in the CNT itself which are strongly driven by the stimulus signal.

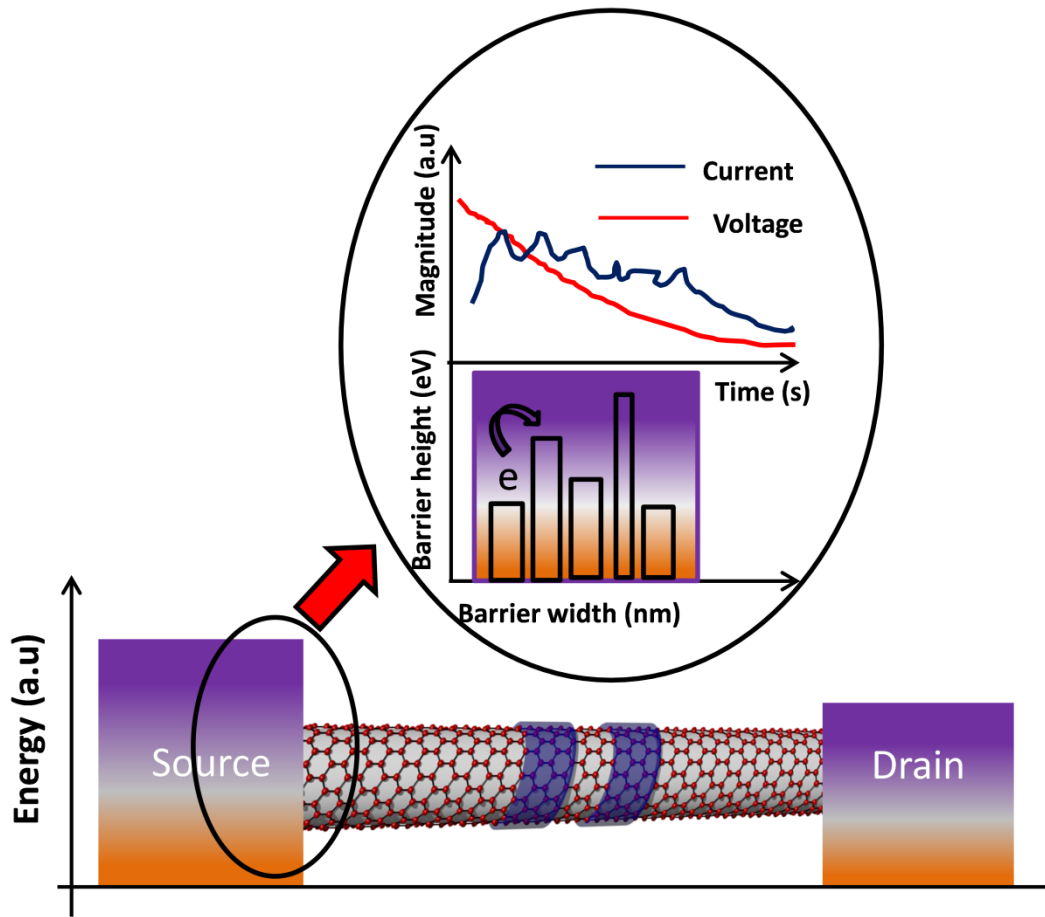


**Figure 4.39:** Schematic diagram illustrating the CNT-electrode configuration and the effects of the contacts to current and voltage.

Associated with these “contact states”, is the microwave power dissipation that happens in the device. This fact is illustrated in the graphs of Figure 4.40, which show that after metal contacts the fractional power loss increases by a factor of 1.5% for tungsten and by 0.8% for platinum at 5 GHz for an individual tube. The microwave power dissipation, as a fraction of the input power, in a symmetric impedance-matched waveguide is given by equation 4.11, below [115].

$$P_{loss} = 1 - (|S_{11}|^2 + |S_{21}|^2) , \quad (4.11)$$

where  $||$  is the magnitude of the S-parameter. The fractional power loss was then calculated by subtracting the power loss of the waveguide alone from that of the device

(CNT + waveguide) i.e.  $P_{loss-cnt} = P_{loss-dut} - P_{loss-open-cpw}$ . In this way the parasitic effects of the waveguide are eliminated.

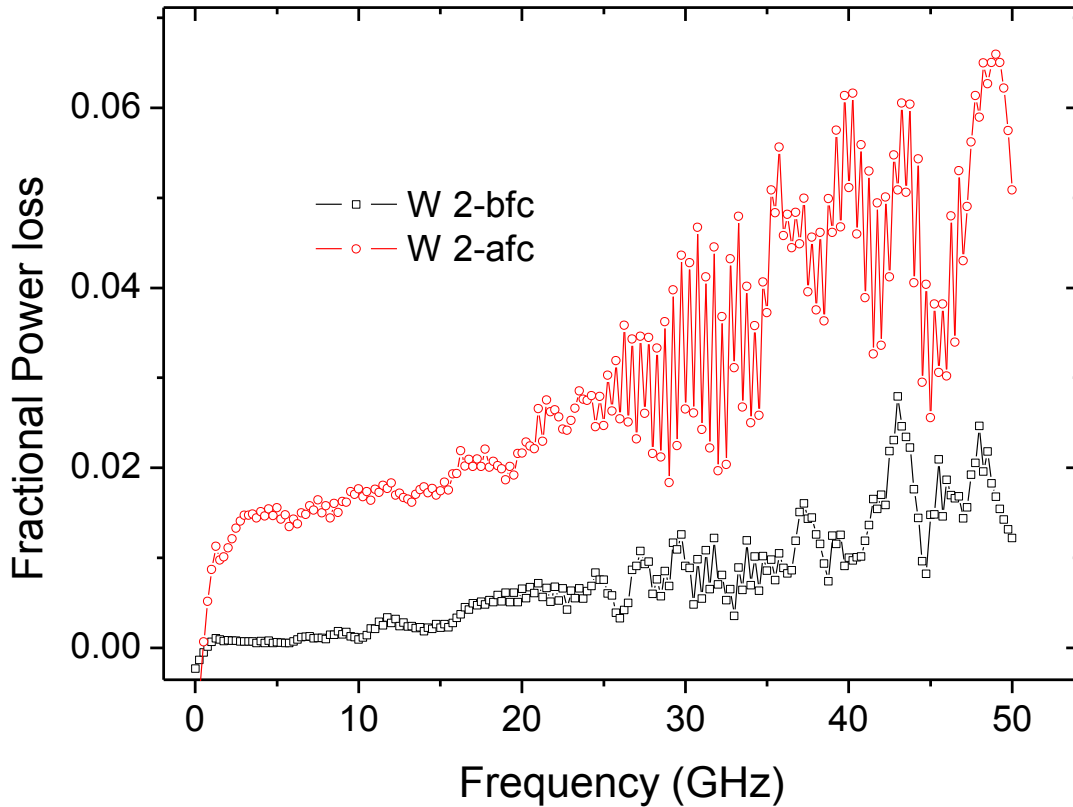


**Figure 4.40:** Fractional power loss relative to that of the Open waveguide for Tungsten contacted sample.

It is noted that the power loss increases with frequency for tungsten contacted MWNTs (Figure 4.40) although the data becomes noisy above 20 GHz most probably due to the noise factor of  $S_{11}$  caused by the reflection from the waveguide itself. The fractional power loss in platinum contacted MWNTs (Figure 4.41), increases and then decrease with frequency above 20 GHz and the explanation for this is still not yet understood but may probably suggests the dominance of the inductive component over the resistive part of the device which would store up energy.

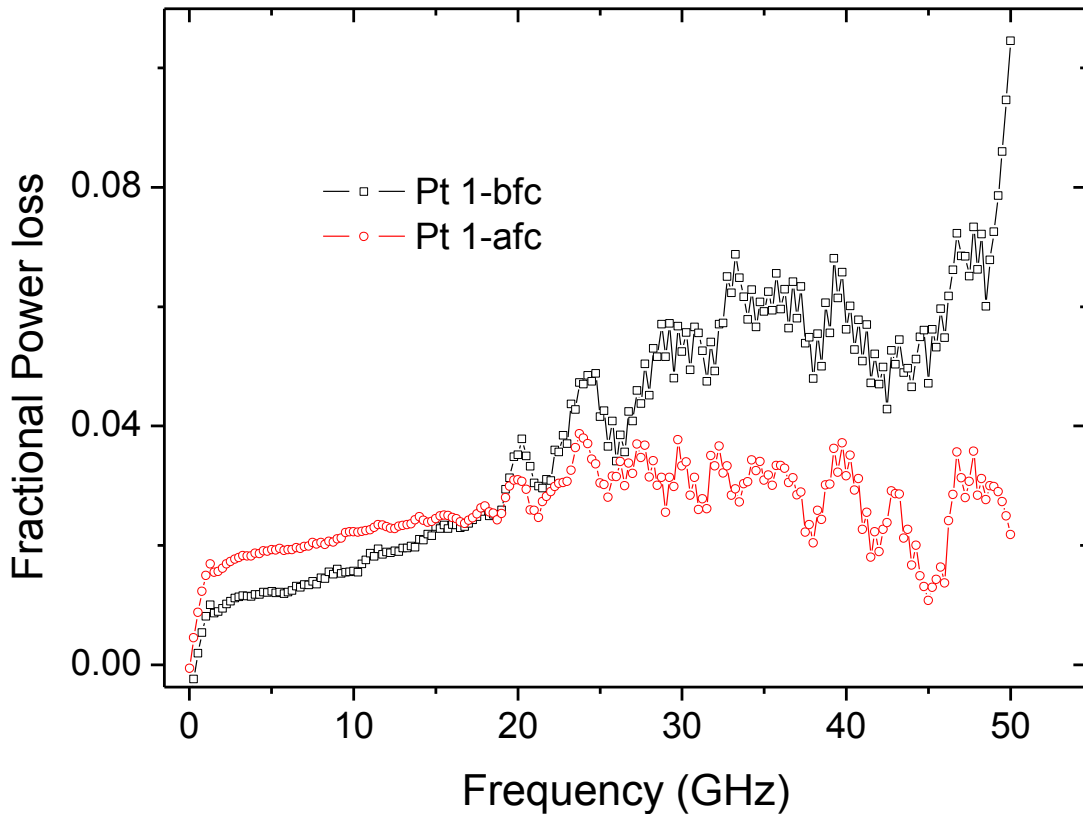


**Figure 4.41:** Fractional power loss relative to that of the Open waveguide for Platinum contacted sample.

By using individual metallic multi-walled carbon nano-tubes (MWNTs), it has been shown that tungsten makes better contacts than platinum for high frequency interconnects or devices. It offers better coupling strength between the CNT and the electrodes observed from both DC and AC measurements. Tungsten significantly improves the electrode-CNT coupling possibly because of the availability of unoccupied *d*- states, and this reduced the contact resistance. It (tungsten), however, suffers relatively higher microwave power loss dissipation. This kind of two fold perceptible has not been shown earlier. Furthermore it has been shown that metal contacts significantly introduce an inductive behaviour on CNT devices or interconnects that is dominant below the 10 GHz threshold. This inductive response appears to be accompanied by an increase in microwave fractional power loss from the MWNT especially for tungsten contacted devices. This knowledge means that above 10



GHz, the choice of contacts is wider making the cost of devices that would operate in that regime cheaper. This work on metal contacts has since been published, see Ref [116].

#### **4.4: Chapter Summary**

Radio frequency transmission in multi, double and single walled carbon nanotubes has been studied from 10 MHz to 65 GHz. Few single walled CNT bundles have shown features associated with Luttinger liquid excitations from both AC impedance studies as well as DC transport measurements. To the best of our knowledge this is the first demonstration of features associated with LL achieved using this technique. The results have shown that using time dependent signals enables observation of ballistic transport in structurally defective CNTs at elevated temperatures. Low temperature measurements gave an insight on the role of physical parameters on the CNT- electrode coupling. This observation was found to be pronounced in double walled CNTs and it resulted in a crossover from diffusive to ballistic happening at lower frequencies as the temperature is reduced. The near perfect (structurally) inner wall of DWNTs that is protected by the outer was suggested to be the reason for the improved sensitivity of DWNTs to temperature changes.

Individual multi-walled CNTs showed the possibility of LL behaviour even in a multi-channel system. The reason for this is probably that in MWNTs only one or a few weakly coupled channels dominate the electrical transport. This work also showed a twofold analysis on the effect of contacts. It showed that tungsten makes better contacts than platinum although it suffers high microwave power dissipation losses as the frequency is increased.

This work has demonstrated experimentally some fundamental physics features that had been predicted theoretical in carbon systems.

# Chapter 5 – Dynamic Transport in Nano-diamond films

## 5.0: Introduction

Diamond in general has extraordinary properties that meet the prerequisites for high speed, high temperature and high power active electronic devices. This is because of its excellent carrier mobility that can be as high as  $4500 \text{ cm}^2/\text{Vs}$ , very high thermal conductivity and a large bandgap [117]. Its chemical inertness and excellent mechanical strength makes it ideal for use in rough or extreme conditions where most current electronic materials cannot operate [118]. As such it has been one of the most researched materials for applications in electronics with the hope that one day it might replace the current materials. Research has shown that reducing the dimensions to the nano-scale does not alter the intrinsic properties of the diamond grains [119].

However the challenge with diamond or nano-diamond in electronic applications has been with the doping process to make it conducting. Impurity donors in diamond are very deep in the bandgap making it difficult to produce useable n-type devices [120]. So far only boron (which is an acceptor) doping has been the workhorse of diamond devices [75]. But full range application will still need n-type devices, and presently this type of conductivity in nano-diamond is still not well understood. A lot of research efforts by a number of groups including ourselves in the past decade have gone into the quest to understand n-type conductivity due to nitrogen incorporation [121]. It is now well established that nano-diamond films can be turned from being insulating ( $T\Omega$ ) to quasi-metallic ( $m\Omega\text{-cm}$ ) by nitrogen incorporation in the gas phase during synthesis. The exact mechanism of the conductivity is still not yet clear as highlighted earlier [122]. Whilst the problem has not been resolved this project attempted probing this conductivity with an AC signals in an effort to solve the puzzle or get better insight into the mechanism.

It is against this background that the discussions in this chapter begin by brief review of the study in this material based on DC measurements, which forms a background to this work. The discussion is meant to give a clearer perspective to the problem at hand. This

discussion is based on our results although the conclusions drawn are compared with other researchers' work.

## 5.1: DC Transport in nitrogen incorporated nano-diamond films - Review

As outlined in chapter 3, nano-crystalline diamond (NCD) films were synthesized by hot filament chemical vapour deposition technique. The conductivity was tuned by varying the amount of nitrogen in the precursor gases during the synthesis process. Four probe measurements were done using the van der pauw configuration, sourcing a constant 10  $\mu\text{A}$  current and measuring the voltage across the other two terminals. The resistance and magneto-resistance measurements were done for a wide range of temperature and magnetic field.

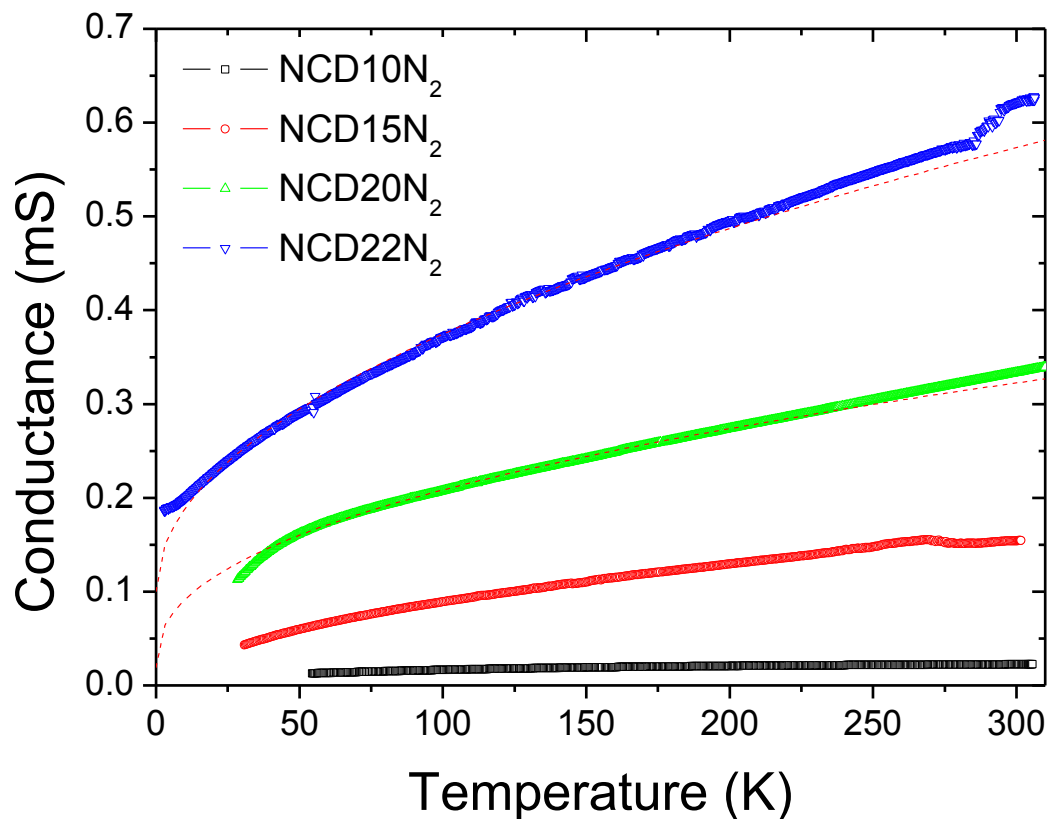


**Figure 5.1:** DC conductance vs temperature graph showing an increase in conductance with nitrogen incorporation. The red dotted lines are weak localisation fits. [121].

The DC results for the different samples showed an increase in conductance with nitrogen incorporation as expected see Figure 5.1. It is known that the role of nitrogen is confined in the grain boundaries (GB) of the diamond films and hence the use of term nitrogen incorporation.

Analysis of the conductance – temperature results showed that the 10% and 15% nitrogen samples could be fitted well with the Mott- 3D variable range hopping model [123]. The 20% nitrogen sample showed thermal activated conduction mechanism and the 22% nitrogen showed quasi-metallic conduction whose conductance and magneto-conductance could be fitted well with a 3D weak localisation (WL) model as shown in ref [121]. The change in conduction mechanism was explained in terms of the disorder level in the films. A schematic diagram below summaries the previous findings see Figure 5.2, which shows a change in conduction mechanism due to an increase in the disorder level in the grain boundaries.

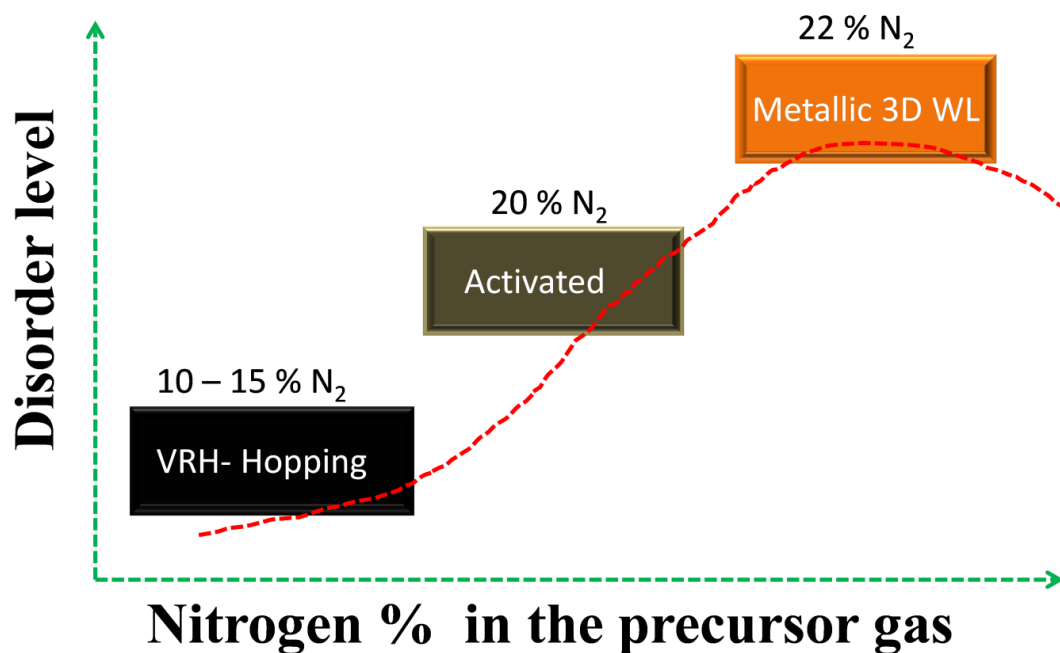


**Figure 5.2:** Illustration of the effect of disorder on the conduction mechanism in nitrogen incorporated nano-diamond films.

Based on our previous work [121] and other researchers' [124], the GB plays an important role on the conduction mechanism. Of interest to the current discussion is how the grain

boundary condition affects the AC conductivity in the films. Using Raman spectroscopy studies the state of the grain boundaries was obtained by monitoring the nano-diamond characteristic peaks. A comparison of DC measurements to AC measurements shall then later be made, with the GB being the centre of discussion. In visible Raman analysis the full width at half maximum (FWHM) of the G-peak (due to bond stretching of all  $sp^2$  atoms in both rings and carbon chain) can be considered as a measure of the disorder level in the films according Ferrari and Robertson [125]. Figure 5.3 shows how the width of this peak changes with increase of nitrogen level in the gas phase.

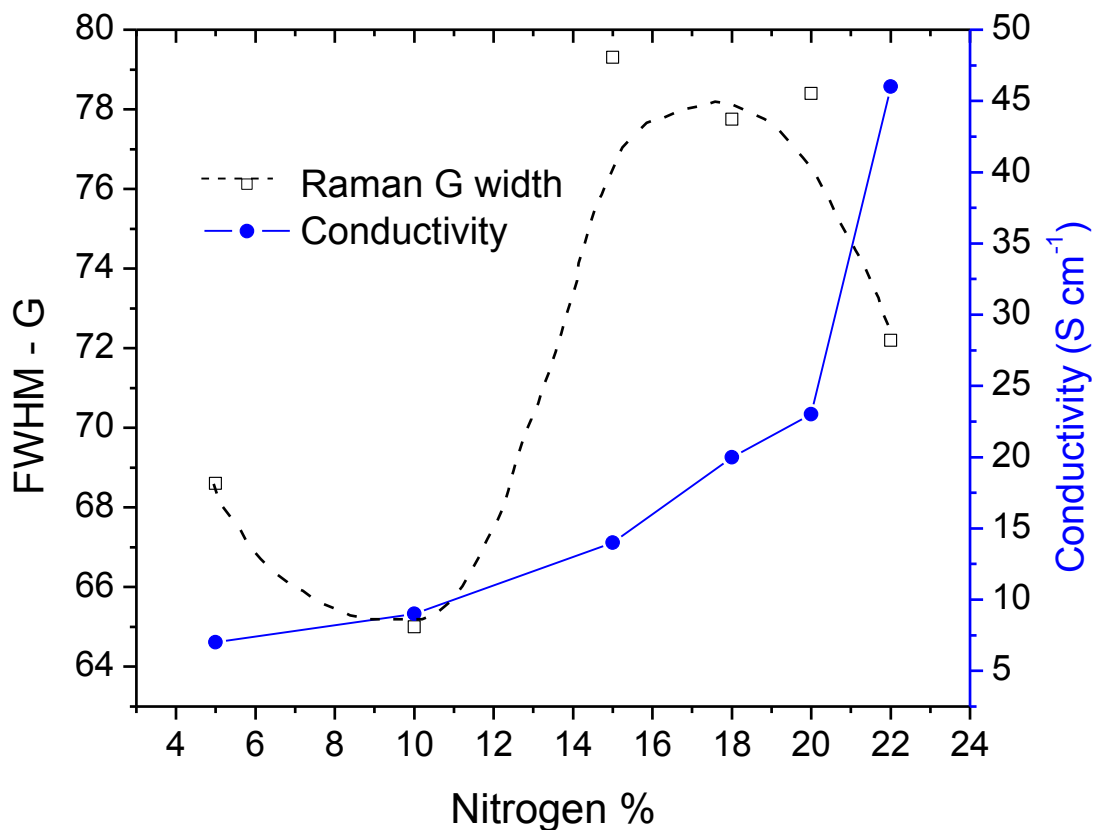


**Figure 5.3:** Full width at half maxima of the Raman G-peak vs nitrogen level as well as the film DC conductivity.

The above graph (Figure 5.3) shows an interesting trend in the variation of the width of the G-peak with nitrogen level as well as the conductivity of the films. It is apparent that at high levels of nitrogen the disorder level begins to drop and the conductivity seems to shot up.

These observations led us to suggest a super-lattice like structure model for this behaviour. In a super-lattice structure the charge carrier mobility and dwell time along the super-lattice layers are different from that perpendicular to the layers. This differences results in some form of anisotropy in the conductivity of a 3D structure. The presence of some form of structural disorder may also alter or affect the dwell time along the layers, which invariably changes the anisotropy factor. With the help from theoretical calculations [126] and fitting the experimental data with the Bryskin - Kleinert (B-K) model [127] the conductivity in polycrystalline NCD films was explained using a super-lattice like structure made of layers of  $sp^3 - sp^2$  in the GB (see Figure 5.4), which forms at high nitrogen level.

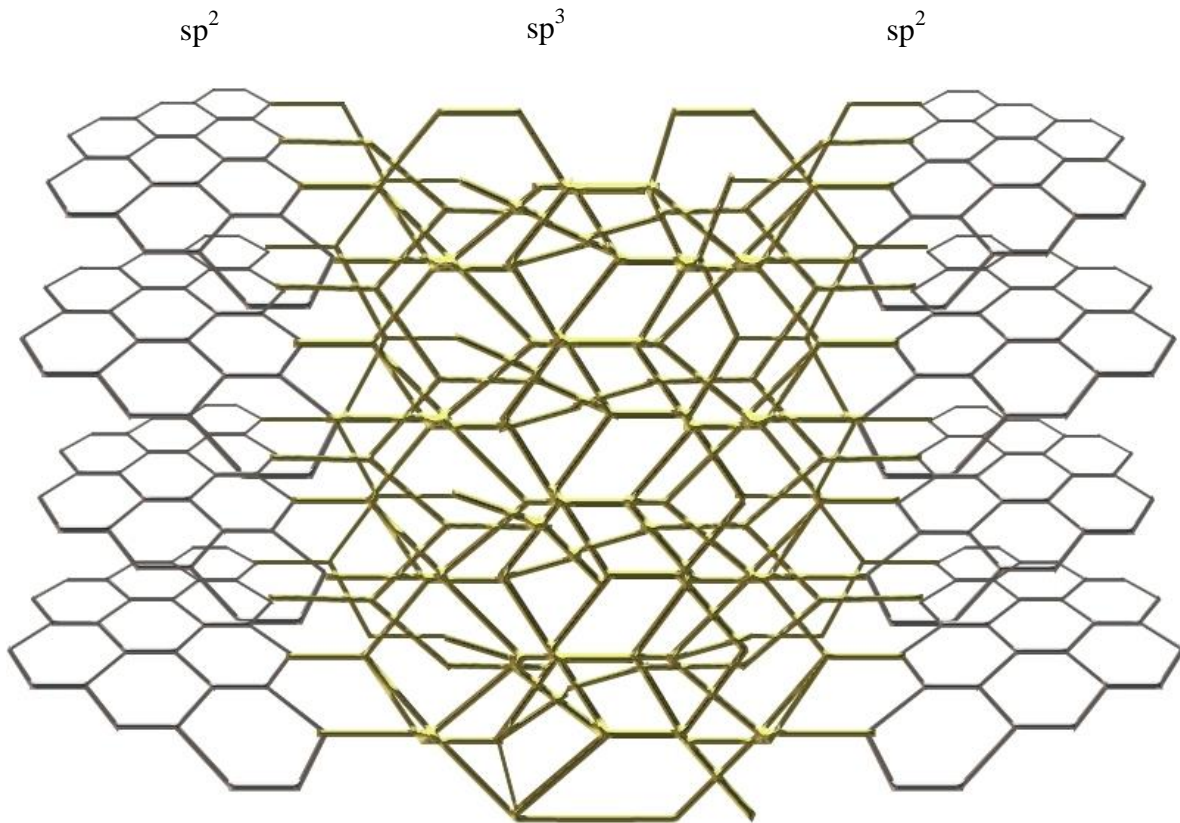


**Figure 5.4:** Schematic illustration of a super-lattice like structure that could exist in the GB of nano-diamond films. [128].

The B-K model is a self-consistent theory that showed that the ratio of the scattering times ( $\tau_0/\tau$ ), (where  $\tau_0$  and  $\tau$  correspond to the renormalized and elastic scattering times respectively), would be a function of the anisotropy factor. The model uses two guiding

anisotropy parameters namely  $\alpha = \sqrt{D_{//}/D_{\perp}}$  (where  $D_{//}$  and  $D_{\perp}$  are the electron diffusion constants parallel and perpendicular to the conduction layers) and  $\gamma = (1/\alpha)(k_z/k_{//})$  with  $k_z$  being momentum cut-off parameter of the wave vector  $k_{//} = 1/v_F\tau_e$  for any arbitrary field orientation. In this experimental set-up the field was perpendicular to the samples therefore only one anisotropy parameter is used. The model gives no restriction on the value of the disorder parameter defined as  $q = k_F\lambda$  in which  $k_F$  and  $\lambda$  are the Fermi wave vector and the electron mean free path respectively. This disorder parameter can vary from one sample to another. For small disorder i.e.  $k_F\lambda \gg 1$ , especially in samples with high nitrogen level the self-consistency of the theory with respect to the renormalized scattering time can be disregarded yielding the corresponding conductivity expression through the Einstein relation  $\sigma_{//} = e^2 D_{//} N(E_F)$  to be  $\sigma_{//} = e^2 D_0 (\tau/\tau_0) N(E_F)$ , thus the parallel conductivity will be a factor of  $(\tau_0/\tau)$ , implying a strong dependence on the anisotropy factor.

In this light the B-K model can be a credible way to theoretically estimate the disorder level in the films with some form of super-lattice structure. It is therefore believed that the super-lattice like structure is the reason for the drop in the disorder and a drastic increase in the conductivity.

Turning back to the experimental argument, another nano-diamond characteristic peak which can give some insight into the GB is the Raman peak at  $1140 \text{ cm}^{-1}$ . This peak for some time was wrongly interpreted as a nano-diamond peak but further research later showed that it is from trans-polyacetylene (TPA) that forms in the GBs [129]. Monitoring of this peak also showed that the GB morphology changes with nitrogen addition as shown in Figure 5.5.

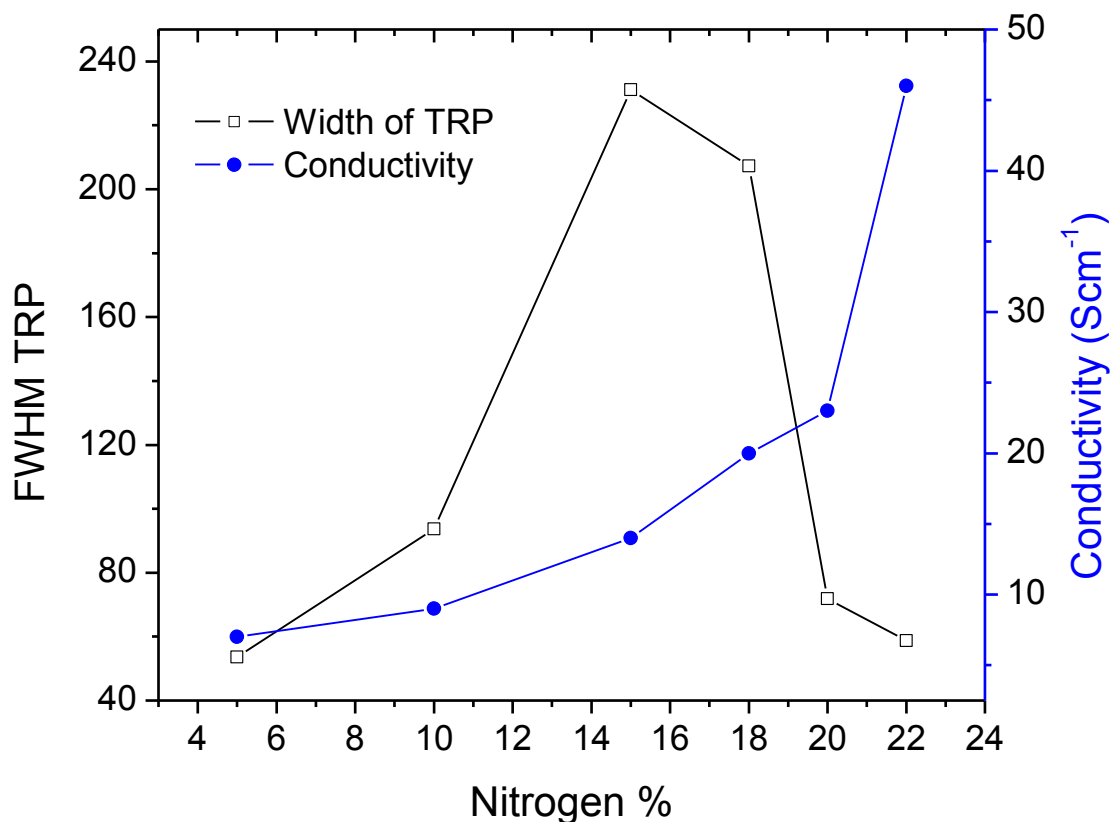


**Figure 5.5:** *Width of the Raman TRP- peak vs nitrogen level as well as the film conductivity.*

The magneto-resistance results of our work in ref [121] showed a weak anisotropy supporting the possibility of a layered structure. These results clearly give solid evidence that the n-type conductivity of nano-diamond films is strongly controlled by the morphology and disorder/order of the grain boundaries. It was then suggested that a band diagram for the layered GB structure will be as shown in Figure 5.6. The band diagram shows that the GB region is composed of  $sp^3$  and  $sp^2$  phases which can have variable widths from 3 nm to 5 nm depending on the nitrogen level. The ordering of this phases is the key to the conduction mechanism. Nitrogen introduction to the system also results in some impurity states above the Fermi level, which explains the activated conduction observed in some samples.



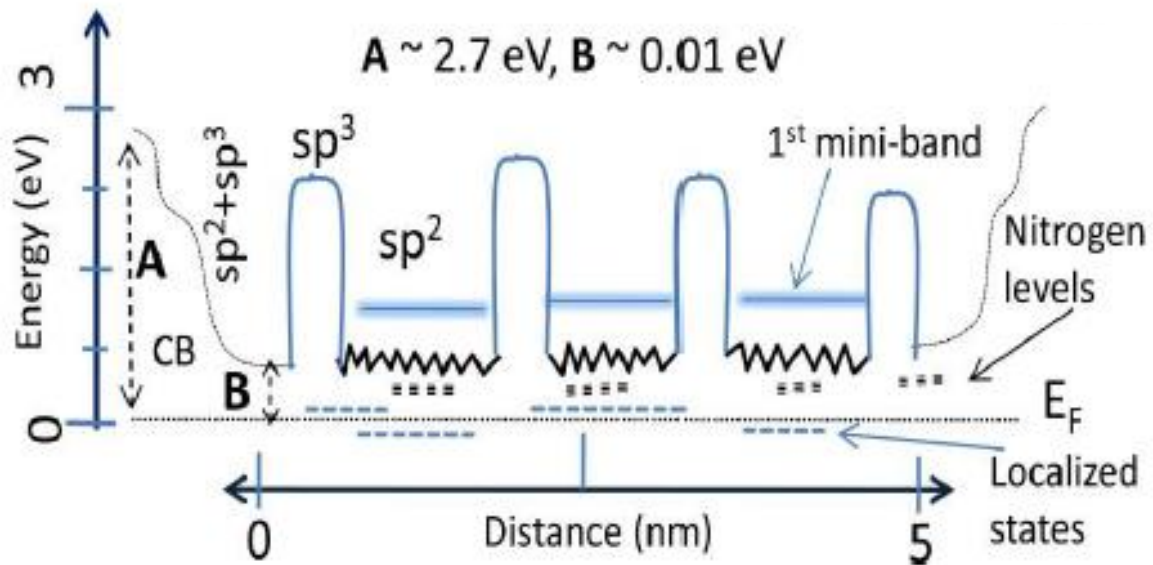


**Figure 5.6:** Schematic band diagram illustrating our suggested band structure of the grain boundary in nano-diamond films [118].

It has already been shown that the amount of nitrogen during synthesis determines the diamond grain size which also means a change in the width of GB [130]. The width of the GB, determines the number of  $sp^3$ - $sp^2$  layers and their coupling strength which was determined theoretically using the B-K model [121]. This background knowledge allowed us to turn our attention to AC measurements and see how they can help to understand n-type conductivity in nano-diamond films synthesized by hot filament chemical vapour deposition. Emphasis should be made on the synthesis method of hot filament CVD because, the grain boundary chemistry and morphology is strongly dependent on the synthesis technique and therefore the conduction mechanism may not be universal to all diamond films. With this perspective, it is noted that a lot of effort has gone into microwave synthesized films, and the results obtained might not be true for HFCVD films. Indirectly this work is also trying to find any overlap between HFCVD films and microwave CVD films.

## 5.2: AC Transport in nitrogen incorporated nano-diamond films

The AC transport properties of nitrogen incorporated nano-diamond films discussed here were obtained by measuring the S-parameters using a newly developed device fabrication technique. The rationale behind the new and non-standard technique was to avoid wet processes that would alter the grain/ cluster boundary morphology and/or chemistry. After synthesis of nano-diamond films on fused quartz substrate, the film was scratched onto predefined waveguide wafer. Using nano-manipulators in the SEM, the film pieces were positioned across the signal terminal of the waveguide and the contacts were made using a combination of e-beam lithography and gas injection system. Only the cauliflower nano-diamond type of 1  $\mu\text{m}$  size was used to enable easier selection and placing of the diamond on the waveguide. Contacts were made using tungsten through a gas injection system.

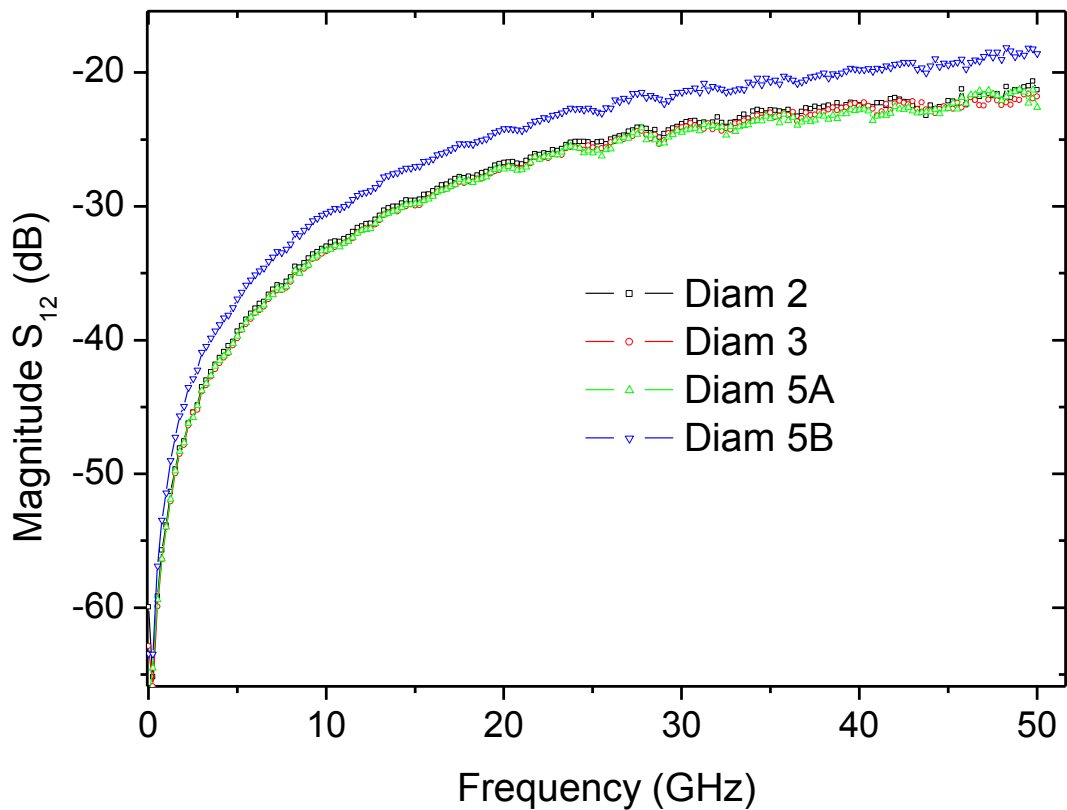


**Figure 5.7:** Transmission coefficient ( $S_{12}$ ) for different nitrogen incorporated nano-diamond samples with different morphologies shown in figures 3.32 to 3.34.

The S-parameter results (Figure 5.7) showed that the transmission properties of nano-diamond films are very much dependent on the morphology. Single clusters (i.e. one big grain) of Diam 2, Diam 3, and Diam 5A, all approximately 1 $\mu$ m in size were found to transmit approximately the same power regardless of the amount nitrogen level during synthesis. Sample Diam 5A and B differ in the morphology see Figures 3.31 and 3.33, with A being a single cluster and B with many clusters (multiple grains), from these two samples an increase in transmission was seen because of the different morphology. *I-V* DC measurements showed that all single cluster films were insulating. It is already known that nitrogen in the diamond grains does not significantly alter the electrical conductivity of the grains because it is a deep donor, and the observed conduction is mainly in the grain boundaries [131]. It can then be said that single cluster films do not have continuous grain boundaries through which conductivity takes place. The increase in transmission observed for Diam 5B might be due to a percolation kind of conduction through the cluster boundaries which are likely to be rich in amorphous or disordered carbon. Any nitrogen in the diamond grains does not seem to play any significant role in the transmission or conductivity.

The next investigation was then to find how the nitrogen level during synthesis affects the nature or composition of the cluster boundaries which seem to be determining the conductivity in these films. As such larger samples (with many clusters) without and with nitrogen (5%, to 25%) were made and measured. Please note we are currently using the term doped loosely to mean nitrogen incorporation.

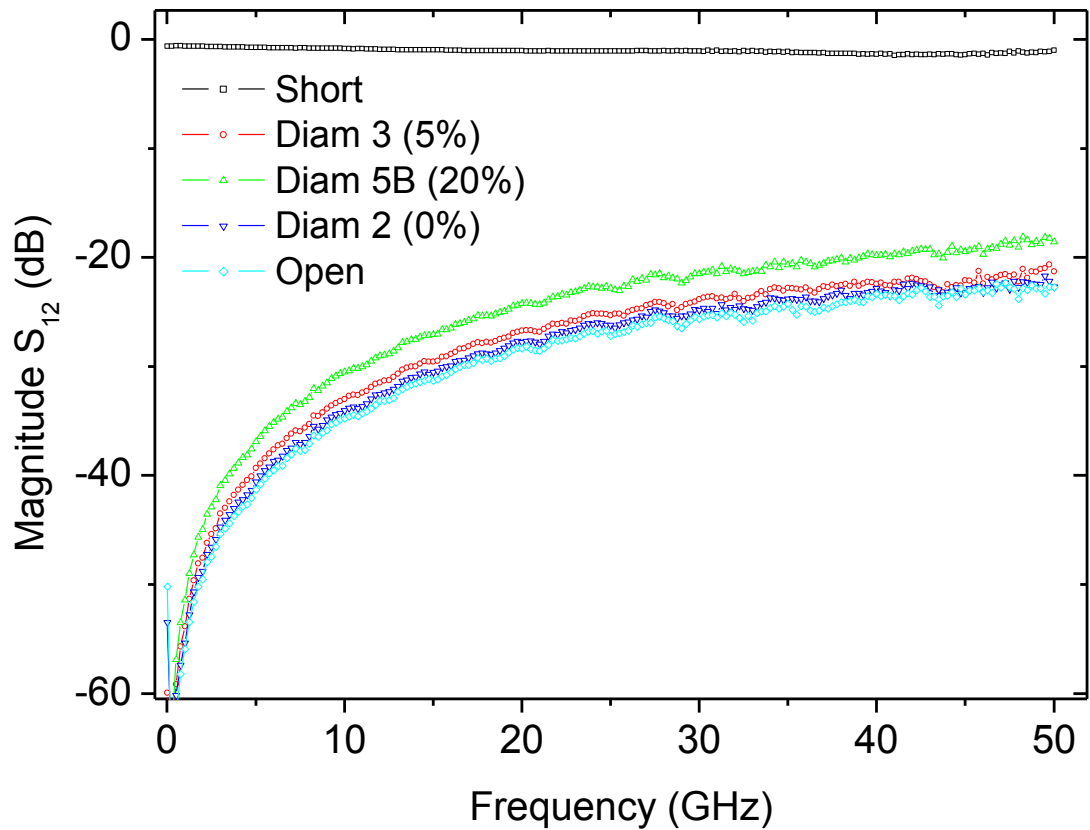


**Figure 5.8:** Transmission coefficient for the “undoped” and “doped” multiple cluster samples. The short and open data is used to de-embed waveguide parasitic effects.

S-parameter data showed that transmission increased with the nitrogen addition for many cluster films as shown in Figure 5.8. The undoped samples showed very small power transmission such that it was almost equal to the waveguide parasitic effects. The increase in power transmission due to increase in nitrogen supports the idea that the conduction is through cluster boundary regions as more nitrogen increases the GB width. Furthermore the increase in power transmission due to nitrogen addition indicates that nitrogen alters the grain boundary chemistry or morphology and hence changing the conductivity of the film. The change in grain boundary morphology is also supported by the Raman spectroscopy results shown in Figure 5.9.

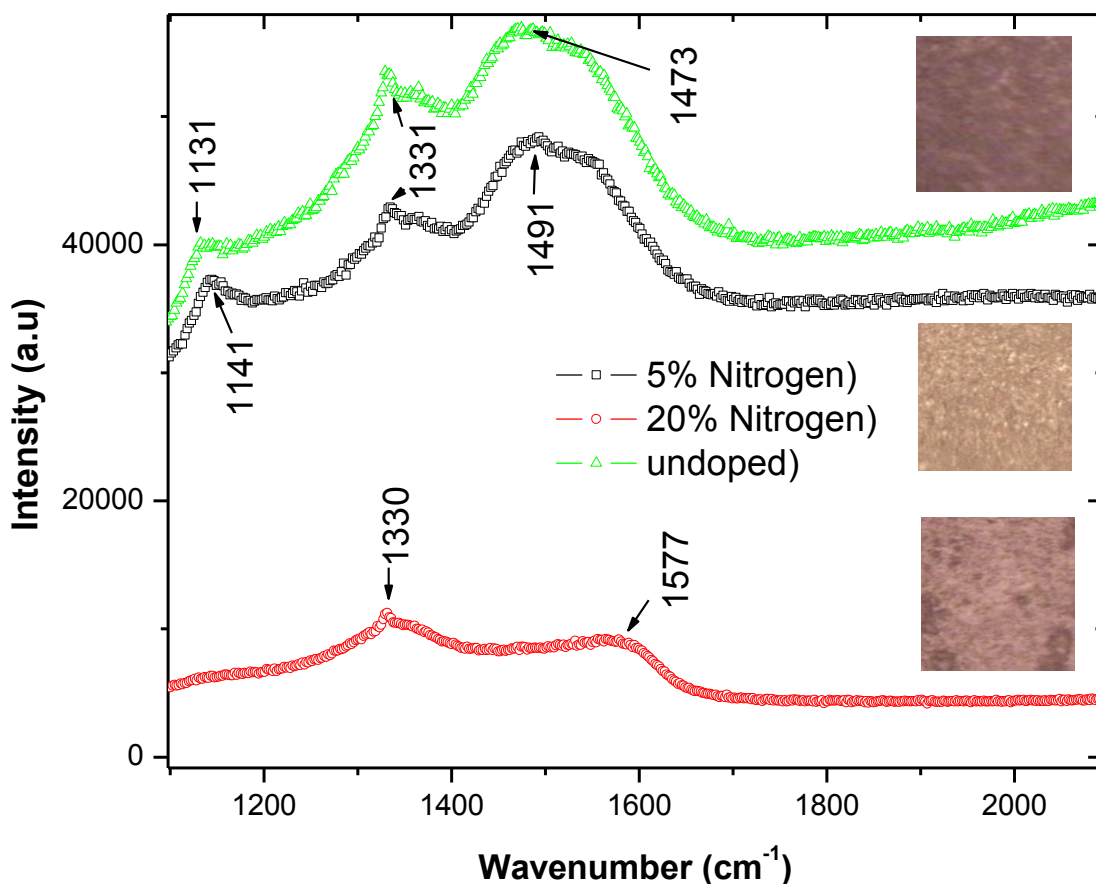


**Figure 5.9:** Raman spectroscopy of “doped” and “undoped” nano-diamond samples. The insets are the optical images from which the spectra were obtained.

The Raman spectra given in Figure 5.9 show two clear trends in the samples as nitrogen content is increased. Firstly, the peak at  $1140\text{ cm}^{-1}$ , which has been attributed to carbon-carbon bond stretching and carbon-hydrogen bending modes in short segments of trans-polyacetylene (TPA) [129], appears to be shifting to higher wavenumbers with nitrogen addition in agreement with previous work in ref [132]. Secondly, the G peak, which is known to be due to bond stretching of all  $sp^2$  atoms in both rings and carbon chains [125], follows a similar trend. Fitting the Raman spectra (see Figure 5.10) with five Gaussian peaks to determine the full width at half maximum (FWHM) for individual nanodiamond characteristic peaks reveals more trends as nitrogen content is increased. Ferrari et. al. [125] pointed out that the  $FWHM_G$  for the G band is a very useful parameter in Raman analysis as it eliminates non-uniqueness problems (i.e. changing of  $sp^2$  configuration independent of

sp<sup>2</sup>: sp<sup>3</sup> ratio) and hence can be used as a monitor of carbon bonding even with single laser wavelength excitation.

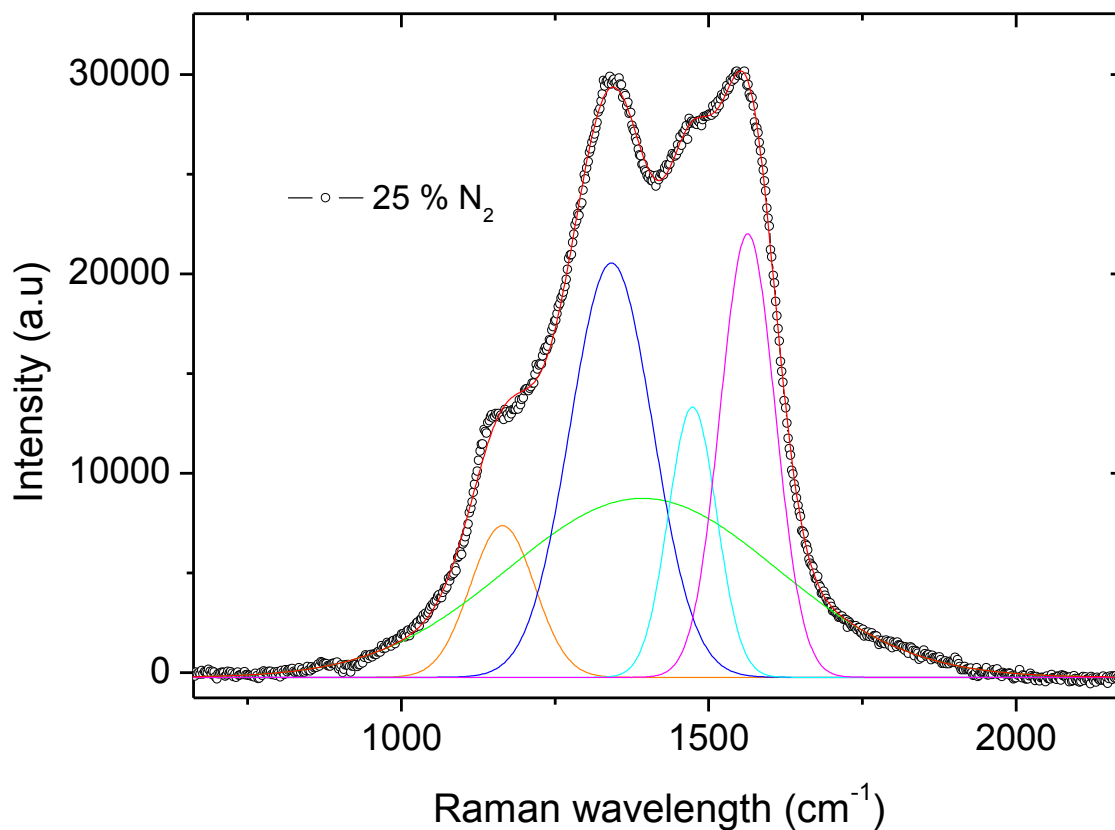


**Figure 5.10:** Raman spectrum for the 25% nitrogen sample fitted with five Gaussian peaks to determine the FWHM of the ND characteristic peaks.

**Table 5.1:** Fitting parameters from the Raman spectroscopy data.

Sample	FWHM $\pm 1$ (cm <sup>-1</sup> )			G-peak	TPA-Peak	I <sub>d</sub> /I <sub>G</sub>
	Diamond	D band	G band	Position	Position	
Diam 2 – 0% N <sub>2</sub>	35	83	161	1504	1131	1.2
Diam 3- 5% N <sub>2</sub>	40	185	129	1553	1141	1.1
Diam 5B - 20% N <sub>2</sub>	43	213	121	1572	1148	1.2
Diam 14- 25% N <sub>2</sub>	48	264	92	1584	1150	1.1

Before a detailed explanation of highlighted trends mentioned earlier is given, additional trends obtained from the fitting of the Raman spectra are outlined first. Table 5.1 shows a decrease in  $\text{FWHM}_G$  as nitrogen content is increased. It further shows the broadening of the D and diamond peaks. Lastly the ratio of the intensity of the diamond peak to the G peak ( $I_d/I_G$ ), which has been used by other groups [133] to indicate phase purity remains pretty much constant. The reason for this is not yet known.

The observed trends in the Raman results pointed out above clearly gives evidence of changes in the microstructure composition of the grain boundaries. The shifting of the TPA and G peaks with increase in nitrogen can be explained in terms of GB sizes. Increase in nitrogen in the chamber results in an increase of CN species which depletes the amount of  $\text{C}_2$  dimer known to promote diamond grain renucleation process [134]. The reduction in the renucleation results in bigger grains and this is accompanied by wider grain boundaries which will result in possible changes of the GB microstructure.

The above arguments show clearly that the grain boundary microstructure and/or composition is the key to electrical conductivity in nanodiamond films. Hence the complex impedance of the doped samples was extracted to see how the AC measurements might compliment DC measurements or shed more light to this complex problem.

After de-embedding the impedance of the films from the waveguide parasitic elements using the open and short S-parameters of dummy waveguides as outlined earlier. The device's impedance (Figure 5.11) shows a significant reduction in the real impedance, with nitrogen addition. The imaginary component of the impedance (Figure 5.12) shows a purely capacitive behaviour for all samples with the effective capacitance decreasing with nitrogen addition. It is however premature at present to conclude that the decrease in capacitive behaviour is due to nitrogen as the cluster sizes could not be made uniform in size (physical dimensions).

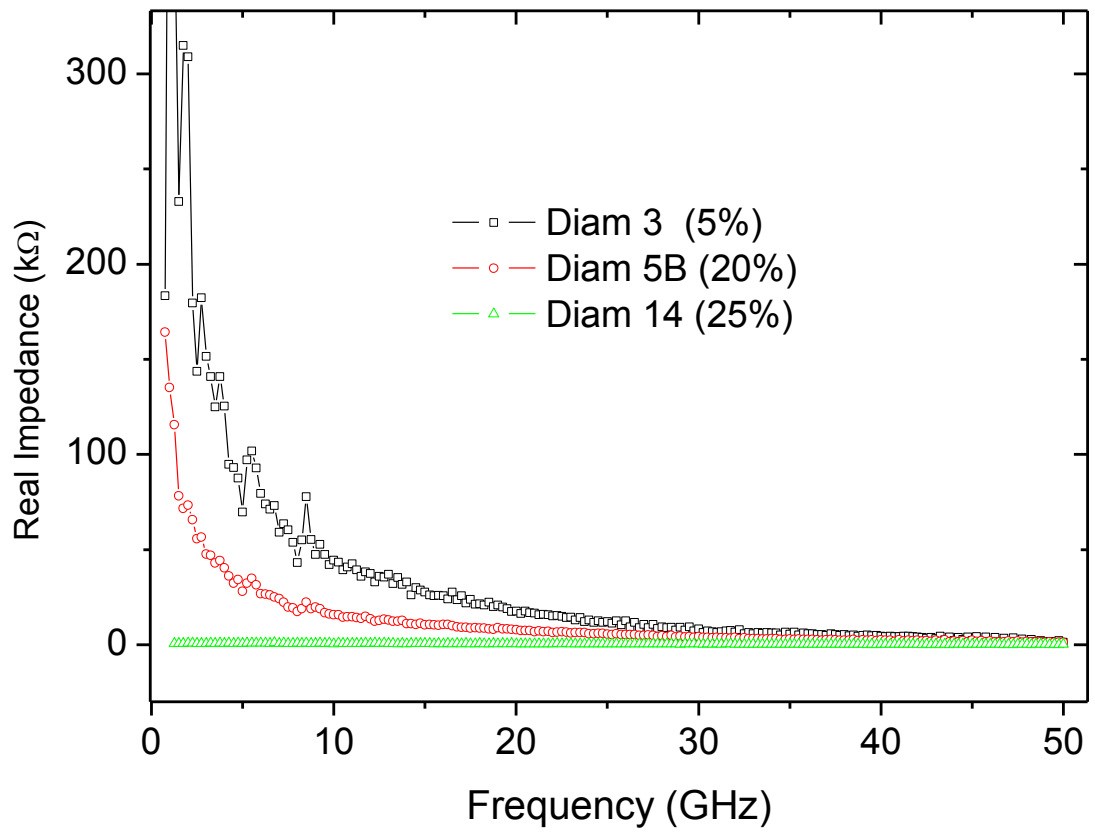


**Figure 5.11:** Resistive component of the AC impedance for Diam 3 (5%), Diam 5B (20%) and Diam 14 (25%) samples.



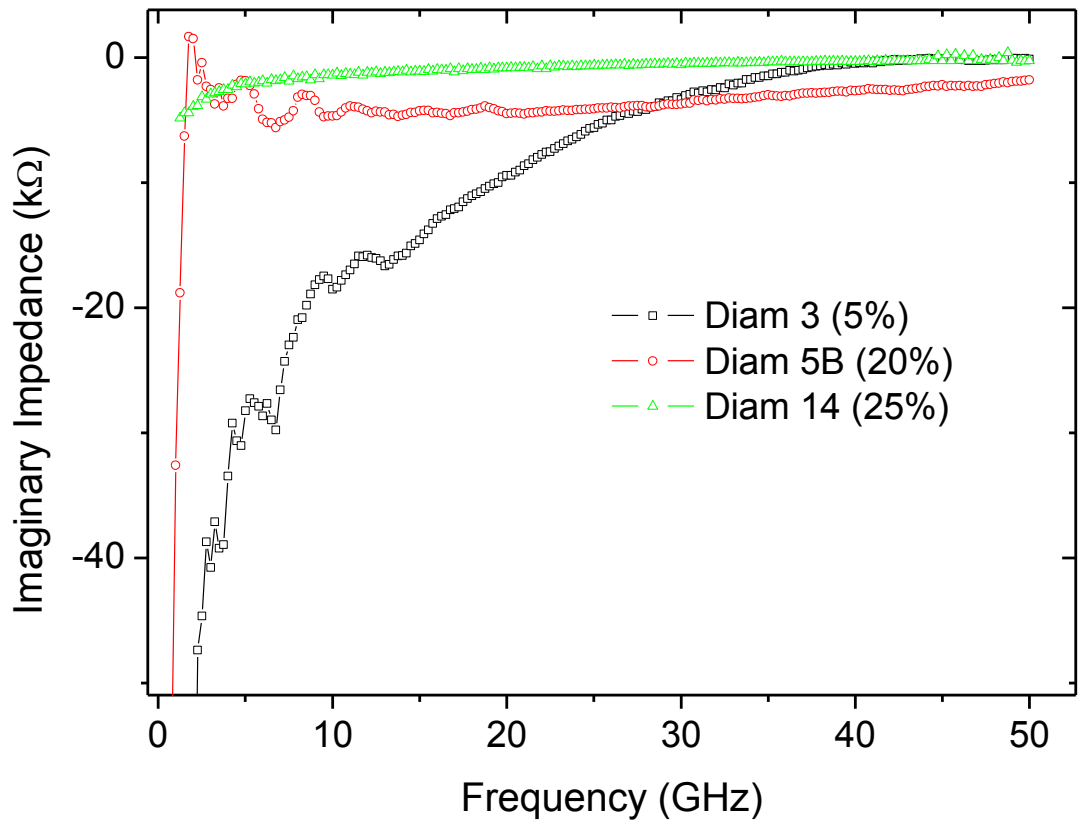


**Figure 5.12:** *Reactive component of the AC impedance for Diam 3 (5%), Diam 5B (20%) and Diam 14 (25%) samples.*

It has thus far been established that the conductivity of these nano-diamond clusters is due to the grain/cluster boundary disordered carbon. And high nitrogen content increases the conductance by about ten times in magnitude. The challenge then is to determine AC conduction mechanism in these films. For convenience the impedance is converted to admittance and the real part of it is defined as the conductance.

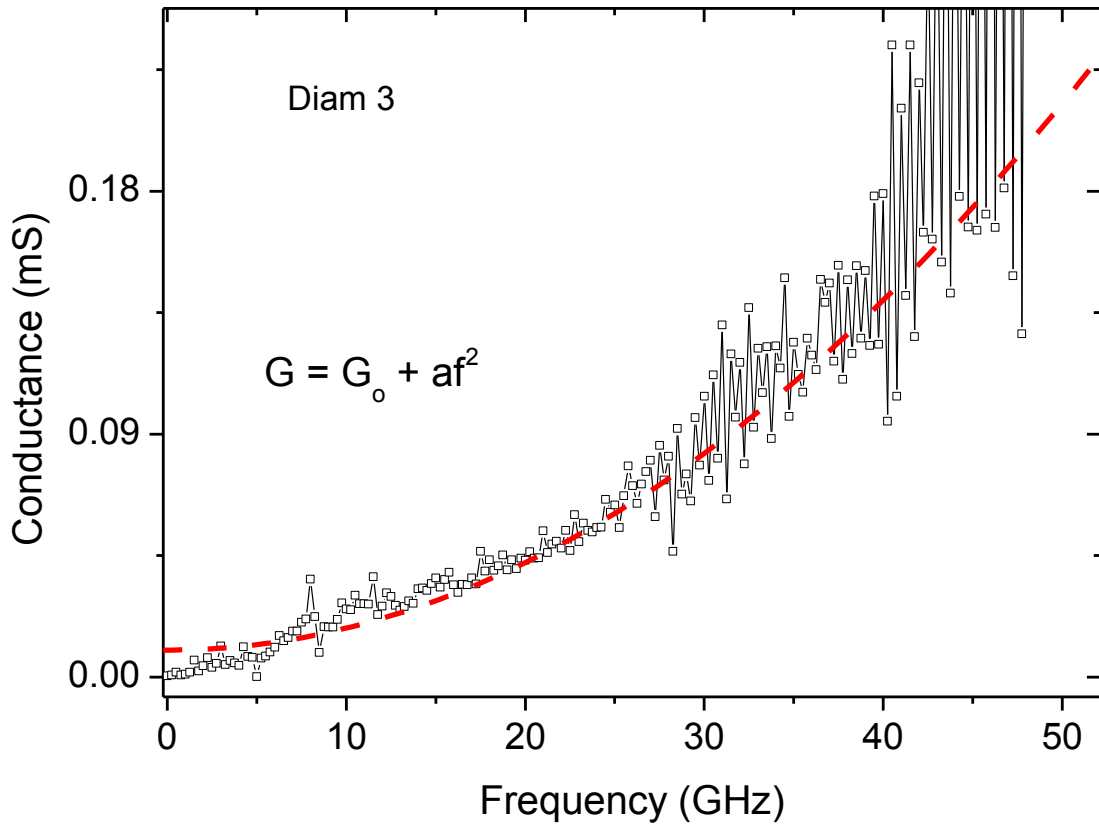


**Figure 5.13:** The real admittance of a “5 % doped” sample Diam 3 fitted with the localization theory for AC conductivity.

As mentioned at the beginning of this chapter, that nitrogen incorporated diamond films can be tuned from insulating to quasi-metallic regime all being driven by disorder in the GBs. Transport models in disordered materials have long shown that the principal difference between metallic and insulating regime originates from the degree of disorder. In the insulating regime the disorder is very strong such that the electronic states at the Fermi level are localised, a form of Anderson localisation [135]. According to localisation theory at low frequency below  $\omega_c$ , where  $\omega_c$  is the crossover frequency below which the effect of localisation is significant. The AC conductivity can be expressed as in equation 5.1 [136]

$$\sigma_{\omega} = \sigma_0 + a\omega^s, \quad (5.1)$$

where  $a$  is constant which depends on the density of states, and  $s = 2$  in the insulating regime and less than one in the metallic regime [136].

The AC conductance of the samples was fitted with the localisation model and the exponent of frequency ( $\omega$ ) was equal to 2, for the 5 % samples (Figure 5.13), indicating the films are in the insulating regime. According to the localisation model in the insulating regime, hopping mechanism is the dominant conduction process below the critical frequency ( $\omega_c$ ). Evident from the graph Figure 5.13 is that the data becomes very noisy at high frequencies; this is probably because of the inherent load mismatch between the instrument and diamond film devices. Highly conducting films were found to be less noisy. The main outstanding feature from these results is that the samples (5 %) appear to be in the insulating regime.

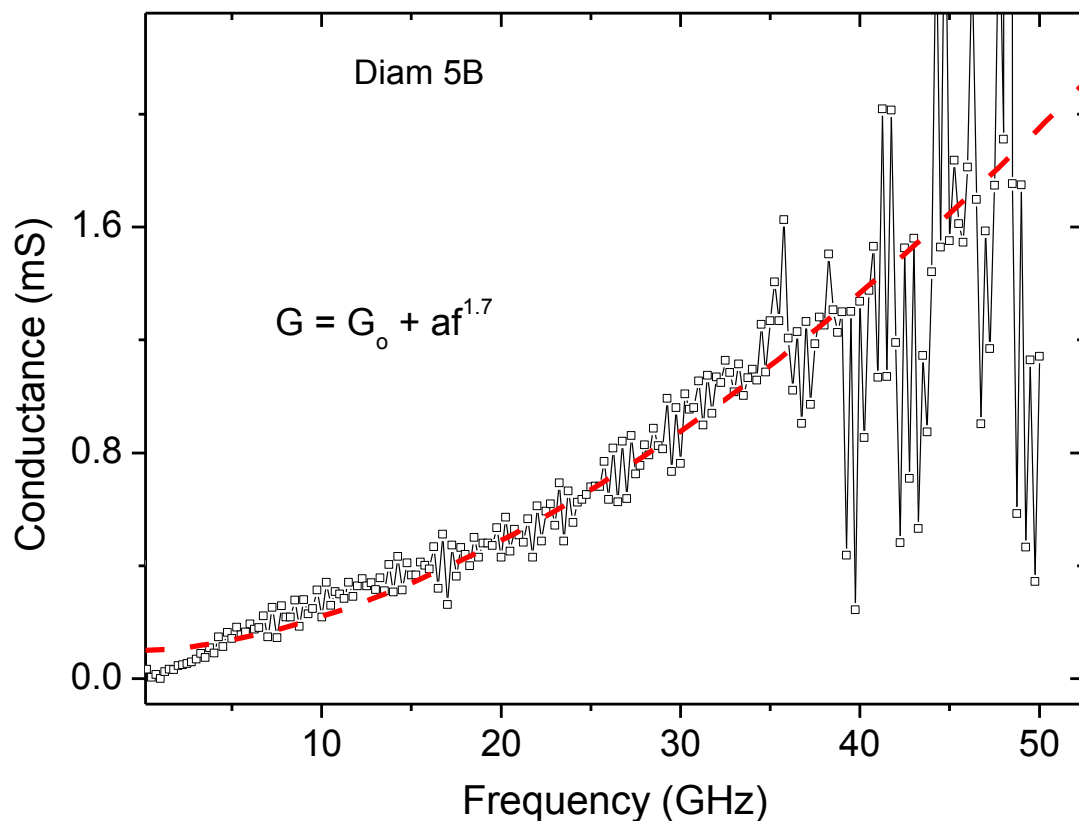


**Figure 5.14:** The real admittance of a “20 % doped” sample Diam 5B fitted with the localization theory for AC conductivity.

These results are in agreement with DC measurements that showed hopping as a major process in 15 % or less doped samples. The 20 % samples could not be fitted well with  $s = 2$  but instead  $s = 1.7$  see Figure 5.14. The reduction of the exponent of frequency  $s$  from 2 to 1.7 definitely signals a transition towards metallic regime in which  $s$  is less than one. This suggests a crossover to metallic conduction as nitrogen addition is increased. Such a crossover would be in agreement with DC measurements that showed a conductivity crossover from hopping, to metallic regime with increase in nitrogen. The analysis was extended to the 25 % nitrogen incorporated samples (see Figure 5.15), which showed a clear transition in behaviour.

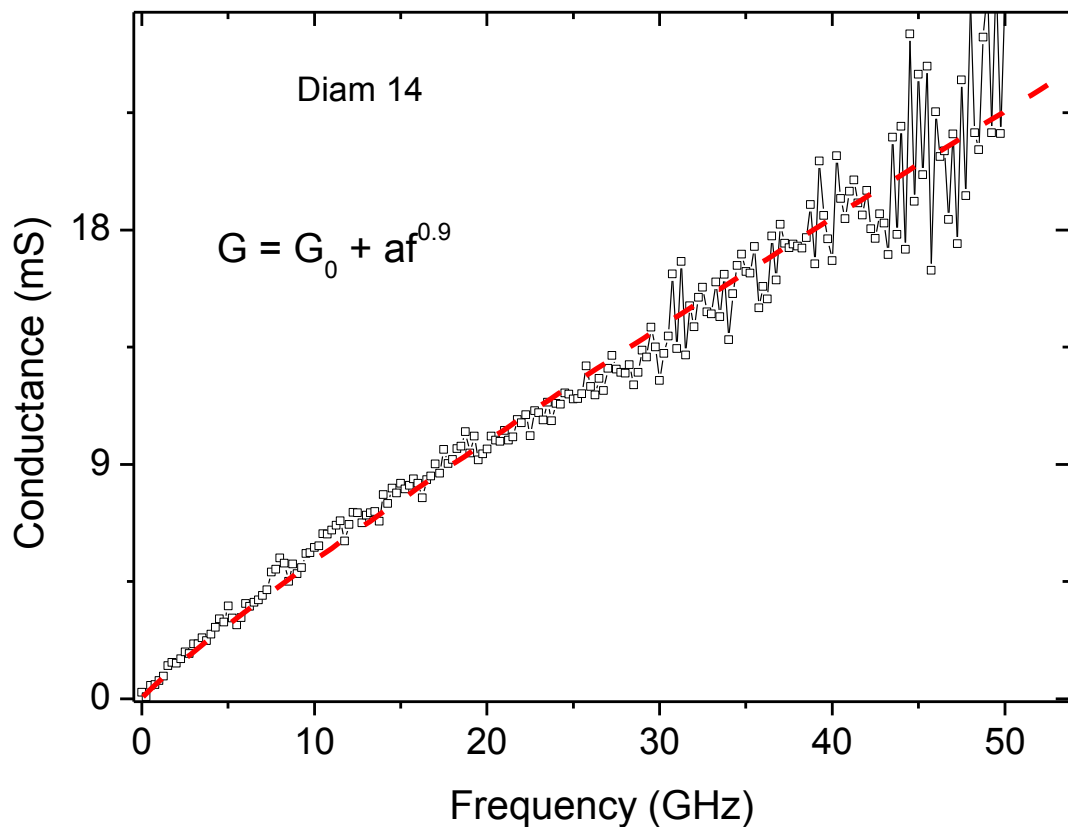


**Figure 5.15:** The real conductance of a “25 % doped” sample Diam 14 fitted with the localization theory for AC conductivity.

From the analysis of the 20 % and 25 % samples, it is evident that the conductance increases, due to nitrogen addition and the exponent ( $s$ ) decreases from 1.7 to 0.9. This is

further proof that the conduction mechanism is turning towards metallic regime in which  $s$  is expected to be less than one as shown in Figure 5.15. Similar power law frequency dependent conductivity in polycrystalline diamond was shown by Sugino *et al.* [137]. The granular morphology of these samples will result in some hopping effects from one metallic region to the other and this might explain why we do not see  $s = 0.33$  as in pure metallic systems. At this moment it is suggested that single crystalline films or films with ultranano-crystalline granules would show distinct metallic behaviour as hopping effects will be totally suppressed.

It is now established, this far that there is conductance crossover in nanodiamond films synthesized in higher nitrogen atmospheres. Plotting the real impedance versus the imaginary impedance popularly known as the Nyquist plot for the nitrogen doped samples further gave some informative insights on the effect of nitrogen in the films.

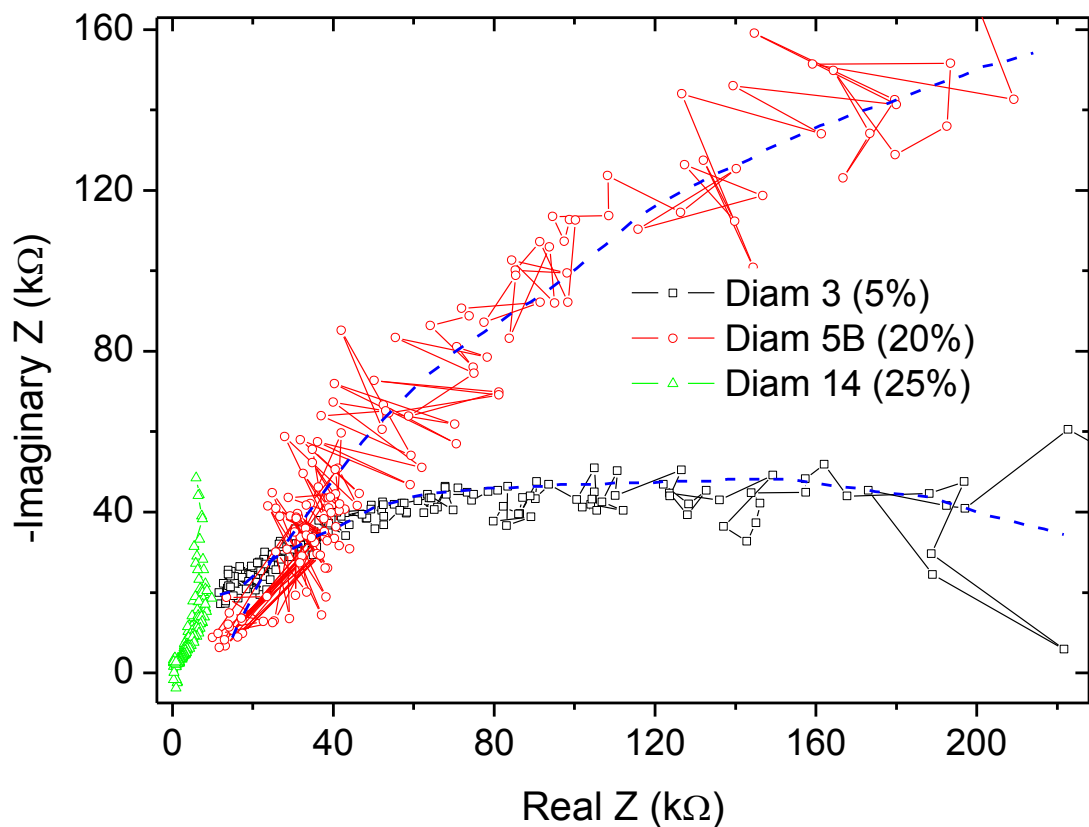


**Figure 5.16:** Nyquist plots for the 5 %, 20 % and 25 % doped samples showing a semi-circular shape for the 5 % sample. The blue dotted lines are to guide the eyes.

The Nyquist plots (Figure 5.16) show that the 5 % nitrogen sample has a semi-circular shape which according to the Nyquist theory would mean that the impedance can be described by a resistor in parallel with a capacitor [138]. In this configuration the impedance ( $Z$ ) can be expressed as shown in equation 5.2 [138].

$$Z = \frac{R}{1 + \omega(RC)^2} - j \frac{\omega R^2 C}{1 + \omega(RC)^2}, \quad (5.2)$$

A similar behaviour has been reported in some metallic oxides as well as polycrystalline diamond in the insulating regime in which hopping processes are the main conduction mechanisms [139]. As the nitrogen level is increased in the samples, the graph (Figure 5.16) shows that the shapes of the plots dramatically change implying the deviation from the RC parallel behaviour. The 25 % samples have a linear tail in the low frequency range which is similar to what has been observed in microwave synthesised ND films although at much lower frequencies [140]. The reduction in the overall impedance would suggest possible contribution from inductive processes and hence the change in shape of the plots. As mentioned earlier the changes in the composition and ordering of the GB is the only likely reason for the change in the shape of the Nyquist plots.

According to our hypothesis for DC conductivity [121], increasing the nitrogen level increases the  $sp^2$  layers in the GB and invariably increases the coupling of the layers as well. As a result it is expected that longer inductive paths are developed in films which makes the Nyquist plot change shape from the suggested RC parallel model. Due to the different morphologies and physical dimensions it is not easy to estimate the additional inductance that comes with an increase in nitrogen in the film. It is therefore recommended that the problem might need to be addressed by using single crystalline films whose dimensions can be accurately determined.

### 5.3: Chapter Summary

While more work still needs to be done this work has nevertheless confirmed that AC transport just like its DC counterpart is strongly dependent on the GB chemistry and/or morphology in polycrystalline films. The GB morphology changes significantly by increasing the nitrogen level during synthesis. This was evidenced by the shifting of the TPA and G peak positions as well as the FWHM of the G–peak. Associated with this GB changes is the conduction behaviour and hence the observed conductivity crossover from insulating to weak metallic regime, with nitrogen addition. Experimental evidence so far shows that nitrogen is a deep donor in nanodiamond grains and hence it does not contribute to the conduction process. This has been confirmed here, as single cluster films were found to be insulating irrespective of the amount of nitrogen used during synthesis. Its role however is that it tunes or drives the level of disorder / order of  $sp^2$  phases in the grain boundaries and this alters the conduction mechanism. This work may suggest that DC transport in ND films is very much similar to AC transport.

# Chapter 6 – Conclusions

The electrical response of carbon nanotubes and nitrogen incorporated nanodiamond films to an alternating current signal in the frequency range of 10 MHz to 65 GHz has been studied and analysed. This has been termed dynamic electrical transport, differentiating it from the electrical response to direct current signal which may be referred as static. Using an on-wafer probing technique, the scattering parameters of few horizontally aligned single, double and multi-walled carbon nanotubes were measured at both room and cryogenic temperatures. The same technique was used to measure the scattering parameters of small nanodiamond films, from which the AC complex impedance and conductance was determined.

Analysis of the carbon nanotubes results, unearthed very interesting quantum effects of strongly interacting electrons, which had been predicted theoretically but not observed experimentally using this technique. Single walled CNTs, showed high amplitude impedance oscillations in the gigahertz range at both room and low temperatures. These oscillations were concluded to be due to standing wave voltages waves, set-up by the finite length of the nanotubes. Based on a semi-classical transmission line theory by P. Burke [15], setting up standing wave voltages in a CNT is equivalent to exciting an infinite number of low energy charge plasmons. Therefore by measuring the plasmon velocity using the resonance frequencies we could directly determine the correlation parameter of the plasmons better known as a Luttinger Liquid. This correlation parameter is a measure of the interaction strength of the charge carriers which in this case are electrons. Our experiments revealed it to be in the range 0.18 to 0.21, which are figures within theoretical estimations.

The Luttinger liquid interpretation was consolidated by direct current measurements that showed power law dependence of the differential conductance of the CNTs with the bias voltage in accordance with LL behaviour. Low temperature results further showed a collapse of the differential conductance measured at different temperatures into one single curve in accordance with the LL scaling law. Observation of oscillatory impedance with a constant period and power law dependence of differential conductance has been suggested as a proof of Luttinger liquid behaviour in one dimensional systems [15] [53].



Simultaneous observations of these two properties eliminate the possibility of dynamic Coulomb blockade which also shows power law dependence of the differential conductance with bias voltage. Furthermore the frequency spectrum in which oscillations are observed eliminates the possibility of van Hove singularities, which would be expected at much higher frequencies.

It can therefore be concluded that this work has demonstrated experimentally some features that are associated with Luttinger liquid excited by high frequency signals in the GHz range. This is a fundamental quantum phenomenon that had been theoretically predicted but not observed experimentally using this technique.

Using an AC signal it was shown that ballistic transport can be achieved in structurally imperfect single walled nanotube bundles by setting the stimulus frequency to be greater than the scattering rate in the tubes. As a result a crossover from diffusive to ballistic transport was observed at room temperature in single walled nanotube bundles as the frequency of the signal was varied.

Studies on double walled nanotubes showed that the near perfect inner wall of the tubes made these DWNTs to be more sensitive to the CNT – electrode coupling as the temperature was lowered. These results also indicated that the observation of impedance oscillations in the GHz for one micron long CNTs is aided by the fact that significant scattering in the CNTs results in a reduced effective velocity of the plasmons and hence resonance is observed in the GHz regime. Proof of this important aspect was provided by low temperature high frequency data of DWNTs which showed “washed out” impedance oscillations in the low temperature regime because of the reduction in phonon scattering. In view of the high frequency results from DWNTs it was concluded that CNT- electrode coupling increases as the temperature is lowered and this results in observation of ballistic transport at lower frequencies as the temperature is reduced.

Multiwalled carbon nanotubes which are known to be primarily metallic have already been suggested for future interconnects in high frequency regime. This work has extended the scope of previous works by investigating the effect of metallic contacts such as tungsten and platinum to the high frequency transport in these interconnects. It is concluded that tungsten makes better contacts than platinum although it suffers relatively high microwave power losses at high frequencies above 20 GHz. These results have also shown that above 10 GHz the metal used for contacts becomes less important if the aspect of micro-wave power loss is

less important. This means that cheaper metals can be used in the sub - THz when making contacts.

Impedance oscillations (a generally one dimensional property) were also observed in individual multi-walled CNTs, indicating that in MWNTs the transport is dominated by one channel or few weakly coupled channels. A similar conclusion has already been made from DC transport measurements [87], and therefore this work shows that AC transport in multi-walled CNTs is also primarily from one or few weakly coupled channels.

Nanocrystalline diamond films were also studied using the same technique of measuring the scattering parameters from which the AC conductance was calculated. It was observed that varying the amount of nitrogen during synthesis resulted in a transition of the conductance from an insulating regime to semi-metallic regime. Analysis of the film micro-structure using Raman Spectroscopy led us to conclude that the conductivity crossover was due to the changes in the morphology and or chemistry of the grain boundary regions of the films. This work has therefore shown that AC transport just like its DC counterpart is determined by the grain boundary morphology and not nitrogen incorporated in the diamond grains.

In conclusion this work has unveiled some fundamental science of the electrical transport in carbon based nanomaterials whose understanding should help us to start working on a new class of electronic devices that should operate at very high speeds but using less energy. Understanding of the Luttinger liquid behaviour will enable the design of better single electron transistors if a third terminal is added to the set-up which was shown in this work. It will also aid our understating of spin-charge separation in devices. Spin – Charge separation is the hallmark of the LL behaviour, although this was not shown in this work, the stage is however set for the observation of this important aspect by showing the other two features. Furthermore achieving ballistic transport at room temperature in electronic devices will mean less power consumption in our future devices.

## **6.1: Future recommendations**

To fully confirm the LL behaviour it is recommended that this work be extended to gated devices. This will most probably be able to be able to unveil the spin-charge separation which will be the ultimate sign of the LL behaviour. Further work is also recommended on the AC conductance of nanocrystalline diamond films. For high frequency transport the work should focus on single crystalline doped diamond with higher mobility.

# References

---

- [1] H. Iwai, *Microelectronic Engineering*, vol. 86, p. 1520, 2009.
- [2] I. Corp, *Intel Corporation Journal*, vol. 6, p. 42, 2002.
- [3] S. L. a. B. B. U. Weissker, *Materials*, vol. 3, p. 4387, 2010.
- [4] E. M. B. M. C. A. Z. S. Demoustier, *C.R. Physique*, vol. 9, p. 53, 2008.
- [5] S. Iijima, *Nature*, vol. 354, p. 56, 1991.
- [6] H. Hall, "Diamond Synthesis". United States Patent 2947, 608, 02 08 1960.
- [7] W. G. E. B. C. e. a. P. Achatz, *Physical Review B*, vol. 79, p. 201203(R), 2009.
- [8] A. Hadjinicolaou, *Biomaterials*, vol. 33, p. 5812, 2012.
- [9] N. Mott, *Journal of Non-crystalline Solids*, vol. 8, no. 10, p. 1, 1972.
- [10] W. W. K. S. F. Y. P. S. R. M. M. Jaiswal, *Physical Review B*, vol. 76, p. 113401, 2007.
- [11] J. a. H. D. C. Zhou, *Physical Review Letters*, vol. 84, p. 5604, 2000.
- [12] T. T. a. Y. I. T. Takano, *Journal of Physical Society of Japan*, vol. 77, p. 124709, 2008.
- [13] C. B. Y. Z. W. W. d. H. P. Poncharal, *Journal of Physical Chemistry B*, vol. 106, p. 12104, 2002.
- [14] Q. X. X. G. Q. L. Q. Z. a. K. Y. L. Hao, *Journal of Applied Physics*, vol. 101, no. 053718, 2007.
- [15] P. Burke, *IEEE Transactions on Nanotechnology*, vol. 1, p. 3, 2002.
- [16] D. T. C. M. P. B. P. H. J. M. M. Nesladek, *Applied Physics Letters*, vol. 88, no. 232111, 2006.
- [17] D. P. B. P. H. J. M. J. K. M. Nesladek, *Diamond and Related Materials*, vol. 15, p. 607, 2006.
- [18] S. Bhattacharyya, *Physical Review B*, vol. 70, no. 125412, 2004.
- [19] T. Kolding, *IEEE Int. Conf. on Microelectronics test structures*, vol. 12, p. 105, 1999.
- [20] S. Wartenberg, *IEEE Transactions on microwave theory technology*, vol. 51, p. 1413, 2003.
- [21] J. C. a. B. Rautio, *Microwave Journal*, July 2012.
- [22] S. Morgan, *Journal of Applied Physics*, vol. 20, p. 352, 1949.

- [23] B. Wadell, *Transmission line Design Handbook*, NY: Artech House Inc, 1991.
- [24] L. Zhou, *IEEE Microwave and Wireless components letters*, vol. 12, p. 175, 2002.
- [25] R. Simons, *Coplanar waveguide circuits, components and systems*, New York: John Wiley and Sons, 2001.
- [26] L. S. J. G. D. Anderson, "S-Parameter Techniques: Test and Measurements: Application note 95-1," Hewlett Packard, US.
- [27] R. G. a. R. C. K.C. Gupta, *Computer Aided Design of microwave circuits*, Debham, MA: Artech House, 1981.
- [28] H. C. a. D. Burk, *IEEE Transactions on electron devices*, vol. 38, p. 1371, 1991.
- [29] "On-Wafer Vector Network Analyzer calibration and measurement," Cascade Microtech, UK.
- [30] P. Smith, *Electronics*, vol. 12, p. 29, 1939.
- [31] P. Smith, *Electronics*, vol. 17, p. 130, 1944.
- [32] Q. L. a. K. Melde, *IEEE Transactions on Advanced packaging*, vol. 33, p. 285, 2010.
- [33] C. C. a. M. Deen, *IEEE Transactions on microwave theory technology*, vol. 49, p. 1004, 2001.
- [34] "Agilent AN1287-9: In fixture Measurements using a vector network analyzer," Agilent, US, 2000.
- [35] E. S. K. J. A. Davidson, "Application Note," Cascade Microtech, UK.
- [36] L. Hayden, "Advancements in mm-wave- On-wafer measurements;," Casacade Microtech, UK.
- [37] J. Weng, *IEEE Transactions on electron devices*, vol. 42, p. 1703, 1995.
- [38] C. Highstrete, *Microwave Spectroscopy of nanowires and nanotubes- PhD Thesis*, New Mexico: University of New Mexico, 2008.
- [39] J. a. T. Hsiang, *Piers Online* , vol. 3, p. 1102, 2007.
- [40] D. Pozar, *Microwave Engineering* 4th Edtion, New York: John wiley and sons, 1998.
- [41] S. S. a. C. S. M. Begliarbekov, *Nanotechnology*, vol. 22, no. 165203, 2011.
- [42] M. N. J. W. a. H. G. C. Roland, *Physical Review Letters*, vol. 84, p. 2921, 2000.
- [43] S. Datta, *Electronic Transport in Mesoscopic systems*, UK: Cambridge University Press, 1995.
- [44] A. E. B. I. Shklovskii, *Electronic properties of doped semiconductors*, Berlin Heidelberg, NY.

Tokyo: Springer Verlag, 1984.

- [45] R. Kubo, *Journal of Physics Society of Japan*, vol. 12, p. 570, 1957.
- [46] D. Greenwood, *Proc. Physical Society*, vol. 71, p. 585, 1958.
- [47] A. Akkala, *NEGF simulation of electron transport in resonant tunneling and resonant interband tunneling diodes*, US: MSc Thesis, 2011.
- [48] M. V. a. F. L. D. Kienle, *Physical Review B*, vol. 81, no. 115455, 2010.
- [49] A. N. a. A. T. A.O. Gogolin, *Bosonization and strongly correlated systems*, UK: Cambridge University Press, 1998.
- [50] L. B. a. K. W. C.S. Peca, *Physical Review B*, vol. 68, no. 205423, 2003.
- [51] A. K. R. E. D. G. a. A. B. B. Gao, *Physical Review Letters*, vol. 92, no. 216804, 2004.
- [52] R. Egger, *Physical Review Letters*, vol. 83, no. 5547, 1999.
- [53] V. Ponomarenko, *Physical Review B*, vol. 54, no. 10328, 1996.
- [54] C. K. a. M. Fisher, *Physical Review Letters*, vol. 68, p. 1220, 1992.
- [55] D. Y. a. L. G. K.A. Matveev, *Physical Review Letters*, vol. 71, no. 3351, 1993.
- [56] N. S. a. D. Maslov, *Physical Review B*, vol. 55, p. 13808, 1997.
- [57] F. H. a. M. B. Y.M. Blanter, *Physical Review Letters*, vol. 81, p. 1925, 1998.
- [58] B. W. P. A. G. R. T. L. a. G. W. Y.P. Zhao, *Physical Review B*, vol. 64, no. 201402 (R), 2001.
- [59] L. D. M. K. a. P. M. S. Ilani, *Nature*, vol. 2, p. 687, 2006.
- [60] T. W. S. R. a. P. K. P. Rice, *Nano Letters*, vol. 7, p. 1086, 2007.
- [61] S. G. E. C. M. F. T. Durkop, *Nano Letters*, vol. 4, p. 35, 2004.
- [62] J. K. R. M. V. D. S. W. a. P. A. J. Appenzeller, *Physical Review Letters*, vol. 89, p. 126801, 2002.
- [63] A. B. J. C. G. F. B. H. T. K. J. B. a. B. P. E. Pallecchi, *Physical Review B*, vol. 83, no. 125408, 2011.
- [64] X. H. S. M. H. K. J. H. Y. J. a. J. K. S.C. Jun, *New Journal of Physics*, vol. 9, p. 265, 2007.
- [65] D. F. a. J. Appenzeller, *IEEE Electron Devices Letters*, vol. 25, p. 34, 2004.
- [66] Google, 2000. [Online]. Available: [www.google/CNT/images](http://www.google/CNT/images). [Accessed 21 July 2014].

- [67] H. K. K. M. Burghard, *Advanced Materials*, vol. 21, p. 2586, 2009.
- [68] G. D. M. D. R. Saito, *Physical properties of carbon nanotubes*, London: London Imperial college Press, 1998.
- [69] H. T. a. M. Terrons, *New Journal of Physics*, vol. 5, p. 1261, 2003.
- [70] P. E. M.S. Dresselhaus, *Advances in Physics*, vol. 49, p. 705, 2000.
- [71] M. B. K. W. C. B. L. a. C. Z. F.Liu, *Applied Physics Letters*, vol. 86, no. 213101, 86.
- [72] "Diamond images," Google, [Online]. Available: [www.google/diamond/images.com](http://www.google/diamond/images.com). [Accessed 10 February 2014].
- [73] A. Badzian, "The status of Diamond electronics," 2007. [Online]. Available: [www.semi1source.com](http://www.semi1source.com). [Accessed March 2014].
- [74] M. Kasu, *Front-line Materials Research: Special Report*, vol. 8, p. 1, 2010.
- [75] V. S. E. B. N. M. N. C. J. T. a. S. S. E.A. Ekimov, *Nature*, vol. 428, p. 542, 2004.
- [76] M. K. M. P. S. D. G. S. E. M. S. B. S. a. E. K. A.Aleksov, *Diamond and Related Materials*, vol. 13, p. 233, 2004.
- [77] M. B. a. N. F. A.F. Azevedo, *Journal of Electrochemistry*, vol. 2012, no. 508453, 2011.
- [78] G. C. Z. C. a. S. B. S.Ncube, *Journal of Applied Physics*, vol. 116, no. 024306, 2014.
- [79] S. E. D. C. J. R. S. S. L. Gomez-Rojas, *Nano Letters*, vol. 7, p. 2672, 2007.
- [80] R. A. P. a. C. L. E.Flahaut, *Chemical Communications (Cambridge)*, vol. 12, p. 1442, 2003.
- [81] E. a. S. G.Chimowa, *APL*, Submitted.
- [82] G.Bepete, *Chemical Vapor growth of nitrogen doped carbon nanotubes and graphene materials for Application in organic photovoltaic devices- PhD Thesis*, Johannesburg: University of the Witwatersrand, 2013.
- [83] V. K. A. B. U. a. Y. K. Y. J. Moscatello, *Materials Society Symposium Proc. ,* vol. 1057, no. II 15-07, 2008.
- [84] "De-embedding and Embedding of S-Parameter networks Application note 13641," Agilent, US, 2004.
- [85] J. G. a. M. V. M.C.A.M. Koolen, in *IEEE Bipolar/BiCMOS circuits and Technology meeting*, 1991.
- [86] G. Chimowa, *Synthesis and Characterisation of Nanodiamond films*, Johannesburg: MSc Thesis

- Wits University, 2011.

- [87] E. L. D. N. C. a. S. B. G. Chimowa, *Physical Review B*, vol. 84, no. 205429, 2011.
- [88] M. L. a. S. D. S. Salahaddin, *IEEE Transactions on electron devices*, vol. 52, p. 1734, 2005.
- [89] V. S. a. B. Shchamkhalova, *Journal of low temperature Physics*, vol. 118, p. 485, 2000.
- [90] K. M. L. D. a. J. J. J. Obrzut, *AIP Conference Proc*, vol. 931, p. 483, 2007.
- [91] E. Y. T. T. W. H. D. R. L. L. C. J. a. S. W. J. Kong, *Physical Review Letters*, vol. 87, no. 106801, 2001.
- [92] P. B. L. P. K. W. S. Kang, *Solid State Electronics*, vol. 48, p. 2013, 2004.
- [93] M. S. a. B. K. G. Cuniberti, *Physical Review B*, vol. 57, p. 1515, 1998.
- [94] T. P. M. K. J. F. a. H. K. H. Rauf, *Physical Review Letters*, vol. 93, no. 096805, 2004.
- [95] K. M. a. L. Glazman, *Physical Review Letters*, vol. 70, p. 990, 1993.
- [96] H. P. L. B. a. C. D. Z. Yao, *Nature*, vol. 402, p. 273, 1999.
- [97] L. S. N. T. E. V. S. Z. a. B. S. B. A. Danilchenko, *Applied Physics Letters*, vol. 97, no. 072106, 2010.
- [98] C. R. a. P. Burke, *Small*, vol. 5, p. 884, 2009.
- [99] D. c. J. A. R. R. S. L. B. a. P. M. M. Bockrath, *Nature (London)*, vol. 397, p. 598, 1999.
- [100] L. B. a. M. F. C. Kane, *Physical Review Letters*, vol. 79, p. 5086, 1997.
- [101] M. M. a. G. Garbarino, *Physical Review Letters*, vol. 97, no. 176401, 2006.
- [102] C. a. A. C. I. Safi, *Physical Review B*, vol. 78, no. 205422, 2008.
- [103] T. S. J. S. F. M. T. S. C. d. L. F. W. d. H. A. c. J. M. Bonard, *Advanced Materials*, vol. 9, p. 827, 1997.
- [104] M. S. E. F. D. C. a. S. B. G. Chimowa, *Journal of Applied Physics*, vol. 110, no. 123708, 2011.
- [105] K. S. a. S. W. T. Yamamoto, *Physical Review B*, vol. 82, no. 205404, 2010.
- [106] K. K. S. K. a. A. M. Tsutsui, *eJ. Surface Science Nanotechnology*, vol. 5, p. 12, 2007.
- [107] P. Bandaru, *Journal of Nanoscience and Nanotechnology*, vol. 7, p. 1, 2007.
- [108] X. H. P. C. Q. L. a. Z. T. M. Zhang, *IEEE Electron device Letters*, vol. 27, p. 668, 2006.



- [109] S. Jun, *Nanotechnology*, vol. 18, no. 255701, 2007.
- [110] T. T. T. Y. I. K. T. Y. A. a. H. K. T. Kanbara, *Applied Physics Letters*, vol. 88, no. 053118, 2006.
- [111] A. A. V. G. A. M. V. J. M. P. a. J. S. Ch. Caillier, *Applied Physics Letters*, vol. 97, no. 173111, 2010.
- [112] A. J. J. K. Q. H. D. D. Mann, *Nano Letters*, vol. 3, p. 1541, 2003.
- [113] N. R. S. A. I. H. S. M. J. P. F. U. a. W. M. M.S. Haque, *Nanotechnology*, vol. 19, no. 025607, 2008.
- [114] A. P.-J. E. L. E. S. F. J. V. J.J. Palacios, *Physical Review Letters*, vol. 90, no. 106801, 2003.
- [115] E. S. M. F. J. D. a. A. T. C. Highstrete, *Applied Physics letters*, vol. 89, no. 173105, 2006.
- [116] G. C. a. S. Bhattacharyya, *AIP Advances*, vol. 4, p. 087136, 2014.
- [117] O. Williams, *Semiconductor Science and Technology*, vol. 21, p. R49, 2006.
- [118] M. K. Y. Y. T. M. M. S. D. T. G. S. a. S. C. K. Ueda, *IEEE Electron devices*, vol. 27, p. 570, 2006.
- [119] O. K. a. L. C.-G. B.I. Kharisov, *Synthesis & Reactivity in Inorganic, Metal-Organic and Nano-Metal Chemistry*, vol. 4, p. 84, 2010.
- [120] T. M. S. Y. a. H. O. H.Kato, *Journal of Physics D: appl. Phys.*, vol. 40, p. 6189, 2007.
- [121] D. C. S. B. G. Chimowa, *Europe Physics Letters*, vol. 99, no. 27004, 2012.
- [122] S.Bhattacharyya, *Physical Review B*, vol. 70, p. 125412, 2004.
- [123] N. Mott, *Conduction in Non-crystalline Materials*, Oxford: Oxford University Press, 1987.
- [124] M. S. L. C. T. F. D. M. G. P. Zapol, *Physical Review B*, vol. 65, no. 045403, 2001.
- [125] A. F. a. J. Robertson, *Phil. Trans. R. Society Lond.*, vol. 362, p. 2477, 2004.
- [126] M. K. a. S. Bhattacharyya, *Journal of Applied Physics* , vol. 111, no. 123711, 2012.
- [127] V. B. a. P. Kleinert, *Z. Physics B*, vol. 101, p. 91, 1996.
- [128] C. Coleman, *Schematic Illustration of a carbon super-lattice structure*, Johannesburg: University of the Witwatersrand, 2012.
- [129] K. T. C. C. J. R. A. F. T. Ikeda, *Journal of Applied Physics*, vol. 104, no. 073720, 2008.
- [130] Z. X. D. Z. Y. G. S.A. Rakha, *Currebt Applied Physics*, vol. 10, p. 171, 2010.

- [131] A. B. C. S. R. K. D. T. B. T. D. G. P. B. L. Gun, *Diamond and Related Materials*, vol. 18, p. 1118, 2009.
- [132] H. K. P. K. S. B. N. S. B. G. R. Pfeiffer, *Diamond and Related Materials*, vol. 12, p. 268, 2003.
- [133] A. F. a. J. Robertson, *Physical Review Letters*, vol. 61, no. 14095, 2000.
- [134] Y. M. L. A. a. J. L. A.N. Goyette, *Journal of Vacuum Science technology*, vol. A16, p. 337, 1998.
- [135] P. A. D. L. a. T. R. E. Abrahams, *Physical Review Letters*, vol. 42, p. 673, 1979.
- [136] P. L. a. T. Ramakrishnan, *Reviews of Modern Physics*, vol. 57, p. 287, 1985.
- [137] Y. M. K. K. J. S. a. K. K. T. Sugino, *Diamond and Related Materials*, vol. 2, p. 803, 1993.
- [138] P. B. D. M. M. B. J. L. a. D. G. R. Arenal, *Physical Review B*, vol. 75, no. 195431, 2007.
- [139] M. B. a. D. Reinhard, *Diamond and Related Materials*, vol. 6, p. 1689, 1997.
- [140] O. W. R. J. R. R. a. A. A. H. Ye, *Phys. Stat. Sol.*, vol. 193, p. 462, 2002.
- [141] C. R. W. a. R. C. A. Afzal, *Diamond and Related Materials*, vol. 7, p. 1033, 1998.

# Appendix

## A1: Matlab code used for De-embedding waveguide parasitic

```
format long
%=====
=
% ===== Frequency =====
freq = xlsread('DutS.xlsx','A2:A202');
%=====
=
% Dut
%=====
=
%import and assign SD11
[num,txt,row] = xlsread('DutS.xlsx','B2:B202');
s11dut=str2num(char(row));
clear num txt row
%import and assign SD12
[num,txt,row] = xlsread('DutS.xlsx','C2:C202');
s12dut = str2num(char(row));
clear num txt row
%import and assign SD21
[num,txt,row] = xlsread('DutS.xlsx','D2:D202');
s21dut = str2num(char(row));
clear num txt row
%import and assign SD22
[num,txt,row] = xlsread('DutS.xlsx','E2:E202');
s22dut = str2num(char(row));
%=====
=
% OPEN
%=====
=
%import and assign SO11
[num,txt,row] = xlsread('OpenS.xlsx','B2:B202');
s11open = str2num(char(row));
clear num txt row
%import and assign SO12
[num,txt,row] = xlsread('OpenS.xlsx','C2:C202');
s12open = str2num(char(row));
clear num txt row
%import and assign SO21
[num,txt,row] = xlsread('OpenS.xlsx','D2:D202');
s21open = str2num(char(row));
clear num txt row
%import and assign SO22
[num,txt,row] = xlsread('OpenS.xlsx','E2:E202');
s22open = str2num(char(row));
%=====
=
% SHORT
%=====
=
%import and assign SS11
[num,txt,row] = xlsread('ShortS.xlsx','B2:B202');
s11short = str2num(char(row));
clear num txt row
```

```

%import and assign SS12
[num,txt,row] = xlsread('ShortS.xlsx','C2:C202');
s12short = str2num(char(row));
clear num txt row
%import and assign SS21
[num,txt,row] = xlsread('ShortS.xlsx','D2:D202');
s21short = str2num(char(row));
clear num txt row
%import and assign SS22
[num,txt,row] = xlsread('ShortS.xlsx','E2:E202');
s22short = str2num(char(row));
clear num txt row
% Number of frequency points
t=201;
% Impedance
z0=50;

%===== convert s parameters to y parameters
=====

for f=1:t
    %===== Creating the matrix of s parameters for dut
    duts = [s11dut(f) s12dut(f);s21dut(f) s22dut(f)];
    % convert dut s matrix to y matrix
    duty = s2y(duts,z0);
    %===== Creating the matrix of s parameters for open
    opens = [s11open(f) s12open(f);s21open(f) s22open(f)];
    % convert open s matrix to y matrix
    openy = s2y(opens,z0);
    %===== Creating the matrix of s parameters for short
    shorts = [s11short(f) s12short(f);s21short(f) s22short(f)];
    % convert short s matrix to y matrix
    shorty = s2y(shorts,z0);

%=====
=
% Y matrix manipulation
%=====
=

    diff1=duty-openy;
    diff2=shorty-openy;
    id1=inv(diff1);
    id2=inv(diff2);
    id3=id1-id2;
    total=inv(id3);
    yd11(f,1)=total(1,1);
    yd12(f,1)=total(1,2);
    yd21(f,1)=total(2,1);
    yd22(f,1)=total(2,2);
    % Defining the y- parameters of device
    y_params=[yd11(f) yd12(f);yd21(f) yd22(f)];
    %converting y device to s - parameters
    sd_params = y2s(y_params);
    %creating and array of s - parameters
    sd11(f,1)=sd_params(1,1);
    sd12(f,1)=sd_params(1,2);
    sd21(f,1)=sd_params(2,1);
    sd22(f,1)=sd_params(2,2);
end

```

```

display (sd11)
display (sd12)
display (sd21)
display (sd22)
%display(freq)
%smat=[s11 s12 s21 s22]

```

## A2: Matlab code used for Simulating S-parameters

```

RESS1 = rfckt.shuntrlc('R',###); %set the value for R1 of input contact
CAPS1 = rfckt.shuntrlc('C',####); %set the value for C1 of input contact
SCOMB = rfckt.series('Ckts',{RESS1,CAPS1});%series combination of R1 and
C1
INPAD = rfckt.seriesrlc('R',###,'C',####); %series input R2 and C2
INPADR = rfckt.seriesrlc('R',###); %series R3
PCOMB = rfckt.parallel ('Ckts',{INPADR,INPAD}); %Parallel comb of R2,C2&R3
INCONTACT = rfckt.cascade ('Ckts',{SCOMB,PCOMB});% Total for input contact
SSCNT = rfckt.seriesrlc('R',####,'L',####);% DUT R4 and L1
CCNT = rfckt.seriesrlc ('C',###); % series DUT C3
WCNT = rfckt.cascade ('Ckts', {SSCNT,CCNT});% Total for DUT
RESS2 = rfckt.shuntrlc('R',###); %set value for R5 of output contact
CAPS2 = rfckt.shuntrlc('C',###); %set value for C4 of output contact
SCOMBO = rfckt.series('Ckts',{RESS2,CAPS2});%series comb of R6 & C4
INPADO = rfckt.seriesrlc('R',###,'C',####);%series output R5 and C5
INPADRO = rfckt.seriesrlc('R',###);%series R7
PCOMBO = rfckt.parallel ('Ckts',{INPADO,INPADRO});%parallel cob of
R5,C5&R6
OPCONTACT = rfckt.cascade ('Ckts',{PCOMBO,SCOMBO});%Total output contact
DUT_model = rfckt.cascade('Ckts', {INCONTACT,WCNT,OPCONTACT});% Toatal ckt
f = 1e7:1e6:50e9 % Frequency range
analyze (DUT_model,f);% simulate freq response of ckt
model = plot(DUT_model,'S21','dB'); % plot S21 in dB
fname = ('SW7RT.dat'); % define expt data file
[freq,fname] = xlsread('SW7RT.xlsx','A1:A201');% read expt data
[rfp,fname] = xlsread ('SW7RT.xlsx','B1:B201');% read expt data
Diamexp = rfp(1:55);

```

## Temperature-dependent diffusive to ballistic transport transition in aligned double walled carbon nanotubes in the high frequency regime

George Chimowa,<sup>1</sup> Emmanuel Flahaut,<sup>2</sup> and Somnath Bhattacharyya<sup>1,a)</sup>

<sup>1</sup>Nano-Scale Transport Physics Laboratory, School of Physics, and DST- NRF Centre of Excellence in Strong materials, University of the Witwatersrand, Johannesburg, South Africa

<sup>2</sup>Université Paul Sabatier, CNRS, Institut Carnot Cirimat, 118, route de Narbonne, F-31062 Toulouse, Cedex 9, France

(Received 8 July 2014; accepted 23 October 2014; published online 31 October 2014)

Low-temperature induced diffusive to ballistic transport in aligned double walled carbon nanotubes (DWNT) is reported. This is evidenced by a crossover of the imaginary (reactive) component of the alternating current impedance being greater than the real (resistive) component, which happens in the range of 9 GHz–1.5 GHz at temperatures 77 K and 4 K from which we estimate a long lifetime of 17 ps and 106 ps in DWNTs, respectively. By simulating the measured scattering parameters of a few aligned DWNTs over a wide temperature range, we show that this observation is strongly influenced by the electrode–DWNT coupling strength. © 2014 AIP Publishing LLC.

[<http://dx.doi.org/10.1063/1.4901025>]

Electrical transport properties of carbon nanotubes (CNTs) are commonly measured after acid purification, surfactant stabilization, and ultrasonication dispersion prior to the deposition of electrodes. These processes can lead to defects and doping of the outerwall in the CNTs which affects the transport mechanism. This is probably why most catalytically produced and lithographically contacted CNTs have been found to be diffusive at room temperature.<sup>1,2</sup> Coherent transport has been observed in singlewalled (SWNT) and multi-walled nanotubes (MWNT) at cryogenic temperatures with the exception of pristine MWNTs measured using an *in-situ* microscopy technique.<sup>3</sup> Transport in SWNTs that are often aligned on top of insulating substrates is influenced by substrate surface roughness as in some graphene devices.<sup>4</sup> Furthermore, multi-walled nanotubes and SWNT networks may suffer from multiple conduction channels depending on the contacting technique.<sup>5</sup> This may make it difficult to compare with theoretical models that assume simplified, strict one-dimensional (1D) channel assumptions. Unlike SWNTs and MWNTs, double walled carbon nanotubes (DWNTs) have only two walls which offer a platform to study ballistic transport features that have been demonstrated in freely suspended pristine multi-walled nanotubes.<sup>3</sup> Earlier experimental and theoretical works on filled DWNTs have shown that these nanotubes demonstrate unique 1D features due to the nearly structurally perfect inner wall that is protected by the outer wall.<sup>6,7</sup> The inner wall thus remains unaffected by the chemical purification processes, and substrate interference effects although the outer wall of DWNTs can be biased in such a manner it behaves as a gate.<sup>8</sup> However, the alignment of the tubes is necessary to observe 1D transport which can be affected by the interaction of tubes in a bundle of CNTs.<sup>5,9–11</sup> In this letter using on-wafer probing on coplanar waveguides (which has now become the standard technique for measuring the scattering (S)-parameters of nano-materials), we show the possibility of 1D

ballistic conduction through the alternating current (AC) impedance of a few horizontally aligned DWNTs.

In previous works on high frequency properties of dense DWNTs networks, fabricated by ink-jet printing onto the waveguide, a strong frequency dependence of DWNTs microwave parameters as well as abrupt changes in effective permittivity was observed. This property could be used in gas sensor applications.<sup>9–11</sup> We extended this work by probing few aligned tubes so as to unearth any unique quantum features regarding this strong frequency dependence. The ideal scenario would be to measure a single tube but unfortunately because of the inherent load mismatch a minimum of four parallel DWNTs was used. This improves the output signal by reducing the effective (quantum) resistance from  $\sim 13 \text{ k}\Omega$  to  $\sim 3 \text{ k}\Omega$  for four CNTs in parallel. This configuration is equivalent to a bundle consisting of a few weakly coupled tubes in parallel. While there is still significant mismatch with the waveguide, the signal level is nevertheless improved greatly.<sup>5,10,11</sup>

Ideally ballistic transport is regarded as the motion of charge carriers without any scattering; however, contact resistance always inhibits this. We however have attempted to achieve ballistic transport in two ways: (i) reducing the sample dimensions to the range of the mean free path<sup>12</sup> or (ii) using a time-dependent signal whose frequency is greater than the scattering rate in the material. In this case, the effect of local defect centres to transport can be reduced. The Drude model for frequency ( $\omega$ ) dependent transport expresses the conductivity ( $\sigma$ ) made of two parts; the real part and imaginary parts given by  $\sigma(\omega) = \frac{ne^2\tau}{m^*} \frac{1}{1+i\omega\tau}$ , where  $\tau$ ,  $m^*$ ,  $e$ , and  $n$  represent the momentum scattering time, effective electron mass, electronic charge, and the carrier density, respectively.<sup>13</sup> The imaginary part of the conductivity is given by  $i\omega\tau$  and it changes sign depending on whether it is capacitive or inductive. We can therefore make use of this fact to determine experimentally whether the transport is the diffusive or ballistic regime if the real and imaginary impedance is known. To complement AC response measurements, two-terminal direct (DC) current-voltage ( $I$ - $V$ ) measurements

<sup>a)</sup>Author to whom correspondence should be addressed. Electronic mail: Somnath.Bhattacharyya@wits.ac.za

were performed and fitted with the Landauer-Büttiker theory, which describes the transmission of electrons from the electrode to the CNT as:

$$I(V) = \frac{2e}{h} \int_{-\infty}^{+\infty} \frac{\Gamma^2}{(E - \Delta E)^2 + \Gamma^2} \times \left[ f_F \left( E - E_F - \frac{eV}{2} \right) - f_F \left( E - E_F + \frac{eV}{2} \right) \right] dE, \quad (1)$$

where  $\Delta E$  and  $f_F$  are the energy difference of the CNT from electrode Fermi energy level ( $E_F$ ) and the Fermi distribution function, respectively.<sup>14</sup> This analysis is very important to determine the strength of CNT-electrode coupling ( $\Gamma$ ) and subsequently the nature of electrical conduction in these devices, namely the crossover of real and imaginary parts of impedance at different temperatures.

DWNTs were synthesized by Catalytic Chemical Vapour Deposition (CCVD) for more details see Ref. 15. Finally, they were dispersed in ( $\sim 0.013 \text{ mg/cm}^3$ ) dichlorobenzene and prepared for high frequency  $S$ -parameter measurements by aligning them on 1 mm long coplanar waveguide (CPW) with a  $1 \mu\text{m}$  gap using dielectrophoresis, which is known to favour alignment of metallic CNTs.<sup>16</sup> Kleindek nanomanipulators in the scanning electron microscope (SEM) were used to remove unwanted CNTs and large bundles.<sup>17</sup> Some of actual SEM micrographs of the devices that were used for HF measurement are shown in Fig. 1(a). The CNTs appear as dark sheds on the waveguide because of charging effects during imaging since the gap is non-conductive. The transmission electron microscope (TEM) image Fig. 1(b) illustrates the high quality of the unaligned DWNT bundles before transferring them for device fabrication.<sup>17</sup>

$S$ -parameter measurements were done using an Agilent Precision Network Analyser (PNA) E8361C at room and low temperatures under vacuum ( $10^{-5}$  millibar) for more details and instrument calibration see references.<sup>17,18</sup> The temperature dependent  $I$ - $V$  measurements were done using the Agilent B1500A semiconductor analyser with a 1 pA

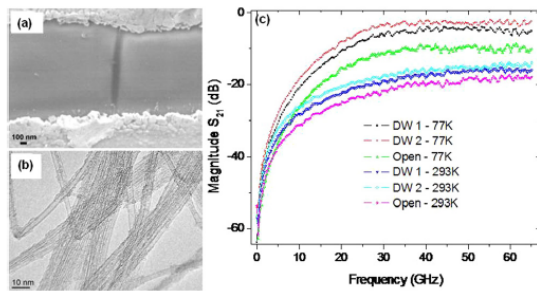


FIG. 1. (a) SEM micrograph of DW1; four DWNTs on separate positions, but because of the scale, only one can be seen. (b) TEM micrograph of DWNTs after catalyst removal and before alignment, showing good quality CNTs with small-diameter bundles. (c) Transmission coefficient for samples DW1 and DW2 at room and 77 K temperatures. The Open data are for the waveguides without CNTs aligned on them and is used to de-embed the parasitic effects.

resolution. Measurement parasitic (i.e., effects due to the substrate) were extracted by using the open-short de-embedding method an industrially accepted technique, see the Eq. (2) below<sup>19</sup>

$$Y_{DUT} = [(Y_{msd} - Y_{open})^{-1} - (Y_{short} - Y_{open})^{-1}]^{-1}, \quad (2)$$

where  $Y_{msd}$  is the measured admittance of the CPW plus the aligned CNT,  $Y_{open}$  and  $Y_{short}$  are the admittance matrices of the open (CPW without CNT) and short (CPW without a gap) dummies. The device under test (DUT), i.e., CNTs data can then be obtained by converting the admittance ( $Y$ ) to  $S$ - or impedance ( $Z$ ) data using standard conversion equations.<sup>20</sup> The transmission coefficient ( $S_{21}$ )  $S$ -parameter results obtained at room and 77 K temperatures are shown in Fig. 1(c). To ensure improved accuracy and reproducibility of the results, measurements were repeated several times and we used two probes. Instrument calibration was also done at the relevant temperatures. Making use of the transmission coefficient rather than the reflection coefficient ( $S_{11}$  or  $S_{22}$ ) is known to improve the accuracy because  $S_{12}$  or  $S_{21}$  have higher signal-to-noise ratio (SNR) compared to  $S_{11}$  or  $S_{22}$ , especially in cases when there is load mismatch.<sup>17</sup>

The sample DW2 has eleven individual DWNTs aligned across the waveguide gap, while sample DW1 has four DWNTs see Fig. 1(a). The average outer diameter of each DWNT was about 2.0 nm see Fig. 1(b) and Ref. 15. After subtracting the Open dummy signal, it is observed that the aligned DWNTs alone transmit on average 3 dB at room temperature and about 6 dB at 77 K. The maximum measurement uncertainty at high frequencies ( $\sim 50$  GHz) was about 0.06 dB, this translates into a SNR of about 50 dB at room temperature and is even higher at low temperature.<sup>17</sup> Such a high SNR is significant to make sensible conclusions about individual HF responses of CNTs especially after repeatable measurement. From Fig. 1(c), it is observed that the eleven DWNTs of DW2 transmit on average about 2 dB more power than the four DWNTs of DW1 device at higher frequencies. A reduction in temperature is evidently accompanied by approximately 9 dB increase in transmission at high frequencies. Furthermore, the low temperature data show transmission saturation at around 40 GHz, which is not observed in the room temperature data. To understand the significance of temperature on the transmission capabilities of the devices, the complex impedance was extracted as outlined earlier.

Figures 2(a)–2(c) show a general decrease of real impedance ( $Z$ ) with temperature particularly in the frequency range between 1 GHz and 25 GHz. This reduction in the resistive component of the impedance explains the increase in power transmission observed in Fig. 1(c). A comparative study of Figures 2(a)–2(c) shows a transition from capacitive (negative  $Z$ ) to inductive (positive  $Z$ ) behavior with a decrease in temperature. The implication of this capacitive to inductive transition can be understood through the realisation that the impedance of this quasi 1D transmission line (TL) network can be expressed as:

$$Z(\omega)^{-1} = \frac{i\omega C}{1 + i\omega RC - \omega^2 LC} + \frac{1}{R_0 + i\omega L_0}, \quad (3)$$

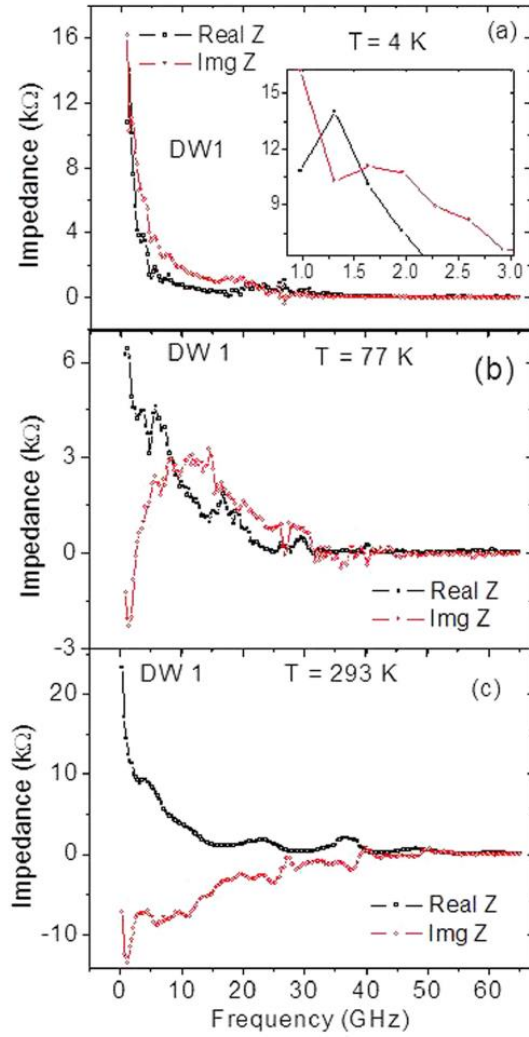


FIG. 2. Complex impedance of DW1 shows a transition from diffusive to ballistic transport (a) at about 1.5 GHz measured at 4 K. (b) at around 9 GHz measured at 77 K. (c) Room temperature measurements do not show any crossover to ballistic transport as was observed from other devices.

where  $R$ ,  $C$ , and  $L$  are the resistance, capacitance, and inductance of the TL, respectively.<sup>21</sup> When the impedance becomes inductive, it means  $LC \gg RC$ , and Eq. (3) reduces to  $Z(\omega) = R_0 + i\omega L_0$ .  $R_0$  can be regarded as the intrinsic CNT resistance plus the contact resistance. Now, using expressions for  $\sigma(\omega)$  and  $Z(\omega)$ , when the real impedance is equal to the imaginary impedance, this corresponds to the point when  $\omega\tau = 1$  if the contact resistance is neglected. This point will therefore signal the crossover point from diffusive  $\omega\tau < 1$  to ballistic transport  $\omega\tau > 1$ . Therefore, plotting the two parts of the impedance on the same axis we see the significance of the capacitive to inductive response as shown in Figs. 2(a)–2(c). Similar results were also observed for other samples (not shown here).<sup>22</sup> Figures 2(a) and 2(b) show transitions from diffusive to ballistic transport at 1.5 GHz and 9 GHz, which correspond to 106 ps and 17 ps of momentum scattering time, respectively, provided that the contact resistance is neglected.

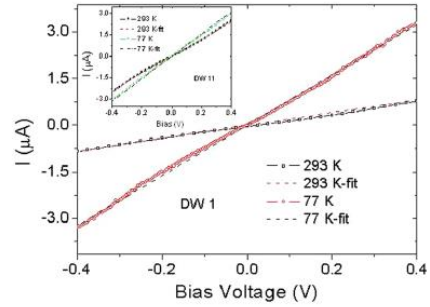


FIG. 3. I-V measurements for sample DW1 and DW11 (inset) fitted with the Landauer-Büttiker equation to determine the CNT – electrode coupling strength.

In the event of significant scattering in the CNTs, ballistic transport can still be realised when the scattering rate is less than the stimulus frequency.

In order to probe the origin of the capacitive to inductive transition as the temperature is reduced, we realise that previous theoretical<sup>9,23</sup> and experimental<sup>24–26</sup> works have predicted and observed a similar capacitive to inductive transition, which was explained in terms of the coupling strength between the electrodes and the CNT devices. To have an idea on this coupling, we fitted the two terminal I-V data with the Landauer-Büttiker formula in Eq. (1), see Fig. 3. The coupling strength of DW1 increased by 1.9 meV, by reducing the temperature to 77 K, similarly, for DW11 (one of the eleventh device with five CNTs), it increased by 1.2 meV. This increase is associated with a decrease in the contact resistance, and this probably explains the increase in high frequency transmission observed earlier in Fig. 1(a). To confirm this observation, we simulated the measured S-parameters using MATLAB RF Simulink package to determine the device parameters given in Fig. 4.

From the fitting of both the low temperature (Fig. 4, inset) and room temperature (Fig. 4) data, we observed a pronounced change in the contact resistance ( $R_3$  &  $R_2$  of Fig. 5) by reducing temperature. The results show a small change of the CNT intrinsic high frequency parameters ( $R_4$ ,  $L_1$ , and  $C_2$  of the equivalent circuit in Fig. 5) with temperature. The

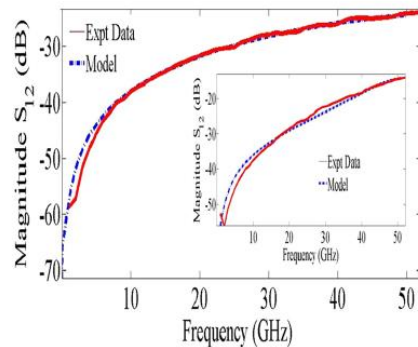


FIG. 4. The transmission coefficient  $S_{12}$  at 293 K for sample DW1, fitted with simulation model so as to determine the circuit parameters. Inset: The transmission coefficient  $S_{12}$  at 77 K for sample DW1, fitted with simulation model.



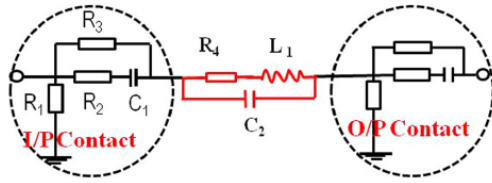


FIG. 5. Equivalent circuit model used for simulating the measured  $S$ -parameters.  $R_4$ ,  $L_1$ , and  $C_2$  are the intrinsic parameters of the CNTs.

TABLE I. The extracted circuit parameters from the fitting of DW1  $S$ -parameters.

Parameter	Value at $T = 293$ K	Value at $T = 77$ K
$R_1$ (M $\Omega$ )	10	10
$R_2$ ( $\Omega$ )	110	10
$R_3$ (k $\Omega$ )	90	90
$R_4$ (k $\Omega/\mu\text{m}$ )	1.2	0.4
$C_1$ (fF)	4.2	8
$C_2$ (fF/ $\mu\text{m}$ )	50	6
$L_1$ (nH/ $\mu\text{m}$ )	3.0	4.1

schematic circuit diagram in Fig. 5 was used to simulate the measured  $S$ -parameter results. Components  $R_3$  and  $R_2$  are associated with the contact and probe pad resistance.  $C_1$  is the contact capacitance and  $R_1$  is the signal-ground resistance. The contact circuit components were found to be symmetric for both input and output terminals as it was with the  $S$ -parameters results. Table I shows the extracted circuit component parameters from the fitting of Fig. 4. It can be seen that the simulation model fit slightly deviates from data at the low frequency regime particularly below 10 GHz of our devices. The exact reason for this is not yet clear but may be due to the fact that it is not easy to find a calibration technique with a very wide band frequency spectrum from 10 MHz to 65 GHz.

Our results in AC transport are consistent with previous DC measurements.<sup>5,10,11</sup> In the well-aligned tubes, current is parallel to the length of the tubes showing 1D transport instead of variable range hopping in three-dimensions. If the tubes are not perfectly aligned, the effect of the defect centres created at the overlapping points of the DWNTs may lead to 3D VRH transport. We have not seen any distinct effect of 3D VRH but only quasi-1D effect and therefore reveal that the tube-tube interactions is minimized here.

In conclusion, the reactive impedance of DWNTs show pronounced sensitivity to temperature changes resulting in a transition from capacitive to inductive response as the temperature is lowered. This crossover is due to a significant reduction in the contact resistance and thus enhancing the electrode-DWNT coupling. The implication of this is that the contact barrier and capacitance are reduced resulting in the crossover to inductive response and more power

transmission at low temperature. In this work, we have established an impedance crossover at low temperatures due to contact effects, and thus, device engineers may consider incorporation of this in their designs. We believe that this work further motivates renewed search for transparent contacts on carbon based materials, so that modern technology can make use of ballistic transport achievable in CNTs.

S.B. acknowledges CSIR-NLC rental pool for establishing the laser deposition technique in our laboratory and NRF(SA) for NNEP and nanotechnology flagship grants.

- <sup>1</sup>J. M. Bonard, T. Stora, J. P. Salvetat, F. Maier, T. Stoeckli, C. Duschl, L. Forro, W. A. de Heer, and A. Chatelaine, *Adv. Mater.* **9**, 827 (1997).
- <sup>2</sup>P. X. Hou, S. Bai, Q. H. Yang, C. Lui, and H. M. Cheng, *Carbon* **40**, 81 (2002).
- <sup>3</sup>P. Poncharal, C. Berger, Y. Yi, Z. L. Wang, and W. A. de Heer, *J. Phys. Chem. B* **106**, 12104 (2002).
- <sup>4</sup>S. Fratini and F. Guinea, *Phys. Rev. B* **77**, 195415 (2008).
- <sup>5</sup>C. L. Pint, Y. Q. Xu, E. Morosan, and R. H. Hauge, *Appl. Phys. Lett.* **94**, 182107 (2009).
- <sup>6</sup>G. Chimowa, M. Sendova, E. Flahaut, D. Churochkin, and S. Bhattacharyya, *J. Appl. Phys.* **110**, 123708 (2011).
- <sup>7</sup>S. Krishnan, H. Yilmaz, R. Vadapoo, and C. Marin, *Appl. Phys. Lett.* **97**, 163107 (2010).
- <sup>8</sup>T. Shimada and T. Sugai, *Appl. Phys. Lett.* **84**, 2412 (2004).
- <sup>9</sup>S. Pacchini, E. Flahaut, N. Fabre, V. Conedera, F. Mesnilgrete, F. Cocchetti, M. Dragon, and R. Plana, *Int. J. Microwave Wireless Tech.* **2**, 471 (2010).
- <sup>10</sup>X. He, N. Fujimura, J. M. Lloyd, K. J. Erickson, A. A. Talin, Q. Zhang, W. Gao, Q. Jiang, Y. Kawano, R. H. Hauge *et al.*, *Nano Lett.* **14**, 3953 (2014).
- <sup>11</sup>C. Zhang, K. Bets, S. S. Lee, Z. Sun, F. Mirri, V. L. Colvin, B. I. Yakobson, J. M. Tour, and R. H. Hauge, *ACS Nano* **6**, 6023 (2012).
- <sup>12</sup>P. J. Burke, *IEEE Trans. Nanotechnol.* **1**, 129 (2002).
- <sup>13</sup>S. Kang, P. J. Burke, L. N. Pfeiffer, and K. W. West, *Solid State Electron.* **48**, 2013 (2004).
- <sup>14</sup>S. Datta, *Electrical Transport in Mesoscopic Systems* (Cambridge University Press, Cambridge, UK, 1995).
- <sup>15</sup>E. Flahaut, R. Bacsa, A. Peigney, and Ch. Laurent, *Chem. Commun. (Cambridge)* **12**, 1442 (2003).
- <sup>16</sup>F. Seichepine, S. Salomon, M. Collet, S. Guillon, L. Nicu, G. Larrieu, E. Flahaut, and C. Vieu, *Nanotechnology* **23**, 095303 (2012).
- <sup>17</sup>See supplementary material at <http://dx.doi.org/10.1063/1.4901025> for finer experimental details and error analysis.
- <sup>18</sup>G. Chimowa and S. Bhattacharyya, *AIP Adv.* **4**, 087136 (2014).
- <sup>19</sup>Q. Liang, J. D. Cressler, G. Niu, Y. Lu, G. Freeman, D. C. Ahlgen, R. M. Malladi, K. Newton, and D. L. Harnome, *IEEE Trans. Microwave Theory Tech.* **51**, 2165 (2003).
- <sup>20</sup>D. M. Pozar, *Microwave Engineering*, 4th ed. (John Wiley & Sons Inc, 1998).
- <sup>21</sup>G. Cuniberti, M. Sasseti, and B. Kramer, *Phys. Rev. B* **57**, 1515 (1998).
- <sup>22</sup>G. Chimowa, "Dynamic electrical Transport in carbon nanotubes and nanodiamond films," Ph.D. thesis (University of the Witwatersrand, Johannesburg, South Africa, 2014).
- <sup>23</sup>T. Yamamoto, K. Sasaoka, and S. Watanabe, *Phys. Rev. B* **82**, 205404 (2010).
- <sup>24</sup>M. Tsutsui, K. Kuno, S. Kurokwa, and A. Sakai, *e-J. Surf. Sci. Nanotech.* **5**, 12 (2007).
- <sup>25</sup>V. K. Ksenevich, N. I. Gorbachuk, N. A. Poklonski, V. A. Samuilov, M. E. Kozlov, and A. D. Wieck, *Fullerenes, Nanotubes, Carbon Nanostruct.* **20**, 434 (2012).
- <sup>26</sup>L. Gomez-Rojas, S. Bhattacharyya, E. Mendoza, D. C. Cox, J. M. Rosolen, and S. R. P. Silva, *Nano Lett.* **7**, 2672 (2007).

## The effect of metal-contacts on carbon nanotube for high frequency interconnects and devices

George Chimowa and Somnath Bhattacharyya

*Nano-Scale Transport Physics laboratory and DST/NRF Centre of Excellence in Strong Materials, University of the Witwatersrand, P. Bag 3, Wits 2050, Johannesburg, South Africa*

(Received 7 March 2014; accepted 12 August 2014; published online 27 August 2014)

High frequency characterisation of platinum and tungsten contacts on individual multi-walled carbon nanotubes (MWNT) is performed from 10 MHz to 50 GHz. By measuring the scattering parameters of aligned individual MWNTs, we show that metal contacts enhance an inductive response due to the improved MWNT-electrode coupling reducing the capacitive effect. This behaviour is pronounced in the frequency below 10 GHz and strong for tungsten contacts. We explain the inductive response as a result of the interaction of stimulus current with the localized (or defects) states present at the contact region resulting in the current lagging behind the voltage. The results are further supported by direct current measurements that show tungsten to significantly increase carbon nanotube-electrode coupling. The immediate consequence is the reduction of the contact resistance, implying a reduction of electron tunnelling barrier from the electrode to the carbon nanotube. © 2014 Author(s). All article content, except where otherwise noted, is licensed under a Creative Commons Attribution 3.0 Unported License. [<http://dx.doi.org/10.1063/1.4894265>]

It is commonly believed that carbon based nano-materials such as carbon nanotubes (CNTs), graphene and nano-diamond films have the potential to replace and even out-perform silicon and copper, particularly in high frequency applications.<sup>1,2</sup> One of the major current challenges of these materials is the lack of understanding on their integration or interfacing to various materials used in industrial electronic devices. From electrical transport experiments of nano-materials, it is well accepted that the type of contacts affects significantly the measured conductance especially for a one dimensional system.<sup>3</sup> Today metallisation of carbon nano-materials is performed extensively using electron-beam (e-beam) lithography and has a tendency to deform, defect or even introduce additional electron states,<sup>4</sup> which will alter the behaviour of the device to alternating currents (AC).

In order to realise commercial applications of carbon based nano-devices operating in the very high frequency (GHz to THz) range and elevated temperatures understanding both the physics and technology of the electronic contacts has to be developed.<sup>5</sup> We note that a lot of work has been done in the development of carbon based devices operating in the direct current (DC) regime.<sup>6,7</sup> While the focus is now being extended to fast switching devices that promise to out shine those of current technology it goes without saying that full characterisation of the effect of nano-contacts must be accomplished.

The nature of contacts and chemical stability becomes crucial in the high frequency regime and at elevated temperatures. This perhaps, is not surprising because the type of contact determines the coupling between the one dimensional (1D) channel being measured and the electron reservoirs of the electrodes. Weak coupling will tend to promote tunnelling effects from the electrode to the 1D wire resulting in power law features of conductance with bias voltage.<sup>8</sup> In the high frequency regime the obvious consequences of weak coupling is an increase in load mismatch between the CNT device and waveguide/instrument normally set at  $50 \Omega$ <sup>9</sup> and hence significant damping of 1D plasmon waves. It is thus the objective of this work to give an insight on the effect of various contacts, such as platinum and tungsten, which have not been explored much at high frequency. Our choice of materials is guided by the fact that other noble metals such as gold and palladium

have been routinely investigated<sup>10,11</sup> and hence our objective is to look for other options. We seek for metals that can be used for sensor devices that operate at elevated temperatures and because tungsten and platinum have very high melting points than many others they do not suffer much from electron migration.<sup>12</sup> Furthermore theoretical calculations have previously suggested that the presence of *d*-states at the Fermi-level will improve electrode- CNT coupling,<sup>13</sup> and hence our choice of tungsten.

By using individual metallic multiwalled carbon nano-tubes (MWNTs), we show that tungsten makes better contacts than platinum for high frequency interconnects or devices. It offers superb coupling strength between the CNT and the electrodes observed from both DC and AC measurements. It (tungsten), however, suffers relatively higher microwave power loss dissipation. This kind of two fold perceptive has not been shown earlier. AC response can be probed by measuring scattering parameters, commonly known as simply S-parameters. The advantage of using this technique is that the complex impedance (*Z*) of the device can be easily determined which unveils the capacitive and inductive reactance from which quantum parameters (such as quantum capacitance and inductance) can be determined that dominants at small scales and high frequency.<sup>14</sup> This work shows that metallisation effects have adverse consequences in the frequency range below 10 GHz, above which it is insignificant. Such knowledge is important in the sense that, above this frequency the type of metal used for making contacts is less significant and hence produce some cost effective sub-THz devices.

A relatively easy technique was developed to assemble individual MWNTs on coplanar waveguides (CPW) for high frequency measurements which is summarised in the schematic diagram, in Fig. 1. The fabrication procedure involves alignment of MWNTs that were dispersed in dichlorobenzene on 1000  $\mu\text{m}$  long coplanar waveguides (CPW) with a 1  $\mu\text{m}$  gap, using dielectrophoresis. Nano-manipulators (Kleindiek- Germany) were used to select the MWNTs leaving only a single MWNT (average diameter of 70 nm to 100 nm) on each waveguide. A combination of e-beam lithography (Raith GmbH, ELPHY Quantum) and a gas injection system (GIS) [OmniGIS, Oxford Instruments] was used to make contacts in a scanning electron microscopy (SEM) [JEOL JEM7100F]. The S-parameters were measured using a network analyser (Agilent PNA- E8361C) on CPW with the aid of two ground-signal-ground (G-S-G) probe tips. Two probe measurements are better than single probe measurements because we make use of the transmission coefficient rather the reflection coefficient which has a lot of noise due to inherent load mismatch between device under test (DUT) and instrument. The measurements were done before and after metallisation at room temperature under vacuum ( $10^{-5}$  mbar), in a state-of-the-art (Janis) cryogenic micro-manipulated probe station in dark atmosphere. The actual SEM micrographs of some of the devices that were used for measurement are shown in figures 3(b)–3(e).

The stimulus power was set at -17 dBm for both probes which is equivalent to 31.6 mV so that the AC current is below saturation. Also to reduce random noise from the PNA, the intermediate frequency (IF) bandwidth was set at 500 Hz. PNA calibration was done using the short-open-load-thru (SOLT) by the GGB CS-15 calibration kit to set the reference of the signal at the probe tips and waveguide parasitic was extracted by using the open – short de-embedding method, see equation (1), where -1 implies the inverse of the matrix.<sup>15</sup>

$$Y_{DUT} = [(Y_{msd} - T_{open})^{-1} - (Y_{short} - Y_{open})^{-1}]^{-1} \quad (1)$$

Caution was exercised to ensure that the scattering parameter measurements are reproducible with minimum systematic and random errors due instrument drift and the contact force exerted by the HF probe onto the CPW. From a number of systematic checks we observed that the highest possible error is less than 0.4% of a dB in the transmitted scattering parameters we have provided additional supporting data to show the credibility of the measurements (see Ax 1). Tests were also done to check the effect of solvent used to disperse the MWNTs, which showed that it did not affect the measurements. DC measurements were conducted first before AC measurement and the results for some selected samples are given in Figs. 2(a) and 2(b).

The current-voltage (*I-V*) DC results, Fig. 2(a) show that tungsten contacts significantly lowers the total resistance ( $R_T = 2R_c + R_{CNT}$ ) of the device when compared to platinum (as seen from the gradients of the curves), where  $R_c$  is the contact resistance and  $R_{CNT}$  is the DC resistance of the

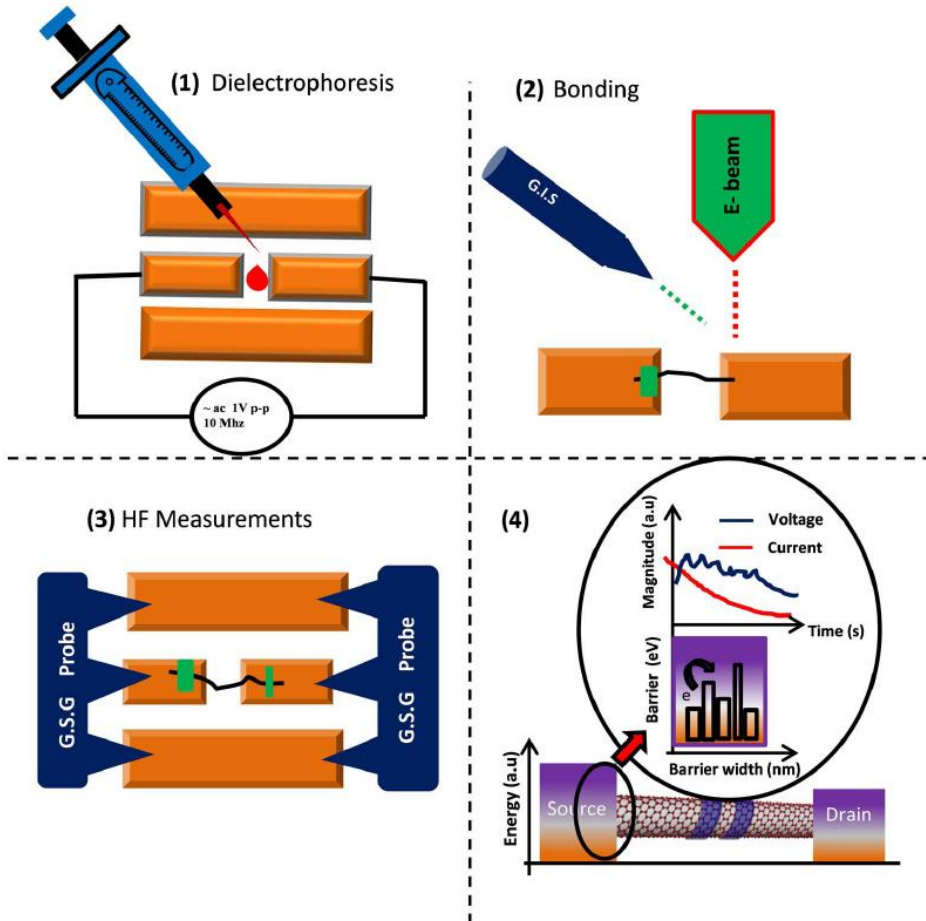


FIG. 1. Schematic diagram of the device fabrication process and the measurement setup. It consists of, (1) CNT alignment using dielectrophoresis, (2) CNT metal contact bonding using e-beam lithography and GIS and (3) HF impedance measurement using G-S-G probes with a  $50 \mu\text{m}$  pitch size. (4) Schematic diagram illustrating the CNT-Electrode configuration and the effects of the contacts to current and voltage.

CNT. From Landauer-Büttiker theory, electron transmission through CNT - electrode junction can be characterised by two important parameters,  $\Delta E$  and  $\Gamma$ , the energy difference of the CNT from electrode Fermi level and the strength of CNT- electrode coupling respectively.  $I$ - $V$  characteristics of such a two terminal set-up are given by equation (2), below.<sup>16</sup>

$$I(V) = \frac{2e}{h} \int_{-\infty}^{+\infty} \frac{\Gamma^2}{(E - \Delta E)^2 + \Gamma^2} \left[ f_F \left( E - E_F - \frac{eV}{2} \right) - f_F \left( E - E_F + \frac{eV}{2} \right) \right] dE \quad (2)$$

In this equation  $f_F$  and  $E_F$  are the Fermi distribution function and the Fermi energy, respectively. We fitted the  $I$ - $V$  data using this equation and thus we were able to determine the CNT-electrode coupling given in Table I. From the fitted data it can be seen that only one sample W2 –after contacts (afc) does not fit well above 0.6 V however, we are concerned with the coupling in the very low bias region about 31 mV comparable to the AC stimulus power for the high frequency measurements. Table I shows, that tungsten contacts increases the coupling strength between the electrodes and the CNT better than platinum. On average there is a 0.7 meV increase from tungsten compared to 0.2 meV from platinum contacts, this translates to lower contact resistance. A direct consequence of this is lower contact resistance and this can significantly change the whole transport mechanism

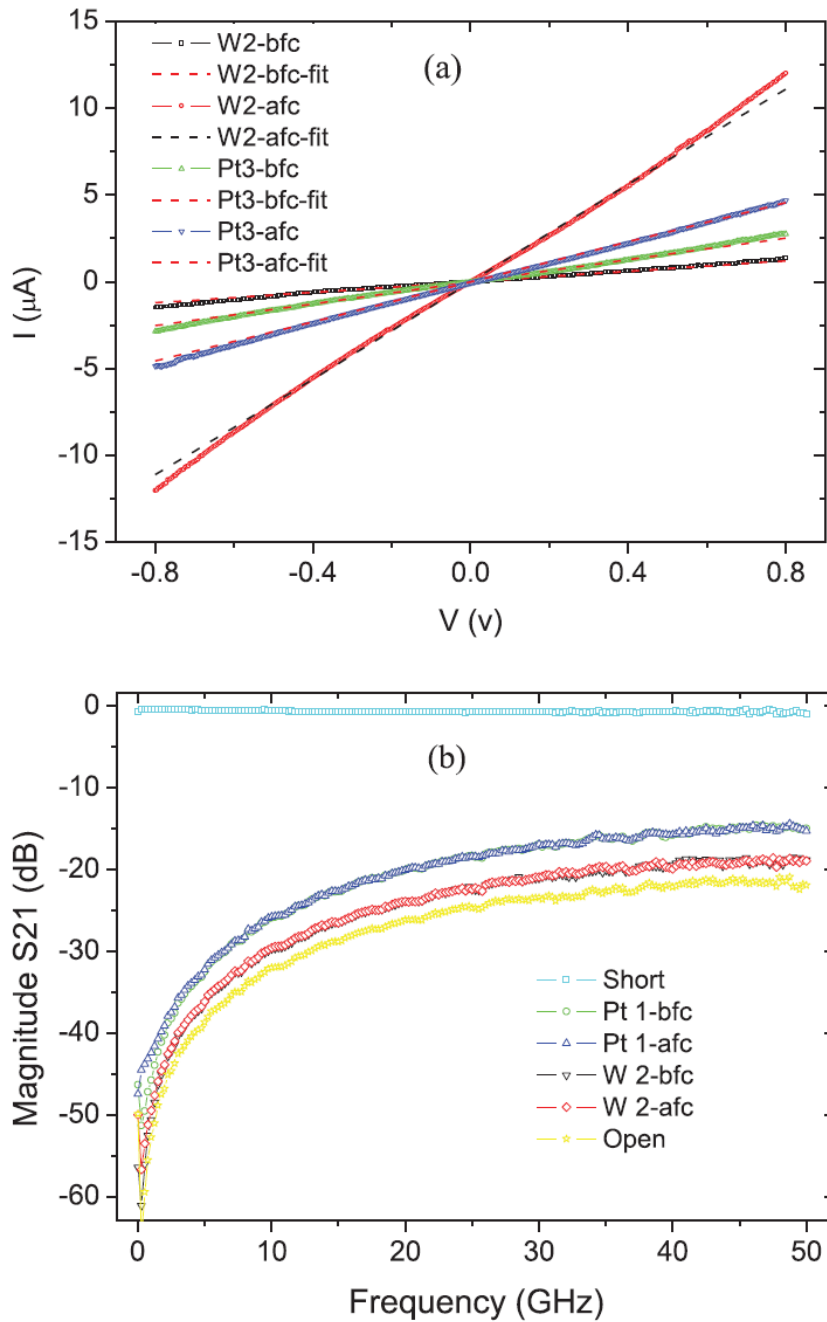


FIG. 2. (a) I-V data for a selected set of sample before (bfc) and after (afc) contact fabrication, the dotted lines are the respective fits. (b) Magnitude of  $S_{21}$  for platinum (Pt) and tungsten (W) samples measured before (bfc) and after (afc) the contacts were fabricated. The Short and Open data is for the thru waveguide and a blank waveguide respectively.

particularly the effect of electron tunnelling. The resistance values shown in table I, were obtained from the raw I-V data and not from the fit.

The magnitude of the transmission coefficient ( $S_{12}$ ) in Fig. 2(b) does not show much difference in the measurement before or after metallisation except that individual CNTs are responsible for about  $3 \pm 0.2$  dB of power transmitted before contacts are made. Considering that the signal to noise

TABLE I.  $\Gamma$  parameter obtained from the fitting of the I-V data before (bfc) and after (afc) metallisation together with total resistance ( $R_T$ ) obtained at 35 meV from the raw I-V data.

	$\Gamma$ (meV) bfc	$\Gamma$ (meV) afc	$R_T$ (k $\Omega$ ) bfc	$R_T$ (k $\Omega$ ) afc
Pt 2	0.92	1.13	80	20
Pt 3	0.78	1.05	404	242
W1	1.89	2.59	26	16
W2	0.65	1.65	707	78
W3	0.79	1.20	112	19

ratio is about 15 dB this amount of power is significant. Fig. 2(b) also shows the reproducibility of the measurements and transmission capability beyond 50 GHz for all MWNT devices. The short and open data is for the waveguide without a gap and with a gap (but with no CNT), respectively. This data (open and short) is used to de-embed the parasitic effects of the waveguide. The phase of the transmission coefficient however, shows a maximum phase change of about  $20^\circ$  after metallisation below 10 GHz giving a hint on the effect of the contacts [see Fig. 3(a)].

The imaginary component of the impedance was then calculated after de-embedding waveguide parasitic which is shown in Fig. 4(a) and 4(b) for different samples. They show that metal contacts enhance a transition from capacitive to inductive response, with tungsten having the largest effect. Our explanation is that the metal contacts improve the CNT–electrode coupling resulting in the suppression of the capacitive response (caused by the difference in work function of the gold electrode and the MWNT) and enhancing the inductive behaviour. This is supported by the DC *I-V* measurements that show improvement of the coupling strength after metallisation. We then explain the inductive response on e-beam fabricated contacts as follows. Lithography techniques are known to induce some defects on the CNTs at the contact regions.<sup>17</sup> This will result in additional states (which we may call “defect states”) at the contact barrier ends of the MWNTs that interact with the stimulus current resulting in the current lagging behind the voltage and hence the inductive behaviour [see Figs. 1–4].

The process can be envisioned as defects on the CNTs and contact metal introducing multiple energy barriers of different widths and heights which result in the current lagging behind voltage as it overcomes the barriers as shown by the schematic diagram Figs. 1–4. In this context it would imply that tungsten introduces more states by virtue of its electronic configuration (i.e. unoccupied *d*-states) and also from the defects it causes. As the frequency of the stimulus is increased localisation of these states at the contacts begins to take effect. This happens as the rate of the charge carrier transfer from the electrode to the MWNT becomes less than the frequency of the stimulus resulting in localisation of the defect states, which also reduces the power transmission through the devices. To explain the physical behaviour we say the initial decrease of capacitance (together with the decrease of the resistance) at the low frequency region is governed by the Mott variable range hopping transport. The capacitive–inductive crossover with the increase of frequency can be explained by the Drude formula where the electronic scattering time governs the electronic transport like other metallic systems. The physics of plane waves showing plane wave solutions for current and voltage can explain the overall frequency dependent features. The resonant frequency of the device can be determined by the analysis of an LCR circuit by adjusting the L and R values. However, we realize that a proper analysis of the impedance variation over the whole frequency regime in this confined CNT system between two contacts is potentially rigorous which needs the inclusion of damping parameters. Therefore, we present this simple model (which applies to other devices as well) to explain how CNT- electrode coupling significantly affects the RF response of CNT devices.

Associated with the CNT – electrode contact barrier is the microwave power dissipation that happens in the device. This fact is illustrated in the graphs of Fig. 5, which show that after metal contacts the fractional power loss increases by a factor of 1.5% for tungsten and by 0.8% for platinum at 5 GHz for an individual tube. The microwave power dissipation, as a fraction of the input power,

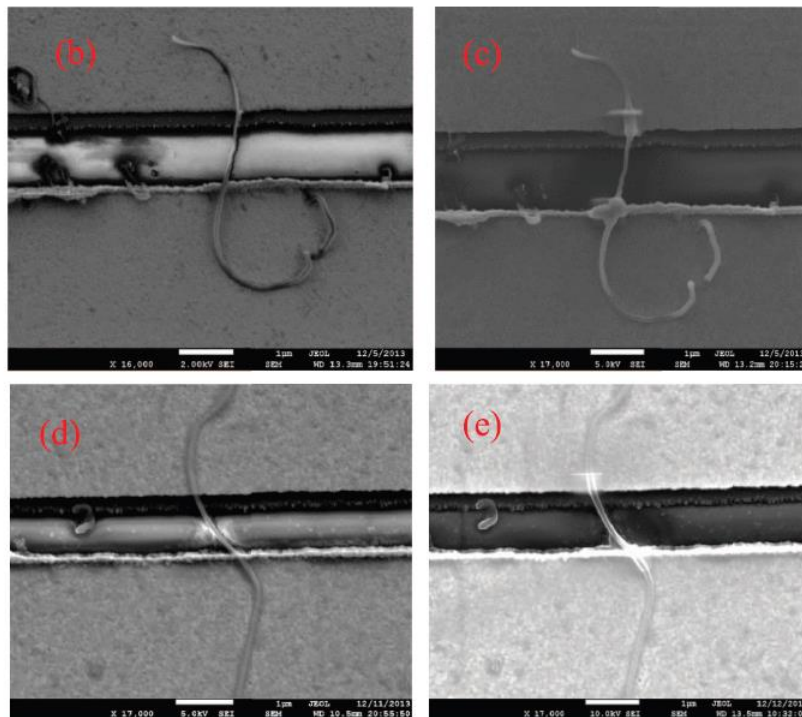
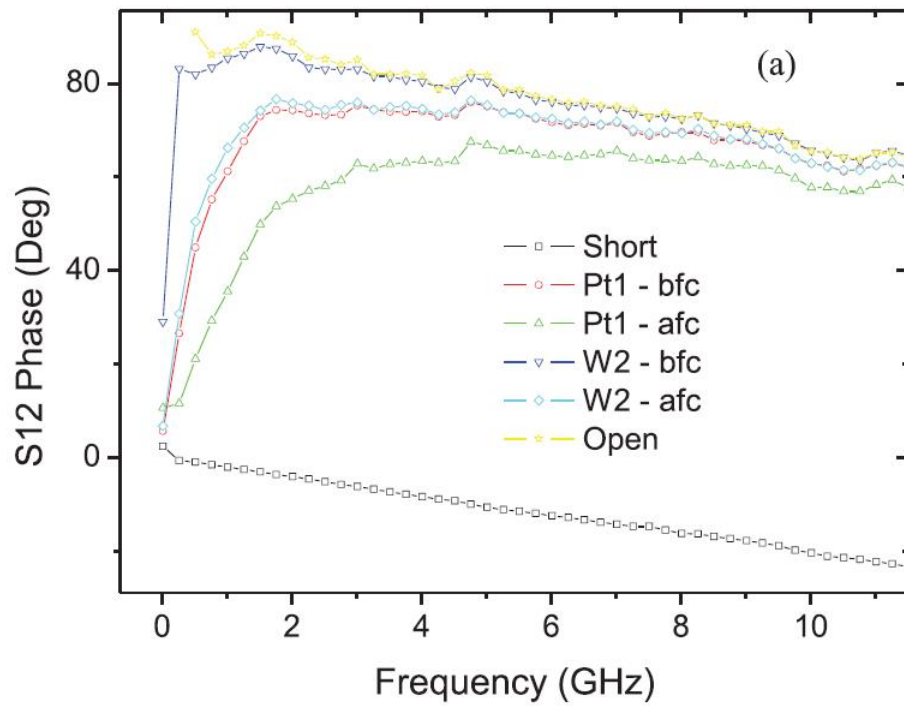
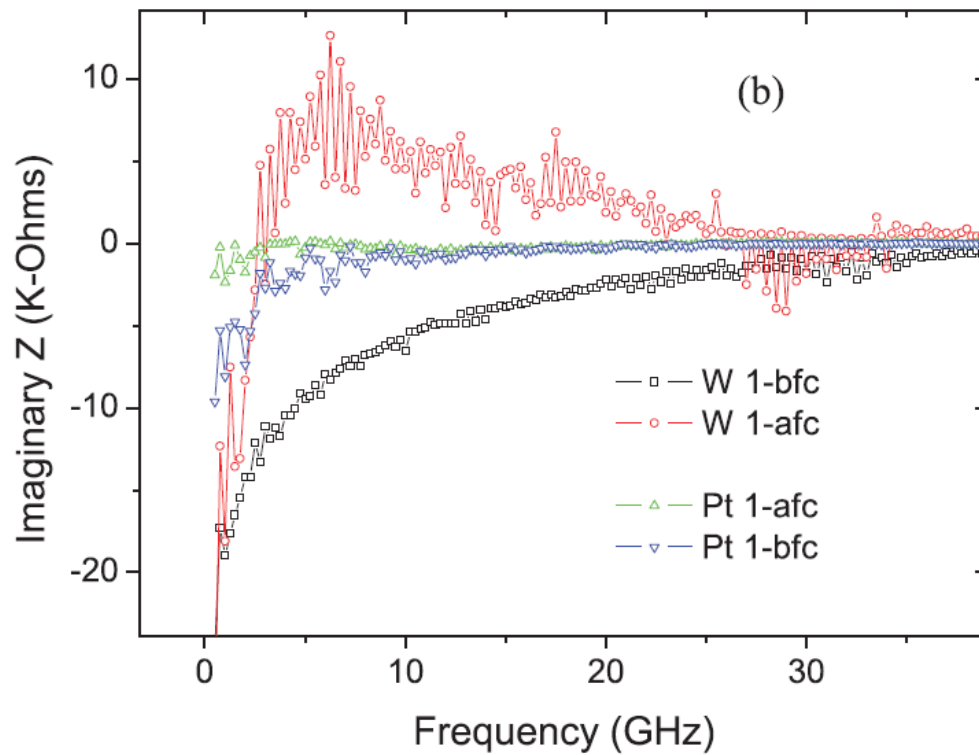
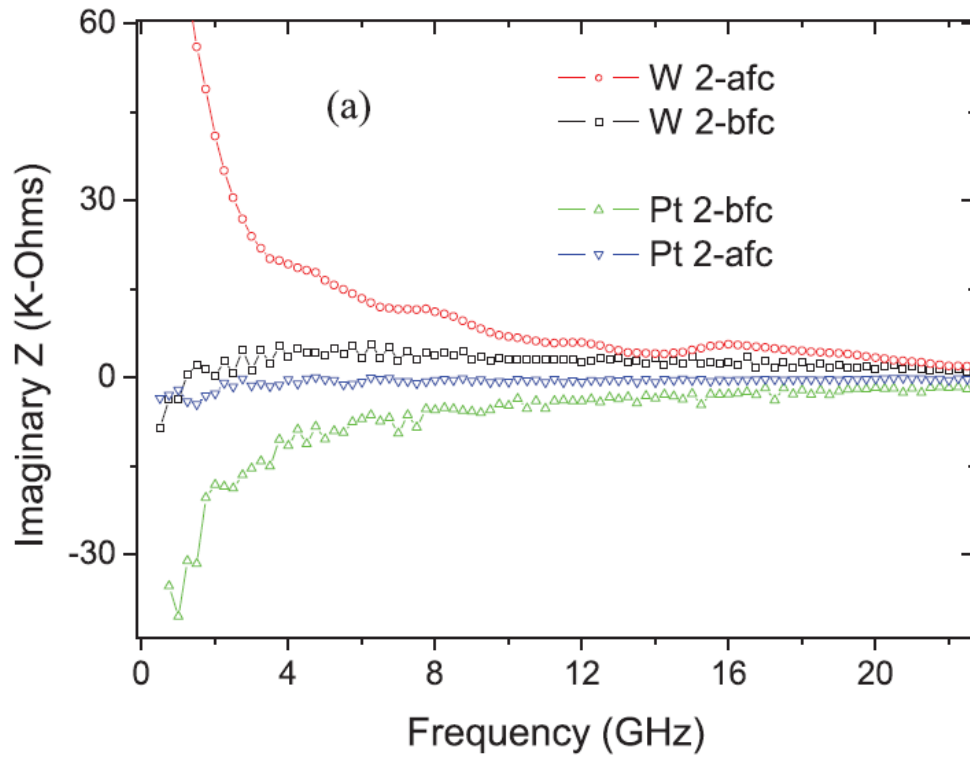


FIG. 3. (a) The phase of S12 for MWNTs measured before (bfc) and after (afc) platinum or tungsten contacts were fabricated. (b and c) SEM images of the Pt 1 sample before and after contacts fabrication, (d-e) SEM images of the W-2 sample before and after contacts fabrication.





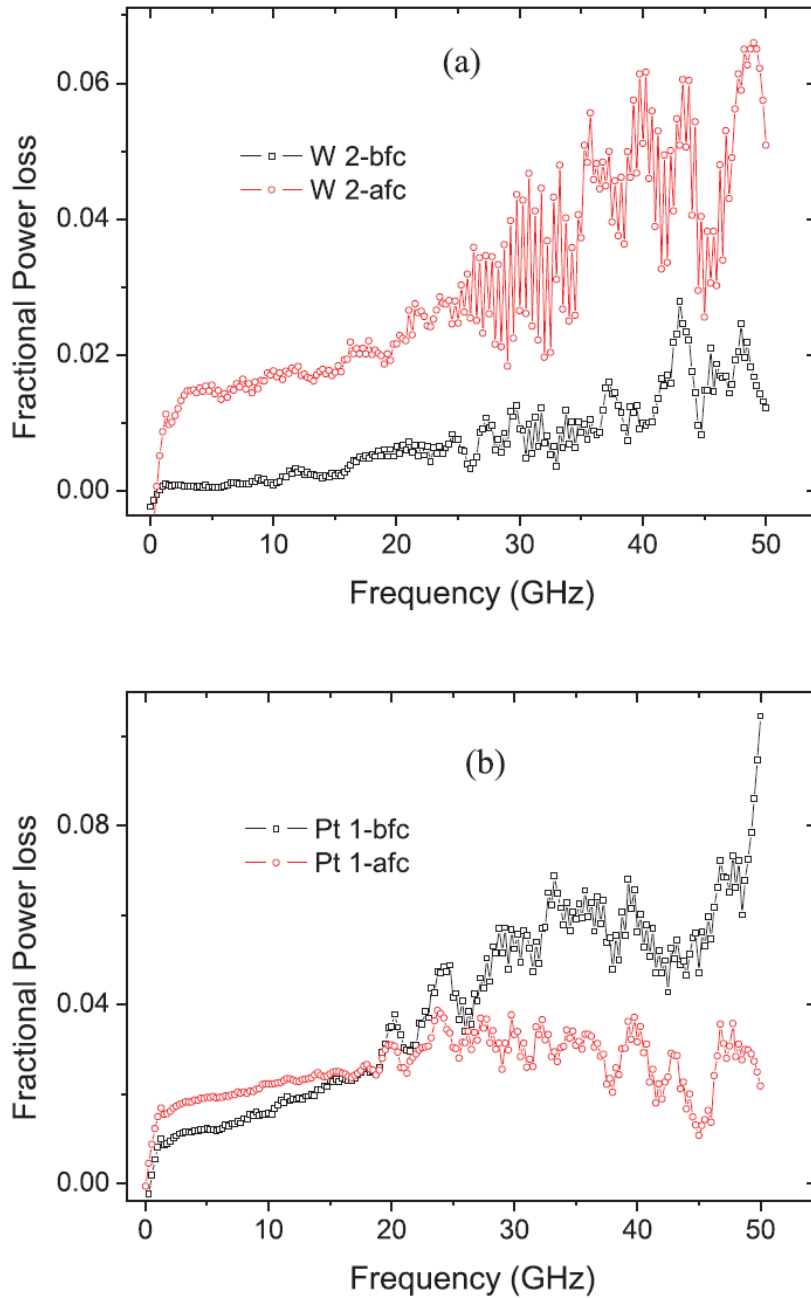


FIG. 5. Fractional power loss relative to that of the Open waveguide for (a) Tungsten contacted sample and (b) Platinum contacted sample.

i.e  $P_{loss-cnt} = P_{loss-dut} - P_{loss-open-cpw}$ . In this way the parasitic effects of the waveguide are eliminated.

We also note that the power loss increases with frequency for tungsten contacted MWNTs although the data becomes noise above 20 GHz most probably due to the noise factor of S11 caused by the reflection from the waveguide itself. The fractional power loss in platinum contacted MWNTs, increases and then decrease with frequency above 20 GHz and the explanation for this is still not yet

understood but may probably suggests the dominates of the inductive component over the resistive part of the device which would store up energy.

From two probe S-parameter measurements we have shown that metal contacts significantly enhance an inductive behaviour on CNT devices or interconnects that is dominant below the 10 GHz threshold. This inductive response appears to be accompanied by an increase in microwave fractional power loss from the MWNT especially for tungsten contacted devices. The results were supported by DC measurements that further showed that tungsten significantly improves the electrode-CNT coupling possibly because of the availability of unoccupied *d*-states, and this reduced the contact resistance. This knowledge means that above 10 GHz, the choice of contacts is wider making the cost of devices that would operate in that regime cheaper.

## ACKNOWLEDGMENTS

G.C. would like to thank George Bepete for the multi-walled carbon nanotubes and Ross McIntosh for valuable discussions. S.B. acknowledges South African-NRF for the Nanotechnology flagship project and CSIR-National Laser Centre for supporting this project.

- <sup>1</sup> C. Kocabas, S. Dunham, Q. Cao, K. Cimino, X. Ho, H. Kim, D. Dawson, J. Payne, M. Stuenkel, and H. Zhang, *Nano. Lett.* **9**, 1937 (2009).
- <sup>2</sup> O. S. Koswatta, A. Valdes-Garcia, M. B. Steiner, Y. M. Lin, and P. Avouris, *IEEE Trans. on MW theory and Tech.* **59**, 2739 (2011).
- <sup>3</sup> P. Rice, T. M. Wallis, S. E. Russek, and P. Kabos, *Nano. Lett.* **7**, 1086 (2007).
- <sup>4</sup> B. W. Smith and D. E. Luzzi, *J. App. Phys.* **90**, 3509 (2001).
- <sup>5</sup> S. C. Jun, *Nanotechnology* **18**, 255701 (2007).
- <sup>6</sup> J. Nygard, D. H. Cobden, M. Bockrath, P. L. McEuen, and P. E. Lindelof, *Appl. Phys. A* **69**, 297 (1999).
- <sup>7</sup> M. Monteverde *et al.*, *Phys. Rev. Lett.* **97**, 176401–1 (2006).
- <sup>8</sup> T. Kanbara, T. Takenobu, T. Takahashi, Y. Iwasa, K. Tsukagoshi, Y. Aoyagi, and H. Kataura, *App. Phys. Lett.* **88**, 053118 (2006).
- <sup>9</sup> P. J. Burke, *IEEE on NanoTech.* **1**, 129 (2002).
- <sup>10</sup> Ch. Caillier, A. Ayari, V. Gouttenoire, A. S. Miguel, V. Jourdain, M. Picher, and J. L. Sauvajol, *App. Phys. Lett.* **97**, 173111 (2010).
- <sup>11</sup> D. Mann, A. Javey, J. Kong, Q. Wang, and H. Dai, *Nano Lett.* **3**, 1541 (2003).
- <sup>12</sup> M. S. Haque, N. L. Rupensinghe, S. Z. Ali, I. Haneef, S. Maeng, J. Park, F. Udrea, and W. I. Milne, *Nanotechnology* **19**, 025607 (2008).
- <sup>13</sup> J. J. Palacios, A. J. Perez-Jimenez, E. Louis, E. San Fabian, and J. A. Verges, *Phys. Rev. Lett.* **90**, 106801 (2003).
- <sup>14</sup> S. Ilani, L. A. K. Donev, M. Kindermann, and P. L. McEuen, *Nature. Phys.* **2**, 687 (2006).
- <sup>15</sup> Q. Liang, J. D. Cressler, G. Niu, Y. Lu, G. Freeman, D. C. Ahlgren, R. M. Malladi, K. Newton, and D. L. Harnage, *IEEE Trans on Microwave theory and Tech.* **51**, 2165 (2003).
- <sup>16</sup> S. Datta, *Electrical transport in Mesoscopic systems* (Cambridge University Press, Cambridge UK 1995).
- <sup>17</sup> P. Poncharal, C. Berger, Y. Yi, Z. L. Wang, and W. A. de Heer, *J. Phys. Chem. B* **106**, 12104 (2002).
- <sup>18</sup> C. Highstrete, E. A. Shaner, M. Lee, F. E. Jones, P. M. Dentinger, and A. A. Talin, *App. Phys. Lett.* **89**, 173105 (2006).

## Conductivity crossover in nano-crystalline diamond films: Realization of a disordered superlattice-like structure

GEORGE CHIMOWA, DIMITRY CHUROCHKIN and SOMNATH BHATTACHARYYA<sup>(a)</sup>

*Nano-Scale Transport Physics Laboratory, School of Physics and DST/NRF Centre of Excellence in Strong Materials, University of the Witwatersrand - Private Bag 3, WITS 2050, Johannesburg, South Africa*

received 24 April 2012; accepted in final form 25 June 2012

published online 27 July 2012

PACS 73.43.Qt – Magnetoresistance

PACS 73.20.Fz – Weak or Anderson localization

**Abstract** – We present the electrical transport characteristics of a batch of nano-crystalline diamond films of varying nitrogen concentrations and explain the conduction mechanism by the disordered quasi-superlattice model applied to semiconductor heterostructures. Synthesized by the hot-filament chemical-vapour deposition technique, the degree of structural disorder in the films, confirmed from Raman spectroscopy, is found to be controllable, resulting in the transition of conduction mechanism from localized and activated to the metallic conduction regime. Hence through high-field magneto-resistance measurements at low temperatures we firmly establish a conductivity crossover from hopping to 3D weak localization. The long electronic dephasing time and its weak temperature dependence suggest the possibility for diamond-based high-speed device applications.

Copyright © EPLA, 2012

**Introduction.** – Nitrogen-doped ultranano-crystalline diamond (UNCD) films prepared by microwave plasma-enhanced chemical-vapor deposition (MPCVD) have been studied extensively and found to be very promising in nano-electronic device applications [1,2]. Generally, the conductivity of these films can be controlled to some extent with the increase of nitrogen level [3] however, it has appeared to be very different from conventional semiconductors. Further studies are therefore required in order to establish the (nitrogen) doping mechanism in these films [4]. Previous studies by researchers on heavily nitrogen-doped UNCD films prepared by MPCVD showed metallic behavior along with negative magneto-resistance (MR) features explained using the 2D weak localization (WL) or hopping model [1,2,5]. In this article we report activated conduction over a wide range of temperatures which has not been demonstrated previously, but it is now observed in NCD samples grown by the hot-filament chemical-vapor deposition (HFCVD) technique.

Inclusion of amorphous carbon in nano-diamond films increases the density of localized states in the band gap and makes the hopping processes dominant in these materials [6]. This observation clearly emphasizes the

importance of the  $sp^2$  phases in the grain boundaries (GB) [6], which depend significantly on the gas chemistry during synthesis. Furthermore, detailed microscopic studies in UNCD films by other researchers have suggested a superlattice-like structure consisting of layers of  $sp^2$ -bonded carbon within the GB separated by diamond grains [7,8]. We extended the idea of previous researchers and employed a disordered quasi-superlattice model that was applied previously to semiconductor heterostructures, which is discussed later. While a great deal of attention has been given to synthesis, microstructure and morphology studies, little has been reported on the low-temperature transport properties of nitrogen-doped NCD films grown particularly by HFCVD [9]. In this work we therefore attempt to explain the electrical transport properties of these HFCVD films (whose grain boundary is different from MPCVD films because of the different gas chemistry) and establish the validity of the recently reported anisotropic 3D WL model in nitrogen-doped nano-crystalline diamond films synthesized by methods other than MPCVD [10]. We report a transition from hopping to activated conduction and finally an anisotropic 3D WL mechanism in the transport properties of the films, as the nitrogen percentage in the HFCVD chamber is increased. With the help of a disordered superlattice model and microstructure studies using Raman

<sup>(a)</sup>E-mail: somnath.bhattacharyya@wits.ac.za

spectroscopy we show how disorder controls the conductivity and the characteristic dephasing time of NCD films.

**Experimental techniques.** – The nitrogen-incorporated nano-crystalline diamond films were synthesized in a commercial HFCVD chamber (Vacutec, SA) at a substrate temperature of approximately 800 °C by introducing 10% to 22% ultra-pure nitrogen (99.999%) in the reaction zone, which are labeled NCD10N<sub>2</sub>, NCD15N<sub>2</sub>, NCD20N<sub>2</sub> and NCD22N<sub>2</sub>. The other reaction gases were methane kept at (4.5%), hydrogen and variable argon concentrations. The argon flow was varied according to the nitrogen flow rate so as to keep the total volume flow at 210 sccm. The low pressure (22 mbar) and relatively high methane concentration lead to the formation of nano-scale grains, possibly due to the high renucleation rate [9]. Four probe conductivity-temperature measurements of these samples (0.4 cm × 0.3 cm, thickness ~ 0.165 μm) deposited on fused-quartz substrates were performed in the temperature range from 2.3 K to 300 K and applying a magnetic field up to 12 T using a fully automated cryogenic free measurement system. A current of 10 μA was sourced from a Keithly 2400 and the voltage was measured using a Keithly 2182A nano-voltmeter using the van der Pauw configuration. The Raman spectroscopy was performed using an argon ion laser (514.5 nm) at an average power of ~1 mW. Details of the NCD film preparation and microscopic characterization are given elsewhere [11].

**Results and discussion.** – It is evident from the Raman spectra (fig. 1(a)) that nitrogen introduction in the chamber significantly reduces the intensity of the diamond peak at (1332 cm<sup>-1</sup>), which is an indication of the increase of the width of the grain boundary regions in the films. Figure 1(b) also shows the change of the Raman *G* peak width with N<sub>2</sub> percentage (N<sub>2</sub>%) used for the synthesis of NCD films, which is an estimation of the disorder level in the films [12]. Although disorder initially increases with the N<sub>2</sub>%, it decreases rapidly in the high N<sub>2</sub>% regime as observed in the Raman spectra of the samples. The conductance of the samples shows an increase with N<sub>2</sub>% in fig. 1(c). The corresponding change of disorder parameter (*q*) is explained from the analysis of conductance data later on in the text. Transmission electron micrographs indicated that the grain sizes are in the range from 15 to 20 nm [11].

**Electrical transport:** Figures 2(a) and (b) show three distinct behaviors at low temperatures namely, weakly conducting (for NCD10N<sub>2</sub> and NCD15N<sub>2</sub>), semiconducting (NCD20N<sub>2</sub>) and semi-metallic (NCD22N<sub>2</sub>) films, respectively. To understand the transport mechanism, plots of  $\ln R$  vs.  $T^{-\chi}$  were done (not shown here), with  $\chi$  being 1/2, 1/3 or 1/4 for 1D, 2D or 3D hopping, respectively. The analysis showed that 3D VRH hopping is applicable for both NCD10N<sub>2</sub> and NCD15N<sub>2</sub> samples

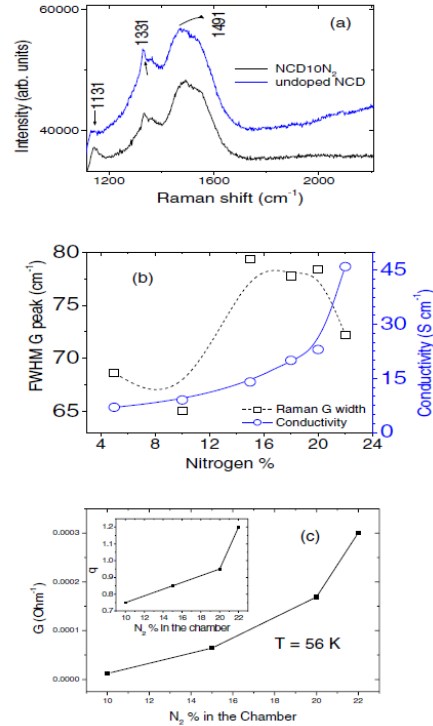


Fig. 1: (Colour on-line) (a) Raman spectra for doped and undoped nano-diamond films prepared by the HFCVD technique. (b) Variation of the *G* linewidth with nitrogen concentration in the film deposition chamber. (c) Conductance dependence on N<sub>2</sub>% in the chamber shows a continuous increase. The insert shows the variation of the disorder parameter *q* with N<sub>2</sub>%.

below 118 K. The Arrhenius plots for all the films in fig. 2(b) clearly show evidence of activated conduction from 28 K to 89 K for the NCD20N<sub>2</sub> films.

This thermally activated conduction is normally expressed in the form of the Arrhenius equation as  $\sigma(0, T) = \sigma_0 \exp(-\frac{\Delta E}{kT})$ , where  $\Delta E$  is the conductivity activation energy and  $\sigma_0$  is the conductivity prefactor [13]. The activation energy calculated from fig. 2(b) is found to be less than 10 meV. The origin of the energy gap can be explained from the effect of disorder on the nitrogen donor level formed close to the conduction band. The hopping mechanism and activated behaviour were not found to be applicable for NCD22N<sub>2</sub> films. In earlier reports, N-UNCVD films were treated as disordered metals or bulk amorphous semiconductors where confinement properties in GB were not included [4,5]. Here, we interpret the transport in the family of NCD films of different conductivity using a quasi-SL structure. Figure 2(a) shows the conductance-*vs.*-temperature (*G-T*) data fitted with eq. (1). In the conventional 3D WL isotropic model the temperature

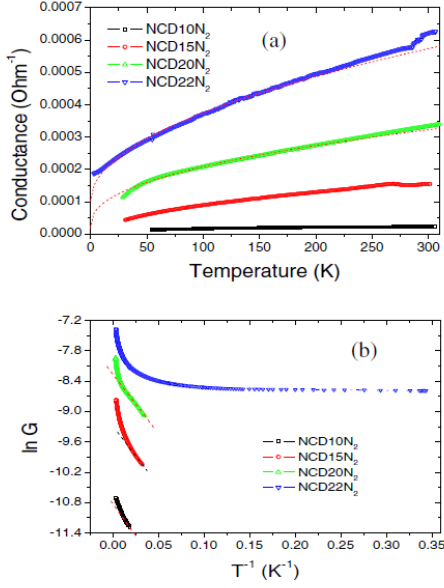


Fig. 2: (Colour on-line) (a) Conductance *vs.*  $T$  fitted with the 3D WL model for NCD films (dotted lines). (b) Arrhenius plot for  $G(T)$  to validate activated conduction.

dependence of the conductance ( $G$ ) is expressed as a sum of the temperature-independent term ( $G_0$ ) as well as the terms consisting of the temperature dependence of the dephasing length and 3D electron-electron ( $e$ - $e$ ) interaction given by

$$G(0, T) = G_0 + a_1 T^{0.35} + a_2 T^{0.5}, \quad (1)$$

where  $a_1 = \frac{S}{l} (e^2/2\pi^2 \hbar L_\phi)$  and  $a_2 = \frac{S}{l} \left( \frac{e^2}{4\hbar\pi^2} \right) \left( \frac{1.3}{\sqrt{2}} \right) \times \left( \frac{4}{3} - \frac{3}{2} F \right) \sqrt{(k_B/\hbar D)}$ , are pre-factors that depend on sample dimensions given on page 2 ( $S$ , cross-sectional area and  $l$ , length), dephasing length ( $L_\phi$ ) and diffusion constant ( $D$ ) [14]. The terms  $F$ ,  $\tau$ , and  $D$  represent the electron screening factor in 3D, the relaxation time for the  $e$ - $e$  interactions, and the diffusion constant, respectively [14]. From the fitting of  $G$ - $T$  data (fig. 2(a)) the values of  $a_1$  and  $a_2$  were evaluated from which  $L_\phi$  can be derived as  $\sim 1.12 \times 10^{-8} T^{-0.33}$  (m) for NCD20N<sub>2</sub> and  $\sim 3.89 \times 10^{-8} T^{-0.35}$  (m) for NCD22N<sub>2</sub> films. Furthermore the weak temperature dependence of the dephasing factor compared to the  $e$ - $e$  interaction in eq. (1) shows that in the semi-metallic regime,  $e$ - $e$  interactions dominate over the quantum interference. These observations are supported by theoretical work by other researchers who predicted the contribution of the nitrogen-related centres to the conductivity by determining the electronic structures of several nitrogen centres (defect centres) in nano-diamond films [6,7]. Here we present a detailed explanation of the conduction in  $n$ -NCD films, in the context of a disordered superlattice-like structure.

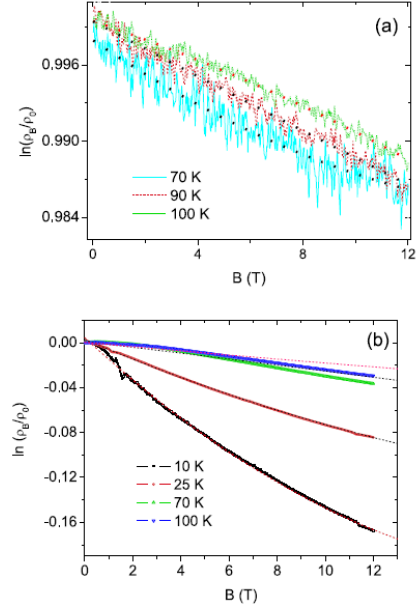


Fig. 3: (Colour on-line) (a)  $\ln(\rho_B/\rho_0)$ -*vs.*- $B$  graph for NCD10N<sub>2</sub> films and (b) NCD15N<sub>2</sub> films fitted with eq. (2) to evaluate the localization lengths.

*Magneto-resistance:* MR features in figs. 3(a) and (b) for NCD10N<sub>2</sub> and NCD15N<sub>2</sub>, respectively, are found to be very weakly  $B$  dependent. At high  $T$  the MR is found to be linear with  $B$ , which is consistent with the 3D VRH mechanism. This confirms the applicability of the VRH mechanism suggested earlier for the weakly conducting samples. The MR data were fitted with eq. (2),

$$\ln\left(\frac{\rho_B}{\rho_0}\right) = -a_1 B + a_2 B^2 + a_3, \quad (2)$$

and using the constant  $T_0$ , the localization length was obtained for NCD10N<sub>2</sub> samples to be 11.98 nm at 100 K. The parameters  $a_1 = N L_c^5 \left( \frac{T_0}{T} \right)^{P1} (e/\hbar)$ ,  $a_2 = \left( \frac{5e^2 L_c^4}{2016 \hbar^2} \right) \left( \frac{T_0}{T} \right)^{P2}$  and  $a_3$  account for the complex behavior of MR at  $B$ . The indexes  $P1$  and  $P2$  are 7/8 and 3/4, respectively in the Mott VRH model [15]. These results are consistent with a previous report on MPCVD-UNCD samples prepared with approximately 1% nitrogen [4]. At present we have observed a transition from VRH to activated conduction with increase in nitrogen percentage, which suggests band modification in these films as a result of nitrogen incorporation and associated structural rearrangement of carbon atoms in the grain boundaries.

The MR data (fig. 3(b)) for NCD15N<sub>2</sub> samples show a clear deviation from the VRH fit at temperatures above 50 K. We estimated the  $N(E_F) \sim 2.54 \times 10^{19} \text{ eV}^{-1} \text{ cm}^{-3}$  at 100 K with the value of  $L_c \sim 11.9$  nm, which is

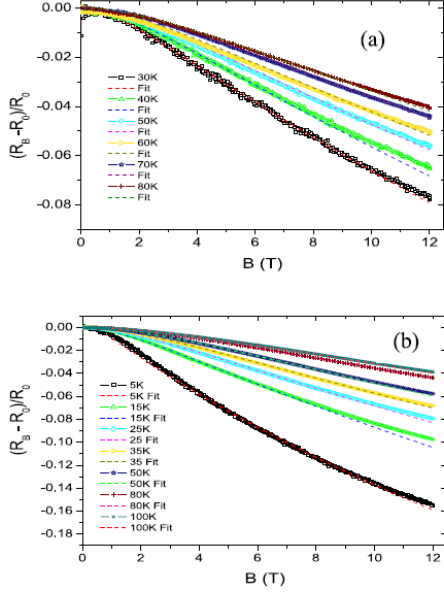


Fig. 4: (Colour on-line) MR results with 3D WL anisotropic fitting for (a) NCD20N<sub>2</sub> and (b) NCD22N<sub>2</sub> films.

slightly greater than  $6.46 \times 10^{18} \text{ eV}^{-1} \text{ cm}^{-3}$  obtained for NCD10N<sub>2</sub> samples. These results are consistent with the observation of increase of conductivity in the films prepared with higher N<sub>2</sub>% (see fig. 1(b)).

Analysis of the NCD22N<sub>2</sub> MR data showed a  $B^{1/2}$  dependence of the MR at high fields, which is characteristic of 3D WL [16,17]. This is in agreement with the reports by other researchers that have indicated a  $B^{1/2}$  or  $B^2$  dependence of MR for UNCD films [10]. The magnitude of this MR decreases with an increase in temperature indicating that WL effects are suppressed at high temperatures in these films. We further attempt to validate the recently reported 3D WL anisotropic model used to explain the conductivity in nano-diamond films [10]. This behavior has been explained in terms of a propagative Fermi surface (PFS).

The PFS model was originally developed to explain transport in disordered artificial SL and was recently used to explain the unusual transport in nano-crystalline silicon films in the diffusive Fermi surface (DFS) limit considering an effective artificially formed SL structure [18]. The behavior is given by

$$\Delta\sigma(B)/\sigma(0, T) = \alpha \left[ \sigma(0, T) \left( \frac{e^2}{2\hbar\pi^2} \right) \left( \frac{eB}{\hbar} \right)^{1/2} \right] f_3 \left[ \frac{\hbar/eB}{4D\tau_\phi} \right]. \quad (3)$$

The function  $f_3$  is the Kawabata function [16]. The anisotropy coefficient  $\alpha = \sqrt{D_{\parallel}/D_{\perp}}$  describes anisotropic transport in 3D, where  $D_{\parallel}$  and  $D_{\perp}$  represent the diffusion coefficient parallel and perpendicular to the film,

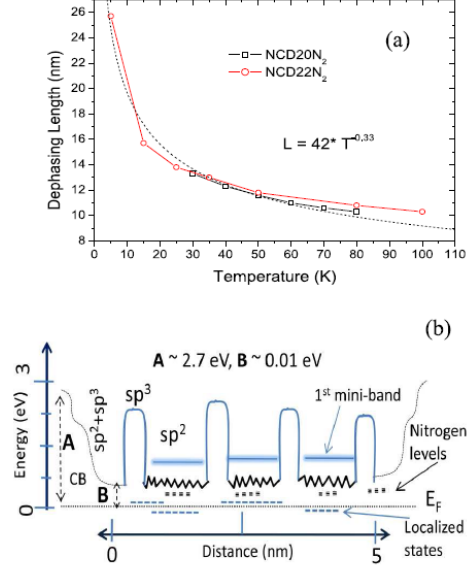


Fig. 5: (Colour on-line) (a) The temperature dependence of the dephasing length for NCD20N<sub>2</sub> and NCD22N<sub>2</sub> samples, *i.e.*,  $L_{\phi} \sim T^{-0.33}$  (see dotted lines). (b) Band energy diagram of NCD films shows disordered  $sp^2$  layers separated by local ( $sp^3$ ) barriers within the GB between two diamond grains. The typical energy levels of localized states and nitrogen levels are marked in the diagram.

respectively. This function predicts a  $B^2$  dependence at low fields and a  $B^{1/2}$  one at high fields. Normalized MR data fitted with eq. (3) confirms that the 3D WL anisotropic model best describes the MR ( $B, T$ ) behavior for NCD20N<sub>2</sub> and NCD22N<sub>2</sub> films see (figs. 4(a) and (b)). The anisotropic coefficient was found to be 1.5 for the NCD20N<sub>2</sub> and 2.1 for the NCD22N<sub>2</sub> films. Our analysis indicates that the anisotropy factor is less in weakly conducting films than in highly conducting films, which is in agreement with previous reports [18]. We explain this from the structural arrangement induced by nitrogen doping leading to the appearance of the layered structure in NCD films at high levels of N<sub>2</sub> concentration [8]. Consequently the highly conducting NCD films prepared with a high N<sub>2</sub> percentage can consist of a large number of layers and show a strong anisotropic nature. From the fitting of the MR data,  $L_{\phi}$  can be extracted whose temperature dependence, *i.e.*,  $L_{\phi} \sim T^{-0.33}$  is plotted (fig. 5(a)) which is similar to that obtained from  $G(T)$ . These results confirm the applicability of the anisotropic 3D WL model to explain the conduction mechanism of highly conducting NCD-N<sub>2</sub> films in the low-to-intermediate temperature range. Now we attempt to show the effect of disorder on the proposed quasi-SL model and investigate the origin of the observed activated conduction in NCD20N<sub>2</sub> films, which appeared as a result of nitrogen

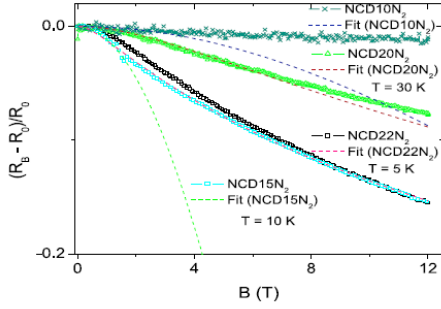


Fig. 6: (Colour on-line) MR data for NCD samples fitted with the B-K model at different temperatures.

incorporation. The band diagram is typical of a disordered superlattice-like structure formed by nano-diamond grains ( $sp^3$ ) and  $sp^2$  carbon layers mainly in the GB. Transport calculations on N-doped disordered carbon SL structures are presented in ref. [10]. Increase in nitrogen in the films results in the widening of GB, which consequently increases the  $sp^2$  layers and hence leads to an increase in the coupling of the diamond grains. In addition to that some nitrogen defects states are also introduced which might explain the activated behaviour in some samples (fig. 5(b)) [3,7].

It is well known that nitrogen incorporation in carbon films introduces  $sp^2$ -bonded clusters [8]. The microstructure of NCD films shows confined  $sp^2$  structures between nano-diamond crystals [8], which can also be treated as a quasi-SL structure consisting of a non-periodic array of conducting ( $sp^2$ ) layers. Some details of our proposed model can be found in our other report [10]. In this regard the microstructure is different to the conventional superlattice structure of compound semiconductors but similar to layered metals or superconductors which show strong anisotropic conductivities. Furthermore the density of planes increases with nitrogen concentration, which corresponds to an increase of coupling between planes that can be explained fairly well by a quasi-SL model [17,18]. We nevertheless point out that the disorder strength can be modified with the change of periodicity. In addition, we believe the highly conducting NCD samples belong to a family of diffusive (or weakly localized) transport regime and the small effect of activation can appear due to the energy difference between the nitrogen level and the conduction band (CB) (1st miniband) of the proposed quasi-SL (see fig. 5(b)) [10]. This concept has been verified from the MR study (see fig. 4 and also in ref. [10]). A transition from VRH to WL has already been shown through the intentional introduction of disorder to artificial SL structures [17,18].

To identify the effect and quantify the degree of disorder in the NCD samples we applied the Bryksin-Kleinert (B-K) model (fig. 6) and analyzed the MR data for all

samples [19]. At low temperatures the electronic transport mechanisms are dominated by elastic scattering from defects, impurities and electron-electron interactions. The B-K model showed in a self-consistent theory that the ratio of the scattering times ( $\frac{\tau_0}{\tau}$ ), where  $\tau$  and  $\tau_0$  correspond to the renormalized and elastic scattering times, respectively, would be a function of the anisotropy factor [19]. In that model (B-K) two guiding anisotropy parameters are used, *i.e.*  $\alpha$ , defined earlier and  $\gamma = (1/\alpha) (k_z/k_{||})$  in which  $k_z$  is the momentum cutoff parameter of the wave vector  $k_z = 1/(v_F\tau_e)$  for any arbitrary field orientation [19]. Since the field was perpendicular to the samples only one anisotropy factor is used. Moreover, there is no restriction on the value of the disorder parameter, *i.e.*  $q = k_F\lambda$ . In this expression  $\lambda$  and  $k_F$  are the electron mean free path and Fermi wave vector, respectively, which can vary from sample to sample, namely from NCD10N<sub>2</sub> to NCD22N<sub>2</sub> films (see fig. 1(b)) and is actually a measure of disorder.

For small disorder *i.e.*  $k_F\lambda \gg 1$  (*i.e.* in NCD22N<sub>2</sub> samples) the self-consistency of the theory with respect to the renormalized scattering time  $\tau$  might be disregarded yielding the corresponding conductivity expression through the Einstein relation  $\sigma_{||} = e^2 D_{||} N(E_F)$  to be  $\sigma_{||} = e^2 D_0 \frac{\tau}{\tau_0} N(E_F) = \sigma_0 \frac{\tau}{\tau_0}$ , where  $D_0 = \frac{1}{2} v^2 \tau_0$ . Hence the parallel component of conductivity is expressed as a function of the ratio  $\frac{\tau}{\tau_0}$ , implying a strong dependence on the anisotropy in the material. The conductance pre-factor  $G_0$  taken from the best fit of  $G$ -*vs.*- $T$  data (using eq. (1)) was considered as the Drude contribution  $\{\sigma_0 = e^2 D_0 N(E_F)\}$ . For the metallic regime (*e.g.*, NCD20N<sub>2</sub> and NCD22N<sub>2</sub> samples)  $G_0$  was estimated on the basis of a constant term in the  $G$ -*vs.*- $T$  fitting. For hopping transport expressed as  $G(0, T) = G_{min} \exp(-(\frac{T_0}{T})^{0.25})$ , applicable to NCD10N<sub>2</sub> and NCD15N<sub>2</sub> samples, the estimation of  $G_0$  was based on the  $G_{min}$  prefactor, which had been considered as an analogue of  $G_0$  in the metallic range. Further simplification was made by keeping the small disorder condition even in the hopping range and by replacing the renormalized scattering time  $\tau$  with  $\tau_0$ . The results of the fit to the MR data for a set of NCD films prepared with different N<sub>2</sub> percentage based on the B-K model (given explicitly in ref. [19]) are shown in fig. 6. This model was found to work well at low fields. We took a constant value of  $\alpha$  given by a PFS model fit for NCD22N<sub>2</sub> samples (see eq. (3)), which is considered nearly the same for all samples. The value of disorder parameter  $q \approx k_F\lambda$  is found to increase with conductivity of the NCD samples from 0.7 to 1.2, shown in inset of fig. 1(c). A remarkable similarity between the conductance *vs.* N<sub>2</sub> concentration (measured at 56 K) curves and the  $q$ -*vs.*-N<sub>2</sub> curve has been found, which clearly establishes the role of disorder in controlling transport in NCD films (fig. 1(c)). This analysis is found to be consistent with the Raman spectra of the film structures (fig. 1(b)).

Furthermore the degree of disorder ( $q = 0.95$ ) for NCD20N<sub>2</sub> was a little bit less than unity symbolizing the

position of the  $E_F$  in the localized states tails. Therefore, electrons require some activation energy to reach the extended states as found from the Arrhenius plots. For NCD10N<sub>2</sub> and NCD15N<sub>2</sub> samples,  $q$  is found to be much less than unity, which means the disorder effect is large and the hopping conduction can be dominant. The level of disorder found in NCD films from transport data analysis is consistent with the analysis of Raman spectra of the samples (figs. 1(a) and (b)). The disorder level in the films is found to decrease with the increase of N<sub>2</sub>% used for the synthesis of the samples that increases the conductivity of the films. This difference of  $q$  suggests a possibility for a M-I transition in NCD20N<sub>2</sub> to NCD10N<sub>2</sub> samples. From the analysis of B-K model we revealed that the temperature dependence of  $\tau_\phi$  is much weaker for the insulating regime of NCD films than for conducting one. The value of  $D$  is also found to decrease from 0.001 m<sup>2</sup>/s to 0.0007 m<sup>2</sup>/s as the samples change from the metallic to the hopping region. The elastic scattering time  $\tau_0$  is  $\sim 32$  fs for all samples. Most importantly,  $\tau_\phi$  increases by an order of magnitude in these samples at a comparable value of the temperature (from 0.028 ps at 10 K in NCD15N<sub>2</sub> to 0.5 ps at 5 K in NCD22N<sub>2</sub>). Such a long dephasing time and its weak temperature dependence show that these films are potential candidates for fast-switching devices.

In conclusion, we have shown a conductivity crossover and related transport features in HFCVD-grown NCD films which has not been seen so clearly in other NCD films. Within a large temperature range the electrical transport for all samples can be described by a disordered (non-periodic) quasi-SL model which can also explain the transport properties of amorphous carbon films [20] having a certain degree of disorder. The conduction for the NCD20N<sub>2</sub> films is typical of semiconductors where thermal activation predominates, while in the NCD22N<sub>2</sub> films we have a semi-metallic behavior in which electron-electron interactions and 3D WL are corrections to the conductivity with the former dominating at low temperatures. We also observed a weak temperature dependence of the dephasing time, *i.e.*,  $\tau_\phi \sim T^{-0.7}$ , which, to our knowledge, has been reported only in artificial superlattices [18]. Such behavior will give a longer dephasing time in these films, a property which might help to realize these films in high-speed electronic devices. Furthermore, we have found the variation of the disorder level derived from the conductivity analysis in the samples is consistent with the Raman analysis. The low activation energy for the NCD20N<sub>2</sub> films is due to both the effect of disorder and the presence of a shallow impurity band below the conduction band which is observed only in HFCVD films. This study in nano-diamond films lays a foundation for a class of novel fast-switching devices and establishes the known conduction models even in HFCVD films, whose GB phase is different from that of MPCVD-grown films.

\*\*\*

The authors are thankful to R. M. ERASMUS for Raman spectroscopy and R. MCINTOSH for correcting the manuscript. SB thanks the NRF (SA) for granting the Nanotechnology Flagship Programme to perform this work and the University of the Witwatersrand Research Council for financial support.

## REFERENCES

- [1] WILLIAMS O. A., NESLADEK M., DAENEN M., MICHAELSON S., HOFFMAN A., OSAWA E. and HAENEN K. JACKMAN R. B., *Diam. Relat. Mater.*, **17** (2008) 1080.
- [2] MARES J. J., NESLADEK M., HUBIK P., KINDL D. and KRISTOFIK J., *Diam. Relat. Mater.*, **16** (2007) 1.
- [3] BHATTACHARYYA S., AUCIELLO O., BIRRELL J., CARLISLE J. A., CURTISS L. A., GOYETTE A. N., GRUEN D. M., KRAUSS A. R., SCHUETER J., SUMANT A. and ZAPOL P., *Appl. Phys. Lett.*, **79** (2001) 1441.
- [4] BHATTACHARYYA S., *Phys. Rev. B*, **70** (2004) 125412; BHATTACHARYYA S., *Phys. Rev. B*, **77** (2008) 233407.
- [5] CHOY T. C., STONEHAM A. M., ORTUNO M. and SOMOZA A. M., *Appl. Phys. Lett.*, **92** (2008) 012120.
- [6] ZAPOL P., STERNBERG M., CURTISS L. A., FRAUENHEIN T. and GRUEN D. M., *Phys. Rev. B*, **65** (2001) 045403.
- [7] BELOBORODOV I. S., ZAPOL P., GRUEN D. M. and CURTISS L. A., *Phys. Rev. B*, **74** (2006) 235434.
- [8] ARENAL R., BRUNO P., MILLER D. J., BLEUEL M., LAL J. and GRUEN D. M., *Phys. Rev. B*, **75** (2007) 195431.
- [9] MAY P. W. *et al.*, *J. Appl. Phys.*, **101** (2007) 053115; *J. Phys. Chem. C*, **112** (2008) 12432.
- [10] SHAH K., CHUROCHKIN D. and CHIGUVARE Z. BHATTACHARYYA S., *Phys. Rev. B*, **82** (2010) 184206; KATKOV M. V. and BHATTACHARYYA S., *J. Appl. Phys.*, **111** (2012) 123711.
- [11] CHIMOWA G., *Synthesis and characterization of nanocrystalline diamond films*, MSc Thesis, University of the Witwatersrand, South Africa (2011).
- [12] FERRARI A. C. and ROBERTSON J., *Phys. Rev. B*, **61** (2000) 14095.
- [13] SHKLOVSKII B. I. and EFROS A., *Electronic properties of Doped Semiconductors* (Springer-Verlag, Berlin) 1984, p. 228.
- [14] DU G., PRIGODIN V. N., BURNS A., JOO J., WANG C. S. and EPSTEIN A. J., *Phys. Rev. B*, **58** (1998) 4458.
- [15] JAISWAL M., WANG W., FERNANDO K. A. S., SUN Y. P. and MENON R., *Phys. Rev. B*, **76** (2007) 113401.
- [16] KAWABATA A., *J. Phys. Soc. Jpn.*, **49** (1980) 628.
- [17] SZOTT W., JEDRZEJEK C. and KIRK W. P., *Phys. Rev. Lett.*, **63** (1989) 1980; CASSM-CHENAI A. and MAILLY D., *Phys. Rev. B*, **52** (1995) 1984.
- [18] PUSEP Y., RIBEIRO A. M. B., ARAKAKI H., DE SOUZA C. A., MALZER S. and DOHLER G. H., *Phys. Rev. B*, **71** (2005) 035323.
- [19] BRYKSIKIN V. V. and KLEINERT P., *Z. Phys. B*, **101** (1996) 91.
- [20] BHATTACHARYYA S. and SILVA S. R. P., *Thin Solid Films*, **482** (2005) 94.